Chemical abundances of metal-poor stars as probes of neutron capture nucleosynthesis

A thesis

submitted for the degree of

Doctor of Philosophy

in

The Department of Physics,

Pondicherry University,

Puducherry - 605 014, India

by

Partha Pratim Goswami

Indian Institute of Astrophysics,

Bangalore - 560 034, India

June 2022

Chemical abundances of metal-poor stars as probes of neutron capture nucleosynthesis

Partha Pratim Goswami

Indian Institute of Astrophysics

Indian Institute of Astrophysics

Bangalore - 560 034, India

Title of the thesis	:	**Chemical abundances of metal-poor stars as probes of neutron capture nucleosynthesis**
Name of the author	:	**Partha Pratim Goswami**
Address	:	Indian Institute of Astrophysics II Block, Koramangala Bangalore - 560 034, India
Email	:	partha.pg@iiap.res.in
Name of the supervisor	:	**Prof. Aruna Goswami**
Address	:	Indian Institute of Astrophysics II Block, Koramangala Bangalore - 560 034, India
Email	:	aruna@iiap.res.in

Declaration of Authorship

I hereby declare that the matter contained in this thesis is the result of the investigations carried out by me at the Indian Institute of Astrophysics, Bangalore, under the supervision of Prof. Aruna Goswami. This work has not been submitted for the award of any other degree, diploma, associateship, fellowship, etc. of any other university or institute.

Signed: 

Date: 12/01/2023

Certificate

This is to certify that the thesis entitled **'Chemical abundances of metal-poor stars as probes of neutron capture nucleosynthesis'** submitted to the Pondicherry University by Mr. Partha Pratim Goswami for the award of the degree of Doctor of Philosophy, is based on the results of the investigations carried out by him under my supervision and guidance, at the Indian Institute of Astrophysics. This thesis has not been submitted for the award of any other degree, diploma, associateship, fellowship, etc. of any other university or institute.

Signed: 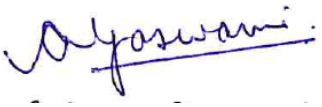

Date: 13.01.2023

List of Publications

7.) **Partha Pratim Goswami**, Aruna Goswami, 2022, "Three Extremely Metal-Poor stars", *Under Preparation*

6.) **Partha Pratim Goswami**, Aruna Goswami, 2022, "Spectroscopic study of Ba and CEMP-s stars: Mass distributions of AGB progenitors", *AJ, Accepted for publication*

5.) **Partha Pratim Goswami**, Aruna Goswami, 2022, "The peculiar abundances of HE 1005-1439. A carbon-enhanced extremely metal-poor star contaminated with products of both *s*-and *i*-process nucleosynthesis", *A&A*, 657, A50

4.) **Partha Pratim Goswami**, Rajeev Singh Rathour, Aruna Goswami, 2021, "Spectroscopic study of CEMP-(s & r/s) stars. Revisiting classification criteria and formation scenarios, highlighting i-process nucleosynthesis", *A&A*, 649, A49

3.) **Partha Pratim Goswami**, Aruna Goswami, 2020, "i-process nucleosynthesis: observational evidences from CEMP stars", *JAA*, 41, 47

2.) J. Shejeelammal, Aruna Goswami, **Partha Pratim Goswami**, Rajeev Singh Rathour, Thomas Masseron, 2020, "Characterizing the companion AGBs using surface chemical composition of barium stars", *MNRAS*, 492, 3708

1.) Meenakshi Purandardas, Aruna Goswami, **Partha Pratim Goswami**, J. Shejeelammal and Thomas Masseron, 2019, "Chemical analysis of CH stars-III. Atmospheric parameters and elemental abundances", *MNRAS*, 486, 3266.

Other publication

1.) Santosh Joshi, Otto Trust, E. Semenko, P. E. Williams, P. Lampens, P. De Cat, L. Vermeylen, D. L. Holdsworth, R. A. García, S. Mathur, A. R. G. Santos, D. Mkrtichian, A. Goswami, M. Cuntz, A. P. Yadav, M. Sarkar, B. C. Bhatt, F. Kahraman Aliçavuş, M. D. Nhlapo, M. N. Lund, **P. P. Goswami**, I. Savanov, A. Jorissen, E. Jurua, E. Avvakumova, E. S. Dmitrienko, N. K. Chakradhari, M. K. Das, S. Chowdhury, O. P. Abedigamba, I. Yakunin, B. Letarte, D. Karinkuzhi, 2022, "Study of Chemically Peculiar Stars-I: High-resolution Spectroscopy and K2 Photometry of Am Stars in the Region of M44", *MNRAS*, 510, 5854.

Presentations

International Conferences

Oral Presentations:

2.) **Title of the talk:** Nucleosynthesis in Carbon Enhanced Metal Poor Stars
Conference: One day Indo-Thai Workshop on "Investigating the Stellar Variability and Star Formation", 2nd March, 2020, ARIES, Nainital, India

1.) **Title of the talk:** i-process nucleosynthesis: observational evidences from CEMP stars
Conference: 150 years of the periodic table: "Chemical elements in the Universe: origin and evolution", 16−19 December, 2019, IIA, Bangalore, India.

National Conferences

Oral Presentations:

3.) **Title of the talk:** An extremely metal-poor star, contaminated with products of both *i*- and *s*-process nucleosynthesis
Conference: 21st National Space Science Symposium, 31st January – 4th February, 2022, IISER Kolkata, India

2.) **Title of the talk:** Metal-poor stars and neutron-capture nucleosynthesis
Conference: ASI 2020, 13−17 February, 2020, IISER Tirupati, Tirupati, India

1.) **Title of the talk:** CEMP-r/s stars and intermediate neutron-capture process.
Conference: Young Astronomers' Meet 2019, 23−27 September, 2019, Kodaikanal Solar Observatory, IIA Kodaikanal, India

Poster Presentations:

3.) **Title of the poster:** HE 1005-1439: observational evidences for a new site where *i*- and *s*-processes operate in succession
Conference: ASI 2022, 25–29 March, 2022, IIT Roorkee, India

2.) **Title of the poster:** Spectroscopic Study of Carbon-Enhanced Metal-Poor stars
Conference: HCT 20 Meeting, 29−30 September, 2020, IIA, Bangalore, India

1.) **Title of the poster:** Chemical analysis of HE 0308−1612 and HE 0017+0055
Conference: ASI 2019, 18−22 February, 2019, Bangalore, India

In-house Conference

Poster Presentation:

1.) **Title of the poster:** Spectroscopic study of CEMP-(s & r/s) stars: classification criteria and formation scenarios
Conference: IIA in-house Meeting, 17 – 18 June 2021, IIA, Bangalore, India

Acknowledgements

I am greatly honoured to acknowledge and express my sincere gratitude to my supervisor Prof. Aruna Goswami, Indian Institute of Astrophysics, under whose guidance, suggestions and encouragement the thesis has been completed. I consider myself fortunate enough to have availed her guidance at every step of my PhD journey.

I am indebted to the Dean, Director and Board of Graduate Studies (BGS) of the Indian Institute of Astrophysics, Bangalore, for giving me the opportunity to pursue my research and contribute to my field of research. I am deeply grateful to my doctoral committee members, Prof. Gajendra Pandey and Dr. K. V. P. Latha, for their invaluable support and guidance during the research process. Their expert suggestions greatly improved the quality of my work. I would like to express my sincere thanks to Shankaranarayanan and Vijayalakshmi for their assistance with the official aspects of my thesis, and to Fayaz and Ashok for their help with computer-related issues. Their expertise and support were crucial to the success of my work, and I am deeply grateful for their contributions.

I would like to offer my special and warmest thanks to my Deuta, Maa, Sister, brother-in-law (Mr. Rananmay Bharadwaj) and all other members of my family without whose blessings, prayers and support this journey of mine would never have been possible. I will always be grateful to all my teachers and mentors throughout my academic life.

I am grateful to my best-friends Mostafizur and Pubali (now fiancée) for their encouragement and help. I cannot thank Mostafizur enough for his financial help, due to which I could attend my PhD interview. Many thanks to you, Pubali, for being with me always.

I would like to convey my gratitude to Shejeela and Meenakshi, Indian Institute of Astrophysics, for their co-operation and guidance in pursuing and completing my research. I am thankful to my batch-mates Athira, Bibhuti, Soumya, Subhankar, Satabdwa, Sharmila, Manika and Suman for their help and co-operation offered to me in completing this work.

I also appreciate the contributions and patience of my roommates- Subhankar, Sandeep and Sayuf. I owe to my seniors viz. Sudip Da, Panini, Rakesh Da, Chayan Da, Samrat Da, Avinash, Manoj, Deepak, Phanindra and Bhoomika di for encouraging me to participate in sports and keeping me physically and mentally fit and healthy. Again, this work would be incomplete without the discourses by Rajeev, Avrajit Da, Raghu and Drisya. I must thank my sisters- Priyanka di, Athira, Deepthi, Sharmila and Saili for their care, support and advice from the beginning of my research. I will remain indebted to the close friends made throughout the journey- Bibhuti, Athira, Ritesh, Priya, Jyoti, Swastik, Shubham, Vikrant, Sharmila, Satabdwa and Bharat who make themselves available whenever I need their help.

I thank all my seniors in Bhaskara and amazing juniors and friends- Ankit, Anirban, Sonith, Fazlu, Indrani, Kshitij, Vishnu, Sioree, Pallavi, Rishabh, Ravi, Anohita, Aratrika, Manju, Sujay, Dhanush, Judhajeet, Neeraj, Sipra, Soumyaranjan, Amrutha, Payel, Anisha, Renu, Khushbu, Sushant, Sunayana, Shubhangi, Nitish, Parvathy, Akhil, Chandan, Rupesh, Pravash, Ameya, Shivani and Kajol. Special thanks to buddies Sharmila, Shubham, Satabdwa and Bharat for making the thesis writing days light and stress-free.

Last but not the least I am thankful to all who have offered their self-less help and time to make this journey of mine wonderful and a successful one.

-Partha 

Data usage

We have acquired spectra of several stars using Hanle Echelle Spectrograph (HESP) attached to Himalayan Chandra Telescope (HCT) at the Indian Astronomical Observatory (IAO) in Hanle. The HCT is remotely controlled from CREST, Hosakote. The IAO and CREST are operated by the Indian Institute of Astrophysics. We would like to convey our gratitude to the staff of IAO and CREST.

We have used archival data from European Southern Observatory (ESO) acquired using FEROS/ESO. We thank the ESO team for the data.

The study is based [in part] on data collected at Subaru Telescope, which is operated by the National Astronomical Observatory of Japan. [Part of] the data are retrieved from the JVO portal (`http://jvo.nao.ac.jp/portal`) operated by the NAOJ.

We are thankful to Melanie Hampel for providing us with the *i*-process yields in the form of number fractions. This work made use of the SIMBAD astronomical database, operated at CDS, Strasbourg, France, the NASA ADS, USA and data from the European Space Agency (ESA) mission Gaia (`https://www.cosmos.esa.int/gaia`), processed by the Gaia Data Processing and Analysis Consortium (DPAC, `https://www.cosmos.esa.int/web/gaia/dpac/consortium`).

Dedicated to

Maa (Bijuli Devi Goswami), Deuta (Late Debendra Ch. Goswami), Maina (Juriti Goswami) and fiancée (Pubali Barthakur)

Abstract

After more than six decades of the pioneering work of Burbidge, Burbidge, Fowler and Hoyle (1957), which first suggested the production channels and the evolution of neutron-capture elements, many details still remain far from being fully understood. As we go more and more towards the metal-poor regime, the abundances of heavy elements show larger and larger scatter that still can not be explained either by abundance estimates uncertainties or based on the existing theories of nucleosynthesis and evolution. The diverse abundance ratios of neutron-capture elements observed in metal-poor stars demand a comprehensive study of the origin and evolution of heavy elements and the abundance pattern exhibited by these elements. The problem can be best addressed through chemical composition studies of stars that exhibit high abundances of heavy elements. Prompted by this idea, we have undertaken to probe the origin and evolution of heavy elements produced by neutron-capture nucleosynthesis processes from a detailed chemical composition study by considering a large sample of potential metal-poor star candidates. Such studies are currently lacking. We have selected twenty potential metal-poor star candidates from various catalogues of metal-poor stars that include the following objects: BD+75 348, BD+09 3019, CD–27 14351, HD 87853, HD 145777, HD 147609, HD 154276, HD 238020, HE 0017+0055, HE 0308–1612, HE 0319–0215, HE 0401–0138, HE 0507–1653, HE 0930–0018, HE 1005–1439, HE 1023–1504, HE 1153–0518, HE 1246–1344, HE 2144–1832 and HE 2339–0837. For this sample, the stellar atmospheric parameters, the effective temperature T_{eff}, the microturbulent velocity ξ, the surface gravity log g, and the metallicity [Fe/H] are derived from local thermodynamic equilibrium analyses using model atmospheres. The sample is found to cover metallicity in the range -0.28 to -3.5 and one object with near solar metallicity. Elemental abundances of C, N, O, α-elements, iron-peak elements, and several neutron-capture elements are estimated using the equivalent width measurement technique as well as spectrum synthesis calculations in some cases. In cases

when the estimates of abundances could not be determined, the upper limits of abundances are estimated whenever possible. From a detailed chemical analysis, we have identified in our sample, one normal metal-poor star, five Ba stars, one CH star, six Carbon-Enhanced Metal-Poor (CEMP)-s stars, three CEMP-r/s stars, one CEMP-no star, two Extremely metal-poor stars, and one unique CEMP star that may be called as CEMP-i/s star. The results presented in this thesis are based on our investigations that include the first time chemical composition studies of twelve objects, updates on abundance estimates of several key elements based on high resolution (R $\geq$ 48,000) spectra and complemented by a comprehensive analysis of compiled literature abundance data of a few hundred objects. The high-resolution spectra were obtained using HCT/HESP, SUBARU/HDS and the Fiber-fed Extended Range Optical Spectrograph (FEROS).

Among the CEMP stars, the so-called CEMP-r/s stars are known to exhibit enhancement of both slow (s-) and rapid (r-) process elements in their surface chemical composition. For these stars, the heavy element abundances cannot be explained either by s-process or r-process nucleosynthesis alone. These two processes produce distinct abundance patterns, as the production sites of s- and r-process elements are very different. Our analysis shows three objects in our sample, HE 0017+0055, HE 2144–1832 and HE 2339–0837, to be bonafide CEMP-r/s stars. These three objects and the objects CD$-$27 14351, HE 0308–1612, HE 0319–0215, HE 0507–1653 and HE 0930–0018 were previously claimed as potential CH star candidates based on low-resolution spectroscopy. To better understand their formation mechanisms using the chemical signatures, we have performed a detailed systematic follow-up spectroscopic study based on high-resolution spectra. In the context of the double enhancement observed in the CEMP-r/s stars, we have discussed all the possible formation scenarios and critically examined if the i-process (intermediate process) nucleosynthesis, that occurs at a high neutron-density (n $\sim 10^{15} cm^{-3}$) could explain the observed abundance patterns. The required high neutron density can be attained during proton-ingestion from a H-rich envelope to the intershell region of an AGB star and is capable of producing both r-

and s-process elements in a single stellar site. We have further extended this study to a sample of eight CEMP-r/s stars from literature to trace the origin of the observed double enhancement. Our analysis shows that the observed abundance patterns of all the CEMP-r/s stars, under this study, could be reproduced fairly well using the i-process model yields.

Among the CEMP stars, distinguishing the CEMP-s and CEMP-r/s stars is crucial in order to understand the physical and nucleosynthetic processes responsible for the abundance patterns of the two subclasses. The CH, CEMP-s and CEMP-r/s stars in our sample show enhanced abundance of Ba and seven of them exhibit enhanced abundance of Eu ([Eu/Fe] $>$ 0.70). Based on our analysis, while three stars are found to show characteristic properties of CEMP-r/s stars, HE 0308–1612 shows characteristic properties of CH stars, and the rest show characteristic properties of CEMP-s stars. However, the object HD 145777 is found to fall into different subclasses when classified based on the different classification schemes put forward by different groups of authors. To remove the uncertainties and clear the confusion regarding its classification, we have revisited the classification schemes of CEMP-s and CEMP-r/s stars found in the literature. From a detailed investigation of different classifiers of CEMP stars, we have seen that none of the existing classification criteria could clearly distinguish the CEMP-s and CEMP-r/s stars. We have put forward a new classification scheme to distinguish the two subclasses. We found that for both CEMP-s and CEMP-r/s stars, [Ba/Eu] and [La/Eu] exhibit positive values and [Ba/Fe] $\geq$ 1.0. However, CEMP-r/s stars satisfy [Eu/Fe] $\geq$ 1.0, 0.0 $\leq$ [Ba/Eu] $\leq$ 1.0, and/or 0.0 $\leq$ [La/Eu] $\leq$ 0.7. CEMP-s stars normally show [Eu/Fe] $<$ 1.0 with [Ba/Eu] $>$ 0.0 and/or [La/Eu] $>$ 0.5. If [Eu/Fe] $\geq$ 1.0, then the condition on [Ba/Eu] and/or [La/Eu] for a star to be a CEMP-s star is [Ba/Eu] $>$ 1.0 and/or [La/Eu] $>$ 0.7.

Using a large sample of CEMP-s and CEMP-r/s stars from the literature we have examined whether the ratio of heavy-s to light-s process elements [hs/ls] can be used as a classifier. In particular, we have examined if there are any limiting values for

[hs/ls] that can be used to distinguish between CEMP-s and CEMP-r/s stars. We have critically examined the heavy elements' abundance ratios and found that, the CEMP-s and CEMP-r/s stars peak at different values of [hs/ls]. However, there is an overlap in the range 0.0 $<$ [hs/ls] $<$ 1.5, and hence, this ratio cannot be used to distinguish between CEMP-s and CEMP-r/s stars. We have noticed a similar overlap in the case of [Sr/Ba] ratios as well in the range $-1.6 <$ [Sr/Ba] < -0.5, and hence this ratio also cannot be used to separate the two subclasses.

Understanding the surface chemical composition of CEMP stars with enhanced abundances of heavy elements still remained problematic. The peculiar abundance pattern observed in the carbon-enhanced extremely metal-poor (EMP) object HE 1005–1439 in our sample was surprisingly found to be enriched with products of both s-process and i-process nucleosynthesis. Observation of such a unique abundance pattern is the first of its kind and certainly points to the discovery of a new class of objects. Nevertheless, understanding the origin of the surface chemical composition of this object posed a real challenge. To address this problem, we have performed a detailed high-resolution spectroscopic analysis of the object using SUBARU/HDS spectra at a resolution of (R $\sim$ 50,000). We have measured the abundances of all the elements that we could estimate for this object. The elemental abundance estimates include ten light elements from C through Ni and twelve heavy elements Sr, Y, Ba, La, Ce, Pr, Nd, Eu, Dy, Er, Hf, and Pb. In order to understand the origin of the observed abundance pattern, we have performed a parametric-model-based analysis of the abundances of the heavy elements. The results of our analysis clearly showed that the surface chemical composition of the object has contributions from both the s-process and i-process nucleosyntheses. We have critically examined the observed abundances and carefully investigated the formation scenarios involving the s-process and the i-process that are available in the literature. We found that neither s-process nor i-process nucleosynthesis alone could explain the observed abundances. We have noted that the radial velocity estimates obtained from several epochs showed variations, and that may be an indication of the presence of a binary companion. Hence, considering a binary system, we proposed a

formation scenario for this object involving effective proton ingestion episodes (PIEs) triggering i-process nucleosynthesis followed by s-process nucleosynthesis with a few third-dredge-up (TDU) episodes in the now extinct companion AGB star. Although based on the CEMP stars' classification criteria, the star is found to belong to CEMP-s category; the observed abundance pattern could not be explained based on the theoretical s-process model predictions. On the contrary, our parametric-model based analysis clearly indicates that the surface chemical composition of the object is influenced by similar contributions from both the s- and i-processes.

Among the fundamental stellar parameters, the mass of a star is the most fundamental parameter and plays a crucial role in its structure, evolution and final fate. We have estimated the masses of the barium stars and the masses of the primary companions of both the barium and the CEMP-s stars in our sample. All the stars show enhanced abundances of heavy elements. We have classified five objects BD+75 348, BD+09 3019, HD 147609, HD 154276 and HD 238020, as Ba stars and CD–27 14351, HD 145777, HE 0319–0215, HE 0507–1653, HE 0930–0018 and HE 1023–1504 as CEMP-s stars. Out of the five Ba stars, HD 154276 and HD 238020 are found to be mild Ba stars, and the other three as strong Ba stars. Using the HR diagram, we have estimated the mass distribution of Ba stars, compiling the data of 205 Ba stars found in the literature along with the barium stars studied here. The average value of the mass distribution is found to be at 1.9 $M_{\odot}$. We have also estimated the initial masses of the companion AGBs of the programme stars with the help of a parametric-model-based analysis using FRUITY models. The same analysis is used to estimate the masses of the companion AGBs of 159 Ba and 36 CEMP-s stars found in the literature. The mass distribution of companion AGBs of Ba stars shows different peaks for mild and strong Ba stars. While the primary mass distribution of mild Ba stars peaks at 3.7 $M_{\odot}$, for the strong Ba stars, the peak appears at 2.5 $M_{\odot}$. We, therefore, propose that the initial masses of the progenitor AGBs of the Ba stars dominantly control the formation of the mild and the strong Ba stars. However, there is a clear overlap between the progenitor masses of both the subclasses of Ba stars in the mass range 1.3 to 4.0 $M_{\odot}$.

So, the contributions of other factors such as metallicities and the orbital periods in the formation of the mild and the strong Ba stars may not be negligible. The progenitor AGBs' mass distribution of CEMP-s stars is found to peak at 2.04 $M_{\odot}$.

The main results obtained from the above studies appeared in parts in several research papers: Purandardas et al., MNRAS, 486, 3266 (2019), Shejeelammal et al., MNRAS, 492, 3708 (2020), Goswami & Goswami, JAA, 41, 47 (2020), Goswami et al., A&A, 649, A49 (2021), Goswami & Goswami, A&A, 657, A50 (2022), Goswami & Goswami, AJ, (2022, Accepted for publication).

Contents

List of Figures

List of Tables

Abbreviations

AGB	**A**symptotic **G**iant **B**ranch
CCD	**C**harge **C**oupled **D**evice
ESO	**E**uropean **S**outhern **O**bservatory
FEROS	**F**iber-fed **E**xtended **R**ange **O**ptical **S**pectrograph
HCT	**H**imalayan **C**handra **T**elescope
HDS	**H**igh **D**ispersion **S**pectrograph
HESP	**H**anle **E**chelle **SP**ectograph
IAO	**I**ndian **A**stronomical **O**bservatory
IRAF	**I**mage **R**eduction and **A**nalysis **F**acility
NASA	**N**ational **A**eronautics and **S**pace **A**dministration
TDU	**T**hird **D**redge **U**p
UT	**U**niversal **T**ime
CEMP	**C**arbon **E**nhanced **M**etal-**P**oor
PIE	**P**roton **I**ngestion **E**pisode
MHD	**M**agneto-**H**ydro **D**ynamic
FRUITY	**F**Ull-Network **R**epository of **U**pdated **I**sotopic **T**ables & **Y**ields
WD	**W**hite **D**warf
RAWD	**R**apidly **A**ccreting **W**hite **D**warf
SDSS	**S**loan **D**igital **S**ky **S**urvey
SEGUE	**S**loan **E**xtension for **G**alactic **U**nderstanding and **E**xploration
LAMOST	**L**arge Sky **A**rea **M**ulti-**O**bject Fiber **S**pectroscopic **T**elescope
LSR	**L**ocal **S**tandard of **R**est

Chapter 1

Introduction

Understanding the chemical and dynamical evolution of our Galaxy (galaxies) is one of the important aspects of contemporary astrophysics. In the past few decades or so, progress in the understanding of chemical evolution of our Galaxy came mainly from observations, i.e., from the chemical composition of stars belonging to the different components of our Galaxy (disk, halo, and bulge). The chemical compositions of stars provide detailed abundance patterns that reveal, in principle, the chemical history of our universe.

The nuclei of the lightest elements in the periodic table, hydrogen (H), helium (He), and lithium (Li), formed between three to twenty minutes after the Big Bang with the mass-densities of 75%, 25%, 2.3×10^{-7}%, respectively (Spergel *et al.* 2007). Neutral atoms of H and He formed 400,000 years after the Big Bang, whereas the first stars in the universe formed after around 400 million years. These stars, commonly known as population III stars, were extremely massive and short-lived (Bromm *et al.* 2002). Soon, they exploded as supernovae and enriched the universe with heavier elements. The next generation of stars, known as Population II

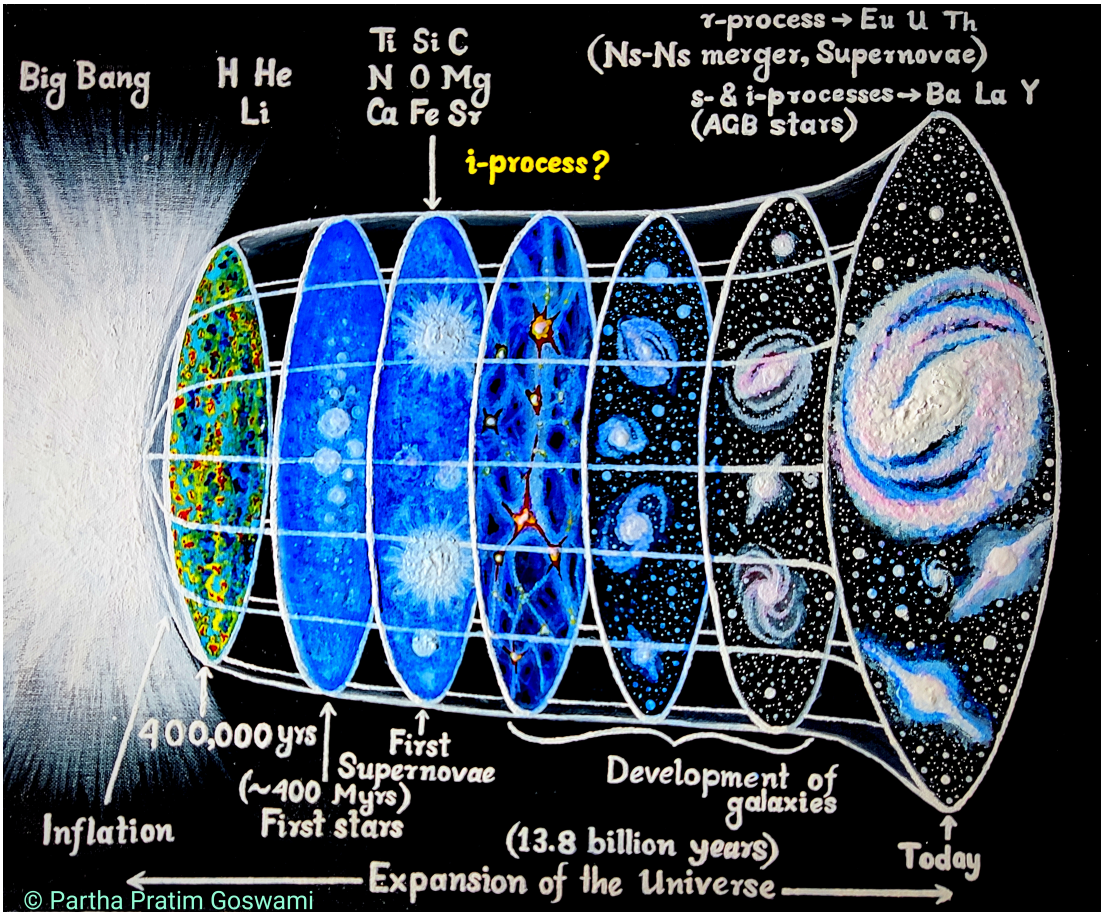

FIGURE 1.1: Artistic impression of the chemical evolution of the universe. Painted on a 16×20 (inches) canvas with acrylic colours. Image credit: Partha Pratim Goswami.

stars, formed with the metal ejecta of the first stars (Larson 1998; Bromm and Larson 2004). Subsequent generations of stars have provided the universe with the present-day metal content (Portinari *et al.* 1998). However, many details about the production and evolution of the elements, especially the elements heavier than iron, still remain poorly understood. Figure 1.1 shows an artistic impression of the chemical evolution of the universe known till date.

1.1 Metal-Poor Stars

The observable metal-poor stars are population II (pop II) stars, which are formed from the ejected material of the first stars in the universe. They carry the relics of the early universe providing the archaeological verification for the early epochs (Frebel 2018). As these stars are not polluted by several generations of star formation, we can trace back the origin of the elements by studying the chemical compositions of metal-poor stars. The Pop II stars with < 0.8 $M_{\odot}$ have lifetimes of about 15–20 billion years, and these stars are still in their main-sequence phase keeping the birth composition unaltered (Frebel and Surman 2020). The search for these stars is still on.

It was assumed till the end of the 1940s that all the stars would have the same metal content as that of the sun. Chamberlain and Aller (1951), with the help of detailed spectroscopic analysis, showed that the peculiarities observed in HD 19445 and HD 140283 could be explained by considering the metal content of these stars to be a factor of 10 less compared to that of the sun. Several other studies of the "weak-lined stars" revealed different metallicities of the stars and also that they signify different epochs of their evolution. Schwarzschild and Schwarzschild (1950) and Roman (1950) demonstrated that the "weak-lined stars" have higher space velocities than the other stars. Later, Eggen *et al.* (1962) also claimed the existence of a strong correlation between the metallicity and the orbital eccentricities of the stars and which marked the beginning of the era of investigating such stars. Search for the metal-poor stars on a large scale started with the low-resolution (5–15 Å), wide-angle spectroscopic surveys known as objective-prism surveys. The HK survey by Beers *et al.* (1985, 1992) was the first objective-prism survey for a systematic search of the metal-poor stars. This was then followed by the Hamburg/ESO survey (HES) (Wisotzki *et al.* 1996; Beers *et al.* 1999; Christlieb *et al.* 2001, 2008). In these surveys, the strength of the Fraunhofer

line Ca II K 3933.66 Å as a function of temperature is used to identify the metal-poor stars. To confirm the metal-deficient nature of the selected stars, medium resolution spectra (R $\sim$ 2000) are used. In the more recent searches, such as the SDSS and its follow-up the SEGUE surveys, slightly modified techniques are being used, where large multi-object spectrographs are used at intermediate resolution (R $\sim$2000) to survey a large part of the sky. While the LAMOST survey (Deng *et al.* 2012) is currently exploring Northern Hemisphere in search of metal-poor stars, SkyMapper Southern Sky Survey (Keller *et al.* 2007a,b) is searching for metal-poor stars in the Southern Hemisphere. After finding the metal-poor candidates, high-resolution (R > 20,000) follow-up study of these stars can provide the detailed parameters and abundances of the elements. The most iron-poor star found till date, SM 0313–6708, is with [Fe/H][†] < –7.3 (Keller *et al.* 2014). Depending on [Fe/H], stars are classified in different subclasses (Beers and Christlieb 2005; Frebel 2018). The definition and nomenclatures of metal-poor stars used in the thesis are adopted from Frebel (2018) (Table 1.1).

The metal-poor stars in Globular Clusters (GCs) (Kraft *et al.* 1997; Ivans *et al.* 2001; Gratton *et al.* 2004) and Ultra Faint Dwarf (UFD) galaxies (Simon *et al.* 2015; Ji *et al.* 2016a; Skúladóttir *et al.* 2020) have also been studied in detail in the last decades as probes of galactic archaeology. Beers and Christlieb (2005) and Jacobson and Frebel (2014) listed out a few hot topics that are being addressed by studying the metal-poor stars. Their lists include- i) the nature of the Big Bang, ii) The nature of the first stars and their mass function, iii) origin, evolution and processes of element production, iv) chemical yields of the early supernovae, v) the process of Galaxy formation and its chemical and dynamical history, vi) a lower limit to the age of the universe, and vii) the astrophysical site(s) of neutron-capture element production. In this thesis, we have tried to understand the last topic, i.e. the origin and evolution of the neutron-capture elements.

[†]**Notation:** $[X/Y] = \log(N_X/N_Y)_* - \log(N_X/N_Y)_\odot$, where N_X and N_Y are number densities.

TABLE 1.1: **Classification of metal-poor stars.**

Description	Definition	Abbreviation
Super-metal-rich	[Fe/H]>0.0	MR
Solar	[Fe/H]<0.0	None
Metal-poor	[Fe/H]<–1.0	MP
Very metal-poor	[Fe/H]<–2.0	VMP
Extremely metal-poor	[Fe/H]<–3.0	EMP
Ultra-metal-poor	[Fe/H]<–4.0	UMP
Hyper-metal-poor	[Fe/H]<–5.0	HMP
Mega-metal-poor	[Fe/H]<–6.0	MMP
Septa-metal-poor	[Fe/H]<–7.0	SMP
Octa-metal-poor	[Fe/H]<–8.0	OMP
Giga-metal-poor	[Fe/H]<–9.0	GMP
Ridiculously metal-poor	[Fe/H]<–10.0	RMP

Note: This classification is adopted from Frebel (2018).

1.2 Neutron (n)-Capture Nucleosynthesis

The elements from helium (He) to iron (Fe) are produced mainly by fusion (Bethe 1939). As the atomic number increases, the number of protons inside the elements' nuclei increases, increasing the coulomb barrier (Burbidge *et al.* 1957). Also, the binding energy per nucleon increases up to iron, and then it starts decreasing. So, fusion (if possible) would absorb rather than release energy for synthesising elements heavier than iron. As we know, fusion inside stars balances the collapse due to the self-gravity of the stars by releasing energy. Therefore, the elements heavier than Fe cannot be produced by fusion. These elements are produced by n-capture nucleosynthesis (Cowan and Sneden 2006). As neutrons are electrically neutral, an atomic nucleus can capture neutrons to produce heavier isotopes. These isotopes then undergo β-decay, a process that transforms one neutron into a proton,

resulting in the creation of heavier elements. Based on the timescales of *n*-capture and β-decay, classically, two processes of *n*-capture nucleosynthesis are known, namely '*s*' or slow and '*r*' or rapid *n*-capture processes. Whereas in *s*-process, the *n*-capture timescale is much longer than the β-decay timescale of the unstable isotopes (Busso *et al.* 1999), the opposite is the case for *r*-process (Cowan *et al.* 2021). A third type of *n*-capture process, known as '*i*' or intermediate *n*-capture process, has been suggested recently (Cowan and Rose 1977; Hampel *et al.* 2019). This process is proposed to operate at a neutron-density intermediate to that of *s*- and *r*-processes.

The abundance pattern of a *n*-capture process depends upon the *n*-capture cross-sections of the isotopes. Some isotopes have very low *n*-capture cross-sections, and the abundances pile up for these isotopes. In the shell model of nuclear structure, some particular numbers- 2, 8, 20, 28, 50, 82, 126, are known as "magic numbers" of nucleons (protons and neutrons). The isotopes with magic numbers of nucleons have very low *n*-capture cross-sections. For the elements heavier than Fe, the abundance patterns pile up around the isotopes with magic neutron numbers of 50, 82 and 126. The element ^{208}Pb, with doubly magic nuclei, is specially stable.

1.2.1 *s*-process

The slow *n*-capture process operates at a neutron-density of $n_n \sim 10^{7-10}$ cm^{-3} (Busso *et al.* 1999). This nucleosynthesis process creates three peaks in the abundance pattern. The first peak appears at N = 50, where the elements ^{86}Kr, ^{87}Rb, ^{88}Sr, ^{89}Y and ^{90}Zr are extensively produced. This peak is called the light-*s* process peak. This peak is considered to be formed by the weak component of *s*-process, which gets activated at a very low neutron-exposure, $\tau^{\dagger} = 0.05$ mb^{-1} (Gallino *et al.* 1998b). The 2nd *s*-process peak appears at N = 82, where ^{138}Ba, ^{139}La, ^{140}Ce,

†**Notation:** $\tau = \int n_n v_t dt$, where n_n is neutron-density and v_t is thermal velocity of neutrons.

^{141}Pr, ^{142}Nd and ^{144}Sm are produced. This peak is called the heavy-*s* process peak, which is considered to be formed by main component of *s*-process. The 3rd peak of Pb and Bi at N = 128 is produced by the strong component of *s*-process. The main and strong components get activated at τ = 0.3 mb^{-1} and 7.0 mb^{-1} respectively (Busso *et al.* 1999).

In the stellar systems, the *s*-process is proposed to have occurred in the intershell region of the asymptotic giant branch (AGB) phase of stars. The AGB phase is the final nuclear burning phase of low ($0.8 < M\ (M_{\odot}) < 2.25$) to intermediate-mass ($2.25 < M\ (M_{\odot}) < 10.0$) stars' lifetime (Karakas and Lattanzio 2014). This phase of stellar evolution comes after the He-flash at the tip of the red giant branch (RGB) stage. A star ascends to the giant branch for the first time when it exhausts the core hydrogen during the main-sequence evolution. The AGB phase consists of a CO degenerate core, a He-burning shell surrounding the core, a huge convective envelope, a H-burning shell at the bottom of the convective envelope and an intershell region between the H- and He-burning shells (Karakas and Lattanzio 2014). The intershell region is where all the rich nucleosynthesis takes place in the AGB star. The two nuclear burning shells operate alternatively. Due to the thinness of the shell, the He shell gets turned on violently in a thermal runaway producing a thermal pulse (TP). The TP, which lasts for around 10–100 years, drives convection in the intershell region, and the outer layers are pushed outward, causing the H-burning shell to disappear. After the TP gets over, the convective envelope penetrates deep into the intershell region and mixes the newly synthesised material into the convective envelope. This process is historically known as the third dredge-up (TDU). After the TDU episode, the H-burning shell gets activated, depositing He in the intershell region. When a critical value of He deposition is reached, the He shell gets turned on again, producing a TP. This double shell-burning process continues till the convective envelope is completely lost due to stellar wind. The time period between two TPs is known as an inter-pulse period ($\sim 10^5$ years).

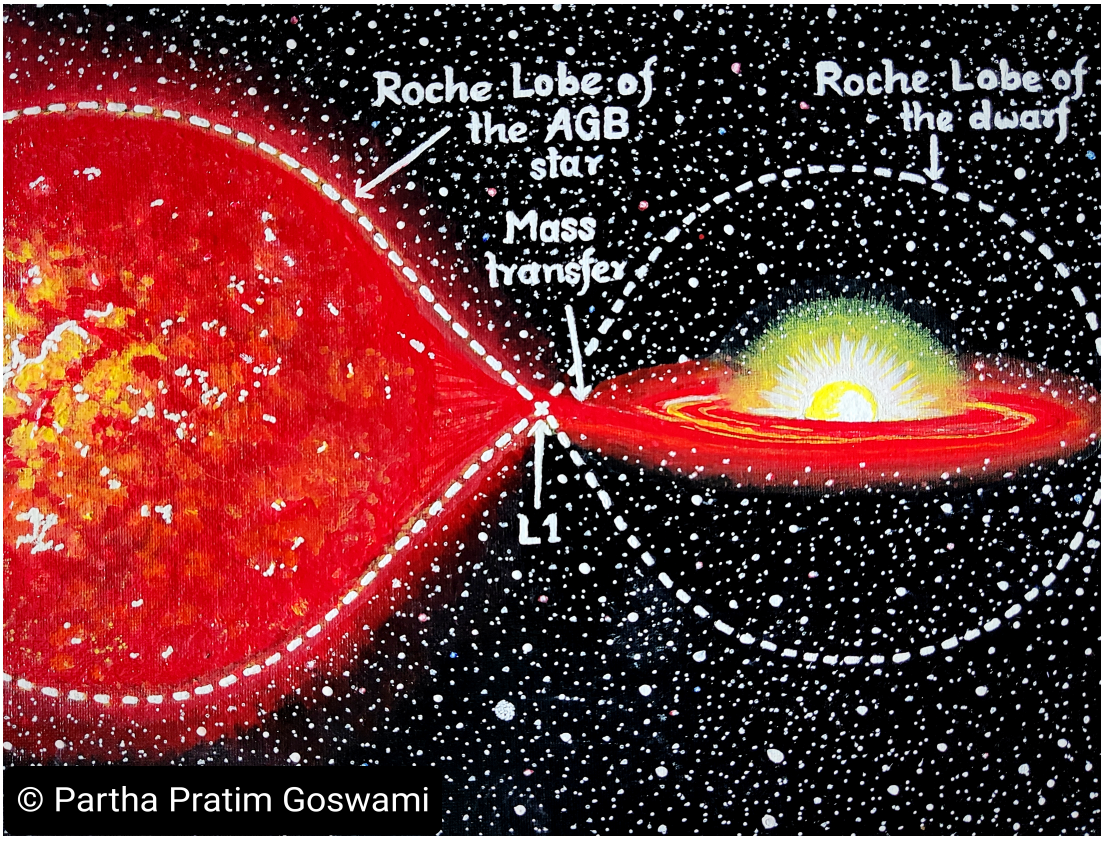

FIGURE 1.2: Artistic impression of the mass-transfer scenario for the formation of *s*-process enriched stars. When the AGB star expands so much that it fills its Roche Lobe, mass-transfer takes place via the Lagrangian 1 (L1) point to enrich the companion main-sequence (dwarf) with *s*-process elements and carbon. Painted on a 9×14 (inches) canvas with acrylic colours. Image credit: Partha Pratim Goswami.

An event known as 'partial mixing of protons' is considered to mix protons near the upper boundary of the intershell region during the inter-pulse period. ^{12}C, present in the intershell region, then captures protons to produce ^{13}N. A ^{13}C pocket is eventually formed in the same region by the β-decay of ^{13}N. The temperature of 1×10^8 K in the region is suitable for the temperature-sensitive reaction ^{13}C (α, n) ^{16}O to take place, which acts as neutron-source for the slow *n*-capture process (Karakas and Lattanzio 2014). Another neutron-source, ^{22}Ne (α, n) ^{25}Mg operates at a temperature of $3{\times}10^8$ K for stars with initial masses more than about 3 $M_\odot$ (Lugaro *et al.* 2012). This neutron-source stay active for a very short time and hence cannot produce enough neutron exposure to produce the heavy-*s* process peak (Gallino *et al.* 1998b). So, the prime neutron source in the intershell region

of AGB stars is the ^{13}C (α, n) ^{16}O reaction. Several mechanisms such as rotation, convective overshooting, and gravity waves have been discussed in the literature (Karakas and Lattanzio (2014) and references therein) to explain the process by which protons are mixed into the intershell region for the ^{13}C pocket formation, but the working of the mixing process is not yet fully understood.

The AGB star gradually loses the envelope with each TP. The material in the convective envelope, which had been previously enriched with *s*-process elements by repeated TDU episodes, now gets transferred to the binary companion (secondary star) via Roche Lobe Over Flow (RLOF) (Figure 1.2) or wind accretion (Abate *et al.* 2013). We observe the secondary star as an *s*-process enriched star, and the primary becomes a white dwarf at the end phase of its evolution.

1.2.2 *r*-process

The rapid *n*-capture process occurs at a neutron-density of $n_n > 10^{22}$ cm^{-3} (Frebel 2018). While the *n*-capture timescale of *s*-process is hundreds to thousand of years, the timescale of *r*-process is of seconds. Eu is the most sought *r*-process element as it is spectroscopically easily detectable. The *r*-process contributes about 94.2 % to the solar Eu abundance (Arlandini *et al.* 1999). The *r*-process abundance pattern in the range $56 \leq Z \leq 70$ is same for all the *r*-process rich stars even if the level of enhancement varies star to star. This universality of *r*-process is known as 'main *r*-process' (Roederer *et al.* 2012). It is noticed in many *r*-process rich stars that the first peak elements and the actinides show high scatter. The scatter of the first peak elements, specially strontium (Sr) goes up to around 1.5 dex (Frebel 2018). This observed deviation of the first peak is considered as the evidence for the existence of multiple *r*-process mechanisms and sites (Sneden *et al.* 2000; Hill *et al.* 2002; Travaglio *et al.* 2004; Hill *et al.* 2017). Due to limited *n*-capture rate, the nucleosynthesis process producing only light *n*-capture elements

(Z < 56) are termed as "weak *r*-process" (Wanajo *et al.* 2001) or "limited *r*-process" (Frebel 2018; Cowan *et al.* 2021). The suggested sites of *r*-process are- the core-collapse supernovae (Schramm 1973; Qian and Woosley 1996; Mirizzi 2015); a magnetorotational magnetohydrodynamical (MHD)-jet supernovae (Symbalisty *et al.* 1985; Obergaulinger *et al.* 2018) or collapsars (Fujimoto *et al.* 2008; Ono *et al.* 2012); and mergers of two neutron-stars (NS-NS) or a neutron-star and a black hole (NS-BH) (Lattimer and Schramm 1974; Eichler *et al.* 1989, 2015; Wu *et al.* 2016; Thielemann *et al.* 2017). The recent detection of gravitational wave GW170817 of the merger of a pair of neutron-stars (Abbott *et al.* 2017) followed by the observation of an accompanying kilonova (Villar *et al.* 2017) have supported the third production site discussed above. However, many details regarding these sites are yet to be understood. The newly discovered *r*-process enriched dwarf galaxies Reticulum II (Ji *et al.* 2016a; Ji and Frebel 2018) and Tucana III (Hansen *et al.* 2017; Marshall *et al.* 2019) are expected to help improve our understanding of the production sites of the elements in the context of galactic archaeology (Frebel 2018; Cowan *et al.* 2021).

1.2.3 *i*-process

The *i*-process operates at a neutron-density, $n_n \sim 10^{15}$ cm^{-3} (Dardelet *et al.* 2014; Roederer *et al.* 2016; Hampel *et al.* 2016; Frebel 2018), intermediate to that of *s*-process and *r*-process. Cowan and Rose (1977) first demonstrated through their simulations that such high neutron-densities can be achieved by adding hydrogen to the convective intershell region in AGB stars. The process now termed as proton ingestion episodes (PIEs) supposedly mixes protons to certain He-rich convective regions where ^{12}C captures protons to produce ^{13}C and the neutron-source ^{13}C (α, n) ^{16}O produces neutron-density sufficient for the operation of *i*-process.

We note that the same neutron-source in the radiative environment produces *s*-process neutron-density. Dardelet *et al.* (2014) and Hampel *et al.* (2016) theoretically calculated *i*-process yields. While Dardelet *et al.* (2014) could reproduce the abundance patterns of three CEMP-*r/s* stars, Hampel *et al.* (2016) reproduced the observed abundances of twenty CEMP-*r/s* stars including the three stars previously studied by Dardelet *et al.* (2014). We will discuss about CEMP-*r/s* stars in more detail in the next section.

The *i*-process sites, where PIEs can take place, still remain a subject of much debate. Stellar sites such as intershell regions of very metal-poor AGB stars (Campbell and Lattanzio 2008; Cristallo *et al.* 2009a; Campbell *et al.* 2010; Stancliffe *et al.* 2011), super-AGB stars (Doherty *et al.* 2015; Jones *et al.* 2016), very late thermal pulse (VLTP) in post-AGB stars (Herwig *et al.* 2011), low-metallicity massive stars (Clarkson *et al.* 2018; Banerjee *et al.* 2018), and rapidly accreting white dwarfs (Denissenkov *et al.* 2017; Côté *et al.* 2018; Denissenkov *et al.* 2019) are some of the proposed sites for the occurrence of *i*-process nucleosynthesis.

1.3 Metal-Poor stars showing enhancement in *n*-capture elements

As discussed in Section 1.1, metal-poor stars found in our Galaxy, GCs and UFDs have been extensively studied to understand the origin and evolution of *n*-capture elements. Chemical abundances obtained for these stars serve as constraints for the theoretical models of *s*-, *i*- and *r*-processes. Here, we have discussed four broad classes of metal-poor stars that show enhancement in heavy elements.

1.3.1 Carbon Enhanced Metal-Poor Stars

This class of metal-poor stars are enhanced in carbon. Among the metal-poor stars, the observed fraction of carbon-enhanced metal-poor (CEMP) stars increases with decreasing metallicity, and it varies between approximately 9 % at [Fe/H] < –2.0 and about 25 % at [Fe/H] < –3.0 (Lucatello *et al.* 2005). While some authors use the carbon enhancement criteria to be [C/Fe] > 1.0 (Beers and Christlieb 2005; Abate *et al.* 2016; Hansen *et al.* 2019), Aoki *et al.* (2007) and Frebel (2018) argue it to be [C/Fe] > 0.7 for $\log(L/L_{\odot}) \leq 2.3$ & [C/Fe] $\geq [3.0 - \log(L/L_{\odot})]$ for $\log(L/L_{\odot}) > 2.3$. In this thesis, we have considered [C/Fe] > 0.7 as the criterion for carbon enhancement. Beers and Christlieb (2005) paved the pathways for classifying these stars depending on the enhancement of *n*-capture elements. Subsequently, many authors (Jonsell *et al.* 2006; Masseron *et al.* 2010; Norris *et al.* 2010; Bisterzo *et al.* 2011; Bonifacio *et al.* 2015; Maeder and Meynet 2015; Yoon *et al.* 2016; Abate *et al.* 2016; Hansen *et al.* 2016c; Frebel 2018; Hansen *et al.* 2019; Skúladóttir *et al.* 2020) have put forward different ways of classifying these CEMP stars.

CEMP-no: These CEMP stars are not enhanced in *n*-capture elements. These stars are identified by the criteria [Ba/Fe] < 0.0 (Beers and Christlieb 2005; Frebel 2018); [Ba/Fe] < 1.0 (Masseron *et al.* 2010); [Ba/Fe] ≤ 1.0 & [Eu/Fe] ≤ 1.0 (Abate *et al.* 2016) and [Sr/Ba] > 0.75 (Hansen *et al.* 2019). Although Hansen *et al.* (2016b) reported a 17 % binary fraction of CEMP-no star in their sample, these stars are mostly found as single stars (Norris *et al.* 2013; Starkenburg *et al.* 2014; Hansen *et al.* 2016b). For the CEMP-*no* stars which are found to be in binary systems, Arentsen *et al.* (2019) suggested that the companion of these stars might have passed through AGB phase without undergoing n-capture nucleosynthesis. Other scenarios put forward to explain the formation of CEMP-*no* stars suggest that these stars originate from the interstellar medium polluted by i) faint supernovae undergoing mixing and fallback (Umeda and Nomoto 2005; Nomoto *et al.*

2013; Tominaga *et al.* 2014), ii) spin stars (Meynet *et al.* 2010; Chiappini 2013), and iii)massive metal-free stars(Heger and Woosley 2010).

CEMP-r: These stars are enhanced in *r*-process elements. Europium is considered as the representative element for *r*-process. These stars are identified by the criteria [Eu/Fe] > 1.0 (Beers and Christlieb 2005); [Ba/Eu] < 0.0 (Masseron *et al.* 2010); [Eu/Fe] > +1.0 & [Ba/Eu] ≤ 0.0 (Abate *et al.* 2016) and [Sr/Ba] < –1.5 (Hansen *et al.* 2019). The *r*-process elements in these stars are proposed to have come either from magnetorotationally MHD jet-driven supernovae or from NS-NS or NS-BH merger events.

CEMP-s: These stars are enhanced in *s*-process elements. Ba & La are considered as representative elements for *s*-process. These stars are identified by the criteria [Ba/Fe] > +1.0 & [Ba/Eu] > 0.5 (Beers and Christlieb 2005); [Ba/Fe] > +1.0 & [Ba/Eu] > 0.0 (Jonsell *et al.* 2006; Masseron *et al.* 2010; Abate *et al.* 2016); [Ba/Fe] > +1.0, [Ba/Eu] > +0.5, [Ba/Pb] > –1.5 (Frebel 2018) and [Sr/Ba] < –1.5 (Hansen *et al.* 2019). The most widely accepted formation scenario for these stars is that they are formed by mass-transfer from companion AGB stars, where carbon and *s*-process elements were synthesised. Several long-term radial-velocity monitoring programmes (McClure 1983, 1984; McClure and Woodsworth 1990; Jorissen *et al.* 1998; Lucatello *et al.* 2005; Jorissen *et al.* 2016b; Hansen *et al.* 2016b; Jorissen *et al.* 2019) have established that CEMP-*s*, CH and barium stars are in binary systems with now invisible white dwarf companions.

CEMP-r/s: This subclass of CEMP stars show enrichment in both *s*- and *r*-process elements. Recent advancements in understanding these stars have led some authors (Hampel *et al.* 2016; Frebel 2018; Hampel *et al.* 2019) to rename this subclass as CEMP-*i*. However, we will use the CEMP-*r/s* nomenclature in the thesis. They are identified by the criteria 0.0 < [Ba/Eu] < 0.5 (Beers and Christlieb 2005); [Eu/Fe] > +1.0, [Ba/Fe] > +1.0, and [Ba/Eu] > 0.0 (Jonsell *et al.*

2006; Masseron *et al.* 2010; Abate *et al.* 2016); 0.0 < [La/Eu] < 0.6 and [Hf/Ir]∼1.0 (Frebel 2018) and –1.5 < [Sr/Ba] < –0.5 (Hansen *et al.* 2019). Numerous formation scenarios are available in the literature (Jonsell *et al.* (2006); Lugaro *et al.* (2009); Abate *et al.* (2016) and references therein) to explain the origin of these stars. These scenarios include radiative levitation, self-pollution (Hill *et al.* 2000; Cohen *et al.* 2003; Jonsell *et al.* 2006) and AGB pollution (Hill *et al.* 2000; Cohen *et al.* 2003; Ivans *et al.* 2005; Jonsell *et al.* 2006; Bisterzo *et al.* 2011) of stars formed from *r*-enriched ISM, a star polluted by a supernova and an AGB in a triple star system (Cohen *et al.* 2003; Jonsell *et al.* 2006), a star polluted by a 1.5 SN (Iben and Renzini 1983; Jonsell *et al.* 2006) or an accretion induced collapse (Qian and Wasserburg 2003; Cohen *et al.* 2003) and an AGB in a binary system. All these scenarios except radiative levitation consider that *s*- and *r*-process elements are produced in different stellar sites with different stellar conditions and somehow they come to the object that we are observing as a CEMP-*r/s* star. A newly suggested scenario, involving *i*-process nucleosynthesis, can produce both *s*- and *r*-process elements in a single stellar site. However, the sites of its occurrence is still a hot topic of debate.

1.3.2 CH stars

Keenan (1942) discovered and named these objects as CH stars due to the presence of a strong *G* band of CH in the spectra of these stars. CH stars exhibit enhancement of *s*-process elements. They are metal-poor warm halo objects. The proposed formation scenario for CH stars is also the same as that of CEMP-*s* stars. In fact, historically CEMP stars were referred to as CH stars before and even after the CEMP star classification of Beers and Christlieb (2005). Several authors have pointed out that CEMP-*s* stars are the low-metallicity analogues of CH stars (Lucatello *et al.* 2005; Starkenburg *et al.* 2014). In the present time classification, CH

stars are carbon enhanced ([C/Fe] > 0.7) halo objects with –1.0 < [Fe/H] < 0.0, showing enhanced abundances of *s*-process elements.

1.3.3 Barium stars

First recognised by Bidelman and Keenan (1951), barium (Ba) stars are characterised by the presence of strong absorption lines of Ba II at 4554 Å and Sr II at 4077 Å in their spectra (Warner 1965). Although not as strong as CH stars, Ba stars also show C_2, CN, and CH molecular bands. CH and Ba stars share the same metallicity range. Similar to CH and CEMP-*s* stars, Ba stars also show enhancement of *s*-process elements. Warner (1965) identified the Ba stars with Ba index 1 – 5 based on the strength of Ba II 4554 Å line. Later, depending on the degree of enhancement of *s*-process elements, Ba stars are divided into two subclasses- mild Ba stars and strong Ba stars (Lu 1991; Jorissen *et al.* 1998; Yang *et al.* 2016; Escorza *et al.* 2017). As their name implies, the strong Ba stars exhibit higher abundances of *n*-capture elements than that of mild Ba stars. Ba stars also form in binary systems similar to CEMP-*s* and CH stars. In the Literature, lower enhancement of heavy elements in mild Ba stars is explained by two plausible formation scenarios- i) a longer orbital period of the binary system and ii) relatively weaker neutron exposure in the AGB companion that pollutes the star (Yang *et al.* 2016). However, no conclusive evidence have yet been found in support of any of the proposed scenarios.

1.3.4 r-I, r-II, r_{lim} stars

The *r*-I & *r*-II stars show main *r*-process abundance pattern. The *r*-I stars are identified by the criteria 0.3 ≤ [Eu/Fe] ≤ 1.0 & [Ba/Eu] < 0.0 and the *r*-II stars

are identified by the criteria [Eu/Fe] > 1.0 & [Ba/Eu] < 0.0 (Frebel 2018). The stars, r_{lim}, which show limited *r*-process patterns are identified by [Eu/Fe] < 0.3, [Sr/Ba] > 0.5, & [Sr/Eu] > 0.0 (Frebel 2018). These *r*-process enriched stars may or may not be carbon enhanced.

In this thesis, we have primarily focused on understanding the *s*- and *i*-processes. We have covered detailed spectroscopic studies of normal MP, Ba, CH, CEMP-*s*, CEMP-*r/s* and CEMP-*no* stars. The *r*-process is out of the scope of this thesis.

1.4 Motivations, Accomplishments and Outline of the Thesis

Motivation 1: The diverse abundance ratios of *n*-capture elements observed in metal-poor stars demand a clear understanding of the origin of this diverse abundance pattern. A comprehensive analysis of the observed abundance peculiarities derived from a significantly large sample of these objects may shed insight into this problem, which is currently lacking.

Accomplishment: As a first step towards achieving the goal, we have performed high-resolution spectroscopic analysis of twenty metal-poor stars providing observational constraints to the theoretical models of *n*-capture nucleosynthesis in terms of elemental abundances derived from the different classes of metal-poor stars. Out of the twenty metal-poor programme stars, this work presents first high precision abundance analysis for twelve stars.

In **Chapter 2**, we have discussed the sources from where the programme stars are selected and how the spectroscopic data are acquired using different facilities worldwide. We have explained the data reduction procedure and the methodology involved in the determination of atmospheric parameters and the derivation of elemental abundances.

In **Chapter 3**, we have discussed in detail the spectroscopic methods of determination of stellar parameters and elemental abundances. The measured radial velocities of the programme stars, the abundance results, the results of the kinematic analysis, the estimation of errors in the elemental abundances, and the classification of the programme stars are presented in this chapter.

Motivation 2: It is noticed from the chemical abundance studies of CEMP-*r/s* stars that the abundance patterns of *n*-capture elements in these stars can neither be reproduced by *s*- or *r*- processes alone nor by any combination of *s*- and *r*-processes. Several scenarios have been proposed to explain the formation of these stars, including a recent suggestion of *i*-process nucleosynthesis as a possible mechanism.

Accomplishment: We have discussed the formation scenarios of CEMP-*s* and CEMP-*r/s* stars in detail to understand the production channels of these two subclasses of CEMP stars. With the help of a parametric-model-based analysis of the heavy elements observed in these stars, we have confirmed the recent claims that *i*-process is responsible for the formation of CEMP-*r/s* stars. This work is discussed in **Chapter 4**. Goswami and Goswami (2020) and Goswami *et al.* (2021) contain most of the results from this work.

Motivation 3: Different authors have introduced different classification schemes to identify the subclasses of CEMP stars, and often we find that these different classification criteria put the same object into different subclasses. In order to understand the physics behind the abundance patterns of CEMP-*s* and CEMP-*r/s* stars, it is important to distinguish the two subclasses. Hence, it is crucial to have a tighter classification scheme.

Accomplishment: We have examined all the available classification criteria of CEMP-*s* and CEMP-*r/s* stars with the help of a large sample of CEMP-*s* and CEMP-*r/s* stars from the literature and found that none of them could uniquely

classify the objects. We have put forward a new classification criterion to distinguish the CEMP-*s* and the CEMP-*r/s* stars, which is found to be more robust. Estimated [hs/ls] values from CEMP-*r/s* stars are generally found to have higher values than that of CEMP-*s* stars. We have investigated if [hs/ls] ratios can be used to classify these two subclasses. We found that [hs/ls] values of these two classes peak at different values but show a clear overlap in the range 0 –1.5. Hence this ratio also cannot be used as an effective classification criterion. This work is discussed in **Chapter 5**. Goswami *et al.* (2021) contains some results from this work.

Motivation 4: The astrophysical sites of *i*-process have been a topic of much debate in the astronomical community. Among the several proposed sites, the one that has gained more confidence over the others involves low-metallicity low-mass AGB stars and is somewhat similar to the proposed site of *s*-process. Recent studies of Cristallo *et al.* (2009b, 2016) and Choplin *et al.* (2021) have shown that both *s*- and *i*-process neutron-densities can be achieved in the same AGB star during different phases of its evolution. However, the condition that makes the final product as either *s*-process enriched or *i*-process enriched still remains unknown.
Accomplishment: We have discovered a carbon enhanced extremely metal-poor object HE 1005–1439, the peculiar abundance pattern of which was found to be enriched with products of both *i*- and *s*-processes. The abundance pattern shown by this object is the first of its kind and possibly forms a new class of objects. The chemical composition of the object could provide important constraints to understand the interplay between the physical conditions producing *s*- and *i*-process neutron densities and hence the conditions resulting in pure *s*- or *i*-process abundance pattern in the low-metallicity low-mass AGB stars. This work is discussed in **Chapter 6**. We have published these results in Goswami and Goswami (2022).

Motivation 5: Mass distribution of Ba stars have been extensively studied by

many authors (Han *et al.* 1995; Mennessier *et al.* 1997; Jorissen *et al.* 1998; Escorza *et al.* 2017; Jorissen *et al.* 2019). Mass distribution of white dwarfs around Ba stars and the orbital periods of mild and strong Ba stars have also been studied recently (Jorissen *et al.* 2019). It was envisaged that the initial mass of the AGB companions might also play a significant role in the formation of mild and strong Ba stars. However, the initial mass distribution of the AGB companions has not yet been studied so far. The production mechanisms leading to the formation of mild and strong Ba stars have not yet been fully understood.

Accomplishment: We have studied the mass distribution of Ba stars considering a large sample of Ba stars compiled from the literature and also including the Ba star sample under this study. We found that the mild and the strong Ba stars occupy a similar mass range, with the high mass tail of the distribution being longer for mild Ba stars. These results are in the line of those reported by Escorza *et al.* (2017) and Jorissen *et al.* (2019). For the first time, we have studied the initial mass distribution of the companions (primary) of the Ba stars using a parametric-model-based study taking AGB yields from FRUITY models. We found that the initial mass distribution of primary stars of mild and strong Ba stars peaks at different values. The primary mass distribution of mild Ba stars peaks at a higher initial mass (3.7 $M_{\odot}$) than that of strong Ba stars (2.5 $M_{\odot}$). We, therefore, propose that the initial masses of the progenitor AGBs dominantly control the formation of mild and strong Ba stars. We have also studied the progenitor AGBs' mass distribution of CEMP-*s* stars. The peak of the distribution for CEMP-*s* stars is found to be at 2.04 $M_{\odot}$. A manuscript containing the main results of this work is accepted for publication in the Astronomical Journal (AJ). This work is discussed in **Chapter 7**.

Chapter 8 summarises the findings of the thesis. We have also discussed the future work in this chapter.

Chapter 2

Methodology*

2.1 Introduction

Investigation of the origin and evolution of n-capture elements requires accurate estimation of stellar atmospheric parameters and elemental abundances of stars that show enhancement of n-capture elements. We have used high-resolution optical spectroscopy to obtain the stellar parameters and the abundances of several light and heavy elements in the sample of stars studied in this thesis. In stellar spectroscopy, we study the light coming from a star, collected with the help of a telescope on a CCD after dispersing with prisms and/or gratings. After following a rigorous data reduction procedure on the data collected on the CCD, we get the science-ready spectrum of the star. Further analyses, such as determining the radial velocity of the stars, estimating the stellar atmospheric parameters, and deriving the elemental abundances, are performed on the science-ready spectrum.

*Some parts of this chapter are presented in Purandardas *et al.* (2019), Shejeelammal *et al.* (2020), Goswami *et al.* (2021), Goswami and Goswami (2022).

In this chapter, we have discussed the selection of programme stars, data acquisition, data reduction, and the procedures involved in data analysis.

2.2 Object Selection

In order to have a variety of different classes of metal-poor stars in our study, showing enhanced abundances of *n*-capture elements, we have selected twenty metal-poor stars from different catalogues available in the literature. HE 0017+0055 is selected from the faint high-latitude carbon stars' list of Christlieb *et al.* (2001). BD+75 348, BD+09 3019, CD–27 14351 and HD 145777 are selected from the CH star catalogue of Bartkevicius (1996). These objects are also listed in the General Catalogue of Galactic Carbon stars (Stephenson 1989). BD+09 3019 is also listed in the carbon star catalogue of Ji *et al.* (2016b) from LAMOST DR2 data. HD 87853, HD 147609, HD 154276 and HD 238020 are taken from the CH star catalogue of Bartkevicius (1996). HE 0308–1612, HE 0319–0215, HE 0507–1653, HE 0930–0018, HE 1005–1439, HE 1023–1504, HE 1153–0518, HE 2144–1832 and HE 2339–0837 are selected from the list of faint high-latitude carbon stars of Christlieb *et al.* (2001). Barklem *et al.* (2005) presented the analysis of "snapshot" spectra of 253 metal-poor halo stars obtained in the Hamburg/ESO R-process Enhanced Star (HERES) survey. HE 0401–0138 and HE 1246–1344 are selected from Barklem *et al.* (2005). Based on medium-resolution spectra, Goswami (2005) confirmed HE 0017+0055, HE 0308–1612, HE 0319–0215, HE 0507–1653, HE 0930–0018, HE 2144–1832 and HE 2339–0837 to be potential CH star candidates.

2.3 Data Acquisition

The high-resolution spectra of the programme stars are acquired using the Hanle Echelle SPectrograph (HESP) attached to HCT. SUBARU/HDS and ESO/FEROS archival high-resolution spectra are also used for a few objects.

2.3.1 HESP/HCT

HESP (Hanle Echelle SPectrograph) (Sriram *et al.* 2018) is attached to 2-m HCT (Himalayan Chandra Telescope) at IAO (Indian Astronomical Observatory), Hanle. The detector is a 4K × 4K CCD with 15 μ pixel size. The wavelength coverage of the spectrograph spans from 3,500−10,000 Å. HESP operates at two resolving powers (R = $\lambda/\delta\lambda \sim$ 30,000 & 60,000) using image slicer.

High-quality, high-resolution spectra of BD+09 3019, BD+75 348, HD 145777, HD 147609, HD 154276, HD 238020, HE 0017+0055, HE 0308–1612 and HE 2144−1832 are obtained using HESP. For the stars brighter than $V_{mag} = 10.5$, the high resolution spectra are taken at resolving power of $\sim$ 60,000 and for the stars fainter than $V_{mag} = 10.5$ the spectra are taken at resolving power of $\sim$ 30,000. We have taken three frames with the same exposure time for each object and combined the frames to get the final spectrum to increase the S/N ratio.

2.3.2 FEROS/ESO

FEROS (Fiber-fed Extended Range Optical Spectrograph) (Kaufer and Pasquini 1998) is attached to the 1.52-m telescope of ESO (European Southern Observatory) at La Silla, Chile. The detector is a back-illuminated 2048 × 4096 EEV CCD with

a pixel size of 15 μ. For the objects CD−27 14351 and HD 87853, we have used high-resolution ($R \sim$ 48,000) FEROS spectra. The wavelength coverage of the spectra is from 3520 − 9200 Å.

2.3.3 SUBARU/HDS

The HDS (High Dispersion Spectrograph) (Noguchi *et al.* 2002) is attached to the 8.2-m Subaru Telescope of NAOJ (National Astronomical Observatory of Japan) at the Mauna Kea Observatory in Hawaii. The detector is a combination of two 4100 × 2048 EEV CCDs with a pixel size of 13.5 μ.

For the objects HE 0319–0215, HE 0401–0138, HE 0507–1653, HE 0930–0018, HE 1005–1439, HE 1023–1504, HE 1153–0518, HE 1246–1344 and HE 2339−0837 in our sample, we have used high-resolution ($R \sim$ 50,000) SUBARU/HDS spectra. The spectra of the stars are taken from the SUBARU archive*. The wavelength coverage of the spectra of HE 0507–1653 spans from 4090–6870 Å, with a gap of 80 Å (from 5430 to 5510 Å). The wavelength coverage of the spectra of the rest of the stars spans from about 4020–6775 Å, with a gap of about 100 Å (from 5340 to 5440 Å). The gap in the wavelength coverage appears due to the physical spacing of the CCD detectors.

2.4 Data Reduction

Following a standard data reduction procedure, we have reduced the spectroscopic data acquired using HESP. We have used IRAF (Image Reduction and Analysis Facility) software packages and the pipeline developed by Arun Surya for data

*`http://jvo.nao.ac.jp/portal`

reduction. Spectroscopic reduction procedures such as trimming, bias subtraction, flat normalisation and extraction are applied to the raw data. Wavelength calibration is done using a high-resolution Th-Ar arc spectrum.

The raw data that we get from the CCD detector is two-dimensional data. We process this data into one-dimensional data using IRAF for further analysis. First, we trim all the images keeping only the regions containing useful data. This is performed using the CCDPROC task.

Bias frames or zero frames are taken with zero exposure time. Using the ZERO COMBINE task in IRAF, the bias frames are combined and created a master bias frame which is used for bias subtraction. All the image frames are bias subtracted using this master bias frame.

The next step is flat fielding. The light sensitivity of each pixel in a CCD is different. These errors are removed by taking calibration frames, taken by evenly illuminating the CCD with bright light like halogen lamps, called flat frames. A number of flat frames are taken and then combined to a master flat using the task FLAT COMBINE in IRAF. It is then normalised, and the object frames are divided by this normalised master flat to reduce the error.

Using the APALL task in apextract, the different orders are extracted, which contains counts vs pixels. The pixels are converted to wavelengths using an arc spectrum for which the wavelengths are known. We have used the Th-Ar arc spectrum. With the help of available identification charts, the spectral lines in the arc spectrum are identified. These arc frames are then used as the reference to the object frames for the wavelength calibration. The wavelength calibrated spectra are then corrected for dispersion and continuum fitted for further analysis. The sample spectra of a few of the programme stars are shown in Figures 2.1, 2.2, 2.3 & 2.4.

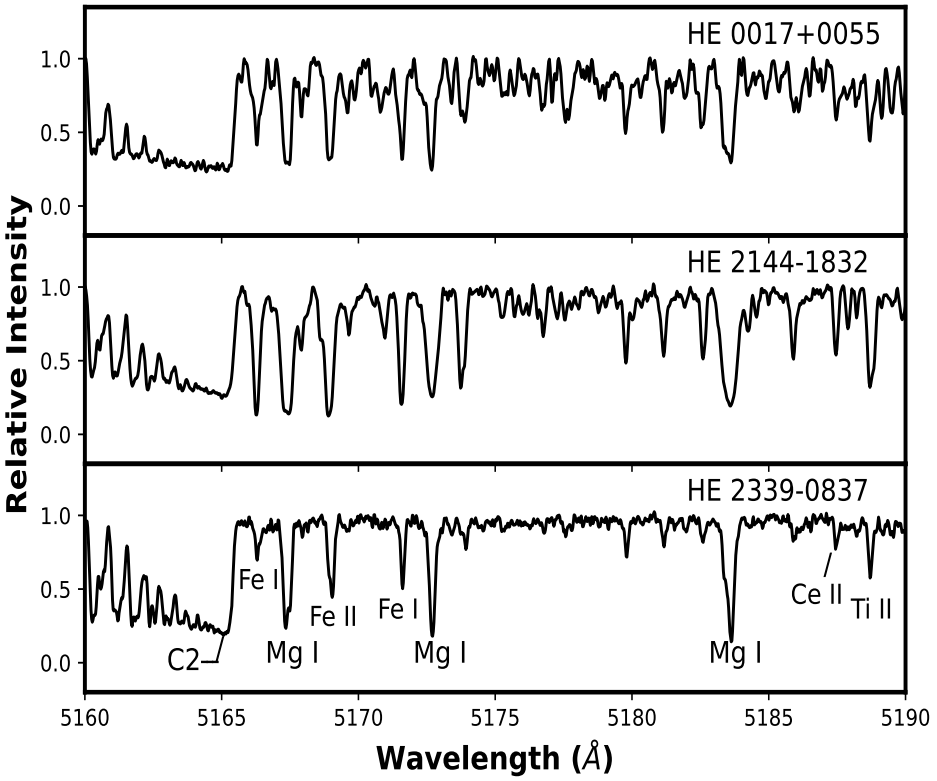

FIGURE 2.1: Sample spectra of the three CEMP-*r/s* stars in the 5160 to 5190 Å wavelength region.

2.5 Data Analysis

By analysing the spectral lines in the high-resolution spectrum of a star, we can determine the stellar properties such as effective temperature, surface gravity, microturbulent velocity, and metallicity and derive the elemental abundances. Stellar spectrum can also infer the binary nature, inflow and outflow of material, luminosity and hence the mass and age of the star and the phase of its evolution. In this section, we have briefly discussed the data analysis techniques. Detailed spectroscopic analysis of the programme stars is presented in Chapter 3.

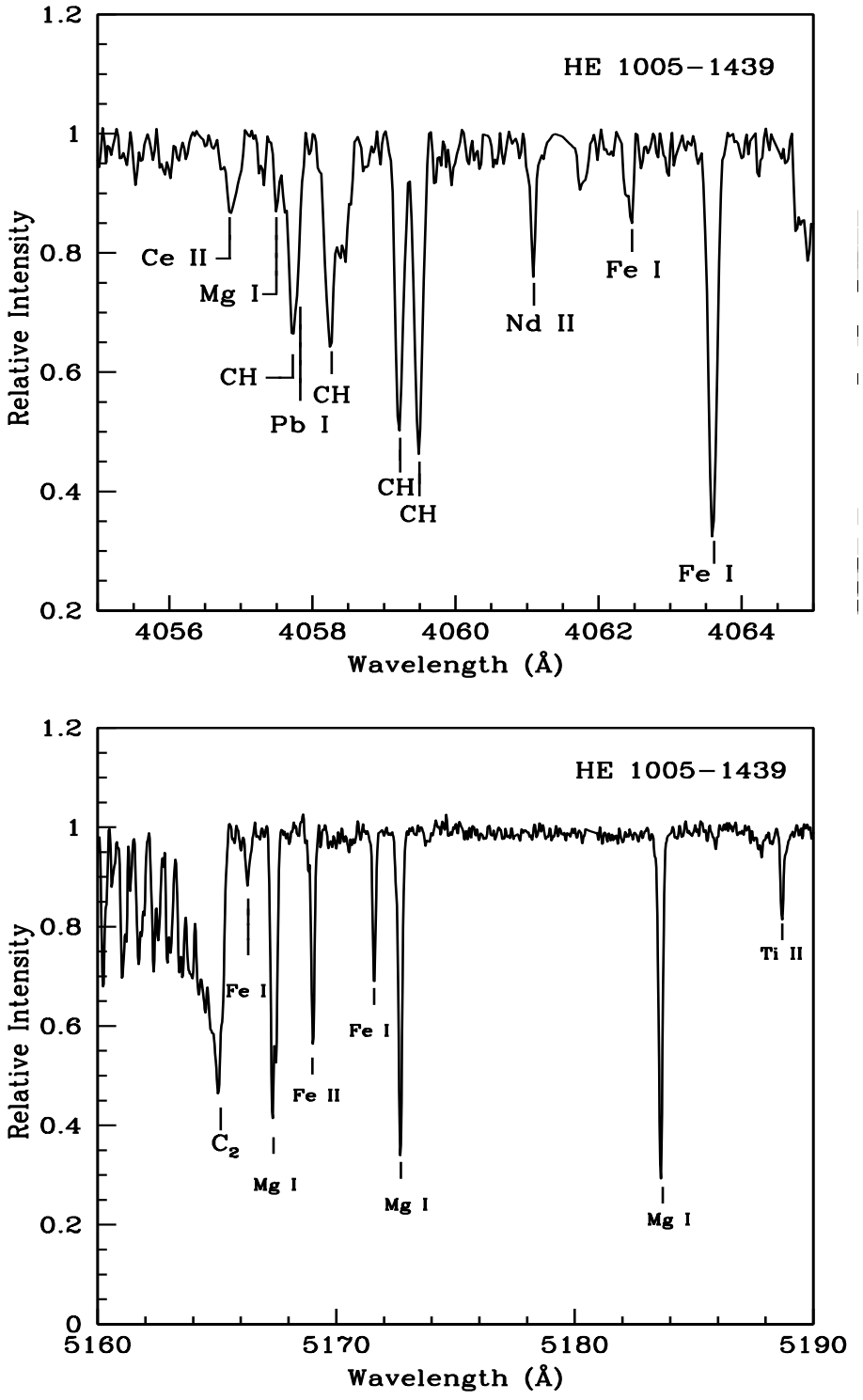

FIGURE 2.2: Sample spectra of the star HE 1005–1439 in the 4055–4065 Å (upper panel) and 5160–5190 Å (bottom panel) wavelength regions.

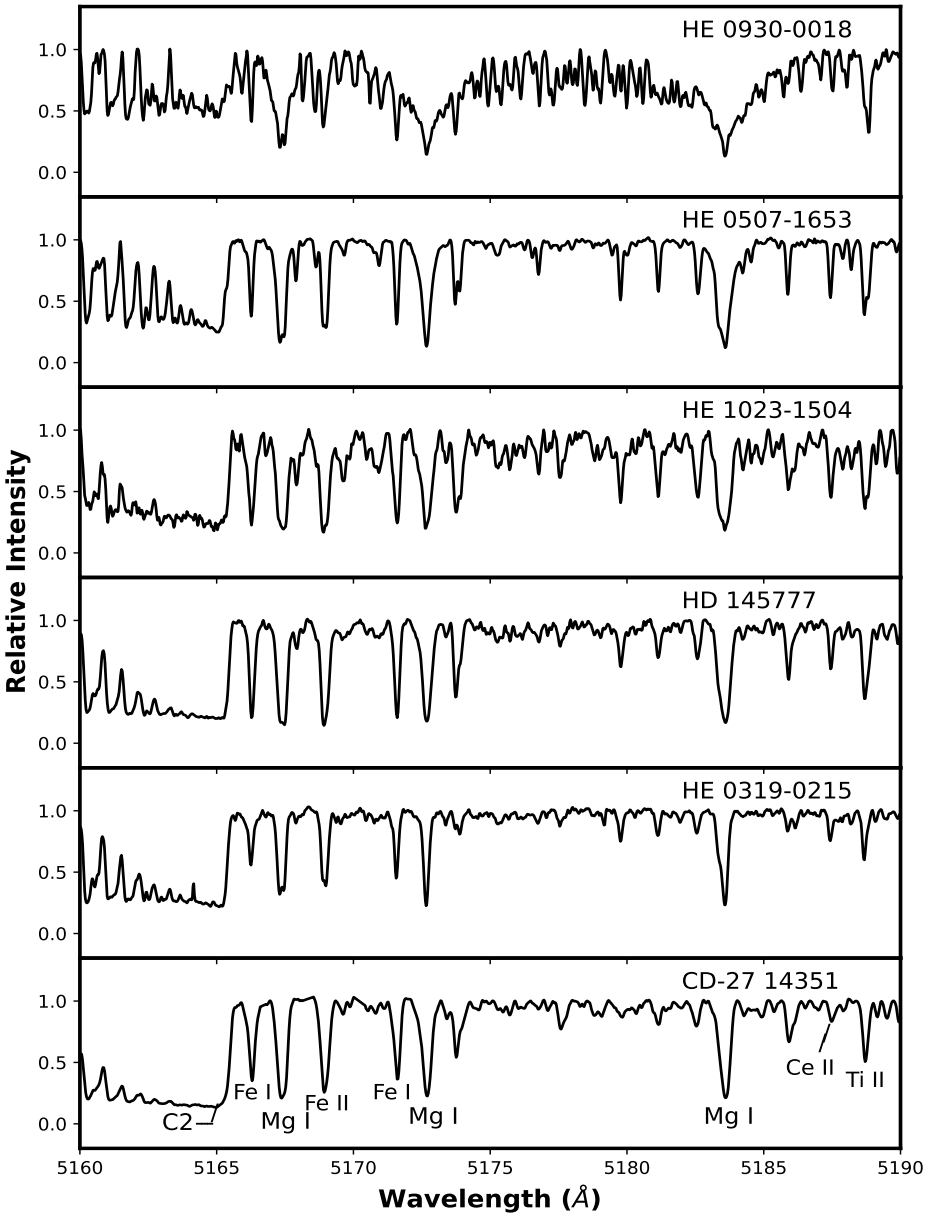

FIGURE 2.3: Sample spectra of the CEMP-*s* stars in the 5160 – 5190 Å wavelength region.

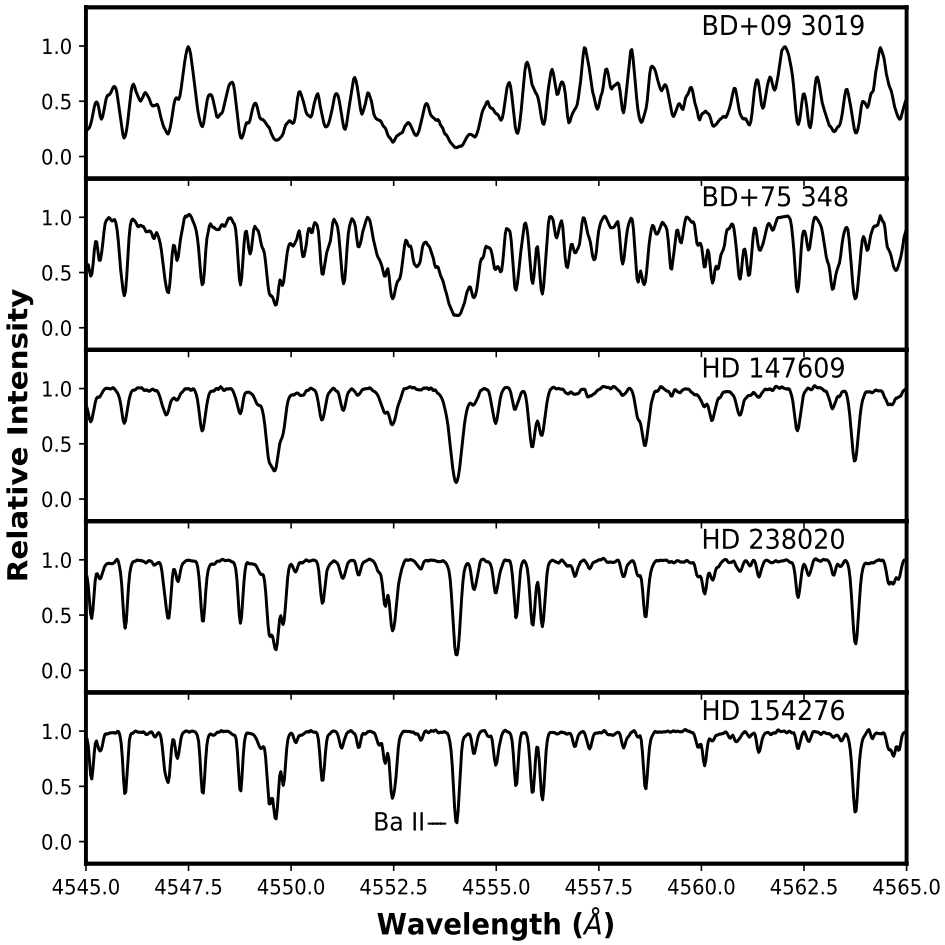

FIGURE 2.4: Sample spectra of the Ba stars in the wavelength region 4545 – 4565 Å.

2.5.1 Line identification

We have identified the spectral absorption lines due to several elements in the dispersion corrected spectra of the programme stars by closely comparing with the lines of Arcturus or the Sun depending on whether the star is a giant or a dwarf.

2.5.2 Equivalent width measurements

The strength of an absorption line depends on the number of absorbers in the photosphere that produces the particular line. However, with the increase in the path length along the photosphere, the number of absorbers increases and the continuous absorption decreases. Therefore, the line strength at a particular frequency is determined by the ratio of line absorption to continuous absorption at that frequency, i.e. l_ν/κ_ν. For a quantitative measure of line strength, equivalent width is used. Equivalent width is defined as $W_\lambda = \int_{\lambda_1}^{\lambda_2} \frac{F_c - F_\lambda}{F_c}\, d\lambda$, where F_c is the continuum flux, F_λ is the flux of the line profile at wavelength λ. The equivalent width of a spectral line is the width of a rectangle, having the same area as that of the line, drawn from zero to the continuum intensity.

Tasks within SPLOT of IRAF are used to measure the equivalent widths of clean, unblended lines in the spectra of the programme stars.

2.5.3 Line-list

We have generated line-lists for each object, including all the elements, taking the most updated values of the lower excitation potential and log gf from the Kurucz database of atomic line-list and the measured equivalent widths. Line-lists generated for the programme stars are presented in Chapter 3.

2.5.4 Atmospheric parameters

The stellar atmospheric parameters, the effective temperature T_{eff}, the log of surface gravity log g, microturbulent velocity ζ and the metallicity [Fe/H] are the prerequisites to any detailed chemical abundance analysis. We have used a set of clean, unblended and symmetric Fe I and Fe II lines for each object to determine their stellar atmospheric parameters. We have chosen the lines with the excitation potential in the range 0.0–6.0 eV. We have used an updated version of the radiative transfer code MOOG[†] of Sneden (1973), that assumes local thermodynamic equilibrium (LTE) for determining the atmospheric parameters. The model atmospheres are taken from the Kurucz grid of model atmospheres[‡]. These model atmospheres were generated considering several assumptions, such as no convective overshooting, plane-parallel atmosphere (usually considered to have seventy-two layers), LTE, radiative equilibrium and hydrostatic equilibrium. At different optical depths, each layer is assigned specific values of temperature, electron pressure, gas pressure, mean molecular weight, and opacity.

Effective Temperature (T_{eff}) of an object is the temperature of a blackbody emitting the same amount of energy as the object. For a star, the temperature at optical depth $\tau = 2/3$ equals its effective temperature.

log g, the surface gravity of a star is the acceleration due to gravity experienced by a test particle on the stellar surface. The surface gravity is expressed in logarithmic scale, in general.

Microturbulent velocity (ξ) is the line of sight velocity of the moving cells in the stellar photosphere. Microturbulence is a parameter having the dimension of velocity, which needs to be assumed along with damping and Doppler broadening for getting the same abundance of an element from different lines with different equivalent widths.

[†] `http://www.as.utexas.edu/~chris/moog.html`
[‡] `http://kurucz.harvard.edu/grids.html`

Metallicity of an object is the measure of the metal content of the particular object. Although astronomers refer to all the elements other than hydrogen and helium as metals, usually [Fe/H] is considered as the metallicity of stars.

The methods of determining the stellar atmospheric parameters and elemental abundances are discussed at length in Chapter 3.

Chapter 3

Spectroscopic Analysis of the programme stars*

Spectroscopy is one of the most accurate techniques to estimate the atmospheric parameters of the main-sequence and evolved stars, and it is the only way to derive the elemental abundances of the stars. We have performed a detailed high-resolution spectroscopic analysis of twenty metal-poor stars selected from several literature sources. In this chapter, we have discussed how we have analysed the science ready spectra of the programme stars.

3.1 Basic Data of the programme stars

In Table 3.1, we have presented the basic data of the programme stars along with observational details.

*Some results presented in this chapter are published in Purandardas *et al.* (2019), Shejeelammal *et al.* (2020), Goswami *et al.* (2021), Goswami and Goswami (2022).

TABLE 3.1: **Basic data for the programme stars.**

Star Name	RA(2000)	Dec.(2000)	B	V	J	H	K	Exposure (seconds)	Date of Obs.	Spectrograph used	Resolving Power
BD+09 3019	15 18 32.06	09 06 09.74	12.04	10.82	7.99	7.24	6.99	2700	24-05-2018	HESP/HCT	60 000
BD+75 348	08 46 11.64	+74 32 31.24	10.63	9.54	7.84	7.33	7.24	2400	08-03-2018	HESP/HCT	60 000
CD–27 14351	19 53 08.00	–27 28 14.97	11.82	9.70	7.02	6.30	6.14	1200	14-07-2000	FEROS/ESO	48 000
HD 87853	10 07 58.78	+08 30 37.24	10.12	9.66	8.81	8.57	8.55	1800	06-01-2000	FEROS/ESO	48 000
HD 145777	16 13 13.87	–15 12 01.25	11.55	10.31	7.73	7.07	6.84	2400	01-06-2017	HESP/HCT	60 000
HD 147609	16 21 51.99	+27 22 27.19	9.69	9.18	8.21	8.04	7.95	2400	01-06-2017	HESP/HCT	60 000
HD 154276	17 03 49.15	+17 11 21.08	9.80	9.13	7.91	7.62	7.55	2400	06-05-2017	HESP/HCT	60 000
HD 238020	11 36 10.99	+56 50 17.66	9.34	8.49	6.90	6.51	6.38	1800	06-05-2017	HESP/HCT	60 000
HE 0017+0055	00 20 21.60	+01 12 06.81	12.99	11.66	9.31	8.70	8.50	2700	21-09-2017	HESP/HCT	60 000
HE 0308–1612	03 10 27.07	–16 00 40.1	12.7	–	10.03	9.48	9.33	2700	24-01-2018	HESP/HCT	60 000
HE 0319–0215	03 21 46.26	–02 04 33.95	15.03	13.60	11.79	11.22	11.06	1800	08-12-2003	HDS/SUBARU	50 000
HE 0401–0138	04 03 49.88	–01 30 02.45	14.72	13.84	11.95	11.46	11.30	1800	27-02-2005	HDS/SUBARU	50 000
HE 0507–1653	05 09 16.56	–16 50 04.69	13.63	12.51	10.88	10.43	10.32	1200	26-10-2002	HDS/SUBARU	50 000
HE 0930–0018	09 33 24.63	–00 31 44.62	16.13	14.70	12.19	11.55	11.34	1800	09-12-2003	HDS/SUBARU	50 000
HE 1005–1439	10 07 52.39	–14 54 20.98	14.44	13.52	12.24	11.75	11.70	1800	08-12-2003	HDS/SUBARU	50 000
HE 1023–1504	10 25 55.55	–15 19 17.08	16.26	14.40	12.32	11.61	11.42	1200	27-02-2005	HDS/SUBARU	50 000
HE 1153–0518	11 55 54.74	–05 34 48.14	16.50	15.07	13.25	12.71	12.56	1200	27-02-2005	HDS/SUBARU	50 000
HE 1246–1344	12 49 20.25	–14 00 41.59	-	14.39	12.70	12.22	12.05	2700	01-03-2005	HDS/SUBARU	50 000
HE 2144–1832	21 46 54.66	–18 18 15.59	12.65	10.97	8.77	8.18	7.96	2700	08-11-2017	HESP/HCT	60 000
HE 2339–0837	23 41 59.93	–08 21 18.61	15.32	14.00	12.63	12.11	12.03	900	27-06-2004	SUBARU/HDS	50 000

3.1.1 Previous studies of the programme stars: A summary, and the novelty of the thesis

HE 0017+0055

This object was discovered by Stephenson (1989) as an R-type star and was assigned number 39 in the General Catalogue of Galactic Carbon Stars. The object is also listed in the faint high-latitude carbon stars' list of Christlieb *et al.* (2001). Kennedy *et al.* (2011) estimated the atmospheric parameters and the abundances of C, N, and O for this object. Jorissen *et al.* (2016a) did a more detailed analysis of this object, deriving the abundances of some of the *n*-capture elements (Y, Zr, La, Ce, Nd, Sm, Eu, Dy, and Er) along with C and N. The effective temperature value for the object estimated by these authors differ from our estimate (by $\sim$120$-$180 K). While Kennedy *et al.* (2011) estimated the log g and [Fe/H] to be 0.18 and $-$2.72, respectively, Jorissen *et al.* (2016a) adopted log g = 1.0 and estimated [Fe/H] = $-$2.40. Both these studies adopt a value of 2 km s^{-1} for microturbulence. Jorissen *et al.* (2016a) determined a low value ($\sim$ 4) for the carbon isotopic ratio ^{12}C/^{13}C, which does not differ much from the value of 1.3 estimated by Goswami (2005) based on medium-resolution spectra. From a long-term radial velocity monitoring programme Jorissen *et al.* (2016b) found this object to exhibit low-amplitude velocity variations with a period of 384 days superimposed on a long-term trend. The 384-days period was attributed either to a low-mass inner companion or to stellar pulsation. The differences in the estimates of the different groups prompted us to re-investigate this object based on a high-resolution spectrum.

BD+75 348, BD+09 3019, CD-27 14351 & HD 145777

These four objects are listed in the carbon star catalogue of Stephenson (1989) and CH star catalogue of Bartkevicius (1996).

BD+75 348: Bergeat *et al.* (2001) and McDonald *et al.* (2012) estimated the effective temperature of BD+75 348 using the spectral energy distribution (SED) method of temperature calibration. Začs *et al.* (2000) derived the atmospheric parameters as well as abundances of ten light and nine heavy elements for BD+75 348. The literature values of T_{eff} for BD+75 348 ranges from 4700–4900 K. Our estimate of T_{eff} ($\sim$ 4840 K) falls within the range.

BD+09 3019: Besides inclusions in the catalogues of Stephenson (1989) and Bartkevicius (1996), BD+09 3019 is also listed in the carbon star catalogue of Ji *et al.* (2016b) from LAMOST DR2 data. Atmospheric parameters and elemental abundances of BD+09 3019 are not reported previously in the literature. This work presents first high-resolution abundance analysis for BD+09 3019.

CD–27 14351: McDonald *et al.* (2012) reported estimates of effective temperatures for a large sample of *Hipparcos* stars including CD−27 14351 using the SED method of temperature calibration. Karinkuzhi *et al.* (2017) performed a detailed chemical composition study for this object and reported it to be a CEMP-*r/s* star with a high value of [Eu/Fe] = 1.65. These authors also obtained a negative value (−0.05) for [hs/ls] for this object, in contrast to all CEMP-*r/s* stars known so far. A survey of the literature shows that, in general, CEMP-*r/s* stars exhibit a positive value ($\sim$ 0.4 < [hs/ls] < 1.7) for [hs/ls]. This discrepancy prompted us to re-investigate the nature of this object. We have therefore re-examined its spectrum covering the wavelength range 3500 to 9000 Å. While the temperature estimate of our work differs from McDonald *et al.* (2012) by $\sim$ 100 K, our estimates for the atmospheric parameters are similar to those of Karinkuzhi *et al.* (2017). However, our estimates of elemental abundances for Ce and Eu differ from those of Karinkuzhi *et al.* (2017) by 0.74 dex and 1.26 dex, respectively.

HD 145777: Bidelman (1956) classified HD 145777 as a CH star differing from the earlier classifications by Mayall and Cannon (1940) and Sanford (1944), who

assigned this object to spectral class R3 and R4 respectively. Bergeat *et al.* (2001) and McDonald *et al.* (2012) derived effective temperature of HD 145777 using the SED method of temperature calibration. Our spectroscopic estimate differs by less than $\sim$ 100 K from these studies. First high-resolution abundance estimates for several elements including C through Zn, and *n*-capture elements are presented for this object.

HD 87853, HD 147609, HD 154276 & HD 238020

These four objects are listed in the CH star catalogue of Bartkevicius (1996).

HD 87853: This object is not studied previously; ours is the first detailed abundance analysis for this object.

HD 147609: In the literature, North *et al.* (1994), Thévenin and Idiart (1999), Allen and Barbuy (2006) and Escorza *et al.* (2019) reported the atmospheric parameters of HD 147609. The reported effective temperature, surface gravity and metallicity of the object range from $5960 < T_{eff}$ (K) < 6411, $3.30 <$ log $g < 3.90$ and $-0.23 <$ [Fe/H] < -0.50 respectively. Our estimates of the atmospheric parameters fall well within these ranges. While North *et al.* (1994) derived the abundances of C, O, Al, Si, S, Ca, Ni, Y, Zr, La and Nd in HD 147609, Allen and Barbuy (2006) performed a more detailed analysis of the object deriving the elemental abundances of thirteen light elements from Na through Zn and fourteen heavy elements from Sr through Pb. We have derived the abundances of twenty-four elements from C through Eu in HD 147609.

HD 154276: Ramírez *et al.* (2013) and Bensby *et al.* (2014) estimated the atmospheric parameters of HD 154276. Our estimates closely match their results. Bensby *et al.* (2014) derived abundances of ten light elements (O to Zn) and two heavy elements (Y & Ba) in HD 154276. We have performed a more detailed

abundance analysis of the object deriving the abundances of fifteen light elements from O through Zn and eight *n*-capture elements from Sr through Sm. We have also estimated the upper limits of Li and Ru in HD 154276.

HD 238020: The chemical composition of this object is not studied previously; ours is the first high-resolution abundance analysis for this object. McDonald *et al.* (2012) derived the effective temperatures of HD 238020 using the SED method of temperature calibration. Our estimate of temperature is hotter by 115 K for HD 238020 than that of McDonald *et al.* (2012).

HE 0308–1612, HE 0319–0215, HE 0507–1653, HE 0930–0018, HE 1023–1504, HE 2144–1832 & HE 2339–0837

These seven objects are taken from the faint high-latitude carbon stars' list of Christlieb *et al.* (2001).

Based on medium-resolution spectra, Goswami (2005) confirmed HE 0308–1612, HE 0319–0215, HE 0507–1653, HE 0930–0018, HE 2144–1832 & HE 2339–0837 to be potential CH star candidates.

Goswami (2005) estimated the $^{12}C/^{13}C$ ratio for HE 0017+0055 ($^{12}C/^{13}C \sim 1.3$), HE 0308–1612 ($^{12}C/^{13}C \sim 2.8$), HE 0319–0215 ($^{12}C/^{13}C \sim 4.7$), HE 0507–1653 ($^{12}C/^{13}C \sim 6.7$), HE 2144–1832 ($^{12}C/^{13}C \sim 2.1$) and HE 2339–0837 ($^{12}C/^{13}C \sim 2.3$) based on medium-resolution spectra.

HE 0308–1612: We have conducted the first detailed abundance analysis for this object.

HE 0319–0215: Kennedy *et al.* (2011) derived atmospheric parameters and abundance of oxygen for HE 0319–0215. Hansen *et al.* (2016c) reported [Fe/H] = –2.30,

[C/Fe] = 2.0, [Ba/Fe] = 0.52 for HE 0319–0215. Karinkuzhi *et al.* (2021) also derived the atmospheric parameters and elemental abundances of HE 0319–0215 and reported the object as a CEMP-*r/s* star. However, the estimates of [Fe/H] and [Ba/Fe] by the studies of Hansen *et al.* (2016c) and Karinkuzhi *et al.* (2021) differ by $\sim$ 0.6 dex and $\sim$ 1.23 dex respectively. These discrepancies in the literature values compelled us to re-investigate this object in detail using high-resolution spectroscopy.

HE 0507–1653: Schuler *et al.* (2008) reported [Fe/H] = –1.42, [C/Fe] = 1.33 and [N/Fe] = 1.20 for HE 0507–1653. Aoki *et al.* (2007) and Yong *et al.* (2013) derived atmospheric parameters and abundances of C, N, Na, Mg, Ca, Sc, Ti, Cr, Ni, Zn and Ba for HE 0507–1653. Karinkuzhi *et al.* (2021) performed a more detailed analysis on this object and reported it to be a CEMP-*s* star. However, this object also shows discrepancies in the atmospheric parameters and the abundance of Ba obtained by different groups. For instance, the ranges of T_{eff}, log g and [Fe/H] are 4880 to 5035 K, 1.50 to 2.40 dex and –1.81 to –1.32 dex respectively and the [Ba/Fe] ranges from 1.56 – 1.89 dex. These differences prompted us to study this object in detail.

HE 0930–0018: We have conducted the first detailed abundance analysis for this object.

HE 1023–1504: Kennedy *et al.* (2011) estimated the atmospheric parameters and the abundance of oxygen for HE 1023–1504. Our estimates of effective temperature and log g closely match with the estimates of Kennedy *et al.* (2011). However, the metallicity ([Fe/H]) estimated by Kennedy *et al.* (2011) is $\sim$ 0.8 dex lower than that of our estimate. This work presents first high precision high-resolution abundance estimates of several light elements and *n*-capture elements for the object.

HE 2144–1832: This object was studied by Stephenson (1989) and found to be

an R-type star. Hansen *et al.* (2016a) reported estimates of stellar atmospheric parameters and abundance estimates for four elements for this object: C, N, Ba, and Sr. This study was based on spectra obtained using X-shooter spectrograph (Vernet *et al.* 2011) covering wavelength regions 3000 - 5000 Å, 5500 -10000 Å, and 10000 - 25000 Å at spectral resolutions of 4350, 7450, and 5300 respectively. We conducted a detailed chemical analysis of this object using a higher resolution (R $\sim$ 60,000) spectrum with high S/N. New estimates for C, N, Ba, and Sr, and first-time abundance estimates for several other elements including *n*-capture elements are presented in this work. We also estimated $^{12}C/^{13}C \sim 2.5$ for this object, which is not too different from the estimated value of 2.1 reported by Goswami (2005) based on a low-resolution spectroscopic study.

HE 2339–0837: Kennedy *et al.* (2011) reported the atmospheric parameters and the abundances of C and O for HE 2339–0837 based on medium-resolution spectra. Detailed chemical abundance studies have not been reported in the literature for this object; our work presents a first high-resolution abundance analysis for this object.

HE 0401−0138 & HE 1246−1344

Barklem *et al.* (2005) presented analysis of "snapshot" spectra of HE 0401−0138 and HE 1246−1344 among 253 metal-poor halo stars. The spectra were obtained using VLT/UVES in the wavelength range 3760–4980 Å with R$\sim$20 000. As initial guess of the atmospheric parameters, Barklem *et al.* (2005) have considered photometric T_{eff}, metallicity estimates from the calibration of the Ca II K line along with B-V colour, log *g* from log *g*–T_{eff} correlation (Honda *et al.* 2004), microturbulent velocity (ζ) = 1.8 km s^{-1} and V_{macro} = 1.5 km s^{-1}. The parameters were then refined using an automated analysis based on the Spectroscopy Made Easy (SME) package by (Valenti and Piskunov 1996). Barklem *et al.* (2005) derived the abundances of eleven light elements from C through Ni and two heavy elements, Sr and Ba, for both HE 0401−0138 and HE 1246−1344. The abundance of Y

is also reported for HE 0401–0138. Zhang *et al.* (2011) adopted the atmospheric parameters from Barklem *et al.* (2005) to derive the abundances of C and Si for HE 0401–0138 and HE 1246−1344. Ren *et al.* (2012) derived the upper limit of [Th/Fe] in 77 metal-poor stars, including HE 1246−1344.

HE 1005−1439 & HE 1153–0518

HE 1005–1439: Aoki *et al.* (2007) estimated for the first-time the atmospheric parameters of HE 1005–1439 and derived abundances of seven light elements (C, N, Na, Mg, Ca, Ti, Cr) and only one heavy element Ba. They have used the empirical temperature scale of Alonso *et al.* (1999) to estimate the effective temperature of the object. Other atmospheric parameters are estimated using the standard Fe I and Fe II line analysis method. Schuler *et al.* (2008) used the same atmospheric parameters as Aoki *et al.* (2007) to derive carbon and nitrogen abundance of the object. They have used C I λ8727 Å line for estimation of carbon abundance and CN λ8005–8020 Å band to estimate the abundance of nitrogen. Using the same parameters as Aoki *et al.* (2007), Caffau *et al.* (2017) estimated [Fe/H] of the object to be –3.08 ± 0.12 with the help of two Fe I lines. Using an automated method, Yong *et al.* (2013) estimated the atmospheric parameters and abundances of Na, Mg, Ca, Ti, Cr and Ba. As the abundances of the *n*-capture elements except Ba are not reported in the literature, we have re-visited the object and derived the atmospheric parameters as well as abundances of ten light elements and twelve heavy elements.

HE 1153–0518: Atmospheric parameters and elemental abundances of HE 1153–0518 are not reported previously in the literature. A first detailed abundance analysis based on high-resolution spectroscopy for HE 1153–0518 is presented here.

Tables 3.4 and 3.38 compare our estimated atmospheric parameters and elemental abundances, respectively, with literature values.

3.2 Radial velocities of the programme stars

The radial velocities of the programme stars are determined by measuring the shifts in the wavelengths with respect to the laboratory wavelengths for a large number of unblended and clean lines in their spectra. For the rest frame laboratory wavelength, we have used Arcturus spectrum (Hinkle *et al.* 2000) as a template. The object Arcturus is chosen so as to have homogeneity in the analysis as it belongs to the giant class and has a comparable temperature as the objects under study. Estimated mean radial velocities along with the standard deviation from the mean values, after correcting for heliocentric motion, are presented in Table 3.2. The literature values are also presented for comparison. We have also used the FXCOR package in IRAF over the whole spectrum to cross-check these calculations and found them to be consistent with those obtained from line to line measurement of clean lines of different elements.

As far as the binary nature of the programme stars is concerned, HD 145777, HE 2144−1832 and HE 0017+0055 are established as radial velocity variables based on long-term radial velocity monitoring programmes, and hence, Jorissen *et al.* (2016b) suggested these objects to be in long-period binaries. From the studies of Hansen *et al.* (2016c) on HE 0319–0215 and Hansen *et al.* (2016c) and Jorissen *et al.* (2016b) on HE 0507–1653, it is found that both the objects exhibit radial velocity variations with periods of 3078 days for HE 0319–0215 and 405 days for HE 0507–1653 confirming their binary nature. Escorza *et al.* (2019) confirmed HD 147609 to be a component of a binary system with a period of 1146 days. We measured the radial velocity of HE 1005–1439 from spectra acquired at four different epochs using several clean unblended lines. The estimated radial velocities show that the object is a radial velocity variable and is likely to be in a binary system. In Table 3.2, we can see significant differences between our estimates of radial velocities and those found in the literature for some objects, which may

TABLE 3.2: **Radial Velocities of the programme stars.**

Star Name	Date of Observation	UT (hh:mm:ss)	V_r (kms^{-1}) (our estimates)	V_r (kms^{-1}) *a*
BD+09 3019*	24-05-2018	19:16:23.1	–9.50±1.77	+8.21±0.65
BD+75 348	08-03-2018	14:30:35.7	+57.70±1.72	+56.91±2.21
CD–27 14351*	14-07-2000	03:15:30.0	+61.1±0.50 [b]	+59.70±0.90
HD 87853*	06-01-2000	07:06:03.0	–3.35±0.05	–2.92±0.005
HD 145777*#	01-06-2017	19:19:24.6	+16.23±0.40	+20.14±0.47
HD 147609#	01-06-2017	17:05:36.0	–18.17±1.47	–17.11±0.82
HD 154276*	06-05-2017	20:42:12.8	–64.17±1.42	–55.94±0.17
HD 238020*	06-05-2017	15:56:20.6	–24.62±1.07	–16.04 ± 0.15
HE 0017+0055#	21-09-2017	19:41:19.5	–80.56±0.52	–80.73±0.23
HE 0308–1612*	24-01-2018	13:50:19.6	+85.5±1.22	+76.41±0.51
HE 0319–0215*#	08-12-2003	07:52:39.9	–257.43±0.61	–232.33±4.38
HE 0401–0138*	27-02-2005	07:24:37.2	+70.02±0.22	+137.4 [c]
HE 0507–1653#	26-10-2002	14:45:45.7	+349.81±0.72	+353.53±2.55
HE 0930–0018	09-12-2003	12:10:11.4	+45.73±0.68	-
HE 1005–1439#	26-10-2002	15:18:27.4	+98.54±0.75	-
	28-10-2002	15:15:08.7	+99.17±0.90	-
	26-05-2003	06:07:10.1	+48.95±0.46	-
	08-12-2003	12:41:04.8	+103.53±0.46	-
HE 1023–1504	27-02-2005	08:32:32.2	–226.15±0.39	-
HE 1153–0518	27-02-2005	09:38:50.0	+83.74±0.50	-
HE 1246–1344*	01-03-2005	10:56:37.5	+67.27±0.41	+47.90 [c]
HE 2144–1832*#	08-11-2017	13:00:19.3	+137.19±0.68	+141.24±0.64
HE 2339–0837	27-06-2004	12:47:15.5	+169.83±0.68	-

a – Gaia Collaboration *et al.* (2018); *b* – Karinkuzhi *et al.* (2017); *c* – Barklem *et al.* (2005); ∗ – Shows radial velocity variations; # – confirmed binaries

be indicative of their binary nature. We have marked the stars showing radial velocity variations with '$*$'s in Table 3.2.

3.3 Atmospheric parameters of the programme stars

3.3.1 Photometric temperatures

Photometric temperatures of the programme stars are determined using broad-band colours, optical and IR, with colour-temperature calibrations available for main-sequence stars (Alonso *et al.* 1996) and giants (Alonso *et al.* 1999), that are based on the infra-red flux method (IRFM). The 2MASS photometric magnitudes for J, H, and K are taken from Cutri *et al.* (2003). The procedure followed is as described in Goswami *et al.* (2006, 2016). As Alonso *et al.* (1996, 1999) reported, the uncertainty in temperature calculations using the IRFM method is about $\sim$ 90 K. Precise photometric data, reliable reddening estimates and metallicity information are required when using this method. We have estimated the photometric temperatures of the stars at several assumed metallicity values. The estimated temperatures, along with the adopted metallicities, are listed in Table 3.3. We have not considered the empirical T_{eff} scale for the B-V colour indices as this calibration relation may not give reliable estimates due to the effect of CH molecular absorption in the B band. The severe blending of the spectra by molecular lines affects the photometric results to a significant extent (Yoon *et al.* 2020). The photometric temperature estimates obtained using J-K calibration relation are used as initial guess for selecting model atmospheres to estimate the spectroscopic temperature of the objects in an iterative process, as this empirical calibration is independent of metallicity (Alonso *et al.* 1996, 1999).

TABLE 3.3: **Temperatures from photometry.**

Star Name	T_{eff} (J-K)	T_{eff} (-1.5) (J-H)	T_{eff} (-2.0) (J-H)	T_{eff} (-2.5) (J-H)	T_{eff} (-1.5) (V-K)	T_{eff} (-2.0) (V-K)	T_{eff} (-2.5) (V-K)	Spectroscopic estimates
CD−27 14351	4097	4119	4099	-	-	-	-	4320
HD 145777	4072	4295	4273	4234	-	-	-	4160
HE 0017+0055	4261	4478	4456	4414	4084	4080	-	4370
HE 0319–0215	4479	4635	4612	4568	4510	4510	4515	4650
HE 0401–0138	4690	4967	4943	4895	4505	4504	4510	4830
HE 0507–1653	4935	5106	5081	5031	4839	4840	4848	4970
HE 0930−0018	4164	4368	4346	4306	3979	3974	-	4190
HE 1005–1439	5017	4959	4934	4886	5265	5277	5296	5170
HE 1023–1504	4062	4154	4133	-	4190	4187	-	4440
HE 1153–0518	4546	4706	4653	4639	4527	4527	4533	4700
HE 1246–1344	4687	4980	4956	4908	4685	4683	4687	4780
HE 2144−1832	4264	4558	4536	4493	4171	4168	-	4190
HE 2339−0837	4812	4797	4773	4727	5086	5093	5107	4940
Star Name	T_{eff} (J–K)	T_{eff} (-0.5) (J–H)	T_{eff} (-1.0) (J–H)	T_{eff} (-1.5) (J–H)	T_{eff} (-0.5) (V–K)	T_{eff} (-1.0) (V–K)	T_{eff} (-1.5) (V–K)	Spectroscopic estimates
BD+75 348	4856	4867	4891	4891	4749	4736	4729	4840
BD+09 3019	3879	4038	4051	4047	3810	3795	-	4220
HD 87853	6414	6330	6344	6358	6397	6410	6431	6250
HD 147609	6414	6827	6839	-	6185	6193	6209	6350
HD 154276	5846	5991	6005	6020	-	-	-	5820
HD 238020	5085	5350	5382	5384	4941	4931	4928	5150
HE 0308–1612	4548	4671	4692	4691	-	-	-	4600

The numbers in the parenthesis below T_{eff} represent the metallicities at which the photometric temperatures are calculated. Temperatures are given in Kelvin.

3.3.2 Spectroscopic determination of atmospheric parameters

The stellar atmospheric parameters, the effective temperature T_{eff}, the surface gravity log g, micro-turbulent velocity ξ, and the metallicity [Fe/H], are determined using a set of clean, unblended Fe I and Fe II lines with excitation potential in the range $0.0 - 6.0$ eV. Due to the presence of molecular lines and bands of carbon all over the spectra, the lines of Fe and other elements are severely blended in most of the programme stars. The lines used for the determination of the atmospheric parameters are selected after strong filtration for clean, unblended and symmetrical lines in the spectra of the objects. The lines are presented in Tables 3.7, 3.8 3.9 & 3.10 along with the measured equivalent widths and atomic line information. A few Fe lines which are not severely blended are also included in the list for which we have used the method of de-blending (with SPLOT task in IRAF) for measuring equivalent widths.

An initial model atmosphere (with no convective overshooting) is selected from the Kurucz grid (`http://kurucz.harvard.edu/grids.html`) of model atmospheres corresponding to the photometric temperature estimate and the initial guess of log g value for giants/dwarfs. The effective temperature is determined by forcing the slope of Fe abundances versus the excitation potential of the measured Fe I lines to zero (top panel of Figure 3.1 shows plots of excitation potential balance for a sample of five stars in our sample). At this particular temperature, the micro-turbulent velocity is fixed to be that value for which there is no dependence of the abundances derived from the Fe lines on the reduced equivalent width (bottom panel of Figure 3.1 shows plots of equivalent width balance). At these fixed values of temperature and micro-turbulent velocity, the surface gravity is obtained by demanding the abundances derived from both Fe I and Fe II lines to be nearly the same. The abundances obtained from the Fe I and Fe II lines give the metallicity. Thus, starting with the initially selected model atmosphere, the

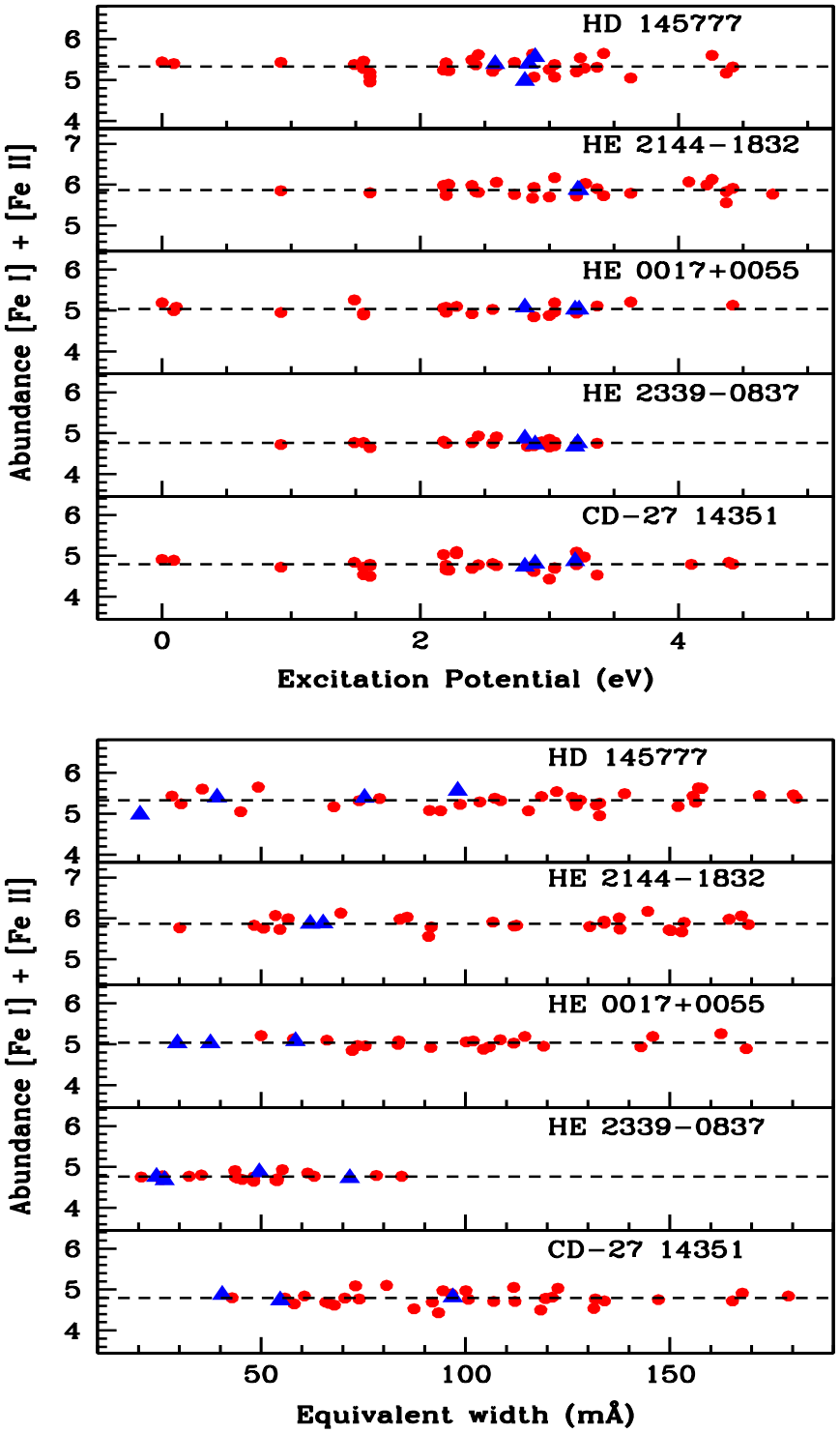

FIGURE 3.1: The iron abundances for individual Fe I and Fe II lines of a sample of five programme stars are shown as a function of excitation potential (Top panel) and equivalent width (Bottom panel). The solid red circles and solid blue triangles represent Fe I lines and Fe II lines, respectively.

final model atmosphere is obtained following the iterative method, which is then adopted to carry out further abundance analysis. The analysis is facilitated by using an updated version of MOOG (Sneden 1973) software, which assumes Local Thermodynamic Equilibrium (LTE) conditions. Solar abundances are adopted from Asplund *et al.* (2009). The absorption lines due to Fe I are affected by 3D non-LTE (NLTE) effects (Amarsi *et al.* 2016). The NLTE effect is negligible in the case of Fe II lines for [Fe/H] ≥ -2.50 and increases with decreasing metallicity (Amarsi *et al.* 2016). However, we have not considered the NLTE corrections for our analysis. Ezzeddine *et al.* (2017) showed that the departure of $[Fe/H]_{NLTE}$ from $[Fe/H]_{LTE}$ anti-correlate with $[Fe/H]_{LTE}$ growing from $\sim$ 0.0 dex at [Fe/H] ~ -1.0 to $\sim$ 1.0 dex at [Fe/H] ~ -8.0. The derived stellar parameters of the programme stars, along with their literature values, are listed in Table 3.4.

3.3.3 Parallax method of estimating log g

We have also used the parallax method to estimate the log g values of our programme stars whenever possible. We have estimated the masses of our programme stars from their positions in the Hertzsprung-Russell (HR) diagram ($\log(L/L_{\odot})$ versus $\log(T_{eff})$ plot). The values of parallax (π) are taken from Gaia Collaboration *et al.* (2018) and V magnitude from SIMBAD. The bolometric corrections (BC) are determined based on the empirical calibration equations of Alonso *et al.* (1996, 1999). Interstellar extinctions (A_v) for the programme stars are estimated using the formulae by Chen *et al.* (1998). The values of $\log(L/L_{\odot})$ are calculated using the equation-

$$log(L/L_{\odot}) = 0.4(M_{bol\odot} - V - 5 - 5log(\pi) + A_v - BC) \tag{3.1}$$

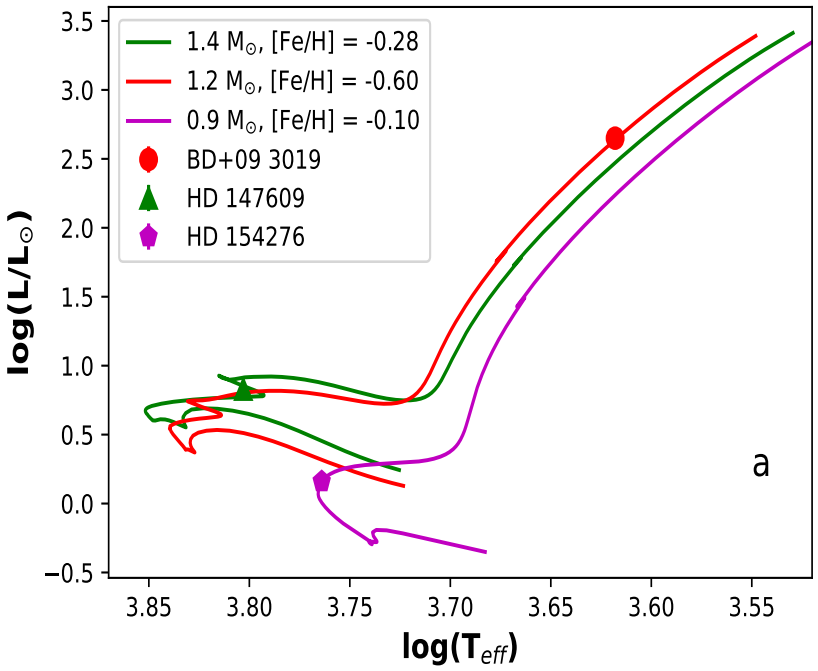

FIGURE 3.2: Hertzsprung-Russel diagram showing evolutionary tracks for different masses at different [Fe/H]. Red filled circle, green filled triangle and magenta filled pentagon represent the positions of three stars BD+09 3019, HD 147609 and HD 154276 respectively.

We have used the updated BaSTI-IAC evolutionary tracks (Hidalgo *et al.* 2018) (`http://basti-iac.oa-abruzzo.inaf.it/`) generated for the respective metallicities of the programme stars, $[\alpha/\mathrm{Fe}] = 0.4$, including overshooting and diffusion to estimate the masses of the stars. The log g value is calculated using the relation-

$$log\ (g/g_{\odot}) = log\ (M/M_{\odot}) + 4log\ (T_{eff}/T_{eff\odot}) + 0.4(M_{bol} - M_{bol\odot}) \qquad (3.2)$$

The adopted solar values are log $g_{\odot}$ = 4.44, $T_{eff\odot}$ =5770 K and $M_{bol\odot}$ = 4.74 mag (Yang *et al.* 2016). We could estimate the log g values using the parallax method only for the normal metal-poor star HD 87853 and the Ba stars. Figure 3.2 shows the position of a sample of three stars in the HR diagram. We have presented the comparison of the spectroscopic log g values and the values

estimated using parallax method in Table 3.4. Jorissen *et al.* (2016a) reported that in many cases, the carbon enhanced stars fall towards the right side of the evolutionary tracks. This may be because the evolutionary tracks and isochrones highly depend on the opacity in the stellar atmospheres (Marigo 2002), and the BASTI-IAC evolutionary tracks are not calculated considering high carbon abundances. So, these evolutionary tracks are not suitable for carbon enhanced stars. That is why log g values determined using such evolutionary tracks and isochrones may lead to erroneous estimates. The use of the evolutionary tracks customised to the observed abundances of the stars is out of the scope of this thesis. We have used spectroscopic log g values for our analysis.

3.4 Abundance Determination

The abundances of various elements are determined from the measured equivalent widths of absorption lines due to neutral and ionised elements using the LTE analysis. Only the symmetric and clean lines are used for our analysis. As equivalent width measurement results depend on personal bias, to avoid it, we have also used '`Tool for Automatic Measurement of Equivalent width (TAME)`' (Kang and Lee 2012) to verify our measurements. `TAME` measures equivalent widths determining the local continuum and using de-blending wherever necessary. A master line-list is generated, including all the elements, taking the oscillator strength (log gf) and excitation potential values from the Kurucz database and the measured equivalent widths. We made use of the LTE line analysis and spectrum synthesis code MOOG 2013[†] for our analysis. The adopted model atmosphere (with no convective overshooting) are taken from the Kurucz grid (`http://kurucz.harvard.edu/grids.html`) of model atmospheres. Elemental abundances of C,

[†]`http://www.as.utexas.edu/~chris/moog.html`

N, O, α-elements, iron-peak elements and several *n*-capture elements are estimated. We have used spectrum synthesis calculations for the elements showing hyperfine splitting, such as Sc, V, Mn, Ba, La and Eu. The lines used in the analysis with the measured equivalent widths and atomic line information are presented in Tables 3.11 through 3.14. Atomic line information, such as oscillator strength (log gf) and the excitation potential values, are taken from the Kurucz database. The lines used for spectrum synthesis calculations are presented in Table 3.15. The abundance results of the twenty programme stars are presented in Tables 3.18 through 3.37. A comparison of our estimated abundances of C, N and *n*-capture elements with literature values is presented in Table 3.38.

3.4.1 Li, Carbon, Nitrogen, Oxygen

Li- We could derive upper limits to the abundance of Li in HD 154276 ([Li/Fe] $<$ –0.25), HE 0401–0138 ([Li/Fe] $<$ 3.20), HE 1153–0518 ([Li/Fe] $<$ 2.99) and HE 1246–1344 ([Li/Fe] $<$ 2.75). Li I 6708 Å is used for the estimates of Li abundance.

O- The abundance of oxygen could be estimated only for four (HD 87853, HD 147609, HD 154276, HD 238020) of the programme stars. For the object HD 238020, we have used the forbidden line of oxygen [O I] 6300 Å, and for the other three objects, oxygen triplet around 7774 Å has been used. The abundance of oxygen could not be measured for the rest of the stars as the oxygen lines are found to be blended and not usable for abundance estimation.

C- The abundance of carbon is estimated using the spectrum synthesis calculation of the C_2 molecular bands near 5165 Å & 5635 Å and CH molecular band near 4310 Å. All the three bands yield almost the same abundance of carbon for the respective stars (within error bars). Carbon is found to be in the range –0.03 $<$

[C/Fe] < 2.98 in the programme stars. Our estimates of carbon abundance are slightly higher than the carbon abundance reported for HE 2144−1832 in Hansen *et al.* (2016a). This discrepancy may arise due to the difference in the adopted oxygen abundance. Estimates of carbon abundance depend on the adopted value of oxygen for the spectrum synthesis calculations. As the abundance of oxygen could not be estimated for many objects, in those cases, we have considered solar value ($\log\epsilon = 8.69$) for the spectrum synthesis calculations. As an example, the spectrum synthesis fits of C_2 and CH molecular bands for a sample of programme stars are shown in Figures 3.3, 3.4, 3.5, 3.6 and 3.7.

N- The abundance of nitrogen is derived using the spectrum synthesis calculations of the CN band at 4215 Å using the estimated carbon abundance. Nitrogen is found to be in the range $0.15 <$ [N/Fe] < 2.83 in the programme stars. The spectrum synthesis fits of the CN molecular band for a few sample of our programme stars are shown in Figure 3.8.

We have estimated the carbon isotopic ratio $^{12}C/^{13}C$ using spectrum synthesis calculation of the ^{12}CN and ^{13}CN features near 8005 Å (Figure 3.9) and $^{12}C^{13}C$ and $^{13}C^{13}C$ features near 4740 Å (Figure 3.10). Figures 3.9, 3.10 and 3.11 show the spectrum synthesis fits of CN and C_2 molecular bands with different $^{12}C/^{13}C$ ratios for a few sample of our programme stars. We have used the wavelengths, lower excitation potentials and log gf values of different molecular transitions for the C_2 band at 5165 Å and CN bands from Brooke *et al.* (2013), Ram *et al.* (2014) and Sneden *et al.* (2014). Line lists of the C_2 bands at 5635 Å & 4740 Å and CH band at 4310 Å are taken from the atomic and molecular line database *linemake*[‡] atomic and molecular line database.

[‡]*linemake* (Placco *et al.* 2021) contains laboratory atomic data (transition probabilities, hyperfine and isotopic substructures) published by the Wisconsin Atomic Physics and the Old Dominion Molecular Physics groups. These lists and accompanying line list assembly software have been developed by C. Sneden and are curated by V. Placco at https://github.com/vmplacco/linemake.

The CH band at 4310 Å and CN band at 4215 Å are saturated in the spectrum of HE 2339−0837, and hence, the abundances of C and N could not be estimated using these bands for this object. In the spectrum of the star HD 238020, the CN molecular band at 4215 Å and the C_2 molecular band at 5635 Å are too weak to be used for abundance estimation. The CH band in the spectrum of HE 0507–1653 and the CN band in the spectrum of BD+09 3019 are found to be saturated and hence, could not be used for abundance estimation. In the spectra of HE 0930–0018 and HE 1023–1504, the S/N (signal to noise ratio) is quite low in the wavelength region of the CH and CN bands. So, these two bands could not be used for abundance determination in the case of HE 0930–0018 and HE 1023–1504.

3.4.2 Na, Mg, Al, Si, Ca, Sc, Ti, V

Na- The abundance of Na ranges from [Na/Fe] = 0.05 to 1.54 dex in our programme stars. Na abundance could not be estimated for HE 0017+0055 as the Na lines are severely blended and not usable for abundance estimation.

Mg- The abundance of Mg in the programme stars is found to be in the range 0.17 $<$ [Mg/Fe] $<$ 2.17. The abundance of Mg could not be derived for HE 0017+0055 and HE 1023–1504 due to the unavailability of usable lines in their spectra.

Al- We could estimate the abundance of Al only for HD 154276, which yields a sub-solar ([Al/Fe] = –0.12) value.

Si- We have derived the abundance of Si for HD 147609, HD 154276 and HD 238020, which ranges from –0.52 $<$ [Si/Fe] $<$ 0.14. We could not determine the abundance of Si for the rest of the objects as no good lines were found.

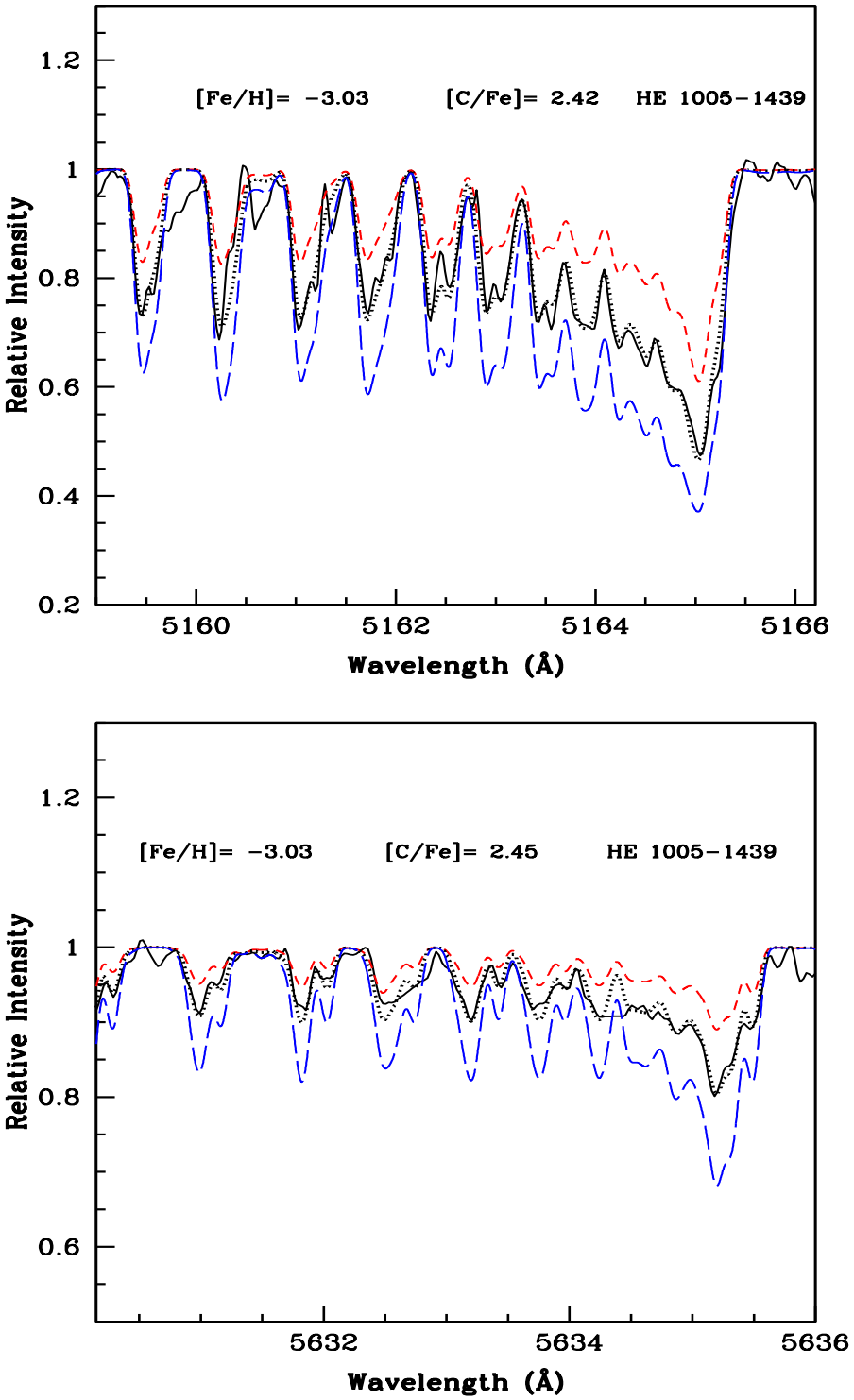

FIGURE 3.3: Spectral synthesis plots of C_2 bands around 5165 Å (top panel) and 5635 Å (bottom panel) for HE 1005–1439. The solid black lines represent the observed spectra. The black dotted lines show the synthesised spectra. Other two synthesised spectra are displayed corresponding to Δ[C/Fe] = −0.3 and +0.3 with short dashed red and long dashed blue lines respectively.

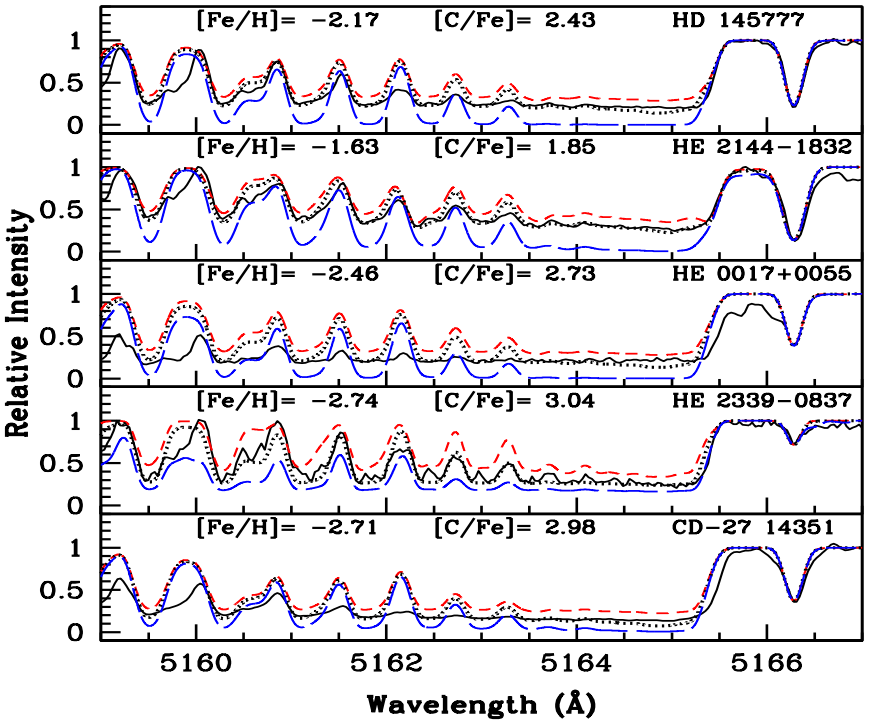

FIGURE 3.4: The spectral synthesis plots of C_2 band around 5165 Å for a sample of five programme stars. The solid black lines show the observed spectra. The dotted black lines represent the synthesised spectra. Two other synthesised spectra are shown corresponding to Δ[C/Fe] = −0.01 and +0.01 with short dashed red and long dashed blue lines respectively in panel 1 (for HD 145777); Δ[C/Fe] = −0.05 and +0.05 with short dashed red and long dashed blue lines respectively in panel 2 (for HE 2144−1832); Δ[C/Fe] = −0.10 and +0.10 with short dashed red and long dashed blue lines respectively in panel 3 (for HE 0017+0055); Δ[C/Fe] = −0.3 and +0.3 with short dashed red and long dashed blue lines respectively in panel 4 (for HE 2339−0837); and Δ[C/Fe] = −0.01 and +0.01 with short dashed red and long dashed blue lines respectively in panel 5 (for CD−27 14351).

Ca- The abundance of Ca ranges from [Ca/Fe] = –0.14 to 0.91 dex in our programme stars, with the minimum for BD+09 3019 and the maximum for CD–27 14351. In the spectrum of HE 0017+0055, no usable lines were found for the determination of Ca abundance.

Sc- We have estimated the abundance of Sc using spectrum synthesis calculations of several lines of Sc II. The abundance of Sc ranges from [Sc/Fe] = –0.39 to 0.77 dex. We could not determine the abundance of Sc for CD–27 14351,

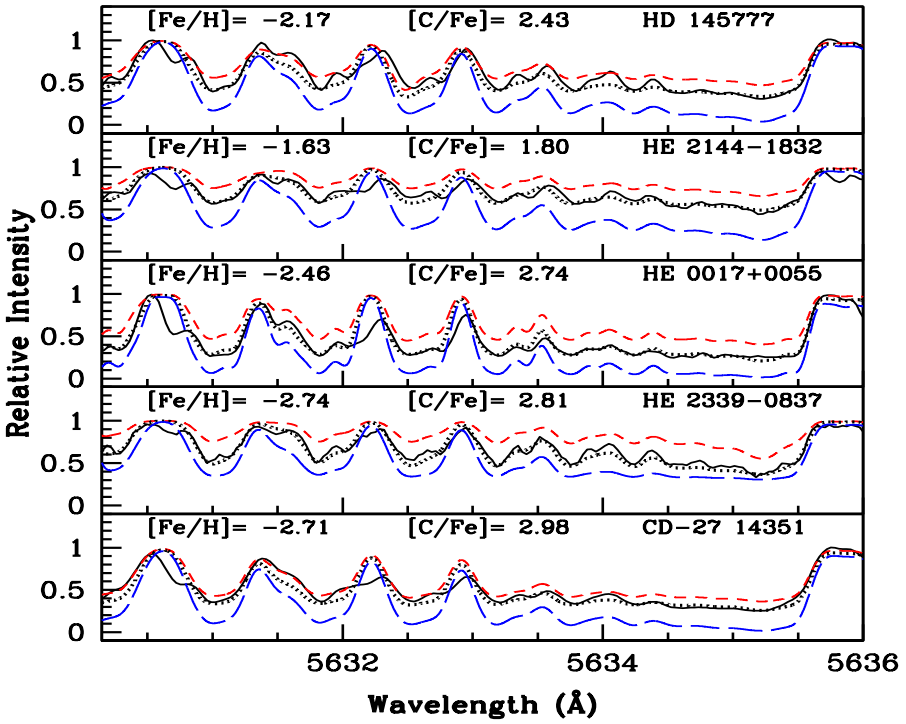

FIGURE 3.5: The spectral synthesis plot of C_2 band around 5635 Å for a sample of five programme stars. The solid black lines represent the observed spectra. The dotted black lines show the synthesised spectra. Other two synthesised spectra are displayed corresponding to Δ[C/Fe] = −0.02 and +0.02 with short dashed red and long dashed blue lines respectively in panel 1 (for HD 145777); Δ[C/Fe] = −0.15 and +0.15 with short dashed red and long dashed blue lines respectively and in panel 2 (for HE 2144−1832); Δ[C/Fe] = −0.05 and +0.05 with short dashed red and long dashed blue lines respectively in panel 3 (for HE 0017+0055); Δ[C/Fe] = −0.3 and +0.3 with short dashed red and long dashed blue lines respectively in panel 4 (for HE 2339−0837); and Δ[C/Fe] = −0.03 and +0.03 with short dashed red and long dashed blue lines respectively in panel 5 (for CD−27 14351).

HE 0017+0055, HE 0319–0215, HE 0930–0018, HE 1023–1504, HE 2144–1832 and HE 2339–0837 as no good lines were found in the spectra of these objects.

Ti- Titanium abundance is estimated using lines from both neutral and ionised species for all the programme stars except HE 2339−0837, BD+09 3019 and HE 1023–1504. While Ti abundance is estimated only using Ti II lines in HE 2339–0837, in BD+09 3019 and HE 1023–1504, Ti abundance is derived using only Ti I

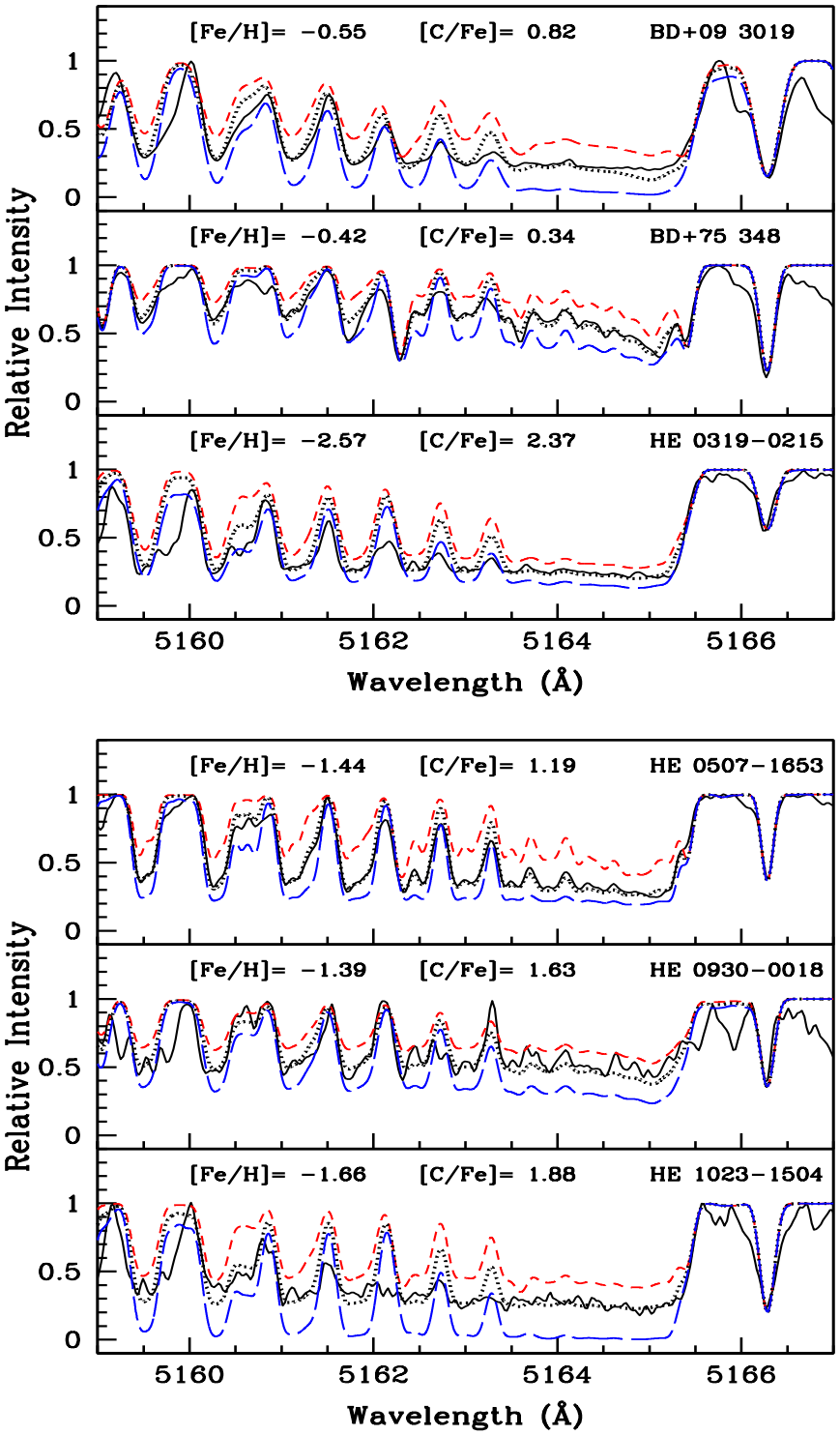

FIGURE 3.6: The spectral synthesis plots of C_2 band around 5165 Å for a few Ba and CEMP-*s* stars. The solid black lines represent the observed spectra. The dotted black lines show the synthesised spectra. Other two synthesised spectra are displayed corresponding to Δ[C/Fe] = −0.3 and +0.3 with short dashed red and long dashed blue lines respectively.

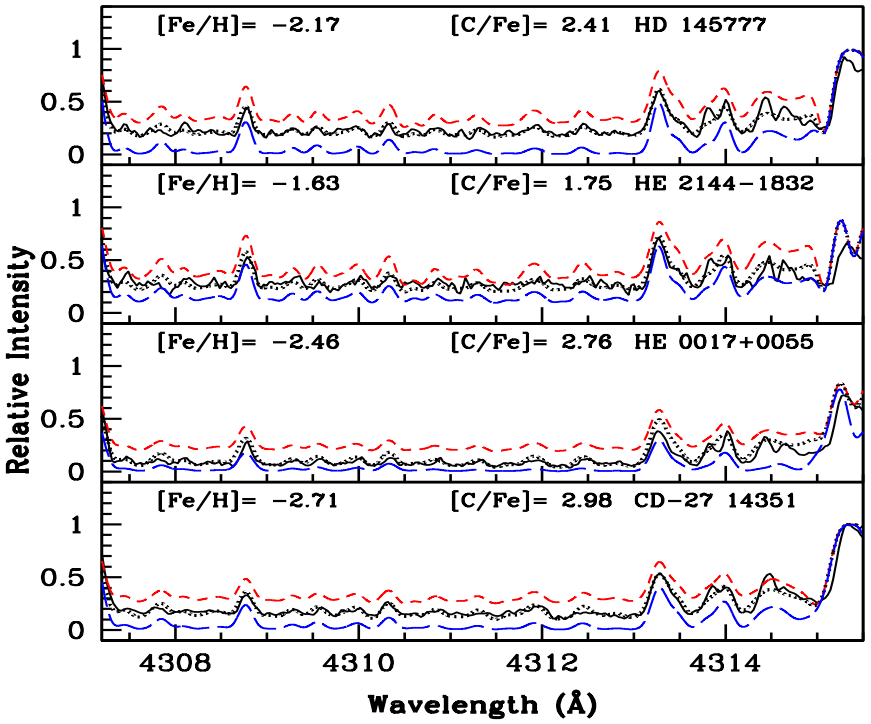

FIGURE 3.7: The spectral synthesis plots of CH band around 4310 Å for a sample of four programme stars. The solid black lines represent the observed spectra. The dotted black lines show the synthesised spectra. Two other synthesised spectra are displayed corresponding to Δ[C/Fe] = −0.05 and +0.05 with short-dashed red and long-dashed blue lines respectively in panel 1 (for HD 145777); Δ[C/Fe] = −0.15 and +0.15 with short-dashed red and long-dashed blue lines respectively in panel 2 (for HE 2144−1832); Δ[C/Fe] = −0.30 and +0.30 with short-dashed red and long-dashed blue lines respectively in panel 3 (for HE 0017+0055); and Δ[C/Fe] = −0.10 and +0.10 with short-dashed red and long-dashed blue lines respectively in panel 4 (for CD−27 14351).

lines. Titanium is found to be in the range –0.10 < [Ti/Fe] < 0.96 with the minimum for HE 0930–0018 and the maximum for CD–27 14351. Although it is seen that due to NLTE effects, the abundances derived from Ti I and Ti II lines may differ (Johnson 2002), we have derived similar abundances from Ti I and Ti II lines for most of our programme stars. The equal abundances found from Ti I and Ti II lines ensure the log g values estimated for our programme stars.

V- We have estimated the abundance of V using spectrum synthesis calculations of several lines of V I. Vanadium in the programme stars ranges from [V/Fe] =

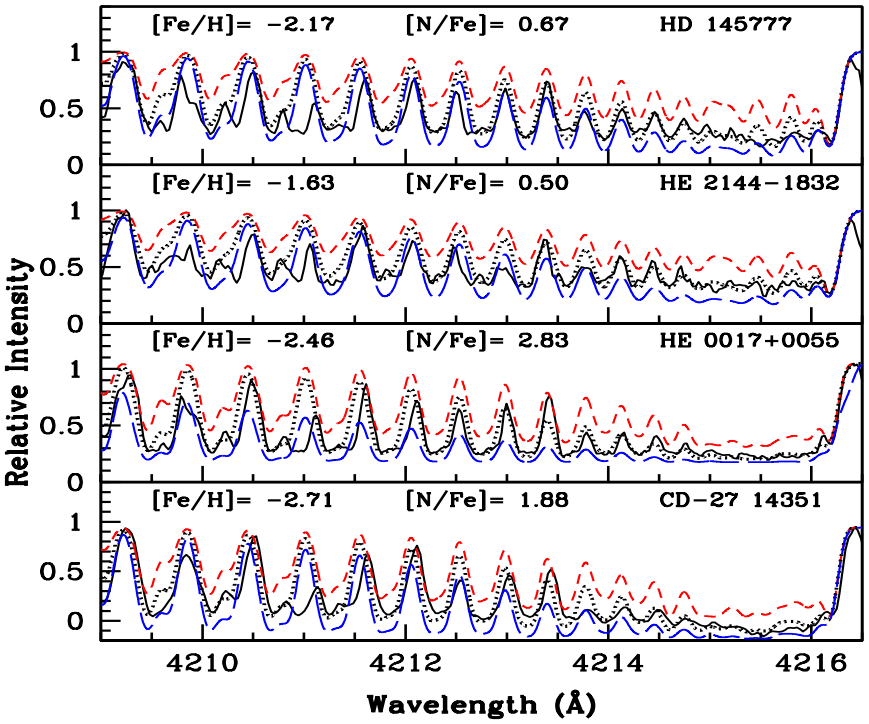

FIGURE 3.8: Spectra synthesis plots of CN band around 4215 Å for a sample of four programme stars. The solid black lines represent the observed spectra. The dotted black lines show synthesised spectra. Other two fits, the short dashed red and the long dashed blue lines are also displayed corresponding to Δ[N/Fe] = −0.3 and +0.3 respectively.

–0.39 to [V/Fe] = 1.11 dex with the minimum for BD+75 348 and the maximum for CD–27 14351. We could not determine the abundance of V for HE 0017+0055, HE 0319–0215, HE 0507–1653, HE 1005–1439, HE 1023–1504 and HE 2339–0837 as no good lines were found in the spectra of these objects.

3.4.3 Cr, Mn, Co, Ni, Cu and Zn

Cr- Abundance of Cr with respect to iron ([Cr/Fe]) of the programme stars ranges from –0.51 to 0.18 dex with the minimum for HE 0930–0018 and the maximum for CD–27 14351. For HD 147609, HD 154276, HD 87853 and HD 238020, both neutral and ionised species are used for abundance determination of Cr. We could

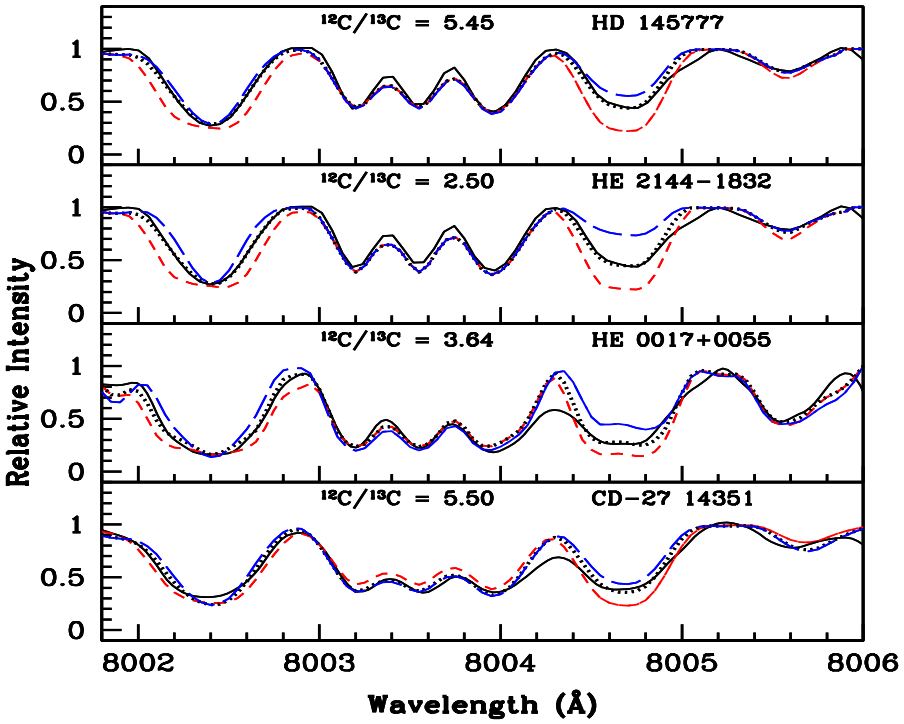

FIGURE 3.9: The spectral synthesis fits of the CN features around 8005 Å, for a sample of four programme stars, obtained with the derived abundances of C & N and $^{12}C/^{13}C$ values are shown with dotted black lines. The solid black curves represent the observed spectra. Other two synthesised spectra with $^{12}C/^{13}C \sim$ 1 and 12 are displayed with short-dashed red and long dashed blue lines.

not determine the abundance of Cr in BD+09 3019 and HE 0319–0215 as no good lines were found in the spectra of these two objects.

Mn- The abundance of Mn is estimated using spectrum synthesis calculations of several Mn I lines in the spectra of the programme stars. For HD 145777, we have used Mn II 5432.543 Å line to derive the abundance of Mn. The abundance of Mn with respect to iron ([Mn/Fe]) of the programme stars ranges from –0.89 to 0.29 dex with the minimum for HE 0930–0018 and the maximum for HE 0308–1612. The abundance of Mn could not be estimated for CD–27 14351, HE 0017+0055, HE 0319–0215 and HE 1023–1504 as no suitable lines were detected for abundance determination.

Co- The abundance of Co with respect to iron ([Co/Fe]) ranges from –0.11 to

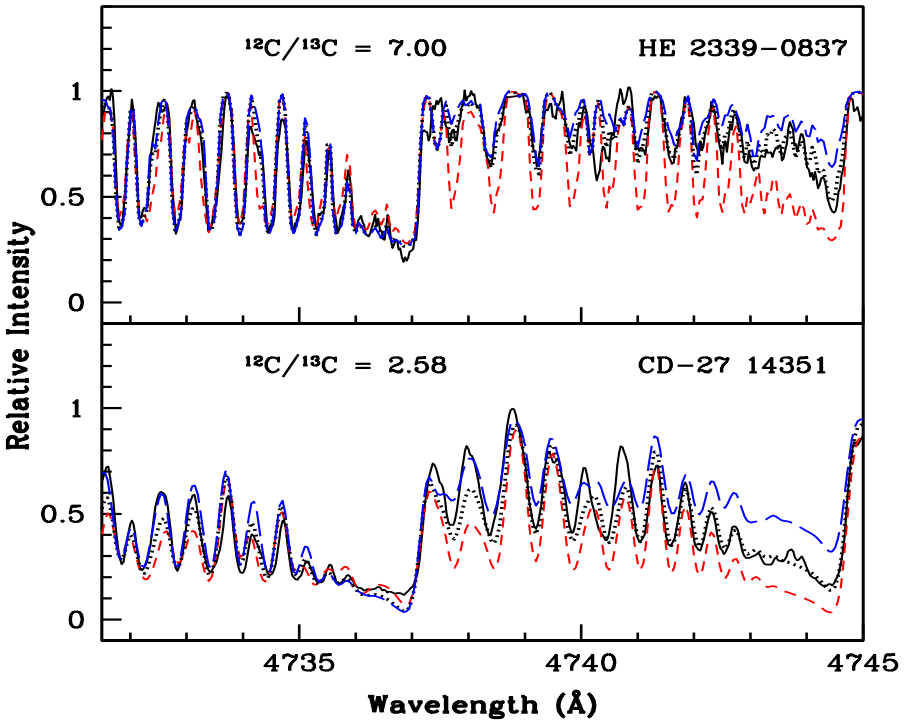

FIGURE 3.10: The spectral synthesis fits of the C_2 features around 4740 Å, for HE 2339–0837 and CD–27 14351, obtained with the derived abundances of C and $^{12}C/^{13}C$ values are shown with dotted black lines. The observed spectra are shown with solid black lines. Two other synthesised spectra with $^{12}C/^{13}C$ $\sim$ 1 and 15 are displayed with short dashed red and long dashed blue lines respectively.

0.24 dex in the programme stars, with the minimum for HE 0930–0018 and the maximum for HE 1005–1439. The abundance of Co could not be derived for BD+09 3019, CD–27 14351, HD 147609, HE 0017+0055, HE 0308–1612, HE 0319–0215, HE 1023–1504 and HE 2339–0837 as no good lines were found for abundance estimation in the spectra of these objects.

Ni- Nickel is found to be in the range –0.06 < [Ni/Fe] < 0.74 in the programme stars. The abundance of Ni could not be estimated for BD+09 3019, CD–27 14351, HD 145777, HE 0017+0055, HE 0319–0215, HE 1023–1504 and HE 2339–0837 as no good lines were found.

Cu- We could estimate the abundance of Cu in only three (BD+75 348, HD 238020

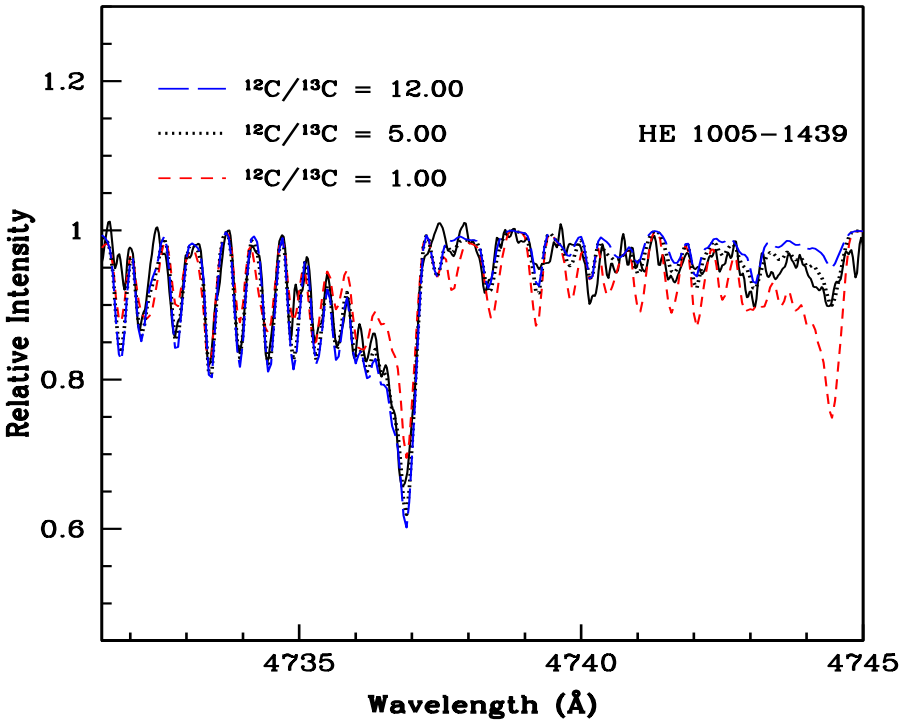

FIGURE 3.11: Spectral synthesis fit of the C_2 features around 4740 Å, for HE 1005–1439, obtained with the derived abundance of C and $^{12}C/^{13}C$ value is shown with dotted black line. The observed spectrum is displayed by a solid black line. Two alternative fits with $^{12}C/^{13}C \sim 1$ and 12 with short dashed red and long dashed blue lines are also displayed.

& HE 0507–1653) of the programme stars and is found to be in the range –0.20 < [Cu/Fe] < 0.38.

Zn- Zinc in the programme stars is found to be in the range –0.19 < [Zn/Fe] < 0.63. The abundance of Zn could not be estimated for BD+09 3019, CD–27 14351, HE 0319–0215, HE 1005–1439, HE 1023–1504 and HE 2339–0837 as no suitable lines were detected for abundance determination.

3.4.4 Sr, Y, Zr, Ru

Sr- The abundance of Sr with respect to iron ([Sr/Fe]) in the programme stars

ranges from –0.22 to 1.74 dex with the minimum for HD 154276 and the maximum for CD–27 14351. We could not determine the abundance of Sr for BD+75 348, HD 87853, HE 0017+0055, HE 0319–0215, HE 0507–1653, HE 0930–0018, HE 1023–1504 and HE 1153–0518 as no good lines could be detected. For HD 238020, HE 1005–1439 and HE 1246–1344, Sr abundance is derived using lines of ionised species (Sr II) of Sr. The estimated Sr abundance is found to be ($\sim$ 0.8 dex) lower than that obtained by Hansen *et al.* (2016a) for the star HE 2144−1832 (Table 3.38), which they had obtained using Sr II 4077.709 Å line on a spectrum of spectral resolution R $\sim$ 7450, and S/N = 6 (at 4000 Å). This line is severely blended in our spectrum, which was obtained at a higher resolution (R $\sim$ 60,000) and could not be used for abundance analysis. The abundance estimated from the blended Sr II line in Hansen *et al.* (2016a) may be the reason for the observed discrepancy.

Y- We have estimated the abundance of Y in all the programme stars except HE 1246–1344. Yttrium is found to be in the range –0.48 $<$ [Y/Fe] $<$ 1.97 in the programme stars, with the minimum for HD 87853 and the maximum for CD–27 14351.

Zr- Zirconium abundance is estimated using lines from both neutral and ionised species for BD+75 348, CD–27 14351, HD 238020 and HE 0507–1653. We could not estimate the abundance of Zr for BD+09 3019, HD 87853, HE 0308–1612, HE 0401–0138, HE 1005–1439, HE 1153–0518 and HE 1246–1344 as no good lines were detected.

Ru- We could derive the upper limit to the abundance of Ru only in HD 154276 ([Ru/Fe] $<$ 0.18). We could not detect lines due to Niobium and Technetium (Tc) in any of the spectra.

3.4.5 Ba, La, Ce, Pr, Nd, Dy, Er, Hf and Pb

Ba- The abundance of Ba is derived using spectrum synthesis calculations of several lines due to Ba II. Figure 3.12 shows the spectrum synthesis fits for a few stars in our sample. Ba is found to be in the range –0.43 $\leq$ [Ba/Fe] $\leq$ 2.30. Abundance of Ba could not be derived for BD+09 3019 as the Ba lines are found to be too strong and saturated.

La- The abundance of La is estimated using the spectrum synthesis calculation of La II lines. Lanthanum ranges from [La/Fe] = 0.20 to [La/Fe] = 2.46 in the programme stars. We could not estimate the abundance of La for HD 87853, HE 0319–0215 and HE 1023–1504 as no good lines were detected. For the stars, HE 0401–0138, HE 1153–0518 and HE 1246–1344, we could estimate only the upper limits of the abundance of La.

Ce, Pr, Nd, Dy, Er, Hf- The abundances of these elements are estimated using the equivalent width measurement technique. Ce, Pr, Nd and Dy in the programme stars range 0.18 $<$ [Ce/Fe] $<$ 2.50, 0.46 $<$ [Pr/Fe] $<$ 2.48, 0.26 $<$ [Nd/Fe] $<$ 2.55 and 0.11 $<$ [Dy/Fe] $<$ 1.88 respectively. The abundance of Ce could be derived for all the programme stars except HD 87853. The abundance of Pr could not be derived for HD 87853, HD 154276 and HE 1023–1504. We could estimate the abundance of Nd for all the objects except HE 1151–0518. For HE 0401–0138 and HE 1246–1344, we could estimate only upper limits to the abundances of Ce, Pr and Nd. The abundance of Dy could be determined for the objects BD+75 348, BD+09 3019, HD 238020 and HE 1005–1439. While the abundance of Er could be derived only for HE 1005–1439, we could determine the abundance of Hf for BD+75 348 and HE 1005–1439.

Pb- We could derive the abundance of Pb only for HE 1005–1439 using the spectrum synthesis calculation of Pb I 4057.81 Å. Pb is found to be highly enhanced

([Pb/Fe] = 1.98) in the object.

3.4.6 Sm, Eu

Sm- The abundance of Sm in the programme stars is found to be in the range $0.07 <$ [Sm/Fe] < 2.37. Sm abundance could not be estimated for HD 87853, CD–27 14351, HE 1005–1439 and HE 1153–0518. For HE 0401–0138 and HE 1246–1344, we could only estimate upper limits to the abundance of Sm.

Eu- The abundance of Eu in most of the programme stars is derived using the spectrum synthesis calculation of Eu II 6645.064 Å line (Figure 3.13), considering hyperfine splitting contributions from Worley *et al.* (2013). The other frequently used lines Eu II 4129.725 Å, 4205.042 Å and 6437.640 Å are found to be severely blended and hence, could not be used for abundance analysis. However, for the abundance determination of HE 0507–1653, Eu II 6645.064 Å and Eu II 6437.640 Å lines are used. The lines Eu II 4129.725 Å and 4205.042 Å are used for estimating the abundance of Eu for HE 1005–1439 and also for deriving the upper limits to the Eu abundance for HE 0401–0138 and HE 1246–1344. We could not derive the abundance of Eu for HD 154276, HD 238020, HE 0930–0018 and HE 1153–0518. For CD−27 14351, we could estimate an upper limit with [Eu/Fe] $\sim$ 0.39. As shown in Figure 3.13, Eu II 6645.064 Å line is blended with two CN lines. It can be clearly seen that Eu II 6645.064 Å line is absent in the spectrum of the object CD−27 14351; a miss identification of the CN line at 6644.750 Å to be Eu II 6645.064 Å line, could result in a much higher abundance of Eu; this may explain the very high abundance recorded for Eu by Karinkuzhi *et al.* (2017).

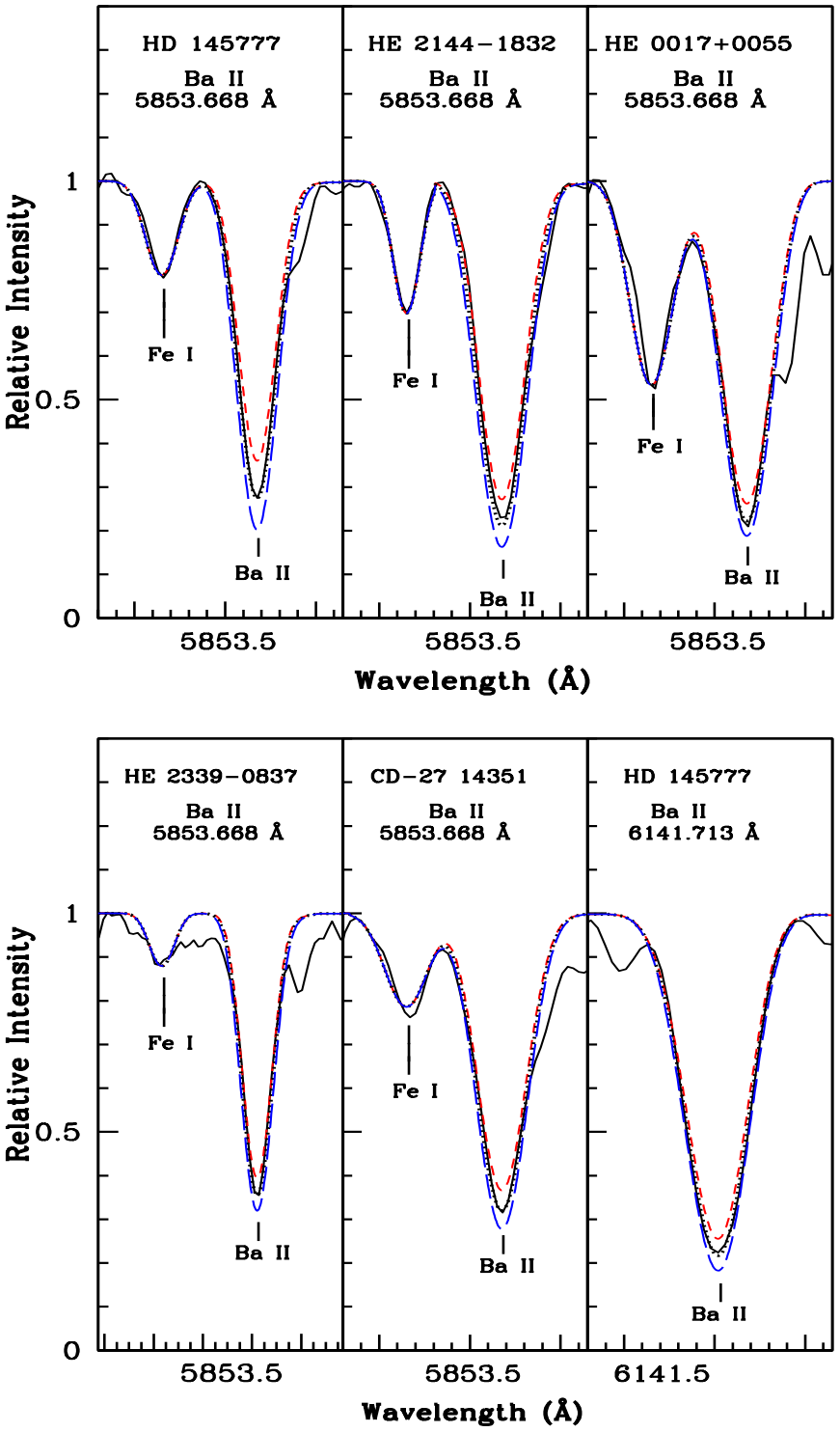

FIGURE 3.12: Spectral synthesis fits of Ba II 5853 Å and Ba II 6141 Å lines. The solid line indicates the observed spectra. Dotted black line represents the best-fit synthesised spectra. Other two synthesis, the short dashed red and the long dashed blue lines are also displayed corresponding to Δ[Ba II/Fe] = -0.3 and $+0.3$ respectively.

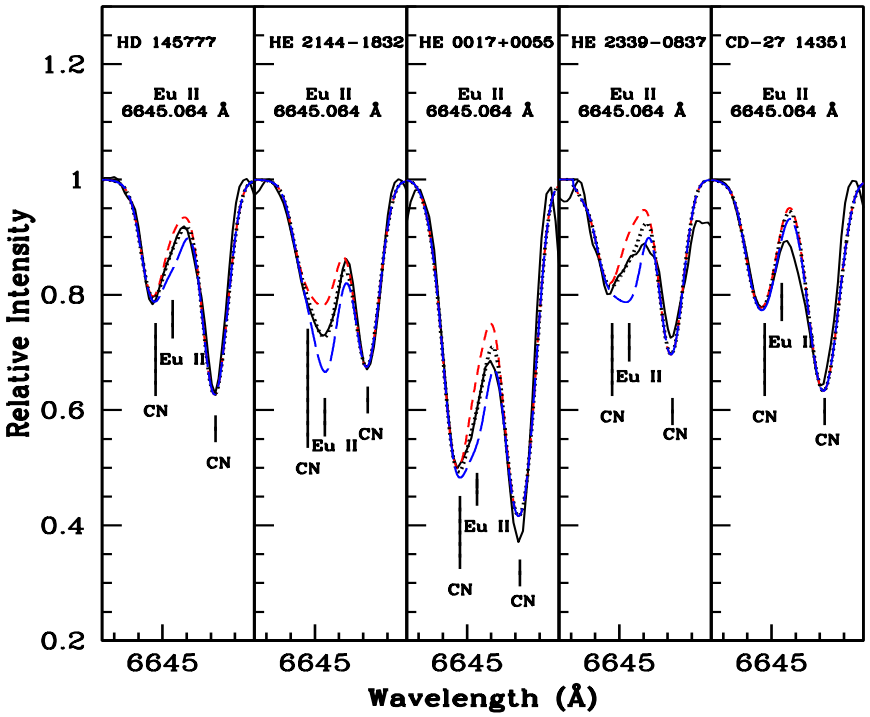

FIGURE 3.13: Synthesis of Eu II 6645 Å line. The solid black line indicates the observed spectra. Dotted black line represents the best-fit synthesised spectra. Other two synthesis, the short dashed red and the long dashed blue lines are also displayed corresponding to Δ[Eu II/Fe] = −0.3 and +0.3 respectively.

3.5 Abundance Uncertainties

Two components, namely random error ($\sigma_{ran} = \frac{\sigma_s}{\sqrt{N}}$, where σ_s represents the standard deviation of the abundance of a particular species derived using N number of lines of that species) and systematic error (σ_{sys}), contribute to the total uncertainties. While the random error arises due to the uncertainties in the factors like oscillator strength, equivalent width measurement, and line blending, the systematic error arises due to the uncertainties in estimating the stellar atmospheric parameters. Finally, the uncertainties on [X/Fe] are derived as follows:

$$\sigma^2_{[X/Fe]} = \sigma^2_{log\epsilon} + \sigma^2_{[Fe/H]}, \tag{3.3}$$

$$\sigma^2_{log\epsilon} = \sigma^2_{ran} + \sigma^2_{sys}, \tag{3.4}$$

$$\begin{aligned}\sigma^2_{sys} = &\left(\frac{\delta log\epsilon}{\delta T}\right)^2 \sigma^2_{T_{eff}} + \left(\frac{\delta log\epsilon}{\delta logg}\right)^2 \sigma^2_{logg} \\ &+ \left(\frac{\delta log\epsilon}{\delta \zeta}\right)^2 \sigma^2_{\zeta} + \left(\frac{\delta log\epsilon}{\delta [Fe/H]}\right)^2 \sigma^2_{[Fe/H]}\end{aligned}, \tag{3.5}$$

where, $\sigma_{T_{eff}}$ = 100 K, σ_{logg} = 0.2 dex, σ_{ζ} = 0.2 km/s^{-1}, and $\sigma_{[Fe/H]}$ = 0.15 dex represent the typical uncertainties on the stellar atmospheric parameters T_{eff}, logg, ζ, and [Fe/H], respectively. When an abundance is based on a single line, we consider σ_{ran} = 0.2 dex. We evaluated the partial derivatives appearing in Equation 3.5 for the programme stars, varying the stellar parameters T_{eff}, logg, ζ, and [Fe/H] by ± 100 K, ± 0.2 dex, ± 0.2 km/s^{-1}, and ± 0.2 dex, respectively. We note that the uncorrelated nature of the uncertainties arising from the different stellar parameters in Equation 3.5 may lead to the overestimation of the calculated uncertainties on log ϵ and [X/Fe]. The resulting differential abundances and the derived uncertainties on [X/Fe] for two objects HE 1005–1439 and HE 2144–1832 are presented as examples in Tables 3.16 & 3.17 respectively. In the columns 5 and 8 of Table 3.32 we have presented the $\sigma_{log\epsilon}$ and $\sigma_{[X/Fe]}$ respectively for HE 1005–1439.

3.6 Kinematic Analysis

Along with the physical parameters and composition, it is also important to know the group of Galactic populations to which the programme stars belong. To determine this, we calculated the space velocities of the programme stars using the

method discussed in Johnson and Soderblom (1987). Using the method given by Bensby *et al.* (2003) and information such as parallax (π) and proper motion (μ_α, μ_δ) from the Gaia (Gaia Collaboration *et al.* 2018) in SIMBAD and radial velocity (V_r) from our estimates, we calculated the components of space velocity with respect to LSR using the relation

$$(U, V, W)_{LSR} = (U, V, W) + (U, V, W)_\odot \; km/s. \tag{3.6}$$

Here U, V, and W are the velocity vectors pointing towards the centre of the Galaxy, the direction in which the Galaxy is rotating, and the North pole of the Galaxy, respectively. The solar U, V, W component velocities (11.1, 12.2, 7.3) km/s are taken from Schönrich *et al.* (2010). The total spatial velocity (V_{spa}) is given by

$$V_{spa} = \sqrt{U_{LSR}^2 + V_{LSR}^2 + W_{LSR}^2}. \tag{3.7}$$

The estimated components of spatial velocity and the total spatial velocity are presented in Table 3.5. Following the procedures of Mishenina *et al.* (2004), Bensby *et al.* (2003, 2004) and Reddy *et al.* (2006), we calculated the probability that the stars are a member of the thin disc, the thick disc, or the halo population. Table 3.5 presents the U_{LSR}, V_{LSR}, W_{LSR}, V_{spa} and the probabilities of the programme stars to be members of different galactic populations. As the parallax values of HE 1023–1504 and HE 1153–0518 are not available in the literature, we could not carry out the kinematic analysis for these two objects.

TABLE 3.4: **Derived atmospheric parameters of our programme stars and literature values.**

Star Name	T_{eff} (K)	log g (spectroscopic) (cgs)	log g (parallax) (cgs)	ζ (km s^{-1})	[Fe I/H]	[Fe II/H]	[Fe/H]	Ref
BD+75 348	4840	2.00	2.51	1.43	−0.41± 0.20	−0.42± 0.18	−0.42	1
	4700	1.80	-	2.00	−0.86± 0.26	−0.88± 0.02	−0.87	2
	4900	-	-	-	-	-	-	3
	4760	-	-	-	-	-	-	4
BD+09 3019	4150	2.00	1.30	2.20	−0.60± 0.16	−0.60± 0.22	−0.60	1
CD−27 14351	4320	0.50	-	2.58	−2.72±0.16	−2.69±0.07	−2.71	1
	4335	0.50	-	2.42	-	-	−2.62	5
	4223	-	-	-	-	-	-	3
HD 87853	6250	2.50	3.81	1.63	–0.72	–0.73	–0.73	1
HD 145777	4160	0.90	-	2.02	−2.17±0.18	−2.17±0.25	−2.17	1
	4245	-	-	-	-	-	-	4
	4216	-	-	-	-	-	-	3
HD 147609	6350	3.50	3.71	1.55	–0.28	–0.28	–0.28	1
	6411	3.90	-	1.26	–0.23	-		6
	5960	3.30	-	1.50	–0.45	+0.08		7
	6270	3.50	-	1.20	-	-		8
	6300	3.61	-	1.20	-	-		9
HD 154276	5820	4.28	4.25	0.63	–0.09	–0.10	–0.10	1
	5722	4.28	-	0.93	–0.29	-	-	10
	5731	4.35	-	1.28	–0.30	-		11
HD 238020	5150	2.10	2.78	1.36	−0.67± 0.15	−0.68± 0.16	−0.68	1
	5035	-	-	-	-	-	-	3
HE 0017+0055	4370	0.80	-	1.94	−2.47±0.12	−2.45±0.03	−2.46	1
	4250	1.00	-	2.00	-	-	−2.40	12
	4185	0.18	-	2.00	-	-	−2.72	13
HE 0308–1612	4600	1.70	-	1.42	–0.72	–0.73	–0.73	1
HE 0319−0215	4650	0.50	-	1.33	−2.58±0.10	−2.56±0.05	−2.57	1
	4416	0.64	-	-	-	-	−2.42	13
	-	-	-	-	-	-	−2.30	14
	4738	0.66	-	2.16	-	-	−2.90	15
HE 0401−0138	4830	1.30	-	0.87	−3.46 ± 0.14	−3.43 ± 0.06	−3.45	1
	4866	1.76	-	1.45	-	-	−3.34	20
	4929	-	-	-	-	-	-	21

TABLE 3.4: *–continued*

Star Name	T_{eff} (K)	log g (spectroscopic) (cgs)	log g (parallax) (cgs)	ζ (km s^{-1})	[Fe I/H]	[Fe II/H]	[Fe/H]	Ref
HE 0507–1653	4970	2.20	-	1.48	−1.46±0.11	−1.42±0.08	−1.44	1
	5000	2.40	-	2.00	−1.38±0.19	−1.39±0.17	−1.38	16
	-	-	-	-	-	-	−1.42	17
	4880	1.50	-	-	-	-	−1.81	13
	4935	1.88	-	-	-	-	−1.32	18
	5035	2.39	-	1.53	-	-	−1.35	15
HE 0930−0018	4190	2.65	-	1.86	−1.39±0.11	−1.39±0.09	−1.39	1
HE 1023–1504	4440	0.50	-	1.67	−1.66±0.14	−1.66±0.07	−1.66	1
	4421	0.66	-	-	-	-	−2.50	13
HE 1005−1439	5170	1.80	-	1.26	−3.04 ± 0.15	−3.01 ± 0.03	−3.03	1
	5000	1.90	-	2.00	−3.17 ± 0.32	−3.15 ± 0.22	−3.17	16
	5202	2.55	-	-	-	-	−3.09	18
	5030	-	-	-	-	-	-	21
HE 1153–0518	4700	0.20	-	1.48	−3.14±0.20	−3.13±0.23	−3.14	1
HE 1246−1344	4780	1.00	-	1.22	−3.51 ± 0.09	−3.48 ± 0.01	−3.50	1
	4853	1.65	-	1.84	-	-	−3.40	20
	4852	-	-	-	-	-	-	21
HE 2144−1832	4190	0.60	-	1.87	−1.63±0.15	−1.63±0.00	−1.63	1
	4200	0.60	-	2.20	-	-	−1.70	19
HE 2339−0837	4940	1.40	-	1.55	−2.74±0.08	−2.74±0.08	−2.74	1
	4939	1.60	-	2.00	-	-	−2.71	13

References: 1. This work, 2. Začs *et al.* (2000), 3. McDonald *et al.* (2012), 4. Bergeat *et al.* (2001), 5. Karinkuzhi *et al.* (2017), 6. Escorza *et al.* (2019), 7. Allen and Barbuy (2006), 8. North *et al.* (1994), 9. Thévenin and Idiart (1999), 10. Bensby *et al.* (2014), 11. Ramírez *et al.* (2013), 12. Jorissen *et al.* (2016a), 13. Kennedy *et al.* (2011), 14. Hansen *et al.* (2016c), 15. Karinkuzhi *et al.* (2021), 16. Aoki *et al.* (2007), 17. Schuler *et al.* (2008), 18. Yong *et al.* (2013), 19. Hansen *et al.* (2016a), 20. Barklem *et al.* (2005), 21. Gaia Collaboration *et al.* (2018).

TABLE 3.5: **Spatial velocity and probability estimates.**

Star Name	$U_{LSR}(km/s)$	$V_{LSR}(km/s)$	$W_{LSR}(km/s)$	V_{spa} (km/s)	P_{thin}	P_{thick}	P_{halo}
BD+75 348	–44.75 ±1.17	43.21 ±0.93	17.28 ±1.07	64.56 ±0.10	0.97	0.03	0.00
BD+09 3019	102.34 ±4.47	−80.69 ±4.10	−60.85 ±3.04	143.83 ±0.41	0.00	0.97	0.03
CD−27 14351	101.95 ±4.04	−213.31 ±24.66	−57.21 ±4.17	243.25 ± 20.88	0.00	0.10	0.90
HD 87853	–43.92 ± 0.96	21.24 ± 0.24	–24.11 ± 0.50	54.42 ± 0.90	0.98	0.02	0.00
HD 145777	−4.51 ±3.22	−155.01 ±17.49	67.18 ±5.62	169.00 ± 13.86	0.00	0.83	0.17
HD 147609	15.75 ± 0.82	–13.98 ± 0.87	–2.66 ± 1.02	21.23 ± 0.09	0.99	0.01	0.00
HD 154276	2.31 ± 0.96	–116.07 ± 0.74	23.08 ± 0.74	118.36 ± 0.56	0.06	0.92	0.02
HD 238020	–43.06 ±1.41	−13.73 ±1.02	−39.08 ±2.60	59.75 ±2.95	0.90	0.10	0.00
HE 0017+0055	16.21 ±2.02	−190.74 ±29.87	−10.33 ±15.90	191.71 ± 30.31	0.00	0.65	0.35
HE 0308–1612	–180.36 ± 17.11	–90.63 ± 10.00	49.69 ± 13.22	207.87 ± 15.98	0.00	0.85	0.15
HE 0319−0215	305.94 ±22.00	–321.86 ±65.35	107.59 ±16.06	456.91 ±27.24	0.00	0.00	1.00
HE 0401−0138	−57.84 ± 2.87	−256.53 ± 48.18	54.79 ± 16.90	268.61 ± 42.95	0.00	0.00	1.00
HE 0507−1653	–247.94 ±1.03	–225.22 ±2.55	−85.75 ±3.89	345.76 ±3.39	0.00	0.00	1.00
HE 0930−0018	–53.49 ±0.42	–0.63 ±0.47	18.80 ±0.40	56.70 ±0.27	0.98	0.02	0.00
HE 1005−1439	313.92 ± 25.79	−249.75 ± 14.04	−72.15 ± 10.65	407.58 ± 9.35	0.00	0.00	1.00
HE 1246−1344	27.87 ± 6.73	−475.47 ± 271.18	−273.19 ± 199.48	549.08 ± 332.01	0.00	0.00	1.00
HE 2144−1832	234.33 ±16.01	8.57 ±6.32	−9.90 ±9.09	234.69 ± 15.82	0.01	0.84	0.15
HE 2339−0837	218.78 ±34.88	−126.66 ±37.83	−224.20±14.05	337.90 ± 4.18	0.00	0.00	1.00

3.7 Classification of the programme stars

We have classified the programme stars (Table 3.6) based on the classification criteria of stars discussed in Chapter 1.

HD 87853

This star is mildly metal-poor with an estimated metallicity [Fe/H] = –0.73. All the elements, including α- and *n*-capture elements show abundances that are generally exhibited by a normal metal-poor star having similar metallicity. The probability estimate and metallicity support the inclusion of HD 87853 into the thin disk population.

BD+75 348, BD+09 3018, HD 147609, HD 154276, HD 238020

These objects show characteristic properties of Ba stars, including strong lines of Sr II 4077 Å and Ba II 4554 Å. Except HD 154276 and HD 238020, all the stars exhibit strong enhancement of *s*-process elements. HD 154276 and HD 238020 show mild enhancement of *n*-capture elements. In Chapter 7, we have discussed these objects in detail and further classified them as mild and strong Ba stars. While the first three stars are found to be strong Ba stars, the other two are classified as mild Ba stars. The probability estimates show that BD+75 348, HD 147609 and HD 238020 are members of the thin disk population, and the other two objects are members of the thick disk population. For the stars for which we could estimate the abundances of both C and O, we find the estimated C/O < 1, as seen in Ba stars in general.

HE 0308–1612

This is a mildly metal-poor object with [Fe/H] = –0.73. We have classified this star as a CH star with [C/Fe] = 0.78, [Ba/Fe] = 1.63 and [Ba/Eu] = 1.28. As we could not estimate the abundance of oxygen in this star, we could not classify

it based on the C/O ratio. The probability estimate show HE 0308–1612 to be a thick disk object.

HE 0401–0138, HE 1153–0518, HE 1246–1344

These three objects are extremely metal-poor (EMP) stars with metallicities in the range –3.14 < [Fe/H] < –3.50. While all the three stars show enhancement of Mg ([Mg/Fe] > 0.7), HE 1153–0518 and HE 1246–1344 show enhancement of Na as well. Other light elements show normal abundances expected for EMP stars. The *n*-capture elements are not enhanced in any of these three stars. The object HE 1153–0518 exhibits enhancement of carbon with [C/Fe] = 2.64 and near solar Ba abundance with [Ba/Fe] = -0.01. Following the classification scheme of Beers and Christlieb (2005), we have classified this object as a CEMP-*no* star. The probability estimates show HE 0401–0138 and HE 1246–1344 to be members of the halo population.

CD–27 14351, HE 0319–0215, HE 0930–0018, HE 1023–1504

These four objects fall in the category of metal-poor and VMP stars with metallicities in the range –1.39 < [Fe/H] < –2.71. Carbon and *s*-process elements are highly enhanced in these stars with 1.65 < [C/Fe] < 2.98 and 1.09 < [Ba/Fe] < 2.08. Following the classification schemes of CEMP stars, we have classified these objects as CEMP-*s* stars. The probability estimates show CD–27 14351, HE 0319–0215 and HE 0930–0018 to be members of the halo population.

HE 0017+0055, HE 2144–1832, HE 2339–0837

These are metal-poor and very metal-poor stars with metallicities in the range –1.63 < [Fe/H] < –2.74. These objects show highly enhanced carbon abundance with 1.80 < [C/Fe] < 2.93 and exhibit enhancement of both *s*- and *r*-process elements with 1.49 < [Ba/Fe] < 2.30 and 1.01 < [Eu/Fe] < 2.14. Following the classification scheme of Beers and Christlieb (2005), we have classified these three objects as CEMP-*r/s* stars. In Chapters 4 & 5, we have discussed the formation

scenarios and classification of these objects in detail. In Chapter 4, we have shown that *i*-process models can explain the abundance peculiarities of these objects. The estimated metallicities and spatial velocities indicate that HE 0017+0055 and HE 2144–1832 are members of the thick disc population. The probability estimates for them being members of the thick disc population are 0.65 and 0.84, respectively. The probability estimates show that the object HE 2339–0837 is a member of the halo population.

HD 154777, HE 0507–1653, HE 1005–1439

HD 145777 is found to be a very metal-poor star with [Fe/H] = –2.17. With enhanced carbon and *n*-capture elements, this object is clearly a CEMP star. However, classification criteria of CEMP stars put forward by different groups place this object in different subclasses. While a few schemes put this object in CEMP-*s* group others place this object in the CEMP-*r/s* group. These discrepancies prompted us to revisit the classification schemes of CEMP-*s* and CEMP-*r/s* stars. We have discussed the existing classification schemes of CEMP-*s* & CEMP-*r/s* stars and put forward a new classification scheme to distinguish these two subclasses. Our classification scheme puts the object in CEMP-*s* subclass. This is discussed in Chapter 5. Further, we have shown that *i*-process model predictions cannot reproduce the abundance pattern of HD 145777 (Chapter 4).

HE 0507–1653 is a CEMP star with [Fe/H] = –1.44 and [C/Fe] = 1.16. The object shows enhancement of both *s*- and *r*-process elements. Existing classification schemes of CEMP stars put this object in the CEMP-*r/s* subgroup. Based on our classification scheme we have placed this object in the CEMP-*s* subclass. In Chapter 7, we have shown that *s*-process AGB model can satisfactorily reproduce the observed abundance pattern of the object.

HE 1005–1439 is an extremely metal-poor star with [Fe/H] = –3.03. Carbon as well as *n*-capture elements are enhanced in the star. The surface chemical

composition of the object is found to be enriched with both *s*-process and *i*-process nucleosynthesis. This object seems to belong to a new class of objects with a distinct abundance pattern observed for the first time in a CEMP star. The peculiar abundance pattern was investigated based on a parametric-model-based analysis that revealed almost equal contributions from both the *s*-process and the *i*-process to its surface chemical composition. In Chapter 6, we have discussed the classification and formation scenario of this object in detail.

TABLE 3.6: **Classification of the programme stars.**

Star Name	[Fe/H]	[C/Fe]	[Ba/Fe]	[La/Eu]	[Eu/Fe]	[Ba/Eu]	[La/Eu]	Classification
BD+75 348	–0.42	0.31	1.62	1.92	0.70	0.92	1.22	Ba
BD+09 3019	–0.60	0.77	-	2.25	1.05	-	1.20	Ba
CD–27 14351	–2.71	2.98	1.82	1.56	< 0.39	> 1.43	> 1.17	CEMP-*s*
HD 87853	–0.73	-	–0.43	-	0.34	–0.77	-	MP
HD 145777	–2.17	2.42	1.27	1.37	0.80	0.47	0.57	CEMP-*s*
HD 147609	–0.28	0.38	1.40	1.27	0.13	1.27	1.14	Ba
HD 154276	–0.10	-	0.22	0.20	-	-	-	Ba
HD 238020	–0.68	–0.04	0.25	0.48	-	-	-	Ba
HE 0017+0055	–2.46	2.74	2.30	2.46	2.14	0.16	0.32	CEMP-*r/s*
HE 0308–1612	–0.73	0.78	1.63	1.43	0.35	1.28	1.08	CH
HE 0319–0215	–2.57	2.41	1.88	-	0.85	1.03	-	CEMP-*s*
HE 0401–0138	–3.45	-	–0.12	< 0.45	< 0.73	$> –0.85$	$> –0.28$	EMP
HE 0507–1653	–1.44	1.16	2.06	1.94	1.03	1.03	0.91	CEMP-*s*
HE 0930–0018	–1.39	1.65	1.09	1.09	-	-	-	CEMP-*s*
HE 1005–1439	–3.03	2.37	1.16	1.25	0.46	0.70	0.79	CEMP-*i/s*
HE 1023–1504	–1.66	1.92	2.08	-	0.89	1.19	-	CEMP-*s*
HE 1153–0518	–3.14	2.64	–0.01	< 0.44	-	-	-	CEMP-*no*
HE 1246–1344	–3.50	0.02	–1.48	< 0.50	< 0.63	$> –2.11$	$> –0.13$	EMP
HE 2144–1832	–1.63	1.80	1.49	1.53	1.01	0.48	0.52	CEMP-*r/s*
HE 2339–0837	–2.74	2.93	2.21	2.24	1.84	0.37	0.40	CEMP-*r/s*

TABLE 3.7: **Equivalent widths (in mÅ) of Fe lines used for the estimation of atmospheric parameters.**

Wavelength (Å)	Element	E_{low} (eV)	log gf	HD 145777	CD−27 14351	HE 0017+0055	HE 2144−1832	HE 2339−0837
4466.573	Fe I	0.11	−4.464	-	-	101.9 (5.08)	-	-
4476.019		2.85	−0.570	-	112.1 (4.71)	-	-	-
4871.318		2.87	−0.410	157.0 (5.63)	-	-	152.9 (5.67)	-
4882.143		3.42	−1.640	49.3 (5.65)	-	-	54.6 (5.73)	-
4890.755		2.88	−0.430	-	131.8 (4.77)	-	-	-
4903.310		2.88	−1.080	93.9 (5.07)	67.9 (4.62)	72.3 (4.85)	133.9 (5.93)	25.7 (4.69)
4924.770		2.28	−2.220	-	80.7 (5.10)	66.1 (5.10)	-	-
4982.499		4.10	0.164	-	55.8 (4.79)	-	-	-
4994.130		0.92	−3.080	155.7 (5.43)	134.0 (4.72)	119.1 (4.95)	169.2 (5.85)	44.3 (4.72)
5006.119		2.83	−0.615	-	-	-	-	53.6 (4.68)
5079.223		2.20	−2.067	108.6 (5.32)	66.6 (4.66)	83.7 (5.08)	133.9 (5.88)	20.7 (4.75)
5166.282		0.00	−4.195	171.9 (5.44)	167.7 (4.91)	145.8 (5.19)	-	-
5171.596		1.49	−1.793	180.9 (5.38)	179.0 (4.84)	162.5 (5.26)	-	84.4 (4.77)
5192.344		3.00	−0.421	-	-	-	-	53.9 (4.66)
5194.941		1.56	−2.090	156.3 (5.28)	131.4 (4.54)	-	-	63.0 (4.77)

In columns 5 to 9, the numbers within bracket '()' indicate the abundances derived from the corresponding line.

Table 3.7: *–continued*

Wavelength (Å)	Element	E_{low} (eV)	log gf	HD 145777	CD−27 14351	HE 0017+0055	HE 2144−1832	HE 2339−0837
5198.711		2.22	−2.135	98.7 (5.23)	58.1 (4.65)	-	137.6 (6.01)	-
5202.336		2.18	−1.838	-	122.6 (5.03)	100.2 (5.06)	-	35.4 (4.80)
5216.274		1.61	−2.150	132.8 (4.95)	118.4 (4.50)	-	-	48.2 (4.65)
5217.389		3.21	−1.162	-	73.1 (5.09)	-	-	-
5226.862		3.04	−0.555	115.4 (5.07)	106.9 (4.71)	114.5 (5.19)	-	45.4 (4.69)
5227.189		1.56	−1.228	-	-	168.7 (4.89)	-	-
5232.940		2.94	−0.190	-	-	-	-	78.2 (4.79)
5242.491		3.63	−0.840	45.0 (5.05)	-	50.0 (5.21)	91.6 (5.79)	-
5247.050		0.09	−4.946	126.1 (5.40)	96.6 (4.89)	83.5 (5.00)	-	-
5253.462		3.28	−1.670	-	-	-	85.7 (6.03)	-
5266.555		3.00	−0.490	132.8 (5.26)	93.4 (4.43)	104.4 (4.88)	150.2 (5.70)	61.4 (4.85)
5281.790		3.04	−1.020	107.2 (5.38)	65.8 (4.69)	73.6 (4.97)	144.6 (6.17)	25.9 (4.78)
5283.621		3.24	−0.630	122.3 (5.54)	100.1 (4.97)	-	-	-
5307.361		1.61	−2.987	91.2 (5.08)	70.5 (4.79)	-	130.4 (5.80)	-
5324.179		3.21	−0.240	127.1 (5.20)	119.5 (4.78)	105.8 (4.94)	149.8 (5.72)	54.0 (4.71)

Table 3.7: *–continued*

Wavelength (Å)	Element	E_{low} (eV)	log gf	HD 145777	CD−27 14351	HE 0017+0055	HE 2144−1832	HE 2339−0837
5328.531		1.56	−1.850	180.2 (5.46)	165.3 (4.72)	142.9 (4.94)	-	-
5339.929		3.27	−0.680	103.5 (5.29)	94.5 (4.97)	-	-	-
5341.024		1.61	−2.060	152.0 (5.18)	147.2 (4.75)	-	-	-
5367.466		4.42	0.350	74.0 (5.32)	42.9 (4.80)	57.9 (5.13)	106.7 (5.91)	-
5369.961		4.37	0.350	67.8 (5.17)	-	-	91.0 (5.56)	-
5415.199		4.39	0.500	-	60.6 (4.84)	-	-	-
5466.396		4.37	−0.630	-	-	-	48.3 (5.83)	-
5586.756		3.37	−0.210	126.8 (5.31)	87.4 (4.53)	108.5 (5.11)	153.5 (5.90)	48.2 (4.75)
5638.262		4.22	−0.870	-	-	-	56.6 (5.99)	-
5753.122		4.26	−0.760	35.6 (5.60)	-	-	69.5 (6.13)	-
6027.051		4.08	−1.210	-	-	-	53.5 (6.07)	-
6056.005		4.73	−0.460	-	-	-	30.1 (5.77)	-
6136.615		2.45	−1.400	157.8 (5.62)	119.7 (4.78)	-	-	55.2 (4.93)
6137.691		2.59	−1.403	128.1 (5.33)	100.7 (4.76)	-	167.5 (6.06)	43.6 (4.91)

Table 3.7: *–continued*

Wavelength (Å)	Element	E_{low} (eV)	log gf	HD 145777	CD−27 14351	HE 0017+0055	HE 2144−1832	HE 2339−0837
6151.617		2.18	−3.299	30.4 (5.24)	-	-	84.0 (5.98)	-
6180.203		2.73	−2.780	28.2 (5.43)	-	-	50.6 (5.76)	-
6230.722		2.56	−1.281	132.0 (5.21)	121.2 (4.81)	111.8 (5.03)	-	43.7 (4.75)
6252.555		2.40	−1.687	138.9 (5.49)	91.9 (4.69)	91.5 (4.92)	164.5 (5.98)	32.4 (4.77)
6318.018		2.45	−2.228	-	-	-	111.9 (5.81)	-
6335.330		2.20	−2.230	118.6 (5.42)	74.0 (4.77)	75.5 (4.96)	137.8 (5.74)	-
6421.350		2.28	−2.027	-	111.8 (5.05)	-	-	-
6593.870		2.43	−2.422	79.0 (5.37)	-	-	112.5 (5.83)	-
4233.172	Fe II	2.58	−2.000	75.3 (5.39)	-	-	-	-
4515.339		2.84	−2.480	39.2 (5.40)	-	-	-	-
4520.224		2.81	−2.600	20.4 (4.98)	-	-	-	-
4583.837		2.81	−2.020	-	54.7 (4.74)	58.4 (5.08)	-	49.6 (4.87)
4923.927		2.89	−1.320	98.1 (5.56)	96.9 (4.81)	-	-	71.7 (4.73)
5197.577		3.23	−2.100	-	-	29.5 (5.03)	62.0 (5.87)	-
5234.625		3.22	−2.050	-	-	-	65.2 (5.88)	24.4 (4.76)
5276.002		3.20	−1.940	-	40.5 (4.87)	37.6 (5.03)	-	26.4 (4.68)

TABLE 3.8: **Equivalent widths (in mÅ) of Fe lines used for the estimation of atmospheric parameters.**

Wavelength (Å)	Element	E_{low} (eV)	log gf	BD+75 348	BD+09 3019	HD 238020	HE 0319–0215	HE 0507–1653	HE 0930–0018	HE 1023–1504
4187.04	Fe I	2.45	–0.548	-	-	-	-	124.8 (6.12)	-	-
4202.03		1.48	–0.708	-	-	-	-	179.4 (6.02)	-	-
4203.57		1.01	–3.869	-	-	73.1 (6.72)	-	-	-	-
4210.343		2.48	–0.870	174.2 (7.17)	-	133.3 (6.95)	-	-	-	-
4213.65		2.85	–1.290	-	-	97.4 (6.88)	-	-	-	-
4217.55		3.43	–0.510	-	-	97.9 (6.75)	-	-	-	-
4222.21		2.45	–0.967	145.8 (6.87)	-	125.3 (6.84)	-	-	-	-
4224.17		3.37	–0.410	-	-	110.0 (6.90)	-	-	-	-
4233.60		2.48	–0.604	-	-	-	-	115.5 (5.96)	-	-
4238.81		3.37	–0.280	133.2 (6.96)	-	118.8 (6.98)	-	-	-	-
4239.36		3.64	–1.520	-	-	51.4 (6.77)	-	-	-	-
4250.12		2.47	–0.405	-	-	149.4 (6.72)	-	134.6 (6.17)	-	-
4250.79		1.56	–0.710	-	-	221.5 (6.70)	-	-	-	-
4276.68		3.88	–1.210	85.5 (7.28)	-	47.3 (6.63)	-	-	-	-
4282.40		2.18	–0.810	-	-	133.9 (6.54)	-	-	-	-
4377.79		3.27	–2.310	-	82.2 (6.85)	-	-	-	-	29.4 (6.04)
4387.89		3.07	–1.470	-	-	70.5 (6.51)	-	-	-	-
4388.41		3.60	–0.590	108.9 (6.93)	-	89.4 (6.72)	-	-	-	-
4430.61		2.22	–1.659	-	-	125.3 (7.20)	-	-	-	-

In columns 5 to 11, the numbers within bracket '()' indicate the abundances derived from the corresponding line.

TABLE 3.8: *–continued*

Wavelength (Å)	Element	E_{low} (eV)	log gf	BD+75 348	BD+09 3019	HD 238020	HE 0319–0215	HE 0507–1653	HE 0930–0018	HE 1023–1504
4432.57		3.57	–1.600	63.2 (6.74)	-	44.3 (6.61)	-	-	-	-
4433.22		3.65	–0.700	117.6 (7.29)	-	89.9 (6.89)	-	-	-	-
4436.92		3.05	–2.110	-	-	71.3 (7.13)	-	-	-	-
4446.83		3.69	–1.330	-	-	66.6 (6.94)	-	-	-	-
4466.55		2.83	–0.590	176.8 (7.23)	-	139.9 (7.06)	60.6 (5.00)	-	-	114.5 (5.64)
4476.02		2.85	–0.570	-	-	-	75.2 (4.99)	-	137.0 (5.98)	-
4482.74		3.65	–1.350	-	-	70.4 (7.01)	-	-	-	-
4490.08		3.02	–1.580	101.5 (7.00)	-	73.8 (6.62)	-	-	-	-
4517.52		3.07	–1.840	-	-	65.3 (6.73)	-	-	-	-
4547.85		3.55	–0.780	100.5 (6.78)	-	80.4 (6.57)	-	-	-	-
4587.13		3.57	–1.780	63.4 (6.89)	-	48.3 (6.85)	-	-	-	-
4596.06		3.60	–1.640	-	-	61.8 (7.02)	-	-	-	-
4602.00		1.61	–3.154	109.4 (7.04)	-	82.4 (6.79)	-	-	-	-
4602.94		1.49	–1.950	163.3 (6.84)	-	123.5 (6.53)	-	-	-	-
4637.50		3.28	–1.390	90.0 (6.78)	-	78.0 (6.81)	-	-	-	-
4647.43		2.95	–1.310	-	-	95.7 (6.81)	-	-	-	-
4704.95		3.69	–1.570	85.0 (7.29)	-	52.9 (6.85)	-	-	-	-
4735.84		4.08	–1.220	-	-	47.5 (6.80)	-	-	-	-
4736.77		3.21	–0.740	-	-	113.1 (6.96)	-	-	-	-
4741.53		2.83	–2.000	-	-	74.8 (6.81)	-	-	-	-

TABLE 3.8: *–continued*

Wavelength (Å)	Element	E_{low} (eV)	log gf	BD+75 348	BD+09 3019	HD 238020	HE 0319–0215	HE 0507–1653	HE 0930–0018	HE 1023–1504
4788.76		3.24	–1.810	104.7 (7.47)	-	66.6 (6.88)	-	-	-	-
4791.25		3.27	–2.510	71.1 (7.41)	75.5 (6.92)	33.7 (6.95)	-	-	-	-
4799.41		3.64	–2.230	-	-	31.0 (7.00)	-	-	-	-
4800.65		4.14	–1.260	79.7 (7.36)	-	51.0 (6.98)	-	-	-	-
4802.88		3.64	–1.514	-	107.0 (6.87)	-	-	-	-	-
4809.94		3.57	–2.720	-	50.3 (7.16)	-	-	-	-	-
4813.11		3.27	–2.890	-	49.4 (6.94)	-	-	-	-	-
4817.78		2.22	–3.530	-	106.9 (6.99)	-	-	-	-	-
4871.32		2.87	–0.410	-	-	-	-	126.8 (6.21)	-	-
4874.35		3.07	–3.030	-	76.2 (7.19)	-	-	-	-	-
4885.43		3.88	–1.095	-	106.7 (6.75)	-	-	-	-	-
4886.33		4.15	–0.685	81.8 (6.84)	119.6 (6.91)	63.5 (6.68)	-	-	-	-
4890.76		2.88	–0.430	-	-	151.4 (7.01)	-	-	-	-
4892.86		4.22	–1.290	66.4 (7.18)	-	36.2 (6.78)	-	-	-	-
4903.31		2.88	–1.080	155.1 (7.37)	-	125.7 (7.17)	48.4 (4.87)	96.6 (6.17)	-	107.6 (5.68)
4909.38		3.93	–1.327	81.7 (7.21)	-	52.0 (6.82)	-	-	-	-
4924.77		2.28	–2.220	122.9 (7.13)	188.4 (7.12)	96.6 (6.90)	-	68.0 (5.96)	100.6 (6.06)	108.5 (6.02)
4927.42		3.57	–1.990	70.2 (7.20)	-	39.6 (6.86)	-	-	-	-
4930.31		3.96	–1.350	81.9 (7.27)	-	56.9 (6.98)	-	-	-	-
4938.17		3.94	–1.018	-	-	72.9 (6.98)	-	-	-	-

TABLE 3.8: *–continued*

Wavelength (Å)	Element	E_{low} (eV)	log gf	BD+75 348	BD+09 3019	HD 238020	HE 0319–0215	HE 0507–1653	HE 0930–0018	HE 1023–1504
4938.81		2.88	–1.077	-	-	103.2 (6.60)	-	-	-	-
4939.69		0.86	–3.340	150.8 (7.11)	-	115.2 (6.82)	-	-	-	-
4946.39		3.37	–1.170	-	-	90.0 (6.91)	-	-	-	-
4950.11		3.42	–1.670	92.4 (7.19)	-	66.9 (6.92)	-	-	-	-
4967.90		4.19	–0.534	-	-	65.8 (6.61)	-	-	-	-
4969.92		4.22	–0.710	84.4 (6.99)	-	60.9 (6.71)	-	-	-	-
4973.10		3.96	–0.950	-	-	76.0 (7.00)	-	-	-	-
4982.50		4.10	0.164	-	-	-	-	84.2 (6.03)	-	-
4985.25		3.93	–0.560	-	135.9 (6.75)	-	-	-	-	-
4985.55		2.87	–1.331	-	189.4 (7.00)	-	-	-	-	-
4994.13		0.92	–3.080	154.5 (6.97)	-	122.6 (6.79)	74.4 (4.83)	-	-	-
5002.79		3.40	–1.580	105.2 (7.38)	-	65.4 (6.77)	-	-	-	-
5006.12		2.83	–0.615	-	-	-	84.2 (5.07)	112.5 (5.99)	-	-
5014.94		3.94	–0.250	-	-	92.1 (6.67)	-	-	-	-
5049.82		2.28	–1.420	167.1 (7.15)	-	132.4 (6.93)	-	-	-	-
5074.75		4.22	–0.200	-	-	93.8 (6.95)	-	-	-	-
5079.22		2.20	–2.067	-	-	-	39.9 (4.83)	83.7 (6.01)	111.8 (5.98)	-
5083.34		0.96	–2.958	160.5 (6.97)	-	128.8 (6.83)	-	-	-	-
5090.77		4.26	–0.400	-	-	75.0 (6.74)	-	-	-	-
5097.00		4.28	–0.196	-	-	75.5 (6.57)	-	-	-	-

TABLE 3.8: *–continued*

Wavelength (Å)	Element	E_{low} (eV)	log gf	BD+75 348	BD+09 3019	HD 238020	HE 0319–0215	HE 0507–1653	HE 0930–0018	HE 1023–1504
5110.41		0.00	–3.760	-	-	152.6 (6.99)	-	-	-	-
5123.72		1.01	–3.068	-	-	118.6 (6.74)	-	-	-	-
5126.19		4.26	–1.080	-	-	60.5 (7.09)	-	-	-	-
5141.74		2.42	–2.150	137.3 (7.48)	-	90.8 (6.79)	-	-	-	-
5150.84		0.99	–3.070	174.5 (7.32)	-	128.7 (6.95)	-	-	-	-
5159.06		4.28	–0.820	69.0 (6.80)	-	55.5 (6.76)	-	-	-	-
5162.27		4.18	0.020	-	-	106.8 (6.98)	-	-	-	-
5166.28		0.00	–4.195	170.9 (7.14)	-	131.1 (6.93)	93.0 (5.02)	-	-	-
5171.60		1.49	–1.793	188.2 (6.80)	-	151.8 (6.73)	109.7 (5.06)	-	-	-
5187.91		4.14	–1.260	60.1 (6.90)	-	38.3 (6.70)	-	-	-	-
5192.34		3.00	–0.421	-	-	-	75.3 (4.84)	112.8 (5.95)	152.5 (6.11)	139.8 (5.80)
5194.94		1.56	–2.090	-	-	132.9 (6.72)	87.4 (4.91)	-	-	156.5 (5.88)
5195.47		4.22	0.018	111.5 (6.84)	-	87.2 (6.56)	-	-	-	-
5198.71		2.22	–2.135	127.5 (6.98)	-	102.4 (6.82)	41.2 (4.93)	80.3 (6.01)	124.7 (6.30)	123.5 (6.08)
5202.34		2.18	–1.838	-	-	-	54.3 (4.82)	105.7 (6.22)	135.7 (6.16)	-
5215.18		3.27	–0.967	-	183.8 (7.01)	-	-	-	-	-
5216.27		1.61	–2.150	156.2 (6.83)	-	127.3 (6.70)	-	-	-	139.8 (5.61)
5217.39		3.21	–1.162	114.9 (6.90)	149.9 (6.59)	93.8 (6.76)	40.2 (5.16)	81.0 (6.21)	105.8 (6.30)	99.1 (5.92)
5226.86		3.04	–0.555	-	-	-	62.7 (4.76)	99.8 (5.83)	144.6 (6.17)	131.1 (5.77)
5227.19		1.56	–1.228	-	-	-	122.6 (4.88)	-	-	-

TABLE 3.8: *–continued*

Wavelength (Å)	Element	E_{low} (eV)	log gf	BD+75 348	BD+09 3019	HD 238020	HE 0319–0215	HE 0507–1653	HE 0930–0018	HE 1023–1504
5228.38		4.22	–1.290	-	-	44.7 (6.94)	-	-	-	-
5229.85		3.28	–1.136	120.7 (7.10)	-	100.2 (6.97)	-	-	-	-
5232.94		2.94	–0.190	-	-	-	89.0 (4.83)	134.3 (6.11)	-	163.9 (5.98)
5242.49		3.63	–0.840	-	153.1 (6.87)	81.4 (6.62)	-	58.8 (5.94)	72.0 (5.93)	77.6 (5.74)
5243.78		4.26	–1.150	73.1 (7.18)	-	47.7 (6.89)	-	-	-	-
5247.05		0.09	–4.946	-	-	-	35.5 (4.86)	-	-	-
5253.46		3.28	–1.670	-	130.2 (6.87)	-	-	49.3 (6.19)	-	-
5263.31		3.27	–0.970	-	-	102.9 (6.85)	-	-	-	-
5266.56		3.00	–0.490	174.8 (7.09)	-	151.8 (7.10)	77.6 (4.95)	111.0 (5.96)	-	-
5281.79		3.04	–1.020	149.6 (7.27)	196.6 (6.92)	121.2 (7.06)	47.7 (4.95)	94.2 (6.15)	116.9 (6.14)	114.5 (5.86)
5283.62		3.24	–0.630	151.7 (7.16)	-	125.2 (6.99)	58.8 (5.01)	102.5 (6.18)	-	-
5288.53		3.69	–1.670	69.2 (6.95)	105.4 (7.03)	46.4 (6.78)	-	-	-	-
5307.36		1.61	–2.987	124.6 (6.95)	183.3 (6.73)	99.4 (6.84)	43.8 (5.04)	-	-	115.8 (5.89)
5322.04		2.28	–3.030	89.7 (7.03)	-	65.4 (6.92)	-	-	-	-
5324.18		3.21	–0.240	-	-	145.5 (6.96)	76.8 (4.93)	108.8 (5.90)	-	-
5328.53		1.56	–1.850	-	-	-	94.7 (4.79)	-	-	-
5339.93		3.27	–0.680	135.3 (6.91)	-	113.7 (6.80)	-	89.8 (5.97)	-	112.0 (5.75)
5341.02		1.61	–2.060	-	-	-	84.3 (4.85)	-	-	-
5364.87		4.45	0.220	116.2 (6.96)	-	93.8 (6.73)	-	-	-	-
5365.40		3.57	–1.020	-	-	73.6 (6.54)	-	-	-	-

TABLE 3.8: *–continued*

Wavelength (Å)	Element	E_{low} (eV)	log gf	BD+75 348	BD+09 3019	HD 238020	HE 0319–0215	HE 0507–1653	HE 0930–0018	HE 1023–1504
5367.47		4.42	0.350	115.2 (6.77)	-	99.1 (6.69)	-	78.2 (6.02)	-	-
5369.96		4.37	0.350	-	-	-	-	81.9 (6.04)	-	-
5373.71		4.47	–0.860	59.0 (6.85)	-	45.7 (6.80)	-	-	-	-
5379.57		3.69	–1.480	84.8 (7.08)	-	52.4 (6.70)	-	-	-	-
5389.48		4.42	–0.410	94.7 (7.08)	-	68.2 (6.74)	-	-	-	-
5397.13		0.92	–1.993	-	-	184.0 (6.68)	-	-	-	-
5400.50		4.37	–0.160	-	-	96.3 (7.08)	-	-	-	-
5415.20		4.39	0.500	130.4 (6.90)	-	107.3 (6.69)	-	88.9 (6.06)	-	-
5424.07		4.32	0.520	152.7 (7.19)	-	119.3 (6.86)	-	-	-	-
5445.04		4.39	–0.020	104.3 (6.85)	156.5 (7.07)	88.6 (6.77)	-	-	-	-
5462.96		4.47	–0.234	-	131.2 (7.00)	-	-	-	-	-
5463.28		4.43	0.110	-	140.8 (6.75)	-	-	-	-	-
5466.40		4.37	–0.630	101.2 (7.38)	-	61.9 (6.78)	-	-	-	-
5473.90		4.15	–0.760	84.2 (6.88)	-	63.2 (6.69)	-	-	-	-
5476.29		4.14	–0.935	-	85.0 (6.58)	-	-	-	-	-
5487.74		4.32	–0.352	-	-	70.7 (6.62)	-	-	-	-
5501.47		0.96	–2.950	173.9 (7.02)	-	131.1 (6.71)	-	-	-	-
5506.78		0.99	–2.797	-	-	136.1 (6.70)	-	-	-	-
5543.94		4.22	–1.140	-	-	47.0 (6.82)	-	-	-	-
5546.51		4.37	–1.310	70.6 (7.40)	-	36.6 (6.95)	-	-	-	-

TABLE 3.8: *–continued*

Wavelength (Å)	Element	E_{low} (eV)	log gf	BD+75 348	BD+09 3019	HD 238020	HE 0319–0215	HE 0507–1653	HE 0930–0018	HE 1023–1504
5554.89		4.55	–0.440	-	-	67.3 (6.89)	-	-	-	-
5557.98		4.47	–1.280	-	-	38.8 (7.07)	-	-	-	-
5560.21		4.43	–1.190	60.9 (7.15)	-	35.4 (6.87)	-	-	-	-
5562.71		4.43	–0.580	77.1 (6.86)	-	-	-	-	-	-
5567.39		2.61	–2.800	-	-	62.0 (6.97)	-	-	-	-
5576.09		3.43	–1.000	-	-	97.8 (6.88)	-	-	-	-
5586.76		3.37	–0.210	-	-	-	63.6 (4.80)	106.8 (5.95)	-	132.9 (5.79)
5624.02		4.39	–1.480	60.8 (7.38)	-	35.2 (7.10)	-	-	-	-
5624.54		3.42	–0.900	148.2 (7.48)	-	108.8 (7.01)	-	-	-	-
5633.95		4.99	–0.270	68.8 (7.03)	-	43.5 (6.70)	-	-	-	-
5653.86		4.39	–1.640	-	58.5 (7.22)	-	-	-	-	-
5662.52		4.18	–0.573	98.3 (7.00)	148.1 (7.19)	74.5 (6.76)	-	-	-	-
5679.02		4.65	–0.920	71.8 (7.34)	-	39.2 (6.90)	-	-	-	-
5731.76		4.26	–1.300	-	-	43.2 (6.93)	-	-	-	-
5752.03		4.55	–0.864	59.2 (6.92)	-	37.1 (6.69)	-	-	-	-
5753.12		4.26	–0.760	85.6 (7.00)	129.6 (7.20)	62.2 (6.76)	-	-	35.0 (6.01)	-
5762.99		4.21	–0.450	-	143.0 (7.02)	-	-	-	-	61.8 (5.77)
5775.08		4.22	–1.298	71.8 (7.20)	-	45.6 (6.94)	-	-	-	-
5806.73		4.61	–1.050	-	74.7 (7.15)	-	-	-	-	-
5848.13		4.61	–1.010	-	47.2 (6.71)	-	-	-	-	-

TABLE 3.8: *–continued*

Wavelength (Å)	Element	E_{low} (eV)	log gf	BD+75 348	BD+09 3019	HD 238020	HE 0319–0215	HE 0507–1653	HE 0930–0018	HE 1023–1504
5859.59		4.55	–0.386	91.9 (7.09)	-	55.6 (6.57)	-	-	-	-
5862.36		4.55	–0.051	-	-	-	-	-	-	57.0 (5.72)
5930.18		4.65	–0.230	102.9 (7.28)	-	67.9 (6.78)	-	-	-	-
5934.65		3.93	–1.170	-	-	60.6 (6.77)	-	-	-	-
5976.78		3.94	–1.503	83.5 (7.30)	-	56.9 (7.04)	-	-	-	-
5984.81		4.73	–0.443	-	-	56.8 (6.85)	-	-	-	-
6003.01		3.88	–1.120	91.1 (6.99)	-	67.4 (6.79)	-	-	-	-
6008.56		3.88	–1.291	94.0 (7.23)	-	69.5 (7.01)	-	-	-	-
6027.05		4.08	–1.210	-	-	-	-	-	36.5 (6.27)	-
6056.01		4.73	–0.460	-	90.2 (6.94)	-	-	-	-	-
6082.71		2.22	–3.573	-	132.6 (7.23)	-	-	-	-	-
6136.61		2.45	–1.400	-	-	-	76.8 (4.99)	109.8 (5.98)	145.9 (6.09)	-
6137.69		2.59	–1.403	158.8 (7.03)	-	126.6 (6.83)	71.8 (5.08)	97.1 (5.92)	135.6 (6.11)	-
6151.62		2.18	–3.299	-	128.4 (6.83)	-	-	29.3 (6.12)	49.0 (6.06)	-
6180.20		2.73	–2.780	-	-	-	-	-	43.8 (6.19)	37.7 (5.78)
6226.73		3.88	–2.220	-	35.6 (6.80)	-	-	-	-	-
6230.72		2.56	–1.281	-	-	134.7 (6.82)	71.1 (4.90)	110.4 (6.00)	-	-
6246.32		3.60	–0.960	118.1 (7.02)	-	95.3 (6.87)	-	-	-	-
6252.56		2.40	–1.687	157.0 (7.02)	-	122.3 (6.77)	58.9 (4.89)	103.6 (6.07)	137.1 (6.14)	-
6254.26		2.28	–2.480	139.3 (7.31)	-	109.3 (7.14)	-	-	-	-

TABLE 3.8: *–continued*

Wavelength (Å)	Element	E_{low} (eV)	log gf	BD+75 348	BD+09 3019	HD 238020	HE 0319–0215	HE 0507–1653	HE 0930–0018	HE 1023–1504
6256.36		2.45	–2.620	123.1 (7.34)	-	-	-	-	-	-
6265.13		2.18	–2.550	147.9 (7.41)	-	95.4 (6.81)	-	-	-	-
6318.02		2.45	–2.228	-	-	-	-	74.6 (6.13)	100.9 (6.14)	-
6335.33		2.20	–2.230	-	-	-	42.1 (4.90)	77.1 (5.87)	-	136.0 (6.03)
6411.65		3.65	–0.820	-	173.6 (7.01)	-	-	-	-	-
6421.35		2.28	–2.027	154.8 (7.11)	-	119.0 (6.86)	-	88.2 (5.96)	-	-
6518.37		2.83	–2.750	-	127.3 (7.14)	-	-	-	-	-
6593.87		2.43	–2.422	-	-	-	-	64.1 (6.10)	84.1 (6.03)	-
6739.52		1.56	–4.950	-	72.8 (6.90)	-	-	-	-	-
4233.17	Fe II	2.58	–2.000	-	-	125.2 (6.91)	-	-	-	-
4491.40		2.86	–2.700	95.9 (7.14)	-	81.3 (6.69)	-	-	-	-
4515.34		2.84	–2.480	92.5 (6.80)	-	87.7 (6.63)	36.5 (4.87)	60.8 (6.00)	29.3 (6.15)	-
4541.52		2.86	–3.050	74.5 (6.90)	-	78.1 (6.94)	-	-	-	-
4520.22		2.81	–2.600	100.5 (7.09)	-	87.5 (6.70)	-	-	-	-
4576.34		2.84	–3.040	-	-	75.0 (6.84)	-	-	-	-
4620.52		2.83	–3.280	71.0 (7.02)	-	64.0 (6.78)	-	-	-	-
4923.93		2.89	–1.320	159.1 (6.99)	152.6 (6.96)	148.4 (6.81)	86.4 (4.99)	115.6 (6.19)	71.6 (6.17)	-
5120.35		2.83	–4.214	-	-	40.4 (7.15)	-	-	-	-
5197.58		3.23	–2.100	109.2 (7.18)	-	90.0 (6.64)	39.2 (4.98)	61.4 (6.04)	-	77.3 (5.89)
5234.62		3.22	–2.050	-	78.1 (6.85)	-	40.5 (4.94)	66.9 (6.10)	20.2 (6.00)	75.7 (5.79)
5256.94		2.89	–4.250	44.0 (7.42)	-	20.7 (6.77)	-	-	-	-

TABLE 3.8: *–continued*

Wavelength (Å)	Element	E_{low} (eV)	log gf	BD+75 348	BD+09 3019	HD 238020	HE 0319–0215	HE 0507–1653	HE 0930–0018	HE 1023–1504
5264.81		3.23	–3.190	49.7 (6.86)	32.7 (7.06)	49.4 (6.75)	-	-	-	-
5276.00		3.20	–1.940	-	-	-	44.4 (4.90)	-	-	-
5414.07		3.22	–3.790	42.2 (7.28)	-	27.3 (6.82)	-	-	-	-
5425.26		3.20	–3.360	60.0 (7.23)	-	44.1 (6.77)	-	-	-	-
5534.85		3.25	–2.930	69.3 (7.06)	-	63.9 (6.83)	-	-	-	-
6147.74		3.89	–2.721	-	-	60.3 (7.22)	-	-	-	-
6238.39		3.89	–2.630	-	-	42.8 (6.73)	-	-	-	-

TABLE 3.9: **Equivalent widths (in mÅ) of Fe lines used for the estimation of atmospheric parameters.**

Wavelength (Å)	Element	E_{low} (eV)	log gf	HE 1005–1439	HE 0401–0138	HE 1246–1344	HE 1153–0518
4045.81	Fe I	1.48	0.280	-	101.3 (4.10)	-	-
4132.06		1.61	−0.650	77.1 (4.40)	-	-	-
4143.87		1.56	−0.450	77.7 (4.16)	-	-	-
4147.67		1.48	−2.104	28.5 (4.56)	-	-	-
4187.04		2.45	−0.548	49.0 (4.51)	-	-	-
4198.30		2.40	−0.719	-	-	46.2 (4.16)	-
4202.03		1.48	−0.708	91.1 (4.71)	-	78.6 (3.85)	-
4216.18		0.00	−3.356	35.9 (4.28)	-	-	-
4227.43		3.33	0.230	33.5 (4.34)	-	-	-
4233.60		2.48	−0.604	38.1 (4.35)	-	33.6 (3.87)	-
4250.12		2.47	−0.405	62.0 (4.67)	-	-	-
4250.79		1.56	−0.710	81.9 (4.49)	64.9 (3.82)	-	-
4260.47		2.40	−0.020	64.2 (4.26)	-	-	-
4271.76		1.48	−0.164	-	-	102.1 (4.01)	-
4375.93		0.00	−3.031	70.7 (4.66)	59.9 (3.98)	-	-
4383.55		1.48	0.200	127.1 (4.70)	96.9 (3.86)	114.5 (3.94)	-
4404.75		1.56	−0.142	-	88.9 (4.02)	97.8 (3.86)	-
4415.12		1.61	−0.615	-	73.7 (4.03)	87.8 (4.10)	-
4427.31		0.05	−3.044	-	68.8 (4.31)	62.2 (3.84)	-
4442.34		2.20	−1.255	-	21.5 (3.93)	35.2 (4.18)	-
4447.72		2.22	−1.342	-	24.8 (4.13)	-	-
4466.57		0.11	−4.464	-	-	-	37.2 (4.63)
4476.02		2.85	−0.570	30.1 (4.52)	-	-	-
4528.61		2.18	−0.822	62.0 (4.71)	-	41.0 (3.83)	-
4602.94		1.48	−1.950	37.3 (4.53)	-	-	46.2 (4.04)
4871.32		2.87	−0.410	-	-	31.1 (4.00)	-
4872.14		2.88	−0.600	25.7 (4.45)	-	22.3 (3.99)	-
4890.76		2.88	−0.430	39.2 (4.56)	-	31.4 (4.03)	72.9 (4.72)
4891.49		2.85	−0.140	51.8 (4.49)	42.5 (4.05)	48.5 (4.05)	79.6 (4.52)
4918.99		2.87	−0.370	35.6 (4.42)	34.0 (4.09)	28.5 (3.90)	-
4920.50		2.83	0.060	55.7 (4.36)	46.7 (3.92)	49.7 (3.85)	66.9 (4.03)
4982.50		4.10	0.164	-	-	-	13.9 (4.33)
4994.13		0.92	−3.080	19.7 (4.58)	-	-	50.2 (4.44)
5006.12		2.83	−0.615	23.4 (4.34)	-	22.6 (3.94)	-
5041.76		1.48	−2.203	-	-	32.2 (4.11)	72.9 (4.67)
5049.82		2.28	−1.420	-	-	19.9 (4.02)	-
5051.64		0.91	−2.795	30.3 (4.05)	30.3 (4.05)	31.6 (3.98)	-
5083.34		0.96	−2.958	-	21.4 (4.05)	20.9 (3.96)	-
5166.28		0.00	−4.195	-	16.6 (3.93)	-	-
5171.60		1.49	−1.793	46.9 (4.50)	44.2 (4.06)	44.6 (3.94)	-

In columns 5 to 8, the numbers within bracket '()' indicate the abundances derived from the corresponding line.

TABLE 3.9: *–continued*

Wavelength (Å)	Element	E_{low} (eV)	log gf	HE 1005–1439	HE 0401–0138	HE 1246–1344	HE 1153–0518
5192.34		3.00	−0.421	27.1 (4.41)	-	21.8 (3.91)	50.5 (4.39)
5194.94		1.56	−2.090	29.4 (4.53)	-	37.7 (4.19)	54.9 (4.33)
5202.34		2.18	−1.838	-	11.6 (4.07)	-	35.0 (4.52)
5216.27		1.61	−2.150	25.6 (4.56)	-	28.0 (4.11)	36.7 (4.14)
5217.39		3.21	−1.162	-	-	-	14.3 (4.59)
5226.86		3.04	−0.555	19.7 (4.39)	17.5 (4.02)	-	33.9 (4.27)
5227.19		1.56	−1.228	59.1 (4.24)	72.8 (4.25)	72.3 (3.98)	94.7 (4.18)
5232.94		2.94	−0.190	34.4 (4.27)	35.5 (4.00)	33.6 (3.88)	64.6 (4.33)
5242.49		3.63	−0.840	-	-	-	5.6 (4.32)
5266.56		3.00	−0.490	29.8 (4.54)	21.4 (4.03)	21.2 (3.96)	43.7 (4.33)
5269.54		0.86	−1.321	89.4 (4.16)	85.7 (3.81)	105.8 (3.95)	127.7 (4.03)
5270.36		1.61	−1.510	65.8 (4.71)	62.1 (4.32)	64.1 (4.15)	95.7 (4.52)
5281.79		3.04	−1.020	-	14.1 (4.37)	-	26.4 (4.57)
5324.18		3.21	−0.240	31.0 (4.54)	20.2 (3.98)	20.9 (3.95)	38.8 (4.24)
5328.04		0.91	−1.466	81.8 (4.18)	83.2 (3.93)	103.3 (4.06)	-
5328.53		1.56	−1.850	35.7 (4.41)	36.6 (4.02)	44.0 (4.05)	61.2 (4.17)
5341.02		1.61	−2.060	-	-	28.5 (4.02)	-
5446.92		0.99	−1.930	63.2 (4.34)	-	77.6 (4.01)	114.6 (4.44)
5455.61		1.01	−2.091	60.1 (4.46)	64.8 (4.17)	67.4 (4.00)	116.2 (4.66)
5497.52		1.01	−2.849	26.7 (4.58)	24.5 (4.04)	27.9 (4.03)	-
5506.78		0.99	−2.797	25.0 (4.46)	32.8 (4.16)	29.8 (3.99)	44.7 (4.09)
5572.84		3.40	−0.310	-	15.5 (4.11)	13.8 (4.00)	-
5586.76		3.37	−0.210	25.5 (4.54)	-	18.3 (4.01)	35.5 (4.32)
5615.64		3.33	−0.140	29.0 (4.50)	-	24.6 (4.06)	-
6136.61		2.45	−1.400	15.6 (4.41)	9.7 (3.80)	-	-
6230.72		2.56	−1.281	16.7 (4.44)	-	-	26.6 (4.17)
6335.33		2.20	−2.230	-	-	-	19.1 (4.48)
6494.98		2.40	−1.273	26.0 (4.48)	21.0 (3.99)	21.6 (3.94)	-
4233.17	Fe II	2.58	−2.000	-	21.0 (4.01)	-	-
4491.40		2.86	−2.700	7.6 (4.53)	-	-	-
4555.89		2.83	−2.290	-	-	10.5 (4.01)	-
4583.84		2.81	−2.020	-	-	-	50.0 (4.53)
4923.93		2.89	−1.320	51.3 (4.46)	37.3 (4.14)	-	-
5018.44		2.89	−1.220	56.5 (4.48)	36.9 (4.04)	-	-
5197.58		3.23	−2.100	-	6.1 (4.10)	-	-
5234.62		3.22	−2.050	-	-	7.7 (4.02)	-
5276.00		3.20	−1.940	16.2 (4.50)	-	-	23.1 (4.21)
5316.61		3.15	−1.850	20.9 (4.51)	-	-	-

TABLE 3.10: **Equivalent widths (in mÅ) of Fe lines used for the estimation of atmospheric parameters.**

Wavelength (Å)	Element	E_{low} (eV)	log gf	HD 147609	HD 154276	HD 87853	HE 0308–1612
4147.67	Fe I	1.49	-2.104	-	-	83.6 (6.82)	-
4184.89		2.83	-0.860	-	-	83.8 (6.79)	-
4187.04		2.45	-0.548	-	-	108.4 (6.78)	-
4202.03		1.49	-0.708	-	-	134.9 (6.72)	-
4203.57		1.01	-3.869	34.6 (7.23)	-	-	-
4210.34		2.48	-0.870	120.4 (7.48)	-	-	-
4213.65		2.85	-1.290	68.5 (6.96)	-	-	-
4217.55		3.43	-0.510	99.6 (7.43)	-	-	-
4222.21		2.45	-0.967	104.9 (7.19)	-	-	-
4224.17		3.37	-0.410	101.2 (7.31)	-	-	-
4238.81		3.37	-0.280	105.7 (7.29)	-	-	-
4239.36		3.64	-1.520	34.7 (7.19)	-	-	-
4240.37		3.55	-1.340	51.4 (7.26)	-	-	-
4250.12		2.47	-0.405	134.5 (7.25)	-	-	-
4250.79		1.56	-0.710	175.9 (7.34)	-	-	-
4276.68		3.88	-1.210	27.5 (6.93)	-	-	-
4282.40		2.18	-0.810	115.4 (7.03)	-	-	-
4327.10		3.55	-0.960	-	88.6 (7.61)	-	-
4343.70		3.05	-1.880	-	62.4 (7.53)	-	-
4347.23		0.00	-5.503	-	26.7 (7.22)	-	-
4348.94		2.99	-2.130	-	39.8 (7.11)	-	-
4352.73		2.22	-1.260	114.2 (7.47)	-	-	-
4360.80		3.64	-1.870	-	39.5 (7.46)	-	-
4365.90		2.99	-2.210	-	42.5 (7.26)	-	-
4369.77		3.05	-0.730	93.0 (7.14)	-	-	-
4373.56		3.02	-1.826	40.2 (7.05)	53.9 (7.21)	-	-
4376.77		3.02	-2.336	-	42.8 (7.42)	-	-
4377.79		3.27	-2.310	-	32.5 (7.37)	-	-
4387.89		3.07	-1.470	67.1 (7.28)	67.0 (7.25)	-	-
4388.41		3.60	-0.590	71.3 (6.96)	80.6 (7.12)	-	-
4389.24		0.05	-4.583	-	65.8 (7.46)	-	-
4392.58		3.88	-2.000	-	31.0 (7.59)	-	-
4423.84		3.65	-1.610	-	42.9 (7.29)	-	-
4430.61		2.22	-1.659	97.0 (7.44)	-	-	-
4432.57		3.57	-1.600	30.6 (7.11)	44.0 (7.23)	-	-
4433.22		3.65	-0.700	60.0 (6.87)	-	-	-
4436.92		3.05	-2.110	36.5 (7.28)	-	-	-

In columns 5 to 8, the numbers within bracket '()' indicate the abundances derived from the corresponding line.

TABLE 3.10: *–continued*

Wavelength (Å)	Element	E_{low} (eV)	log gf	HD 147609	HD 154276	HD 87853	HE 0308–1612
4442.83		2.18	-2.792	-	55.7 (7.43)	-	-
4445.47		0.09	-5.441	-	31.4 (7.35)	-	-
4446.83		3.69	-1.330	35.5 (7.04)	63.9 (7.56)	-	-
4447.13		2.20	-2.590	-	53.1 (7.17)	-	-
4447.72		2.22	-1.342	107.7 (7.37)	-	-	-
4454.38		2.83	-1.250	-	84.0 (7.22)	64.6 (6.71)	123.6 (6.84)
4456.33		3.05	-2.170	-	45.1 (7.34)	-	-
4461.65		0.07	-3.210	-	-	97.2 (6.85)	-
4466.55		2.83	-0.590	123.0 (7.47)	-	102.6 (6.92)	-
4481.61		3.69	-1.420	-	47.4 (7.23)	-	-
4482.74		3.65	-1.350	52.0 (7.35)	-	-	-
4484.22		3.60	-0.720	-	83.8 (7.31)	62.0 (6.80)	-
4485.68		3.69	-1.020	-	69.5 (7.38)	-	-
4489.74		0.12	-3.966	-	86.3 (7.49)	53.2 (6.73)	-
4490.08		3.02	-1.580	48.5 (6.95)	-	-	-
4502.59		3.57	-2.350	-	22.1 (7.40)	-	-
4517.52		3.07	-1.840	40.2 (7.10)	66.2 (7.59)	-	-
4531.63		3.21	-2.511	24.1 (7.55)	-	-	-
4547.85		3.55	-0.780	69.4 (7.05)	78.9 (7.23)	-	107.7 (6.80)
4587.13		3.57	-1.780	26.4 (7.19)	46.5 (7.46)	-	-
4595.36		3.30	-1.720	-	60.1 (7.51)	-	-
4596.06		3.60	-1.640	48.9 (7.53)	-	-	-
4596.41		3.65	-2.320	-	24.3 (7.50)	-	-
4602.00		1.61	-3.154	45.3 (7.21)	65.0 (7.49)	-	-
4602.94		1.49	-1.950	93.1 (6.92)	-	-	-
4619.29		3.60	-1.120	-	71.2 (7.44)	50.8 (6.99)	-
4630.12		2.28	-2.600	-	-	32.9 (6.95)	-
4632.91		1.61	-2.913	71.6 (7.49)	-	-	-
4635.85		2.85	-2.420	-	45.5 (7.39)	-	-
4637.50		3.28	-1.390	47.3 (6.96)	75.2 (7.52)	-	-
4741.53		2.83	-2.000	-	-	34.1 (6.86)	-
4647.43		2.95	-1.310	88.4 (7.47)	79.8 (7.25)	-	-
4657.59		2.85	-2.900	-	25.1 (7.34)	-	-
4661.97		2.99	-2.460	-	37.4 (7.36)	-	-
4678.85		3.60	-0.660	-	86.8 (7.29)	-	-
4679.22		4.56	-1.115	-	37.8 (7.45)	-	-
4683.56		2.83	-2.530	-	43.4 (7.42)	-	-
4690.14		3.69	-1.680	-	45.3 (7.43)	-	-
4704.95		3.69	-1.570	35.1 (7.25)	57.5 (7.62)	-	-
4705.46		3.55	-2.310	-	25.1 (7.41)	-	-
4707.49		2.85	-2.340	-	56.6 (7.60)	-	-

TABLE 3.10: *–continued*

Wavelength (Å)	Element	E_{low} (eV)	log gf	HD 147609	HD 154276	HD 87853	HE 0308–1612
4721.00		2.99	-2.801	-	39.9 (7.76)	-	-
4728.55		3.65	-1.280	-	68.0 (7.56)	-	-
4733.59		1.49	-2.710	-	65.9 (6.92)	-	-
4735.84		4.08	-1.220	35.5 (7.25)	48.3 (7.39)	-	-
4736.77		3.21	-0.740	99.5 (7.38)	-	-	-
4741.53		2.83	-2.000	52.1 (7.26)	61.9 (7.38)	-	-
4745.80		3.65	-1.270	-	64.6 (7.46)	-	-
4749.95		4.56	-1.340	-	24.0 (7.34)	-	-
4768.32		3.69	-1.115	52.8 (7.14)	-	-	-
4772.80		1.56	-2.897	-	81.2 (7.59)	-	-
4786.81		3.02	-1.590	-	72.7 (7.42)	-	-
4787.83		3.00	-2.770	-	-	-	59.7 (6.89)
4788.76		3.24	-1.810	40.2 (7.20)	55.7 (7.40)	-	-
4789.65		3.55	-0.840	-	72.3 (7.12)	-	-
4791.25		3.27	-2.510	22.0 (7.54)	-	-	-
4798.27		4.19	-1.550	-	26.3 (7.27)	-	-
4798.73		1.61	-4.250	-	27.3 (7.53)	-	-
4799.41		3.64	-2.230	20.0 (7.49)	25.7 (7.43)	-	-
4800.65		4.14	-1.260	27.8 (7.18)	54.3 (7.62)	-	-
4802.88		3.64	-1.514	-	50.8 (7.35)	-	-
4842.79		4.10	-1.560	-	33.3 (7.39)	-	-
4843.14		3.40	-1.840	-	56.0 (7.59)	-	-
4844.01		3.55	-2.030	-	38.2 (7.46)	-	-
4845.65		3.27	-2.687	-	34.4 (7.76)	-	-
4871.32		2.87	-0.410	-	-	100.6 (6.64)	162.8 (6.61)
4875.88		3.33	-2.020	-	47.7 (7.49)	-	-
4882.14		3.42	-1.640	-	61.1 (7.53)	-	-
4885.43		3.88	-1.095	-	61.1 (7.40)	-	-
4886.33		4.15	-0.685	51.6 (7.09)	63.7 (7.27)	-	-
4890.76		2.88	-0.430	120.2 (7.21)	-	-	-
4892.86		4.22	-1.290	28.9 (7.29)	40.7 (7.39)	-	-
4896.44		3.88	-2.050	-	27.5 (7.52)	-	-
4903.31		2.88	-1.080	96.3 (7.33)	-	-	137.9 (6.86)
4907.73		3.43	-1.840	-	-	-	77.4 (6.86)
4909.38		3.93	-1.327	34.5 (7.20)	-	-	-
4924.77		2.28	-2.220	67.3 (7.27)	-	-	113.8 (6.66)
4927.42		3.57	-1.990	26.1 (7.37)	-	-	-
4930.31		3.96	-1.350	42.1 (7.40)	-	-	73.8 (6.93)
4938.17		3.94	-1.018	51.6 (7.23)	-	-	-
4938.81		2.88	-1.077	78.2 (6.90)	-	-	-
4939.69		0.86	-3.340	65.2 (7.06)	-	52.1 (6.72)	148.4 (6.74)

TABLE 3.10: *–continued*

Wavelength (Å)	Element	E_{low} (eV)	log gf	HD 147609	HD 154276	HD 87853	HE 0308–1612
4946.39		3.37	-1.170	77.2 (7.41)	-	-	-
4950.11		3.42	-1.670	43.2 (7.26)	-	-	-
4967.90		4.19	-0.534	59.8 (7.13)	-	-	-
4969.92		4.22	-0.710	47.4 (7.08)	-	-	-
4973.10		3.96	-0.950	60.1 (7.35)	-	-	-
4985.25		3.93	-0.560	-	-	-	89.0 (6.46)
4994.13		0.92	-3.080	75.0 (7.04)	-	-	-
5001.86		3.88	0.010	-	-	83.8 (6.74)	112.1 (6.38)
5002.79		3.40	-1.580	44.8 (7.19)	-	-	-
5005.71		3.88	-0.142	-	-	73.3 (6.67)	-
5014.94		3.94	-0.250	79.8 (7.04)	-	-	-
5022.24		3.98	-0.530	-	-	54.2 (6.77)	-
5049.82		2.28	-1.420	100.9 (7.22)	-	85.8 (6.75)	-
5051.64		0.92	-2.795	100.7 (7.34)	-	81.1 (6.74)	-
5074.75		4.22	-0.200	87.9 (7.39)	-	-	-
5083.34		0.96	-2.958	81.8 (7.10)	-	69.6 (6.72)	-
5090.77		4.26	-0.400	68.0 (7.21)	-	-	-
5097.00		4.28	-0.196	71.1 (7.09)	-	-	-
5110.41		0.00	-3.760	94.8 (7.29)	-	-	-
5123.72		1.01	-3.068	84.5 (7.31)	-	-	-
5126.19		4.26	-1.080	42.6 (7.39)	-	-	-
5127.36		0.92	-3.307	-	-	52.0 (6.72)	-
5141.74		2.42	-2.150	56.9 (7.11)	-	44.1 (6.80)	-
5150.84		0.99	-3.070	83.9 (7.27)	-	-	-
5159.06		4.28	-0.820	42.6 (7.15)	-	-	-
5162.27		4.18	0.020	95.3 (7.30)	-	-	-
5166.28		0.00	-4.195	74.1 (7.27)	-	62.8 (6.93)	176.4 (6.84)
5171.60		1.49	-1.793	117.9 (7.23)	-	106.7 (6.81)	-
5187.91		4.14	-1.260	22.5 (7.03)	-	-	-
5194.94		1.56	-2.090	92.3 (7.00)	-	-	-
5195.47		4.22	0.018	80.6 (7.02)	-	-	-
5198.71		2.22	-2.135	66.2 (7.09)	-	-	134.2 (6.89)
5215.18		3.27	-0.967	-	-	63.1 (6.72)	111.6 (6.52)
5216.27		1.61	-2.150	93.0 (7.12)	-	-	-
5217.39		3.21	-1.162	78.7 (7.27)	-	-	-
5228.38		4.22	-1.290	37.2 (7.46)	44.1 (7.47)	-	-
5229.85		3.28	-1.136	81.6 (7.37)	-	-	-
5232.94		2.94	-0.190	-	-	120.1 (6.87)	-
5242.49		3.63	-0.840	67.3 (7.08)	75.9 (7.23)	47.1 (6.63)	-
5243.78		4.26	-1.150	33.3 (7.27)	-	-	-
5247.05		0.09	-4.946	-	58.5 (7.46)	-	118.6 (6.44)

TABLE 3.10: *–continued*

Wavelength (Å)	Element	E_{low} (eV)	log gf	HD 147609	HD 154276	HD 87853	HE 0308–1612
5250.65		2.20	-2.050	-	-	55.9 (6.70)	-
5253.46		3.28	-1.670	-	-	-	99.0 (6.94)
5263.31		3.27	-0.970	-	-	66.2 (6.77)	-
5266.56		3.00	-0.490	126.1 (7.42)	-	100.8 (6.77)	-
5269.54		0.86	-1.321	168.6 (7.06)	-	-	-
5281.79		3.04	-1.020	94.1 (7.31)	-	77.4 (6.84)	145.1 (7.01)
5283.62		3.24	-0.630	104.7 (7.33)	-	90.9 (6.93)	-
5288.53		3.69	-1.670	28.0 (7.18)	47.2 (7.44)	-	-
5307.36		1.61	-2.987	66.9 (7.39)	76.3 (7.50)	-	123.6 (6.64)
5322.04		2.28	-3.030	23.2 (7.18)	49.7 (7.50)	-	95.4 (6.90)
5324.18		3.21	-0.240	127.6 (7.37)	-	105.1 (6.82)	-
5329.99		4.08	-1.300	-	45.3 (7.37)	-	-
5332.90		1.56	-2.940	-	75.1 (7.37)	-	-
5339.93		3.27	-0.680	85.6 (6.98)	-	75.7 (6.67)	-
5341.02		1.61	-2.060	118.6 (7.59)	-	-	-
5349.74		4.39	-1.300	-	36.0 (7.43)	-	-
5364.87		4.45	0.220	80.6 (6.99)	-	70.5 (6.74)	-
5365.40		3.57	-1.020	52.1 (6.90)	-	-	-
5367.47		4.42	0.350	96.9 (7.17)	-	74.5 (6.66)	116.2 (6.70)
5369.96		4.37	0.350	-	-	75.0 (6.63)	120.1 (6.73)
5373.71		4.47	-0.860	36.1 (7.22)	49.6 (7.39)	-	76.8 (7.09)
5379.57		3.69	-1.480	33.3 (7.10)	50.3 (7.32)	-	-
5383.37		4.31	0.500	-	-	95.8 (6.86)	138.3 (6.87)
5389.48		4.42	-0.410	59.3 (7.17)	-	-	-
5391.46		4.15	-0.812	-	68.0 (7.47)	-	-
5397.13		0.92	-1.993	129.6 (7.10)	-	-	-
5398.28		4.45	-0.670	-	61.6 (7.43)	-	-
5400.50		4.37	-0.160	84.1 (7.38)	-	-	-
5415.20		4.39	0.500	105.5 (7.17)	-	-	-
5424.07		4.32	0.520	116.2 (7.29)	-	-	-
5436.59		2.28	-3.390	-	28.7 (7.32)	-	-
5441.34		4.31	-1.730	-	21.8 (7.42)	-	-
5445.04		4.39	-0.020	84.2 (7.25)	-	-	-
5466.40		4.37	-0.630	55.5 (7.28)	-	-	-
5472.71		4.21	-1.720	-	31.5 (7.57)	-	-
5473.90		4.15	-0.760	48.8 (7.09)	-	-	-
5487.74		4.32	-0.352	54.3 (6.92)	-	-	-
5501.47		0.96	-2.950	83.1 (7.07)	-	-	-
5506.78		0.99	-2.797	88.2 (7.05)	-	-	-
5522.45		4.21	-1.550	-	32.8 (7.44)	-	-
5525.54		4.23	-1.330	-	43.2 (7.49)	-	-

TABLE 3.10: *–continued*

Wavelength (Å)	Element	E_{low} (eV)	log gf	HD 147609	HD 154276	HD 87853	HE 0308–1612
5543.94		4.22	-1.140	34.0 (7.23)	48.1 (7.40)	-	-
5546.51		4.37	-1.310	21.9 (7.26)	-	-	-
5554.89		4.55	-0.440	59.3 (7.31)	76.8 (7.59)	42.3 (6.94)	-
5557.98		4.47	-1.280	27.5 (7.45)	-	-	-
5560.21		4.43	-1.190	28.1 (7.34)	40.4 (7.46)	-	-
5562.71		4.43	-0.580	32.9 (6.83)	-	-	-
5563.60		4.19	-0.990	50.3 (7.37)	-	-	-
5567.39		2.61	-2.800	25.8 (7.30)	52.8 (7.65)	-	-
5569.62		3.42	-0.540	-	-	82.5 (6.79)	-
5576.09		3.43	-1.000	72.6 (7.15)	-	63.4 (6.88)	-
5586.76		3.37	-0.210	-	-	100.0 (6.78)	-
5615.64		3.33	-0.140	-	-	111.3 (6.92)	-
5618.63		4.21	-1.380	-	37.9 (7.39)	-	42.6 (6.59)
5624.02		4.39	-1.480	20.1 (7.39)	-	-	-
5624.54		3.42	-0.900	79.0 (7.17)	-	-	-
5633.95		4.99	-0.270	46.5 (7.27)	50.6 (7.24)	-	-
5638.26		4.22	-0.870	-	65.1 (7.51)	-	-
5653.86		4.39	-1.640	-	25.8 (7.51)	-	-
5662.52		4.18	-0.573	48.5 (6.91)	-	-	-
5679.02		4.65	-0.920	31.9 (7.34)	45.1 (7.49)	-	-
5717.83		4.28	-1.130	-	48.9 (7.46)	-	-
5731.76		4.26	-1.300	34.6 (7.43)	45.4 (7.52)	-	-
5752.03		4.55	-0.864	30.3 (7.16)	41.6 (7.27)	-	-
5753.12		4.26	-0.760	49.6 (7.18)	-	-	86.2 (6.89)
5775.08		4.22	-1.298	27.7 (7.25)	47.0 (7.52)	-	-
5809.22		3.88	-1.840	23.5 (7.40)	35.6 (7.47)	-	-
5816.37		4.55	-0.680	-	63.6 (7.56)	-	-
5852.22		4.55	-1.330	-	29.3 (7.43)	-	-
5856.09		4.29	-1.640	-	23.6 (7.35)	-	-
5859.59		4.55	-0.386	43.1 (6.94)	57.2 (7.13)	-	-
5862.36		4.55	-0.051	-	-	-	81.3 (6.42)
5916.25		2.45	-2.994	-	45.4 (7.48)	-	-
5927.79		4.65	-1.090	-	31.5 (7.34)	-	-
5930.18		4.65	-0.230	60.9 (7.21)	74.0 (7.40)	-	-
5934.65		3.93	-1.170	47.7 (7.26)	-	-	-
5949.35		4.61	-1.248	-	25.0 (7.29)	-	-
5956.69		0.86	-4.605	-	38.6 (7.33)	-	-
5976.78		3.94	-1.503	34.5 (7.35)	52.8 (7.59)	-	-
5984.81		4.73	-0.443	49.1 (7.27)	-	-	-
5987.06		4.76	-0.654	-	55.4 (7.55)	-	-
6003.01		3.88	-1.120	53.1 (7.26)	69.0 (7.53)	-	-

TABLE 3.10: *–continued*

Wavelength (Å)	Element	E_{low} (eV)	log gf	HD 147609	HD 154276	HD 87853	HE 0308–1612
6007.96		4.65	-0.978	-	41.0 (7.45)	-	-
6008.56		3.88	-1.291	50.0 (7.39)	-	-	-
6024.06		4.55	-0.120	-	87.9 (7.45)	53.7 (6.85)	-
6027.05		4.08	-1.210	-	53.4 (7.44)	-	-
6056.01		4.73	-0.460	-	59.0 (7.40)	-	-
6082.71		2.22	-3.573	-	24.3 (7.29)	-	78.6 (6.90)
6127.91		4.14	-1.399	-	38.2 (7.33)	-	-
6136.61		2.45	-1.400	-	-	78.8 (6.64)	165.6 (6.75)
6137.69		2.59	-1.403	87.8 (7.07)	-	76.0 (6.71)	-
6151.62		2.18	-3.299	-	40.2 (7.36)	-	-
6157.73		4.08	-1.260	-	51.1 (7.43)	-	-
6165.36		4.14	-1.550	-	32.3 (7.34)	-	58.0 (6.93)
6173.33		2.22	-2.880	-	57.0 (7.40)	-	-
6180.20		2.73	-2.780	-	40.2 (7.39)	-	87.5 (6.92)
6200.31		2.61	-2.437	-	61.9 (7.46)	-	-
6213.43		2.22	-2.660	-	70.9 (7.52)	-	-
6219.28		2.20	-2.433	-	78.8 (7.46)	-	131.9 (6.77)
6229.23		2.85	-2.970	-	27.7 (7.38)	-	-
6230.72		2.56	-1.281	104.5 (7.26)	-	90.2 (6.84)	-
6232.64		3.65	-1.200	-	67.6 (7.36)	-	-
6240.65		2.22	-3.380	-	37.3 (7.42)	-	104.5 (7.17)
6246.32		3.60	-0.960	72.4 (7.22)	-	-	130.7 (7.11)
6252.56		2.40	-1.687	87.6 (7.16)	-	70.5 (6.72)	-
6254.26		2.28	-2.480	71.2 (7.50)	-	-	-
6256.36		2.45	-2.620	51.1 (7.44)	-	-	-
6265.13		2.18	-2.550	48.9 (7.08)	74.6 (7.45)	-	-
6270.22		2.86	-2.710	-	37.3 (7.37)	-	-
6290.97		4.73	-0.874	-	51.0 (7.63)	-	-
6297.79		2.22	-2.740	-	64.3 (7.43)	-	-
6301.50		3.65	-0.672	-	-	64.0 (6.74)	114.4 (6.54)
6302.49		3.69	-1.131	-	69.7 (7.36)	-	-
6322.69		2.59	-2.426	-	62.7 (7.43)	-	104.3 (6.68)
6335.33		2.20	-2.230	-	84.0 (7.36)	-	137.2 (6.64)
6336.82		3.69	-1.050	-	86.7 (7.62)	-	-
6344.15		2.43	-2.923	-	47.4 (7.40)	-	-
6380.74		4.19	-1.400	-	40.7 (7.42)	-	-
6408.02		3.69	-0.970	-	-	45.5 (6.74)	-
6419.95		4.43	-0.240	-	68.2 (7.10)	-	-
6421.35		2.28	-2.027	82.8 (7.28)	-	63.5 (6.81)	161.7 (7.00)
6469.19		4.83	-0.770	-	42.6 (7.43)	-	-
6475.62		2.56	-2.940	-	43.8 (7.45)	-	-

TABLE 3.10: *–continued*

Wavelength (Å)	Element	E_{low} (eV)	log gf	HD 147609	HD 154276	HD 87853	HE 0308–1612
6481.87		2.28	-2.984	-	51.9 (7.41)	-	-
6494.98		2.40	-1.273	-	-	96.5 (6.78)	-
6495.74		4.83	-0.940	-	29.2 (7.28)	-	-
6593.87		2.43	-2.422	-	-	-	24.9 (6.84)
6597.56		4.79	-1.070	-	-	-	37.3 (6.84)
6677.98		2.69	-1.470	-	-	65.9 (6.67)	-
6739.52		1.56	-4.950	-	-	-	32.6 (6.59)
4233.17	Fe II	2.58	-2.000	123.6 (7.09)	-	129.7 (6.83)	-
4369.41		2.78	-3.670	46.5 (7.08)	-	-	-
4416.83		2.78	-2.600	-	75.4 (7.48)	-	-
4489.18		2.83	-2.970	90.3 (7.38)	-	-	-
4491.40		2.86	-2.700	93.0 (7.20)	63.7 (7.31)	-	-
4508.29		2.86	-2.210	-	80.8 (7.28)	-	-
4515.34		2.84	-2.480	101.5 (7.17)	-	-	-
4520.22		2.81	-2.600	105.8 (7.39)	-	-	-
4541.52		2.86	-3.050	87.8 (7.42)	60.0 (7.55)	-	-
4576.34		2.84	-3.040	82.0 (7.25)	60.5 (7.54)	-	-
4582.84		2.84	-3.100	-	52.1 (7.34)	-	-
4620.52		2.83	-3.280	66.1 (7.11)	46.9 (7.35)	-	-
4629.34		2.81	-2.370	-	-	-	87.9 (6.60)
4731.45		2.89	-3.360	72.1 (7.36)	-	-	-
4923.93		2.89	-1.320	170.8 (7.27)	-	139.1 (6.70)	143.7 (6.84)
5120.35		2.83	-4.214	31.1 (7.32)	-	-	-
5197.58		3.23	-2.100	97.6 (6.94)	71.9 (7.22)	-	-
5234.62		3.22	-2.050	-	78.8 (7.33)	-	-
5256.94		2.89	-4.250	24.0 (7.24)	-	-	-
5264.81		3.23	-3.190	53.9 (7.08)	-	-	-
5414.07		3.22	-3.790	33.9 (7.28)	-	-	-
5425.26		3.20	-3.360	57.0 (7.28)	-	-	-
5534.85		3.25	-2.930	70.0 (7.15)	-	-	-
6147.74		3.89	-2.721	57.2 (7.23)	-	-	-
6149.26		3.89	-2.724	-	30.4 (7.29)	-	-
6238.39		3.89	-2.630	59.8 (7.19)	36.1 (7.36)	-	-
6247.56		3.89	-2.329	-	49.1 (7.41)	-	49.1 (6.88)
6432.68		2.89	-3.708	-	34.4 (7.43)	-	-
6456.38		3.90	-2.075	-	55.6 (7.33)	-	-
6516.08		2.89	-3.450	-	56.7 (7.75)	-	-

TABLE 3.11: **Equivalent widths (in mÅ) of lines used for calculation of elemental abundances.**

Wavelength (Å)	Element	E_{low} (eV)	log gf	HD 145777	CD−27 14351	HE 0017+0055	HE 2144−1832	HE 2339−0837
5682.633	Na I	2.10	−0.700	40.2 (4.61)	52.9 (5.05)	-	69.8 (5.05)	36.3 (5.06)
5688.205		2.10	−0.450	45.1 (4.44)	51.0 (4.77)	-	93.7 (5.16)	47.2 (5.02)
6160.747		2.10	−1.260	-	-	-	45.1 (5.20)	-
4571.096	Mg I	0.00	−5.691	-	-	-	-	-
5528.405		4.35	−0.620	149.7 (6.42)	170.9 (6.70)	-	176.5 (6.71)	142.2 (7.03)
5711.088		4.35	−1.833	53.9 (6.09)	-	-	94.4 (6.56)	-
4318.652	Ca I	1.90	−0.208	106.5 (4.45)	79.3 (4.36)	-	138.1 (5.08)	53.4 (4.10)
5349.465		2.71	−1.178	36.5 (4.91)	-	-	-	-
5512.980		2.93	−0.290	-	-	-	67.3 (4.82)	-
5588.749		2.53	0.210	-	-	-	-	36.6 (3.93)
5590.114		2.52	−0.710	57.6 (4.50)	-	-	86.3 (4.97)	-
5594.462		2.52	−0.050	-	-	-	-	40.8 (4.27)
5857.451		2.93	0.230	101.4 (4.80)	-	-	-	-
6102.723		1.88	−0.890	97.8 (4.31)	79.6 (4.34)	-	151.4 (5.15)	-
6166.439		2.52	−0.900	61.7 (4.68)	42.9 (4.67)	-	100.1 (5.28)	-

In columns 5 to 9, the numbers within bracket '()' indicate the abundances derived from the corresponding line.

TABLE 3.11: *–continued*

Wavelength (Å)	Element	E_{low} (eV)	log gf	HD 145777	CD−27 14351	HE 0017+0055	HE 2144−1832	HE 2339−0837
6169.042		2.52	−0.550	94.8 (4.84)	76.5 (4.79)	-	113.6 (5.16)	-
6169.563		2.53	−0.270	93.4 (4.54)	-	-	125.1 (5.07)	-
6439.075		2.53	0.470	169.9 (4.87)	135.4 (4.56)	-	-	58.0 (4.06)
6572.779		0.00	−4.290	-	-	-	147.5 (5.34)	-
4840.874	Ti I	0.90	−0.509	-	82.1 (3.34)	-	123.3 (3.54)	-
4926.148		0.82	−2.170	-	-	-	38.8 (3.70)	-
4999.503		0.83	0.250	165.8 (3.32)	123.1 (2.97)	-	-	-
5024.844		0.82	−0.602	-	83.2 (3.27)	-	131.1 (3.57)	-
5210.385		0.05	−0.884	-	-	118.3 (3.13)	-	-
5460.499		0.05	−2.880	-	-	-	75.5 (3.60)	-
5918.535		1.07	−1.460	-	-	-	47.3 (3.33)	-
5922.109		1.05	−1.466	-	-	-	58.8 (3.46)	-
5978.541		1.87	−0.496	49.5 (3.56)	-	-	-	-
4443.794	Ti II	1.08	−0.700	-	-	-	-	101.3 (2.65)
4563.761		1.22	−0.960	-	-	-	-	93.6 (2.82)
4764.526		1.24	−2.770	60.3 (3.43)	-	-	-	-

Table 3.11: *–continued*

Wavelength (Å)	Element	E_{low} (eV)	log gf	HD 145777	CD−27 14351	HE 0017+0055	HE 2144−1832	HE 2339−0837
4779.985		2.05	−1.370	72.8 (3.39)	82.0 (3.27)	66.1 (3.19)	-	-
4798.521		1.08	−2.430	86.2 (3.35)	92.9 (3.18)	-	-	-
4805.085		2.06	−1.100	93.4 (3.56)	82.2 (3.01)	75.6 (3.12)	90.3 (3.54)	-
4865.612		1.12	−2.610	-	-	-	78.2 (3.46)	-
5185.913		1.89	−1.350	94.4 (3.44)	-	-	-	-
5226.543		1.57	−1.300	-	-	104.3 (3.10)	-	56.5 (2.53)
5336.771		1.58	−1.700	-	109.7 (3.18)	-	102.6 (3.53)	33.5 (2.49)
5381.015		1.57	−2.080	-	99.7 (3.37)	-	-	-
5206.037	Cr I	0.94	0.019	-	-	-	-	58.9 (2.56)
5296.691		0.98	−1.400	104.2 (3.31)	-	-	145.6 (4.04)	-
5298.272		0.98	−1.150	122.1 (3.34)	65.4 (2.95)	-	-	-
5300.745		0.98	−2.120	49.0 (3.22)	-	-	101.7 (4.00)	-
5345.796		1.00	−0.980	136.3 (3.41)	86.1 (3.07)	-	-	-
5348.315		1.00	−1.290	91.8 (3.03)	-	33.4 (2.68)	129.9 (3.65)	-
5409.784		1.03	−0.720	142.5 (3.26)	121.6 (3.30)	-	172.3 (3.89)	-
4813.467	Co I	3.22	0.050	-	-	-	44.9 (3.46)	-

Table 3.11: *–continued*

Wavelength (Å)	Element	E_{low} (eV)	log gf	HD 145777	CD−27 14351	HE 0017+0055	HE 2144−1832	HE 2339−0837
5342.695		4.02	0.690	-	-	-	24.9 (3.41)	-
5483.344		1.71	−1.490	51.4 (2.85)	-	-	-	-
6116.996		1.79	−2.490	-	-	-	22.4 (3.39)	-
4756.510	Ni I	3.48	−0.270	-	-	-	80.4 (4.85)	-
5146.480		3.71	0.120	-	-	-	94.4 (4.87)	-
6175.360		4.09	−0.530	-	-	-	57.3 (5.16)	-
6176.807		4.09	−0.530	-	-	-	58.7 (5.19)	-
6177.236		1.83	−3.500	-	-	-	51.5 (4.91)	-
4810.528	Zn I	4.08	−0.137	58.0 (3.02)	-	45.0 (2.62)	49.6 (2.85)	-
4854.863	Y II	0.99	−0.380	-	-	74.1 (0.42)	-	41.4 (0.18)
5200.406		0.99	−0.570	-	-	63.0 (0.27)	130.8 (1.71)	35.8 (0.21)
5205.724		1.03	−0.340	-	-	73.1 (0.30)	-	35.8 (0.03)
5289.815		1.03	−1.850	-	63.2 (1.36)	-	-	-
5402.774		1.84	−0.510	56.4 (1.25)	90.9 (1.50)	-	83.5 (1.83)	-
5662.925		1.94	0.160	89.7 (1.28)	132.6 (1.56)	-	105.3 (1.68)	-
4739.480	Zr I	0.65	0.230	57.0 (1.55)	-	-	-	-

Table 3.11: *–continued*

Wavelength (Å)	Element	E_{low} (eV)	log gf	HD 145777	CD−27 14351	HE 0017+0055	HE 2144−1832	HE 2339−0837
4772.323		0.62	0.040	-	-	-	79.1 (2.03)	-
4805.889		0.69	−0.420	-	-	-	27.0 (1.72)	-
6134.585		0.00	−1.280	29.4 (1.36)	34.9 (2.07)	-	79.7 (2.02)	-
4048.680	Zr II	0.80	−0.345	-	-	-	-	75.3 (1.48)
4457.418		1.37	−0.610	-	-	51.0 (1.64)	-	-
4962.310		0.97	−2.000	-	-	27.1 (1.49)	-	-
5112.297		1.67	−0.590	-	102.1 (2.09)	73.2 (1.89)	-	-
4257.119	Ce II	0.46	−1.116	-	-	-	-	30.2 (1.18)
4336.244		0.70	−0.564	-	-	-	74.2 (1.45)	-
4427.916		0.54	−0.460	89.1 (1.29)	-	-	-	-
4460.207		0.17	0.478	-	160.4 (0.79)	-	-	-
4483.893		0.86	0.010	88.0 (1.26)	83.3 (0.91)	-	103.1 (1.70)	-
4486.909		0.30	−0.474	-	-	-	107.2 (1.43)	-
4562.359		0.48	0.081	119.2 (1.23)	-	-	-	-
4725.069		0.52	−1.204	-	-	-	77.2 (1.71)	34.0 (1.35)
4873.999		1.11	−0.892	-	-	-	58.2 (1.80)	-

Table 3.11: *–continued*

Wavelength (Å)	Element	E_{low} (eV)	log gf	HD 145777	CD−27 14351	HE 0017+0055	HE 2144−1832	HE 2339−0837
5187.458		1.21	−0.104	66.1 (1.16)	45.6 (0.59)	66.8 (1.19)	93.9 (1.80)	-
5191.633		0.87	−0.689	-	-	72.0 (1.28)	-	-
5330.556		0.87	−0.760	53.0 (1.07)	-	-	-	27.5 (1.10)
5259.728	Pr II	0.63	0.080	-	-	-	64.4 (0.79)	37.8 (0.09)
5322.772		0.48	−0.315	70.5 (0.22)	-	90.6 (0.68)	106.1 (0.99)	-
6165.891		0.92	−0.205	46.8 (0.22)	44.3 (-0.03)	-	68.1 (0.64)	26.9 (0.39)
4451.980	Nd II	0.00	−1.340	-	30.3 (-0.09)	-	-	-
4594.447		0.20	−1.550	-	-	68.3 (1.07)	-	-
4645.760		0.56	−0.750	-	-	-	90.2 (1.40)	-
4706.543		0.00	−0.880	-	-	-	-	77.6 (1.31)
4797.153		0.56	−0.950	47.3 (0.61)	-	81.0 (1.35)	75.1 (1.22)	-
4811.342		0.06	−1.140	91.9 (0.91)	57.1 (0.12)	-	-	67.0 (1.31)
4825.478		0.18	−0.860	-	78.0 (0.32)	-	126.2 (1.65)	64.8 (1.10)
5212.361		0.20	−0.870	-	55.1 (-0.09)	-	-	-
5255.505		0.20	−0.820	104.7 (0.87)	68.1 (0.03)	-	-	74.8 (1.28)
5293.163		0.82	−0.060	90.4 (0.76)	73.5 (0.18)	108.5 (1.20)	120.7 (1.48)	70.7 (1.15)

Table 3.11: *–continued*

Wavelength (Å)	Element	E_{low} (eV)	log gf	HD 145777	CD−27 14351	HE 0017+0055	HE 2144−1832	HE 2339−0837
5356.967		1.26	−0.250	-	-	-	71.3 (1.30)	-
5442.264		0.68	−0.910	-	-	-	94.1 (1.53)	-
5688.518		0.99	−0.250	56.7 (0.50)	-	96.2 (1.23)	91.9 (1.21)	-
4318.927	Sm II	0.28	−0.613	-	-	-	-	47.3 (0.37)
4424.337		0.48	−0.260	-	-	-	-	62.5 (0.65)
4458.509		0.10	−1.110	69.5 (0.44)	-	65.0 (0.45)	106.5 (1.34)	41.9 (0.51)
4704.400		0.00	−1.562	-	-	-	84.7 (1.03)	-
4815.805		0.18	−1.420	-	-	54.3 (0.50)	-	-
4854.368		0.38	−1.873	17.3 (0.40)	-	-	39.2 (0.95)	-

Table 3.12: **Equivalent widths (in mÅ) of lines used for calculation of elemental abundances.**

Wavelength (Å)	Element	E_{low} (eV)	log gf	BD+75 348	BD+09 3019	HD 238020	HE 0319–0215	HE 0507–1653	HE 0930–0018	HE 1023–1504
5682.633	Na I	2.10	–0.700	115.8 (6.25)	172.5 (6.08)	64.4 (5.62)	22.4 (4.71)	45.2 (5.19)	112.1 (5.39)	51.5 (5.06)
5688.205		2.10	–0.450	140.3 (6.42)	170.6 (5.81)	87.1 (5.77)	25.3 (4.53)	58.7 (5.17)	136.8 (5.43)	-
6154.23		2.10	–1.560	59.1 (6.14)	-	16.1 (5.50)	-	-	-	-
6160.75		2.10	–1.260	88.1 (6.30)	-	30.1 (5.55)	-	19.7 (5.21)	-	-

In columns 5 to 11, the numbers within bracket '()' indicate the abundances derived from the corresponding line.

TABLE 3.12: *–continued*

Wavelength (Å)	Element	E_{low} (eV)	log gf	BD+75 348	BD+09 3019	HD 238020	HE 0319–0215	HE 0507–1653	HE 0930–0018	HE 1023–1504
4571.10	Mg I	0.00	–5.691	181.2 (7.59)	-	131.6 (7.27)	62.7 (5.51)	113.8 (6.62)	-	-
4702.99		4.35	–0.666	178.2 (7.37)	-	161.8 (7.38)	-	-	-	-
5528.40		4.35	–0.620	191.2 (7.39)	-	163.1 (7.31)	-	143.8 (6.81)	-	-
5711.09		4.35	–1.833	101.3 (7.18)	-	86.6 (7.19)	-	61.1 (6.62)	105.1 (6.69)	-
6318.72		5.11	–1.730	-	170.8 (8.31)	-	-	-	-	-
6237.32	Si I	5.61	–0.530	-	-	35.6 (6.31)	-	-	-	-
4283.01	Ca I	1.89	–0.224	155.1 (6.04)	-	132.8 (6.01)	-	-	-	-
4318.65		1.90	–0.208	142.4 (5.84)	-	125.7 (5.87)	-	110.2 (5.30)	-	-
4425.44		1.88	–0.385	152.8 (6.12)	-	118.6 (5.87)	-	-	-	-
4434.96		1.89	–0.029	169.5 (5.98)	-	-	-	-	-	-
4585.86		2.53	–0.186	-	-	116.7 (6.23)	-	-	-	-
5260.39		2.52	–1.900	-	69.7 (5.65)	-	-	-	-	-
5512.98		2.93	–0.290	-	-	62.6 (5.49)	-	-	120.1 (5.33)	-
5581.97		2.52	–0.710	-	-	84.7 (5.94)	-	-	-	-
5588.75		2.53	0.210	136.2 (5.71)	-	126.8 (5.90)	57.9 (4.39)	-	-	-
5590.11		2.52	–0.710	108.1 (6.07)	159.3 (5.64)	81.5 (5.86)	-	62.8 (5.32)	128.6 (5.36)	98.5 (5.67)
5594.46		2.52	–0.050	143.5 (6.08)	-	111.1 (5.85)	59.9 (4.68)	113.4 (5.68)	-	122.3 (5.48)
5598.48		2.52	–0.220	-	-	104.9 (5.88)	-	-	-	-
5601.28		2.53	–0.690	125.5 (6.40)	-	90.7 (6.05)	-	-	-	-
5857.45		2.93	0.230	138.9 (6.14)	-	105.6 (5.86)	-	95.0 (5.47)	-	107.9 (5.39)

TABLE 3.12: *–continued*

Wavelength (Å)	Element	E_{low} (eV)	log gf	BD+75 348	BD+09 3019	HD 238020	HE 0319–0215	HE 0507–1653	HE 0930–0018	HE 1023–1504
6102.72		1.88	–0.890	139.4 (6.00)	-	112.8 (5.96)	40.6 (4.24)	-	-	-
6122.22		1.89	–0.409	184.7 (6.20)	-	142.7 (6.04)	-	-	-	-
6162.17		1.90	0.100	-	-	162.3 (5.83)	-	-	-	-
6166.44		2.52	–0.900	82.6 (5.68)	-	56.5 (5.49)	-	45.5 (5.15)	115.1 (5.31)	-
6169.04		2.52	–0.550	105.9 (5.78)	-	74.3 (5.51)	-	64.9 (5.18)	154.0 (5.45)	-
6169.56		2.53	–0.270	125.9 (5.90)	-	92.9 (5.64)	-	78.5 (5.18)	180.0 (5.43)	-
6439.07		2.53	0.470	156.7 (5.64)	-	136.6 (5.71)	84.7 (4.65)	114.5 (5.12)	-	-
6449.81		2.52	–0.550	116.4 (5.95)	-	90.4 (5.83)	-	-	-	-
6572.78		0.00	–4.290	-	-	37.8 (5.69)	-	-	120.6 (5.13)	-
4533.24	Ti I	0.85	0.476	133.6 (4.33)	-	108.6 (4.32)	-	-	-	-
4820.41		1.50	–0.441	-	179.5 (4.92)	-	-	-	-	-
4840.87		0.90	–0.509	97.8 (4.40)	-	74.1 (4.39)	-	67.0 (4.00)	111.7 (3.25)	-
4926.15		0.82	–2.170	28.5 (4.57)	-	-	-	-	42.2 (3.64)	-
4937.73		0.81	–2.254	-	115.5 (4.65)	-	-	-	-	-
4981.73		0.85	0.504	163.8 (4.66)	-	121.6 (4.46)	-	-	-	-
4991.06		0.84	0.380	152.2 (4.58)	-	118.3 (4.49)	-	-	-	-
4999.50		0.83	0.250	-	-	118.2 (4.60)	-	-	-	-
5016.16		0.85	–0.574	112.1 (4.68)	-	82.2 (4.56)	-	-	-	-
5024.84		0.82	–0.602	113.3 (4.69)	-	77.3 (4.44)	-	58.1 (3.78)	111.5 (3.17)	99.1 (3.79)
5064.65		0.05	–0.991	145.8 (4.81)	-	101.4 (4.52)	-	-	-	-

TABLE 3.12: *–continued*

Wavelength (Å)	Element	E_{low} (eV)	log gf	BD+75 348	BD+09 3019	HD 238020	HE 0319–0215	HE 0507–1653	HE 0930–0018	HE 1023–1504
5173.74		0.00	–1.118	-	-	91.6 (4.32)	-	-	-	-
5192.97		0.02	–1.006	161.0 (5.02)	-	107.6 (4.61)	-	-	-	-
5210.39		0.05	–0.884	146.0 (4.63)	-	108.2 (4.54)	62.5 (3.16)	90.7 (3.87)	-	161.7 (4.09)
5460.50		0.05	–2.880	45.7 (4.60)	-	13.9 (4.40)	-	-	57.7 (3.42)	-
5918.53		1.07	–1.460	-	-	-	-	-	57.2 (3.42)	-
5922.11		1.05	–1.466	51.1 (4.46)	-	23.0 (4.35)	-	-	69.1 (3.56)	52.0 (3.98)
5978.54		1.87	–0.496	78.7 (4.98)	-	23.1 (4.30)	-	-	69.6 (3.76)	-
4163.65	Ti II	2.59	–0.400	-	-	100.2 (4.62)	-	-	-	-
4443.79		1.08	–0.700	-	-	157.3 (4.33)	-	148.1 (3.90)	122.9 (3.17)	-
4450.48		1.08	–1.450	137.1 (4.72)	-	-	-	-	-	-
4464.45		1.16	–2.080	-	-	104.0 (4.72)	-	-	-	-
4468.51		1.13	–0.600	-	-	158.6 (4.29)	-	-	-	-
4470.86		1.16	–2.280	-	-	95.9 (4.70)	-	-	-	-
4501.27		1.12	–0.750	-	-	152.9 (4.35)	-	-	-	-
4518.33		1.08	–2.555	83.0 (4.48)	-	74.6 (4.31)	-	-	-	-
4563.76		1.22	–0.960	-	-	144.6 (4.53)	118.2 (3.43)	-	121.9 (3.57)	-
4571.97		1.57	–0.530	-	-	158.4 (4.67)	-	-	-	-
4589.96		1.24	–1.790	117.5 (4.76)	-	110.0 (4.64)	-	-	-	-
4764.53		1.24	–2.770	77.1 (4.70)	-	58.7 (4.29)	-	48.1 (3.89)	-	-
4779.98		2.05	–1.370	95.5 (4.68)	-	82.6 (4.36)	60.0 (3.18)	76.5 (4.03)	-	-

TABLE 3.12: *–continued*

Wavelength (Å)	Element	E_{low} (eV)	log gf	BD+75 348	BD+09 3019	HD 238020	HE 0319–0215	HE 0507–1653	HE 0930–0018	HE 1023–1504
4798.52		1.08	–2.430	-	-	70.3 (4.03)	-	65.0 (3.71)	-	-
4805.09		2.06	–1.100	-	-	102.6 (4.62)	73.3 (3.29)	86.4 (4.01)	57.6 (3.60)	-
4865.61		1.12	–2.610	81.7 (4.49)	-	66.4 (4.16)	-	49.0 (3.60)	-	-
5129.15		1.89	–1.390	-	-	91.2 (4.37)	-	-	-	-
5154.07		1.57	–1.920	115.4 (5.08)	-	88.8 (4.47)	-	-	-	-
5185.91		1.89	–1.350	99.0 (4.50)	-	84.4 (4.15)	-	64.0 (3.51)	-	-
5226.54		1.57	–1.300	-	-	112.9 (4.43)	-	-	76.0 (3.44)	-
5336.77		1.58	–1.700	108.8 (4.68)	-	92.7 (4.33)	-	95.0 (4.17)	-	-
5381.02		1.57	–2.080	-	-	79.4 (4.38)	-	-	-	-
5418.75		1.58	–1.999	84.5 (4.41)	-	70.1 (4.09)	-	-	-	-
4545.95	Cr I	0.94	–1.370	-	-	92.5 (5.06)	-	-	-	-
4616.12		0.98	–1.190	137.9 (5.44)	-	92.8 (4.91)	-	-	-	-
4626.17		0.97	–1.320	-	-	83.2 (4.77)	-	-	-	-
4646.16		1.03	–0.700	148.8 (5.19)	-	104.6 (4.79)	-	-	-	-
4651.28		0.98	–1.460	-	-	82.2 (4.89)	-	-	-	-
4652.16		1.00	–1.030	138.8 (5.30)	-	105.2 (5.10)	-	-	-	-
5206.04		0.94	0.019	-	-	172.3 (5.02)	-	125.8 (4.01)	-	-
5296.69		0.98	–1.400	135.3 (5.32)	-	95.3 (5.03)	-	75.6 (4.32)	-	-
5298.27		0.98	–1.150	-	-	105.8 (5.04)	-	86.5 (4.33)	-	-
5300.74		0.98	–2.120	90.7 (5.06)	-	56.7 (4.85)	-	30.2 (4.11)	82.8 (3.65)	63.9 (4.05)

TABLE 3.12: *–continued*

Wavelength (Å)	Element	E_{low} (eV)	log gf	BD+75 348	BD+09 3019	HD 238020	HE 0319–0215	HE 0507–1653	HE 0930–0018	HE 1023–1504
5345.80		1.00	–0.980	-	-	111.9 (5.03)	-	-	173.0 (3.92)	-
5348.31		1.00	–1.290	125.2 (5.01)	-	99.5 (5.04)	-	72.2 (4.16)	130.7 (3.64)	100.8 (3.90)
5409.78		1.03	–0.720	169.6 (5.27)	-	129.9 (5.18)	-	104.2 (4.36)	-	-
4558.65	Cr II	4.07	–0.660	-	-	80.8 (5.01)	-	-	-	-
4121.31	Co I	0.92	–0.320	-	-	124.3 (4.40)	-	-	-	-
4813.47		3.22	0.050	66.3 (4.56)	-	36.0 (4.20)	-	15.7 (3.52)	37.0 (3.57)	-
5342.69		4.02	0.690	-	-	22.1 (4.08)	-	-	-	-
5483.34		1.71	–1.490	-	-	61.1 (4.52)	-	-	58.1 (3.40)	-
6117.00		1.79	–2.490	23.0 (4.41)	-	-	-	-	-	-
4714.41	Ni I	3.38	0.260	-	-	108.9 (5.79)	-	-	-	-
4756.51		3.48	–0.270	98.2 (5.85)	-	68.4 (5.39)	-	47.5 (4.73)	-	-
4855.41		3.54	0.000	107.1 (5.84)	-	83.4 (5.57)	-	-	-	-
4980.17		3.61	0.070	116.6 (6.04)	-	88.9 (5.69)	-	-	-	-
5035.36		3.64	0.290	102.0 (5.51)	-	82.6 (5.34)	-	55.8 (4.51)	-	-
5080.53		3.66	0.330	104.9 (5.55)	-	87.1 (5.43)	-	-	-	-
5081.11		3.85	0.300	88.6 (5.41)	-	79.4 (5.47)	-	61.6 (4.86)	-	-
5137.07		1.68	–1.990	-	-	103.0 (5.92)	-	73.0 (4.92)	-	-
5146.48		3.71	0.120	94.9 (5.57)	-	78.1 (5.45)	-	-	139.0 (5.67)	-
5476.90		1.83	–0.890	173.0 (5.77)	-	145.0 (5.78)	-	-	-	-
6175.36		4.09	–0.530	-	-	30.9 (5.40)	-	-	61.9 (5.66)	-

TABLE 3.12: *–continued*

Wavelength (Å)	Element	E_{low} (eV)	log gf	BD+75 348	BD+09 3019	HD 238020	HE 0319–0215	HE 0507–1653	HE 0930–0018	HE 1023–1504
6176.81		4.09	–0.530	78.3 (6.17)	-	45.5 (5.71)	-	-	-	-
6177.24		1.83	–3.500	43.6 (5.77)	-	13.8 (5.40)	-	-	50.0 (5.39)	-
6643.63		1.68	–2.300	134.0 (6.05)	-	103.8 (5.97)	-	-	-	-
6767.77		1.83	–2.170	115.1 (5.72)	-	86.9 (5.63)	-	-	-	-
5105.54	Cu I	1.39	–1.516	-	-	96.4 (3.89)	-	-	-	-
5218.20		3.82	0.476	69.7 (3.66)	-	-	-	17.4 (2.55)	-	-
4722.15	Zn I	4.03	–0.338	-	-	66.8 (3.78)	-	-	-	-
4810.53		4.08	–0.137	85.8 (4.12)	-	70.3 (3.72)	-	56.3 (3.21)	43.0 (3.30)	-
4607.33	Sr I	0.00	–0.570	-	-	-	-	-	-	-
4872.49		1.80	–0.200	-	98.0 (3.99)	-	-	-	-	-
4215.52	Sr II	0.00	–0.145	-	-	338.1 (2.27)	-	-	-	-
4317.30	Y II	0.71	–1.380	-	177.2 (3.66)	-	-	-	-	-
4854.86		0.99	–0.380	140.1 (3.10)	-	62.1 (1.27)	71.0 (0.76)	98.3 (1.97)	81.0 (1.32)	-
4883.68		1.08	0.070	183.9 (3.27)	-	75.9 (1.28)	-	-	-	-
4900.12		1.03	–0.090	-	-	75.5 (1.38)	-	-	-	-
5087.42		1.08	–0.170	135.7 (2.86)	-	62.6 (1.14)	-	-	-	-
5200.41		0.99	–0.570	128.7 (2.98)	-	54.9 (1.24)	-	87.8 (1.82)	-	113.0 (1.52)
5205.72		1.03	–0.340	150.9 (3.19)	-	63.9 (1.27)	-	97.1 (1.87)	-	-
5289.81		1.03	–1.850	78.2 (3.08)	-	-	-	43.4 (2.09)	18.5 (1.62)	-
5402.77		1.84	–0.510	83.0 (2.81)	-	14.8 (1.12)	-	62.4 (2.10)	-	-

TABLE 3.12: *–continued*

Wavelength (Å)	Element	E_{low} (eV)	log gf	BD+75 348	BD+09 3019	HD 238020	HE 0319–0215	HE 0507–1653	HE 0930–0018	HE 1023–1504
5544.61		1.74	–1.090	82.8 (3.25)	-	-	-	-	-	-
5662.93		1.94	0.160	121.9 (3.14)	178.5 (3.88)	51.7 (1.94)	59.1 (0.83)	81.1 (1.97)	60.2 (1.64)	108.3 (1.82)
5728.89		1.84	–1.120	64.5 (2.95)	-	-	-	-	-	-
4739.48	Zr I	0.65	0.230	-	-	9.4 (1.97)	-	-	66.0 (1.57)	-
4772.32		0.62	0.040	68.6 (3.13)	-	8.1 (2.05)	-	40.4 (2.78)	-	-
4805.89		0.69	–0.420	41.9 (3.11)	-	-	-	14.3 (2.65)	-	-
6134.59		0.00	–1.280	57.2 (3.25)	-	-	-	-	-	-
4379.74	Zr II	1.53	–0.356	99.3 (3.44)	-	44.2 (1.93)	-	-	-	-
4457.42		1.37	–0.610	-	-	-	21.9 (0.63)	-	-	-
4962.31		0.97	–2.000	70.6 (3.49)	-	-	-	41.4 (2.62)	-	59.3 (2.23)
5112.30		1.67	–0.590	-	-	-	-	79.6 (2.91)	-	-
5350.09		1.83	–1.240	53.9 (3.31)	-	-	-	-	-	-
5350.37		1.77	–1.276	-	-	8.2 (1.98)	-	-	-	-
4257.12	Ce II	0.46	–1.116	69.5 (2.74)	-	-	-	59.0 (2.26)	-	-
4336.24		0.70	–0.564	-	127.3 (2.89)	-	-	-	-	-
4427.92		0.54	–0.460	-	-	30.7 (1.22)	-	74.8 (2.11)	-	-
4460.21		0.17	0.478	-	-	-	-	149.0 (2.31)	-	-
4483.89		0.86	0.010	86.8 (2.55)	-	25.6 (0.97)	-	77.4 (2.07)	-	-
4486.91		0.30	–0.474	115.4 (3.14)	-	34.0 (1.04)	-	-	-	-
4515.85		1.06	–0.612	65.0 (2.76)	-	9.3 (1.24)	-	-	-	-

TABLE 3.12: *–continued*

Wavelength (Å)	Element	E_{low} (eV)	log gf	BD+75 348	BD+09 3019	HD 238020	HE 0319–0215	HE 0507–1653	HE 0930–0018	HE 1023–1504
4560.96		0.68	–0.546	101.4 (3.28)	-	-	-	-	-	-
4562.36		0.48	0.081	120.4 (2.88)	-	49.3 (1.04)	-	96.3 (2.06)	-	-
4628.16		0.52	0.008	-	-	42.5 (0.99)	-	-	-	-
4725.07		0.52	–1.204	74.5 (2.92)	-	-	-	50.8 (2.12)	28.6 (1.54)	-
4874.00		1.11	–0.892	67.3 (3.10)	-	-	-	41.0 (2.26)	-	82.1 (2.44)
5187.46		1.21	–0.104	91.9 (3.02)	-	-	43.6 (0.92)	66.1 (2.15)	45.2 (1.66)	109.7 (2.34)
5274.23		1.04	–0.323	92.5 (3.03)	145.6 (3.16)	15.6 (1.15)	-	-	-	-
5330.56		0.87	–0.760	83.5 (3.02)	136.0 (3.18)	-	36.6 (0.94)	57.0 (2.17)	22.8 (1.40)	96.1 (2.15)
5472.28		1.25	–0.544	77.3 (3.08)	-	-	-	-	-	-
6043.37		1.21	–0.772	72.2 (3.06)	-	-	-	-	-	-
5219.05	Pr II	0.79	–0.240	73.4 (2.02)	139.7 (2.48)	-	-	-	-	-
5220.11		0.80	0.160	93.5 (2.16)	-	17.9 (0.36)	-	-	-	-
5259.73		0.63	0.080	-	-	-	-	-	35.5 (0.35)	-
5292.62		0.65	–0.300	90.4 (2.33)	167.2 (2.77)	17.6 (0.63)	-	-	-	-
5322.77		0.48	–0.315	102.6 (2.44)	176.4 (2.69)	-	43.4 (0.48)	-	32.5 (0.48)	-
6165.89		0.92	–0.205	68.0 (1.90)	-	-	-	47.0 (1.25)	-	-
4061.08	Nd II	0.47	0.550	-	-	69.3 (1.08)	-	-	-	-
4109.07		0.06	0.280	-	-	77.1 (1.14)	-	-	-	-
4109.45		0.32	0.300	-	-	79.5 (1.49)	-	-	-	-
4451.56		0.38	–0.040	124.6 (2.80)	-	-	-	-	-	-

TABLE 3.12: *–continued*

Wavelength (Å)	Element	E_{low} (eV)	log gf	BD+75 348	BD+09 3019	HD 238020	HE 0319–0215	HE 0507–1653	HE 0930–0018	HE 1023–1504
4451.98		0.00	–1.340	-	-	35.4 (1.40)	53.4 (0.93)	78.9 (2.25)	47.6 (1.11)	95.9 (1.69)
4594.45		0.20	–1.550	65.4 (2.45)	-	-	23.5 (0.48)	52.0 (1.93)	-	-
4645.76		0.56	–0.750	84.6 (2.61)	-	-	-	-	-	-
4706.54		0.00	–0.880	-	-	36.9 (0.94)	-	86.9 (1.93)	-	-
4797.15		0.56	–0.950	78.4 (2.59)	-	11.4 (0.90)	29.8 (0.45)	57.0 (1.84)	27.2 (1.07)	96.3 (1.90)
4811.34		0.06	–1.140	-	160.4 (2.77)	28.1 (1.05)	-	-	47.6 (0.95)	-
4825.48		0.18	–0.860	-	-	-	-	89.1 (2.15)	51.9 (0.91)	-
5092.79		0.38	–0.610	94.0 (2.37)	-	20.6 (0.66)	-	-	-	-
5132.33		0.56	–0.770	-	-	16.7 (0.90)	-	-	-	-
5212.36		0.20	–0.870	112.0 (2.84)	-	-	67.0 (0.83)	78.3 (1.81)	52.8 (0.93)	134.6 (2.01)
5255.51		0.20	–0.820	-	-	-	72.6 (0.94)	87.5 (1.99)	47.9 (0.79)	137.8 (2.00)
5293.16		0.82	–0.060	-	-	30.2 (0.84)	66.9 (0.79)	88.0 (1.98)	43.0 (0.80)	130.4 (1.94)
5311.45		0.99	–0.420	94.2 (2.89)	-	-	-	-	-	-
5319.81		0.55	–0.210	120.7 (2.78)	-	34.5 (0.78)	-	-	-	-
5356.97		1.26	–0.250	71.7 (2.46)	-	-	-	71.1 (2.24)	-	-
5442.26		0.68	–0.910	75.3 (2.49)	-	-	-	66.3 (2.08)	-	-
5688.52		0.99	–0.250	92.4 (2.59)	-	15.8 (0.79)	-	72.2 (1.90)	40.5 (1.16)	-
5825.86		1.08	–0.760	-	115.8 (2.85)	-	-	-	-	-
4318.93	Sm II	0.28	–0.613	-	-	34.8 (0.71)	50.1 (0.28)	-	-	92.8 (1.14)
4424.34		0.48	–0.260	-	-	-	55.0 (0.30)	89.9 (1.81)	44.7 (0.41)	-

TABLE 3.12: *–continued*

Wavelength (Å)	Element	E_{low} (eV)	log gf	BD+75 348	BD+09 3019	HD 238020	HE 0319–0215	HE 0507–1653	HE 0930–0018	HE 1023–1504
4458.51		0.10	–1.110	-	-	-	40.2 (0.17)	-	42.1 (0.69)	-
4499.48		0.25	–1.413	-	128.8 (2.61)	9.4 (0.67)	-	-	-	-
4519.63		0.54	–0.751	-	-	17.0 (0.63)	-	-	-	-
4566.20		0.33	–1.245	68.7 (2.15)	141.9 (2.79)	-	-	-	-	-
4577.69		0.25	–1.234	67.6 (2.00)	-	17.3 (0.80)	-	-	-	-
4704.40		0.00	–1.562	-	-	-	-	59.4 (1.60)	-	-
4791.58		0.10	–1.846	-	139.7 (2.94)	-	-	-	-	-
4815.81		0.18	–1.420	-	-	-	23.2 (0.01)	52.1 (1.48)	-	-
4854.37		0.38	–1.873	40.2 (2.10)	-	-	-	23.5 (1.51)	-	54.6 (1.34)
4103.31	Dy II	0.10	–0.346	81.0 (1.49)	-	46.4 (0.53)	-	-	-	-
4923.17		0.10	–2.384	-	76.7 (2.43)	-	-	-	-	-
4093.16	Hf II	0.45	–1.090	89.5 (2.33)	-	-	-	-	-	-

TABLE 3.13: **Equivalent widths (in mÅ) of lines used for calculation of elemental abundances.**

Wavelength (Å)	Element	E_{low} (eV)	log gf	HE 1005–1439	HE 0401–0138	HE 1246–1344	HE 1153–0518
5889.95	Na I	0.00	0.117	158.8 (4.53)	87.7 (3.06)	146.0 (4.25)	218.7 (5.02)
5895.92		0.00	−0.184	143.9 (4.60)	72.1 (2.95)	134.4 (4.31)	191.3 (5.05)
4571.10	Mg I	0.00	−5.691	16.4 (5.05)	-	13.2 (4.56)	-
5172.68		2.71	−0.402	124.5 (5.09)	121.6 (5.16)	-	156.5 (5.58)
5183.60		2.72	−0.180	133.3 (5.05)	126.1 (5.03)	-	169.5 (5.55)
5528.40		4.35	−0.620	34.5 (5.10)	28.5 (4.94)	30.5 (4.96)	-
4226.73	Ca I	0.00	0.243	149.9 (4.06)	102.3 (3.41)	115.1 (3.56)	-
4283.01		1.89	−0.224	-	-	20.4 (3.44)	-
4302.53		1.90	0.275	-	-	30.3 (3.22)	-
4318.65		1.90	−0.208	21.5 (3.54)	23.1 (3.52)	17.3 (3.33)	-
4434.96		1.89	−0.029	-	32.4 (3.58)	27.8 (3.43)	-
4435.68		1.89	−0.500	26.9 (3.95)	-	-	-
4454.78		1.90	0.252	-	-	36.5 (3.37)	-
4585.86		2.53	−0.186	10.4 (3.77)	-	-	-
5265.56		2.52	−0.260	13.5 (3.94)	-	-	-
5588.75		2.53	0.210	25.6 (3.84)	-	18.7 (3.55)	-
5594.46		2.52	−0.050	20.0 (3.93)	9.2 (3.43)	-	-
5857.45		2.93	0.230	-	-	-	16.6 (3.86)
6102.72		1.88	−0.890	-	8.0 (3.44)	-	-
6122.22		1.89	−0.409	23.3 (3.68)	22.4 (3.53)	23.3 (3.52)	-
6162.17		1.90	0.100	36.4 (3.50)	24.0 (3.08)	28.5 (3.15)	-
6439.07		2.53	0.470	28.9 (3.63)	23.2 (3.40)	19.1 (3.25)	-
4246.82	Sc II	0.32	0.320	100.6 (0.89)	68.7 (0.02)	77.2 (-0.03)	103.7 (0.39)
4320.73		0.61	−0.260	-	36.1 (-0.20)	41.6 (-0.23)	-
4400.39		0.61	−0.510	-	-	29.6 (-0.29)	-
4415.56		0.60	−0.640	54.2 (0.75)	-	31.8 (-0.12)	-
5031.02		1.36	−0.260	-	-	12.2 (-0.26)	-
5657.90		1.51	−0.500	-	-	11.8 (0.07)	-
4533.24	Ti I	0.85	0.476	-	14.5 (1.86)	-	-
4981.73		0.85	0.504	24.2 (2.31)	16.3 (1.85)	17.2 (1.85)	-
4991.06		0.84	0.380	13.9 (2.11)	12.1 (1.79)	17.0 (1.95)	-
4999.50		0.83	0.250	-	-	12.9 (1.92)	-
5007.21		0.82	0.112	17.6 (2.48)	14.0 (2.11)	11.0 (1.96)	-
5192.97		0.02	−1.006	-	13.1 (2.23)	-	24.2 (2.48)
5210.39		0.05	−0.884	10.7 (2.36)	-	-	-
4028.34	Ti II	1.89	−1.000	-	11.9 (1.73)	-	-
4290.22		1.16	−1.120	63.8 (2.54)	54.7 (2.33)	47.8 (1.85)	-
4300.05		1.18	−0.770	-	46.8 (1.72)	-	-

In columns 5 to 8, the numbers within bracket '()' indicate the abundances derived from the corresponding line.

TABLE 3.13: *–continued*

Wavelength (Å)	Element	E_{low} (eV)	log gf	HE 1005–1439	HE 0401–0138	HE 1246–1344	HE 1153–0518
4312.86		1.18	−1.160	-	47.5 (2.12)	-	-
4395.03		1.08	−0.660	75.7 (2.33)	61.8 (2.01)	74.9 (2.13)	-
4417.72		1.16	−1.430	-	-	46.6 (2.09)	-
4443.79		1.08	−0.700	-	65.3 (2.16)	74.1 (2.12)	94.9 (2.40)
4444.56		1.12	−2.030	-	9.5 (1.67)	-	-
4450.48		1.08	−1.450	29.8 (1.93)	37.9 (1.96)	37.4 (1.78)	-
4468.51		1.13	−0.600	72.3 (2.19)	-	70.4 (1.94)	-
4470.86		1.16	−2.280	-	9.5 (1.96)	-	-
4501.27		1.12	−0.750	-	62.8 (2.14)	63.6 (1.83)	-
4533.97		1.24	−0.770	-	-	59.0 (1.85)	-
4563.76		1.22	−0.960	61.8 (2.33)	42.9 (1.76)	57.3 (1.94)	-
4571.97		1.57	−0.530	-	-	51.5 (1.77)	-
4589.96		1.24	−1.790	-	-	23.0 (1.92)	-
4779.98		2.05	−1.370	-	-	-	35.1 (2.50)
4805.09		2.06	−1.100	17.7 (2.31)	-	12.7 (1.84)	-
4865.61		1.12	−2.610	-	-	-	18.3 (2.17)
5129.15		1.89	−1.390	-	15.6 (2.12)	-	-
5185.91		1.89	−1.350	-	11.7 (1.92)	-	-
5188.68		1.58	−1.210	31.0 (2.21)	-	28.9 (1.82)	-
5226.54		1.57	−1.300	19.5 (2.00)	-	29.2 (1.89)	51.8 (2.11)
4254.34	Cr I	0.00	−0.114	73.4 (2.60)	52.7 (1.97)	56.1 (1.89)	-
4274.80		0.00	−0.231	76.3 (2.80)	-	54.5 (1.94)	-
4289.72		0.00	−0.361	-	49.7 (2.09)	55.2 (2.10)	-
5204.51		0.94	−0.208	39.4 (2.66)	-	-	-
5206.04		0.94	0.019	39.9 (2.44)	-	32.1 (2.01)	61.4 (0.94)
5208.43		0.94	0.158	46.7 (2.46)	-	-	-
4030.75	Mn I	0.00	−0.470	80.3 (2.61)	33.4 (0.98)	-	-
4033.06		0.00	−0.618	71.0 (2.43)	44.0 (1.50)	38.1 (1.18)	-
4034.48		0.00	−0.811	-	-	27.0 (1.06)	-
4092.38	Co I	0.92	−0.940	14.9 (2.23)	-	-	-
4118.77		1.05	−0.490	25.7 (2.24)	-	16.1 (1.67)	-
4121.31		0.92	−0.320	33.3 (2.12)	28.8 (1.80)	-	-
4714.41	Ni I	3.38	0.260	-	-	5.7 (2.86)	-
5476.90		1.83	−0.890	33.6 (3.42)	23.6 (2.94)	20.7 (2.80)	42.2 (3.24)
4077.71	Sr II	0.00	0.167	96.7 (−0.05)	73.0 (-0.53)	58.5 (-1.56)	-
4215.52		0.00	−0.145	98.9 (0.26)	73.8 (-0.26)	46.4 (-1.78)	-
4177.53	Y II	0.41	−0.160	-	21.8 (-1.03)	-	-
4883.68		1.08	0.070	15.6 (−0.55)	-	-	-
4900.12		1.03	−0.090	13.3 (−0.53)	-	-	22.5 (–0.88)
5087.42		1.08	−0.170	22.8 (−0.10)	-	-	-
5350.09	Zr II	1.83	−1.240	-	-	-	5.2 (0.87)

TABLE 3.13: *–continued*

Wavelength (Å)	Element	E_{low} (eV)	log gf	HE 1005–1439	HE 0401–0138	HE 1246–1344	HE 1153–0518
5350.37		1.77	−1.276	-	-	-	7.8 (1.02)
4554.03	Ba II	0.00	0.170	-	-	15.3 (-2.85)	114.8 (–0.22)
4934.08		0.00	−0.150	-	43.5 (-1.39)	8.7 (-2.89)	103.9 (–0.38)
5853.67		0.60	−1.000	52.5 (0.37)	-	-	-
6141.71		0.70	−0.076	89.2 (0.65)	26.2 (-1.43)	-	85.4 (–0.52)
6496.90		0.60	−0.377	93.5 (0.90)	24.8 (-1.32)	-	-
4086.71	La II	0.00	−0.150	31.6 (−0.69)	-	-	-
4123.22		0.32	0.120	31.1 (−0.62)	-	-	-
4921.78		0.24	−0.680	15.7 (−0.46)	-	-	-
4137.65	Ce II	0.52	0.246	14.3 (−0.26)	-	-	-
4486.91		0.30	−0.474	11.5 (0.05)	-	-	-
4562.36		0.48	0.081	20.5 (0.02)	-	-	-
4179.39	Pr II	0.20	0.310	16.4 (−0.74)	-	-	-
4061.08	Nd II	0.47	0.550	31.2 (−0.30)	-	-	-
4109.07		0.06	0.280	31.6 (−0.49)	-	-	-
4156.08		0.18	0.200	25.0 (−0.46)	-	-	-
4451.56		0.38	−0.040	20.5 (−0.17)	-	-	-
4129.73	Eu II	0.00	0.204	7.3 (−2.18)	-	-	-
4205.04		0.00	0.117	10.4 (−1.92)	-	-	-
3944.68	Dy II	0.00	0.030	8.3 (−1.41)	-	-	-
4000.45		0.10	0.009	12.3 (−1.08)	-	-	-
4077.97		0.10	−0.058	6.4 (−1.36)	-	-	-
3896.23	Er II	0.05	−0.243	12.0 (−0.99)	-	-	-
3906.31		0.00	−0.052	12.1 (−1.24)	-	-	-
3793.38	Hf II	0.38	−0.950	6.7 (−0.72)	-	-	-
3918.09		0.45	−1.010	5.0 (−0.74)	-	-	-

TABLE 3.14: **Equivalent widths (in mÅ) of lines used for calculation of elemental abundances.**

Wavelength (Å)	Element	E_{low} (eV)	log gf	HD 147609	HD 154276	HD 87853	HE 0308–1612
5682.63	Na I	2.10	-0.700	66.2 (6.13)	83.5 (6.23)	-	-
5688.20		2.10	-0.450	98.2 (6.39)	-	-	-
6154.23		2.10	-1.560	-	27.4 (6.13)	-	-
6160.75		2.10	-1.260	-	47.9 (6.22)	-	-
4571.10	Mg I	0.00	-5.691	-	108.9 (7.88)	-	-
4702.99		4.35	-0.666	156.2 (7.56)	-	142.2 (7.55)	177.7 (7.22)
4730.03		4.35	-2.523	32.3 (7.48)	60.2 (7.80)	-	-
5528.40		4.35	-0.620	153.3 (7.53)	-	-	190.6 (7.23)
5711.09		4.35	-1.833	68.1 (7.38)	101.4 (7.76)	-	-
6696.02	Al I	3.14	-1.347	-	36.2 (6.29)	-	-
6698.67		3.14	-1.647	-	18.4 (6.17)	-	-
5645.61	Si I	4.93	-2.140	20.5 (7.37)	30.8 (7.52)	-	-
5665.56		4.92	-2.040	26.7 (7.41)	35.6 (7.51)	-	-
5690.43		4.93	-1.870	29.2 (7.30)	43.5 (7.50)	-	-
5793.07		4.93	-2.060	-	39.6 (7.62)	-	-
5948.54		5.08	-1.230	63.9 (7.41)	74.9 (7.54)	-	-
4098.53	Ca I	2.53	-0.540	-	-	44.9 (5.60)	-
4283.01		1.89	-0.224	-	-	107.6 (6.09)	-
4318.65		1.90	-0.208	105.4 (6.02)	116.3 (5.91)	-	-
4425.44		1.88	-0.385	113.0 (6.33)	-	98.5 (5.99)	-
4435.68		1.89	-0.500	-	123.6 (6.27)	-	-
4455.89		1.90	-0.510	-	137.6 (6.43)	93.9 (6.02)	-
4456.62		1.90	-1.660	51.6 (6.32)	68.6 (6.53)	-	-
4526.93		2.71	-0.430	51.6 (5.78)	77.4 (6.10)	-	-
4578.55		2.52	-0.560	61.7 (5.94)	71.0 (5.99)	-	-
4585.86		2.53	-0.160	98.6 (6.28)	132.1 (6.45)	-	-
5260.39		2.52	-1.900	-	26.9 (6.38)	-	-
5261.70		2.52	-0.730	-	-	-	110.8 (6.02)
5512.98		2.93	-0.290	52.0 (5.82)	76.7 (6.13)	41.3 (5.59)	-
5581.97		2.52	-0.710	68.9 (6.20)	85.8 (6.39)	53.6 (5.87)	-
5588.75		2.53	0.210	121.1 (6.29)	133.6 (6.10)	104.7 (6.01)	-
5590.11		2.52	-0.710	64.7 (6.11)	86.7 (6.40)	-	107.4 (5.87)
5594.46		2.52	-0.050	-	130.4 (6.31)	105.7 (6.28)	-
5601.28		2.53	-0.690	-	89.3 (6.42)	-	-
5857.45		2.93	0.230	104.1 (6.28)	114.8 (6.15)	-	-
6102.72		1.88	-0.890	89.0 (6.19)	-	-	-
6122.22		1.89	-0.409	-	158.6 (6.42)	-	-
6161.30		2.52	-1.020	33.7 (5.84)	53.7 (6.05)	-	-
6162.17		1.90	0.100	142.1 (6.20)	175.5 (6.04)	121.9 (5.89)	-

In columns 5 to 8, the numbers within bracket '()' indicate the abundances derived from the corresponding line.

TABLE 3.14: *–continued*

Wavelength (Å)	Element	E_{low} (eV)	log gf	HD 147609	HD 154276	HD 87853	HE 0308–1612
6166.44		2.52	-0.900	36.1 (5.76)	62.2 (6.10)	-	-
6169.04		2.52	-0.550	57.9 (5.82)	82.1 (6.14)	-	-
6169.56		2.53	-0.270	73.9 (5.84)	98.3 (6.12)	-	-
6439.07		2.53	0.470	129.3 (6.13)	144.6 (5.90)	116.1 (5.95)	-
6449.81		2.52	-0.550	-	-	52.4 (5.67)	-
6455.60		2.52	-1.350	-	51.0 (6.31)	-	-
6471.66		2.53	-0.590	60.4 (5.90)	84.5 (6.21)	60.1 (5.86)	133.5 (6.11)
6493.78		2.52	0.140	101.4 (5.94)	115.5 (5.92)	-	156.8 (5.73)
6499.65		2.52	-0.590	55.9 (5.80)	79.7 (6.11)	-	138.0 (6.17)
6717.68		2.71	-0.610	-	101.9 (6.64)	-	-
6245.64	Sc II	1.51	-0.980	-	-	-	98.0 (2.95)
4417.27	Ti I	1.89	-0.020	-	39.0 (4.97)	-	-
4449.14		1.89	0.500	-	51.6 (4.76)	-	-
4453.31		1.43	-0.051	35.2 (4.76)	59.9 (5.10)	-	-
4453.70		1.87	-0.010	-	36.5 (4.88)	-	-
4465.81		1.74	-0.163	-	37.0 (4.91)	-	-
4471.24		1.73	-0.103	-	42.1 (4.97)	-	-
4480.59		1.74	-0.847	-	32.5 (5.49)	-	-
4512.73		0.84	-0.480	39.3 (4.74)	65.7 (5.11)	-	-
4518.02		0.83	-0.325	41.2 (4.61)	69.6 (5.05)	-	-
4527.30		0.81	-0.470	-	76.9 (5.37)	-	-
4534.78		0.84	0.280	72.8 (4.63)	92.3 (5.00)	-	-
4548.76		0.83	-0.354	36.7 (4.55)	68.7 (5.05)	-	-
4617.27		1.75	0.389	37.5 (4.64)	61.4 (4.98)	26.5 (4.34)	106.3 (4.53)
4656.47		0.00	-1.345	30.8 (4.68)	67.2 (5.18)	-	123.7 (4.34)
4681.91		0.05	-1.071	-	75.0 (5.16)	-	-
4742.79		2.24	0.210	-	28.7 (4.79)	-	-
4758.12		2.25	0.425	20.0 (4.64)	39.3 (4.85)	-	-
4759.27		2.26	0.514	24.3 (4.67)	47.7 (4.96)	-	-
4778.26		2.24	-0.220	-	-	-	52.9 (4.49)
4805.41		2.35	0.150	-	29.8 (4.98)	-	-
4820.41		1.50	-0.441	-	41.9 (5.05)	-	-
4840.87		0.90	-0.509	-	57.9 (4.94)	-	-
4870.13		2.25	0.340	-	48.4 (5.14)	-	-
5064.65		0.05	-0.991	-	-	-	167.0 (4.74)
5210.39		0.05	-0.884	52.3 (4.62)	85.5 (5.14)	-	169.5 (4.60)
5512.52		1.46	-0.350	-	48.7 (5.03)	-	-
5866.45		1.07	-0.840	-	45.2 (5.03)	-	-
5978.54		1.87	-0.496	-	15.8 (4.72)	-	-
6126.22		1.07	-1.425	-	21.4 (5.02)	-	-
4161.53	Ti II	1.08	-2.360	-	-	69.2 (4.35)	-

TABLE 3.14: *–continued*

Wavelength (Å)	Element	E_{low} (eV)	log gf	HD 147609	HD 154276	HD 87853	HE 0308–1612
4394.05		1.22	-1.590	-	88.1 (5.26)	-	-
4395.85		1.24	-2.170	-	65.7 (5.27)	-	-
4417.72		1.17	-1.430	-	-	103.7 (4.26)	-
4418.33		1.24	-2.460	-	-	65.1 (4.47)	-
4421.94		2.06	-1.770	56.8 (4.81)	-	-	-
4443.79		1.08	-0.700	142.3 (4.76)	133.8 (4.97)	-	-
4464.45		1.16	-2.080	83.0 (4.86)	-	-	-
4468.51		1.13	-0.600	-	133.4 (4.90)	-	-
4470.86		1.17	-2.280	65.0 (4.66)	67.7 (5.34)	-	-
4493.51		1.08	-2.730	33.6 (4.44)	33.6 (4.78)	-	-
4533.97		1.24	-0.770	-	131.6 (5.14)	-	-
4563.76		1.22	-0.960	-	130.2 (5.28)	127.9 (4.40)	-
4568.31		1.22	-2.650	-	32.2 (4.80)	-	-
4571.97		1.57	-0.530	-	140.8 (5.29)	-	-
4583.41		1.17	-2.720	-	33.1 (4.83)	-	-
4708.66		1.24	-2.210	-	53.3 (4.91)	-	-
4764.53		1.24	-2.770	-	34.4 (4.98)	-	-
4779.98		2.05	-1.370	72.2 (4.67)	67.5 (5.22)	-	-
4798.52		1.08	-2.430	-	43.6 (4.71)	-	-
4805.09		2.06	-1.100	-	-	81.2 (4.16)	-
5226.54		1.57	-1.300	-	-	-	125.4 (4.52)
5336.77		1.58	-1.700	-	76.3 (5.27)	-	-
5381.02		1.57	-2.080	64.2 (4.73)	59.9 (5.21)	-	-
5418.75		1.58	-1.999	50.8 (4.42)	52.7 (4.95)	-	-
4274.80	Cr I	0.00	-0.231	149.5 (5.38)	-	-	-
4289.72		0.00	-0.361	-	164.8 (5.04)	-	-
4351.05		0.97	-1.449	-	75.8 (5.74)	-	-
4600.75		1.00	-1.260	54.6 (5.16)	74.2 (5.50)	44.1 (4.87)	-
4616.12		0.98	-1.190	66.6 (5.31)	81.8 (5.59)	47.4 (4.84)	-
4626.17		0.97	-1.320	47.7 (5.05)	73.9 (5.50)	36.1 (4.74)	100.2 (4.29)
4652.16		1.00	-1.030	74.3 (5.34)	88.8 (5.60)	52.7 (4.80)	-
4737.35		3.09	-0.099	-	41.5 (5.41)	-	-
5206.04		0.94	0.019	135.8 (5.53)	163.0 (5.34)	-	-
5247.56		0.96	-1.640	39.1 (5.16)	69.9 (5.62)	-	111.6 (4.66)
5345.80		1.00	-0.980	82.0 (5.39)	95.1 (5.56)	57.9 (4.80)	-
5348.31		1.00	-1.290	61.0 (5.25)	88.2 (5.73)	-	125.3 (4.63)
4588.20	Cr II	4.07	-0.630	92.5 (5.42)	64.0 (5.49)	-	-
4592.05		4.07	-1.220	59.5 (5.24)	41.6 (5.46)	-	-
4634.07		4.07	-1.240	-	-	55.3 (4.77)	-
4812.34		3.86	-1.800	39.4 (5.22)	29.1 (5.49)	-	-
4451.59	Mn I	2.89	0.278	-	75.6 (5.17)	-	-

TABLE 3.14: *–continued*

Wavelength (Å)	Element	E_{low} (eV)	log gf	HD 147609	HD 154276	HD 87853	HE 0308–1612
4470.14		2.94	-0.444	-	38.5 (5.00)	-	-
4634.07		4.07	-1.240	-	47.5 (5.65)	-	-
4739.09		2.94	-0.490	-	40.5 (5.08)	-	94.6 (5.10)
4761.51		2.95	-0.138	-	55.0 (5.10)	-	-
4765.85		2.94	-0.080	-	62.9 (5.23)	-	-
4766.42		2.92	0.100	-	79.6 (5.42)	-	109.9 (4.84)
4783.43		2.30	0.042	-	-	-	157.8 (5.04)
4848.23		3.86	-1.140	-	53.8 (5.53)	-	-
4121.31	Co I	0.92	-0.320	-	-	79.9 (4.30)	-
4749.67		3.05	-0.321	-	28.9 (4.92)	-	-
4792.85		3.25	-0.067	-	25.9 (4.77)	-	-
4470.47	Ni I	3.40	-0.310	51.8 (5.72)	70.0 (6.11)	44.1 (5.49)	-
4714.41		3.38	0.260	88.8 (5.95)	106.0 (6.12)	72.3 (5.48)	-
4732.46		4.11	-0.550	27.4 (6.05)	34.3 (6.08)	-	-
4821.12		4.15	-0.850	-	30.5 (6.33)	-	-
4852.55		3.54	-1.070	-	35.4 (6.11)	-	-
4855.41		3.54	0.000	-	-	40.0 (5.21)	-
4937.34		3.61	-0.390	47.6 (5.88)	66.0 (6.24)	31.8 (5.49)	95.2 (5.86)
4953.20		3.74	-0.580	24.0 (5.68)	43.6 (6.01)	-	-
4980.17		3.61	0.070	72.1 (5.92)	87.7 (6.19)	54.8 (5.49)	111.3 (5.77)
5035.36		3.63	0.290	75.2 (5.80)	84.5 (5.95)	55.4 (5.30)	-
5081.11		3.85	0.300	70.0 (5.85)	78.8 (6.00)	-	-
5082.34		3.66	-0.540	42.9 (5.97)	52.8 (6.11)	-	-
5084.09		3.68	0.030	58.4 (5.73)	76.6 (6.09)	48.2 (5.46)	-
5099.93		3.68	-0.100	57.7 (5.84)	71.0 (6.10)	51.3 (5.65)	-
5102.96		1.68	-2.620	-	38.6 (5.93)	-	-
6086.28		4.27	-0.530	21.6 (6.00)	31.8 (6.11)	-	-
6111.07		4.09	-0.870	-	25.8 (6.13)	-	46.6 (5.73)
6176.81		4.09	-0.260	37.9 (5.94)	52.2 (6.16)	-	73.5 (5.68)
6186.71		4.11	-0.960	-	22.3 (6.14)	-	-
6643.63		1.68	-2.300	48.1 (5.98)	83.9 (6.60)	-	147.9 (6.01)
4722.15	Zn I	4.03	-0.338	65.7 (4.35)	65.3 (4.65)	42.3 (3.74)	-
4810.53		4.08	-0.137	68.5 (4.25)	72.2 (4.64)	51.9 (3.76)	-
4607.33	Sr I	0.00	-0.570	-	-	-	95.0 (3.24)
4883.68	Y II	1.08	0.070	119.5 (3.12)	50.7 (2.10)	53.2 (1.06)	152.9 (2.74)
4854.86		0.99	-0.380	-	-	30.3 (0.98)	-
5087.42		1.08	-0.170	104.8 (2.97)	41.4 (2.01)	35.9 (0.96)	128.0 (2.52)
5119.11		0.99	-1.360	56.5 (2.92)	-	-	-
5205.72		1.03	-0.340	113.6 (3.28)	43.1 (2.17)	-	-
5289.81		1.03	-1.850	27.9 (2.85)	-	-	67.0 (2.61)
5544.61		1.74	-1.090	37.8 (2.93)	-	-	-

TABLE 3.14: *–continued*

Wavelength (Å)	Element	E_{low} (eV)	log gf	HD 147609	HD 154276	HD 87853	HE 0308–1612
5546.01		1.75	-1.100	41.5 (3.02)	-	-	-
5662.93		1.94	0.160	84.6 (2.87)	40.6 (2.45)	-	103.0 (2.59)
6613.73		1.75	-1.110	45.7 (3.06)	-	-	-
4418.78	Ce II	0.86	0.177	60.1 (2.59)	-	-	-
4427.92		0.54	-0.460	36.1 (2.38)	-	-	-
4560.28		0.91	0.000	53.5 (2.62)	-	-	-
4562.36		0.48	0.081	69.2 (2.53)	19.2 (1.63)	-	-
4628.16		0.52	0.008	69.7 (2.64)	-	-	-
4747.17		0.32	-1.246	20.2 (2.56)	-	-	-
4773.94		0.92	-0.498	22.9 (2.43)	-	-	-
4874.00		1.11	-0.892	-	-	-	57.6 (2.63)
5274.23		1.04	-0.323	-	-	-	83.7 (2.59)
5330.56		0.87	-0.760	27.8 (2.73)	-	-	71.1 (2.47)
5292.62	Pr II	0.65	-0.300	19.6 (1.79)	-	-	-
4446.38	Nd II	0.20	-0.590	44.9 (2.24)	-	-	-
4451.56		0.38	-0.040	-	-	56.5 (1.63)	-
4811.34		0.06	-1.140	36.5 (2.44)	-	-	-
5130.59		1.30	0.570	41.6 (1.95)	-	-	-
4947.02		0.56	-1.250	-	-	-	61.1 (2.15)
4961.39		0.63	-0.710	-	-	-	97.2 (2.66)
4989.95		0.63	-0.500	32.7 (2.22)	-	-	-
5212.36		0.20	-0.870	23.3 (1.97)	-	-	112.8 (2.57)
5276.87		0.86	-0.440	-	-	-	81.4 (2.19)
5287.13		0.74	-1.300	-	-	-	67.3 (2.53)
5293.16		0.82	-0.060	53.8 (2.38)	-	-	116.0 (2.62)
5311.45		0.99	-0.420	-	-	-	84.0 (2.39)
5319.81		0.55	-0.210	52.3 (2.23)	-	-	110.4 (2.27)
5371.93		1.41	0.003	24.9 (2.24)	-	-	-
5718.12		1.41	-0.340	-	-	-	71.9 (2.49)
5825.86		1.08	-0.760	-	-	-	64.9 (2.31)
4424.34	Sm II	0.48	-0.260	43.0 (1.79)	-	-	-
4434.32		0.38	-0.576	42.2 (1.99)	-	-	-
4519.63		0.54	-0.751	22.7 (1.86)	-	-	-
4674.59		0.18	-1.055	-	-	-	72.5 (1.58)
4791.58		0.10	-1.846	-	-	-	54.4 (1.78)
4205.04	Eu II	0.00	0.117	-	-	52.3 (0.13)	-

TABLE 3.15: **Lines (in Å) used for spectrum synthesis calculations.**

Star Name	Sc II	V I	Mn	Sr I	Zr II	Ba II	La II	Eu II
BD+75 348	5526.790[a]	5727.652[a]	Mn I 4754.042[a]	-	-	5853.668[c]	4921.776[d]	6645.064[e]
	5641.001[a]	-	Mn I 4762.367[a]	-	-	6141.713[c]	-	-
	5657.896[a]	-	Mn I 4823.524[a]	-	-	-	-	-
	5667.149[a]	-	-	-	-	-	-	-
BD+09 3019	5641.001[a]	5727.652[a]	Mn I 4754.042[a]	-	-	-	4921.776[c]	6645.064[e]
	5657.896[a]	-	-	-	-	-	-	-
CD–27 14351	-	-	-	-	-	5853.668[c]	4921.776[c]	6645.064[c]
	-	-	-	-	-	6141.713[c]	-	-
HD 87853	5031.021[g]	-	Mn I 4041.355[g]	-	-	5853.668[c]	-	-
HD 145777	6245.637[f]	-	Mn II 5432.543[g]	-	-	5853.66[c]8	4921.776[c]	6645.064[c]
	-	-	-	-	-	6141.713[c]	-	-
HD 147609	5526.790[g]	4379.230[g]	Mn I 4766.418[g]	4607.327[g]	4208.977[g]	5853.668[c]	4322.503[a]	4129.725[c]
HD 154276	5526.790[g]	4406.633[g]	-	4607.327[g]	4208.977[g]	5853.668[c]	4921.776[c]	-
	-	-	-	-	-	6141.713[c]	-	-

References: a- *linemake*, b- , c- McWilliam (1998), d- Jonsell *et al.* (2006), e- Worley *et al.* (2013), f- Prochaska and McWilliam (2000), g- Kurucz database of atomic line-list

Table 3.15: *–continued*

Star Name	Sc II	V I	Mn	Sr I	Ba II	La II	Eu II
HD 238020	4415.557[a]	5727.652[a]	Mn I 4754.042[a]	-	6141.713[c]	4921.776[d]	-
	5031.021[a]	-	Mn I 4762.367[a]	-	-	-	-
	5526.790[a]	-	Mn I 4823.524[a]	-	-	-	-
	5641.001[a]	-	-	-	-	-	-
	5657.896[a]	-	-	-	-	-	-
	5667.149[a]	-	-	-	-	-	-
HE 0017+0055	-	-	-	-	5853.668[c]	4921.776[d]	6645.064[e]
	-	-	-	-	-	4808.996[a]	-
HE 0308–1612	6245.637[f]	5727.048[f]	-	4607.327[g]	5853.668[c]	4921.776[d]	6645.064[e]
	-	5727.652[f]	-	-	-	-	-
	-	5737.059[f]	-	-	-	-	-
HE 0319–0215	-	-	-	-	5853.668[c]	-	6645.064[e]
	-	-	-	-	6141.713[c]	-	-
HE 0507–1653	5641.001[a]	-	Mn I 4754.042[a]	-	6141.713[c]	4921.776[d]	6437.640[e]
	5657.896[a]	-	-	-	6496.897[c]	-	6645.064[e]
HE 0930–0018	-	5727.652[a]	Mn I 4762.042[a]	-	5853.667[c]	4921.776[d]	-
	-	-	-	-	6141.713[c]	-	-

Table 3.15: *–continued*

Star Name	Sc II	Mn	Ba II	La II	Ce II	Pr II	Nd II	Sm II	Eu II
HE 1005–1439	4246.822[a]	Mn I 4030.753[a]	5853.668[c]	4086.71[a]	-	-	-	-	4129.725[a]
	4415.557[a]	Mn I 4033.062[a]	6141.713[c]	4123.218[a]	-	-	-	-	4205.042[a]
	-	-	6496.897[c]	4921.776[d]	-	-	-	-	-
HE 1023–1504	-	-	5853.668[c]	-	-	-	-	-	6645.064[c]
HE 2144–1832	-	Mn I 4765.846[g]	5853.668[c]	4921.776[d]	-	-	-	-	6645.064[c]
	-	Mn I 4766.418[g]	-	-	-	-	-	-	-
HE 2339–0837	-	-	5853.668[c]	4921.776[d]	-	-	-	-	6645.064[c]
	-	-	6141.713[c]	-	-	-	-	-	-
HE 0401–0138	4246.822[a]	Mn I 4030.753[a]	6141.713[c]	4921.776[d]	4186.594[a]	4179.395[a]	4156.078[a]	4424.337[a]	4129.725[a]
	4320.732[a]	Mn I 4033.062[a]	6496.897[c]	4123.218[a]	4460.207[a]	4222.093[a]	4303.570[a]	-	4205.042[a]
HE 1153–0518	4246.822[a]	-	4554.054[a]	4921.776[d]	-	-	-	-	-
	-	-	5853.668[c]	-	-	-	-	-	-
	-	-	6141.713[c]	-	-	-	-	-	-
HE 1246–1344	4246.822[a]	Mn I 4033.062[a]	4554.054[a]	4921.776[d]	4186.594[a]	4179.395[a]	4156.078[a]	4318.930[a]	4129.725[c]
	4320.732[a]	Mn I 4766.418[a]	-	4123.218[a]	-	4222.093[a]	4303.570[a]	4424.337[a]	4205.042[c]
	-	-	-	-	-	-	-	4467.320[a]	-

TABLE 3.16: **Differential abundance ($\Delta\log\epsilon$) of different species due to the variations in stellar atmospheric parameters for HE 1005–1439.**

Element	ΔT_{eff} (+100 K)	ΔT_{eff} (−100 K)	$\Delta\log g$ (+0.2 dex)	$\Delta\log g$ (−0.2 dex)	$\Delta\zeta$ (+0.2 kms^{-1})	$\Delta\zeta$ (−0.2 kms^{-1})	Δ[Fe/H] (+0.2 dex)	Δ[Fe/H] (−0.2 dex)	$\sigma\log\epsilon$ (+Δ)	$\sigma\log\epsilon$ (−Δ)	σ[X/Fe] (+Δ)	σ[X/Fe] (−Δ)
C (CH, 4310 Å)	0.08	-0.10	0.00	0.00	0.00	0.00	-0.05	0.05	0.22	0.23	0.27	0.27
C (C_2, 5165 Å)	0.15	-0.15	-0.02	0.05	0.00	0.00	0.00	-0.02	0.21	0.22	0.26	0.27
C (C_2, 5635 Å)	0.15	-0.15	-0.03	0.02	0.00	0.00	0.00	0.00	0.21	0.21	0.26	0.26
Na I	0.10	-0.12	-0.06	0.04	-0.10	0.07	-0.02	0.07	0.16	0.16	0.22	0.22
Mg I	0.09	-0.09	-0.03	0.03	-0.06	0.06	-0.01	0.06	0.12	0.12	0.19	0.19
Ca I	0.07	-0.07	-0.01	0.02	-0.02	0.02	0.00	0.05	0.09	0.10	0.18	0.18
Sc II	0.06	-0.06	0.05	-0.05	-0.12	0.13	-0.01	0.06	0.16	0.17	0.22	0.23
Sc II*	0.06	-0.06	0.05	-0.05	-0.12	0.13	-0.01	0.06	0.14	0.16	0.22	0.23
Ti I	0.11	-0.11	-0.01	0.01	-0.01	0.01	-0.01	0.04	0.14	0.14	0.21	0.21
Ti II	0.04	-0.04	0.05	-0.06	-0.06	0.08	-0.01	0.04	0.11	0.13	0.19	0.20
Cr I	0.11	-0.11	-0.02	0.02	-0.09	0.10	-0.01	0.06	0.16	0.17	0.22	0.23
Mn I	0.12	0.12	-0.03	0.03	-0.18	0.19	-0.01	0.08	0.24	0.25	0.28	0.30
Mn I*	0.12	-0.12	-0.03	0.03	-0.18	0.19	-0.01	0.08	0.22	0.24	0.27	0.28
Fe I	0.12	-0.12	0.01	0.01	-0.05	0.06	-	-	0.13	0.14	-	-
Fe II	-0.03	0.04	0.08	-0.08	-0.03	0.04	-	-	0.09	0.10	-	-
Co I	0.12	-0.12	-0.01	0.01	-0.02	0.02	-0.01	0.04	0.13	0.13	0.20	0.20
Ni I	0.10	-0.11	-0.01	0.00	-0.03	0.03	-0.01	0.04	0.23	0.23	0.27	0.28

* abundance is derived using spectrum synthesis calculations.

TABLE 3.16: *–continued*

Element	ΔT_{eff} (+100 K)	ΔT_{eff} (−100 K)	Δlog g (+0.2 dex)	Δlog g (−0.2 dex)	$\Delta\zeta$ (+0.2 kms^{-1})	$\Delta\zeta$ (−0.2 kms^{-1})	Δ[Fe/H] (+0.2 dex)	Δ[Fe/H] (−0.2 dex)	σlog ϵ (+Δ)	σlog ϵ (−Δ)	σ[X/Fe] (+Δ)	σ[X/Fe] (−Δ)
Sr II	0.08	-0.08	0.03	-0.03	-0.20	0.18	-0.01	0.08	0.27	0.26	0.31	0.30
Y II	0.05	-0.06	0.06	-0.06	-0.02	0.01	-0.01	0.02	0.18	0.18	0.23	0.23
Ba II	0.08	-0.09	0.04	-0.06	-0.19	0.21	-0.01	0.07	0.26	0.29	0.30	0.32
Ba II*	0.08	-0.09	0.04	-0.06	-0.19	0.21	-0.01	0.07	0.25	0.28	0.29	0.32
La II	0.07	-0.07	0.06	-0.06	-0.03	0.05	0.00	0.03	0.12	0.13	0.19	0.20
La II*	0.07	-0.07	0.06	-0.06	-0.03	0.05	0.00	0.03	0.10	0.11	0.18	0.19
Ce II	0.08	-0.07	0.06	-0.05	-0.01	0.02	0.00	0.03	0.14	0.13	0.21	0.20
Pr II	0.08	-0.07	0.06	-0.05	-0.01	0.02	0.00	0.03	0.22	0.22	0.27	0.27
Nd II	0.08	-0.07	0.06	-0.05	-0.03	0.05	0.00	0.03	0.13	0.13	0.20	0.20
Eu II	0.07	-0.07	0.06	-0.06	-0.01	0.01	-0.01	0.03	0.17	0.16	0.22	0.22
Dy II	0.07	-0.08	0.05	-0.06	-0.01	0.01	-0.01	0.02	0.14	0.15	0.21	0.21
Er II	0.07	-0.07	0.05	-0.06	-0.01	0.01	-0.01	0.02	0.17	0.17	0.22	0.23
Hf II	0.07	-0.06	0.06	-0.05	0.00	0.01	0.00	0.03	0.16	0.15	0.18	0.18
Pb II	0.05	-0.02	0.02	-0.02	0.00	0.00	0.00	0.00	0.11	0.10	0.19	0.18

TABLE 3.17: **Differential abundance ($\Delta\log\epsilon$) of different species due to the variations in stellar atmospheric parameters for HE 2144−1832.**

Element	ΔT_{eff} (+100 K)	ΔT_{eff} (−100 K)	Δlog g (+0.2 dex)	Δlog g (−0.2 dex)	$\Delta\zeta$ (+0.2 kms^{-1})	$\Delta\zeta$ (−0.2 kms^{-1})	Δ[Fe/H] (+0.2 dex)	Δ[Fe/H] (−0.2 dex)	$(\Sigma\sigma_i^2)^{1/2}$ (+Δ)	$(\Sigma\sigma_i^2)^{1/2}$ (−Δ)	σ[X/Fe] (+Δ)	σ[X/Fe] (−Δ)
C (C_2, 5165 $\AA$)	-0.03	0.02	0.01	0.00	0.00	0.00	0.00	0.01	0.03	0.02	0.15	0.15
C (C_2, 5635 $\AA$)	-0.04	0.05	0.03	-0.02	0.00	0.00	-0.01	0.01	0.05	0.05	0.16	0.16
C (CH, 4310 $\AA$)	-0.04	0.04	0.01	0.00	0.00	0.00	-0.04	0.03	0.06	0.05	0.16	0.16
N	0.10	-0.10	-0.15	0.13	0.00	0.00	0.00	0.00	0.18	0.16	0.23	0.22
Na I	0.10	-0.10	-0.03	0.03	-0.04	0.04	-0.04	0.04	0.12	0.12	0.20	0.20
Mg I	0.09	-0.08	-0.04	0.03	-0.09	0.08	-0.03	0.03	0.14	0.12	0.22	0.21
Ca I	0.16	-0.16	-0.03	0.03	-0.10	0.11	-0.05	0.05	0.20	0.20	0.25	0.26
Ti I	0.24	-0.22	-0.01	0.02	-0.06	0.08	-0.03	0.05	0.25	0.24	0.30	0.29
Ti II	-0.03	0.04	0.05	-0.03	-0.09	0.12	0.03	-0.01	0.11	0.13	0.19	0.20
V I	0.22	-0.21	0.00	0.00	-0.03	0.03	-0.04	0.04	0.23	0.22	0.27	0.26
Cr I	0.23	-0.20	0.00	0.02	-0.14	0.18	-0.03	0.05	0.27	0.27	0.32	0.32
Mn I	0.15	-0.12	-0.02	0.04	0.02	-0.02	-0.04	0.05	0.16	0.14	0.22	0.20
Fe I	0.10	-0.10	0.10	-0.08	-0.12	0.14	0.20	-0.20	0.27	0.27	-	-
Fe II	-0.13	0.18	0.13	-0.09	-0.06	0.09	0.20	-0.20	0.28	0.30	-	-
Co I	0.10	-0.08	0.00	0.01	-0.02	0.02	0.00	0.01	0.10	0.08	0.18	0.17
Ni I	0.06	-0.04	0.00	0.01	-0.07	0.07	-0.01	0.01	0.09	0.08	0.19	0.19
Zn I	-0.09	0.10	0.03	-0.01	-0.06	0.06	0.01	0.00	0.11	0.12	0.19	0.19

TABLE 3.17: *–continued*

Element	ΔT_{eff} (+100 K)	ΔT_{eff} (−100 K)	Δlog g (+0.2 dex)	Δlog g (−0.2 dex)	$\Delta\zeta$ (+0.2 kms^{-1})	$\Delta\zeta$ (−0.2 kms^{-1})	Δ[Fe/H] (+0.2 dex)	Δ[Fe/H] (−0.2 dex)	$(\Sigma\sigma_i^2)^{1/2}$ (+Δ)	$(\Sigma\sigma_i^2)^{1/2}$ (−Δ)	σ[X/Fe] (+Δ)	σ[X/Fe] (−Δ)
Sr I	0.20	-0.20	0.00	0.00	-0.05	0.05	-0.03	0.03	0.21	0.21	0.26	0.26
Y II	-0.01	0.02	0.06	-0.05	-0.14	0.16	0.04	-0.03	0.16	0.17	0.22	0.23
Zr I	0.25	-0.24	-0.01	0.01	-0.04	0.05	-0.03	0.04	0.26	0.25	0.31	0.31
Ba II	0.01	-0.02	0.03	-0.03	-0.16	0.16	0.02	-0.03	0.16	0.17	0.22	0.22
La II	0.10	-0.05	0.10	-0.05	-0.15	0.25	0.00	0.00	0.21	0.26	0.25	0.30
Ce II	0.02	-0.02	0.04	-0.03	-0.12	0.15	0.02	-0.02	0.13	0.16	0.21	0.23
Pr II	0.03	-0.02	0.07	-0.07	-0.09	0.11	0.05	-0.04	0.13	0.14	0.22	0.22
Nd II	0.02	-0.02	0.06	-0.05	-0.13	0.16	0.03	-0.03	0.15	0.17	0.22	0.24
Sm II	0.04	-0.04	0.05	-0.05	-0.11	0.12	0.03	-0.03	0.13	0.14	0.23	0.24
Eu II	0.00	0.00	0.10	-0.05	0.00	0.02	0.05	-0.02	0.11	0.06	0.18	0.16

TABLE 3.18: **Elemental abundances in BD+75 348.**

Element	Z	solar $log\epsilon^a$	$log\epsilon$ (dex)	[X/H]	[X/Fe]
C (C_2, 5165 Å)	6	8.43	8.35 (syn)	−0.08	0.34
C (C_2, 5635 Å)	6	8.43	8.30 (syn)	−0.13	0.29
C (CH, 4310 Å)	6	8.43	8.30 (syn)	−0.13	0.29
N (CN, 4215 Å)	7	7.83	8.20 (syn)	0.37	0.79
Na I	11	6.24	6.28±0.12 (4)	0.04	0.46
Mg I	12	7.60	7.38±0.17 (4)	−0.22	0.20
Ca I	20	6.34	5.97±0.21 (16)	−0.37	0.05
Sc II*	21	3.15	2.71±0.09 (5)	−0.44	−0.02
Ti I	22	4.95	4.65±0.20 (13)	−0.30	0.12
Ti II	22	4.95	4.65±0.19 (10)	−0.30	0.12
V I*	23	3.93	3.12 (1)	−0.81	−0.39
Cr I	24	5.64	5.23±0.15 (7)	−0.41	0.01
Mn I*	25	5.43	4.58±0.02 (3)	−0.85	−0.43
Fe I	26	7.50	7.09±0.20 (85)	−0.41	-
Fe II	26	7.50	7.08±0.18 (12)	−0.42	-
Co I	27	4.99	4.49±0.10 (2)	−0.50	−0.08
Ni I	28	6.22	5.77±0.24 (12)	−0.45	−0.03
Cu I	29	4.19	3.66 (1)	−0.53	−0.11
Zn I	30	4.56	4.12 (1)	−0.44	−0.02
Y II	39	2.21	3.06±0.16 (10)	0.85	1.27
Zr I	40	2.58	3.16±0.08 (3)	0.58	1.00
Zr II	40	2.58	3.41±0.09 (3)	0.83	1.25
Ba II*	56	2.18	3.38±0.13 (2)	1.20	1.62
La II*	57	1.10	2.60 (1)	1.50	1.92
Ce II	58	1.58	2.97±0.20 (13)	1.39	1.81
Pr II	59	0.72	2.17±0.22 (5)	1.45	1.87
Nd II	60	1.42	2.63±0.18 (11)	1.21	1.63
Sm II	62	0.96	2.08±0.07 (3)	1.12	1.54
Eu II*	63	0.52	0.80 (1)	0.28	0.70
Dy II	66	1.10	1.49 (1)	0.39	0.81
Hf II	72	0.85	2.33 (1)	1.48	1.90

* abundance is derived using spectrum synthesis calculations. The number inside the parenthesis shows the number of lines used for the abundance determination.
(a) Asplund *et al.* (2009).

TABLE 3.19: **Elemental abundances in BD+09 3019.**

Element	Z	solar $log\epsilon^a$	$log\epsilon$ (dex)	[X/H]	[X/Fe]
C (C_2, 5165 Å)	6	8.43	8.70 (syn)	0.27	0.82
C (C_2, 5635 Å)	6	8.43	8.71 (syn)	0.28	0.83
C (CH, 4310 Å)	6	8.43	8.55 (syn)	0.12	0.67
Na I	11	6.24	5.95±0.20 (2)	−0.29	0.26
Mg I	12	7.60	8.31 (1)	0.71	1.26
Ca I	20	6.34	5.65±0.00 (2)	−0.69	−0.14
Sc II*	21	3.15	3.15±0.00 (2)	0.00	0.55
Ti I	22	4.95	4.78±0.19 (2)	−0.17	0.38
V I*	23	3.93	3.88 (1)	−0.05	0.50
Mn I*	25	5.43	3.55 (1)	−1.88	−1.33
Fe I	26	7.50	6.95±0.18 (36)	−0.55	-
Fe II	26	7.50	6.96±0.11 (3)	−0.54	-
Sr I	38	2.87	3.99 (1)	1.12	1.67
Y II	39	2.21	3.52±0.20 (2)	1.31	1.86
La II*	57	1.10	2.80 (syn)	1.70	2.25
Ce II	58	1.58	3.07±0.16 (3)	1.49	2.04
Pr II	59	0.72	2.65±0.15 (3)	1.93	2.48
Nd II	60	1.42	2.81±0.06 (2)	1.39	1.94
Sm II	62	0.96	2.78±0.16 (3)	1.82	2.37
Eu II*	63	0.52	1.02 (1)	0.50	1.05
Dy II	66	1.10	2.43 (1)	1.33	1.88

* abundance is derived using spectrum synthesis calculations. The number inside the parenthesis shows the number of lines used for the abundance determination.
(a) Asplund *et al.* (2009).

TABLE 3.20: **Elemental abundances in CD−27 14351.**

Element	Z	solar $log\epsilon^a$	$log\epsilon$ (dex)	[X/H]	[X/Fe]
C (C_2, 5165 Å)	6	8.43	8.70 (syn)	0.27	2.98
C (C_2, 5635 Å)	6	8.43	8.70 (syn)	0.27	2.98
C (CH, 4310 Å)	6	8.43	8.70 (syn)	0.27	2.98
N (CN, 4215 Å)	7	7.83	7.00 (syn)	−0.83	1.88
Na I	11	6.24	4.91±0.20 (2)	−1.33	1.38
Mg I	12	7.60	6.70 (1)	−0.90	1.81
Ca I	20	6.34	4.54±0.20 (5)	−1.80	0.91
Ti I	22	4.95	3.19±0.20 (3)	−1.76	0.95
Ti II	22	4.95	3.20±0.13 (5)	−1.75	0.96
V I*	23	3.93	2.33 (1)	−1.60	1.11
Cr I	24	5.64	3.11±0.18 (3)	−2.53	0.18
Fe I	26	7.50	4.78±0.16 (33)	−2.72	-
Fe II	26	7.50	4.81±0.07 (3)	−2.69	-
Sr I*	38	2.87	1.90 (1)	−0.97	1.74
Y II	39	2.21	1.47±0.10 (3)	−0.74	1.97
Zr I	40	2.58	2.07 (1)	−0.51	2.20
Zr II	40	2.58	2.09 (1)	−0.49	2.22
Ba II*	56	2.18	1.29±0.09	−0.89	1.82
La II*	57	1.10	−0.05	−1.15	1.56
Ce II	58	1.58	0.76±0.16 (3)	−0.82	1.89
Pr II	59	0.72	−0.03 (1)	−0.75	1.96
Nd II	60	1.42	0.08±0.16 (6)	−1.34	1.37
Eu II*	63	0.52	< -1.80	< -2.32	< 0.39
$^{12}C/^{13}C$ (C_2, 4740 Å) = 2.58					
$^{12}C/^{13}C$ (CN, 8005 Å) = 5.50					

* abundance is derived using spectrum synthesis calculations. The number inside the parenthesis shows the number of lines used for the abundance determination.

(a) Asplund *et al.* (2009).

TABLE 3.21: **Elemental abundances in HD 87853.**

Element	Z	solar $log\epsilon^a$	$log\epsilon$ (dex)	[X/H]	[X/Fe]
O	8	8.69	8.35(syn)	−0.34	0.39
Na I	11	6.24	6.89(1)	0.65	1.38
Mg I	12	7.60	7.55(1)	−0.05	0.68
Ca I	20	6.34	5.90± 0.20(12)	−0.44	0.29
Sc II*	21	3.15	5.30	2.15	2.88
Ti I	22	4.95	4.34(1)	−0.61	0.12
Ti II	22	4.95	4.33± 0.12(5)	−0.62	0.11
V I*	23	3.93	3.24(1)	−0.69	0.04
Cr I	24	5.64	4.81± 0.05(5)	−0.83	−0.10
Cr II	24	5.64	4.65± 0.18(2)	−0.99	−0.26
Mn I*	25	5.43	4.33	−1.10	−0.37
Fe I	26	7.50	6.78± 0.09(53)	−0.72	-
Fe II	26	7.50	6.76± 0.09(2)	−0.74	-
Co I	27	4.99	4.30(1)	−0.69	0.04
Ni I	28	6.22	5.45± 0.13(8)	−0.77	−0.04
Zn I	30	4.56	3.75±0.02 (2)	−0.81	− 0.08
Y II	39	2.21	1.00±0.05(3)	−1.21	−0.48
Ba II*	56	2.18	1.02	−1.16	−0.43
Nd II	60	1.42	1.63(1)	0.21	0.94
Eu II*	63	0.52	0.13(1)	−0.39	0.34

* abundance is derived using spectrum synthesis calculations. The number inside the parenthesis shows the number of lines used for the abundance determination.
(a) Asplund *et al.* (2009).

TABLE 3.22: **Elemental abundances in HD 145777.**

Element	Z	solar $log\epsilon^a$	$log\epsilon$ (dex)	[X/H]	[X/Fe]
C (C_2, 5165 Å)	6	8.43	8.69 (syn)	0.26	2.43
C (C_2, 5635 Å)	6	8.43	8.69 (syn)	0.26	2.43
C (CH, 4310 Å)	6	8.43	8.67 (syn)	0.24	2.41
N (CN, 4215 Å)	7	7.83	6.33 (syn)	−1.50	0.67
Na I	11	6.24	4.52±0.12 (2)	−1.72	0.45
Mg I	12	7.60	6.25±0.23 (2)	−1.35	0.82
Ca I	20	6.34	4.66±0.21 (9)	−1.68	0.49
Sc II*	21	3.15	1.75 (1)	−1.40	0.77
Ti I	22	4.95	3.44±0.17 (2)	−1.51	0.66
Ti II	22	4.95	3.43±0.08 (5)	−1.52	0.65
V I*	23	3.93	1.65 (1)	−2.28	−0.11
Cr I	24	5.64	3.26±0.13 (6)	−2.38	−0.21
Mn II*	25	5.43	2.45 (1)	−2.98	−0.81
Fe I	26	7.50	5.33±0.18 (33)	−2.17	-
Fe II	26	7.50	5.33±0.25 (4)	−2.17	-
Co I	27	4.99	2.85 (1)	−2.14	0.03
Zn I	30	4.56	3.02 (1)	−1.54	0.63
Sr I*	38	2.87	1.37 (1)	−1.50	0.67
Y II	39	2.21	1.26±0.02 (2)	−0.95	1.22
Zr I	40	2.58	1.46±0.14 (2)	−1.12	1.05
Ba II*	56	2.18	1.28 (2)±0.03	−0.90	1.27
La II*	57	1.10	0.30 (1)	−0.80	1.37
Ce II	58	1.58	1.20±0.09 (5)	−0.38	1.79
Pr II	59	0.72	0.22±0.00 (2)	−0.50	1.67
Nd II	60	1.42	0.73±0.18 (5)	−0.69	1.48
Sm II	62	0.96	0.42±0.03 (2)	−0.54	1.63
Eu II*	63	0.52	−0.85 (1)	−1.37	0.80

$^{12}C/^{13}C$ (C_2, 4740 Å) = 5.50

$^{12}C/^{13}C$ (CN, 8005 Å) = 5.45

* abundance is derived using spectrum synthesis calculations. The number inside the parenthesis shows the number of lines used for the abundance determination.

(a) Asplund *et al.* (2009).

TABLE 3.23: **Elemental abundances in HD 147609.**

Element	Z	solar $log\epsilon^a$	$log\epsilon$ (dex)	[X/H]	[X/Fe]
C (C_2, 5165 Å)	6	8.43	8.53 (syn)	0.10	0.38
O I	8	8.69	9.05 (syn)	0.36	0.64
Na I	11	6.24	6.26±0.19 (2)	0.02	0.30
Mg I	12	7.60	7.49±0.08 (4)	−0.11	0.17
Si I	14	7.51	7.37±0.05 (4)	−0.14	0.14
Ca I	20	6.34	6.04±0.21 (21)	−0.30	0.21
Sc II*	21	3.15	2.90 (1)	−0.25	0.03
Ti I	22	4.95	4.66±0.06 (10)	−0.29	–0.01
Ti II	22	4.95	4.67±0.16 (8)	−0.28	0.00
V I*	23	3.93	3.53 (1)	−0.40	−0.12
Cr I	24	5.64	5.29±0.15 (9)	−0.35	–0.07
Cr II	24	5.64	5.29±0.11 (3)	−0.35	–0.07
Mn I*	25	5.43	5.03 (1)	−0.40	–0.12
Fe I	26	7.50	7.22±0.16 (151)	−0.28	-
Fe II	26	7.50	7.22±0.12 (20)	−0.28	-
Ni I	28	6.22	5.88±0.11 (14)	−0.34	–0.06
Zn I	30	4.56	4.30±0.07 (2)	−0.26	0.02
Sr II*	38	2.87	4.10 (1)	1.23	1.51
Y II	39	2.21	3.00±0.14 (9)	0.79	1.07
Zr II*	40	2.58	3.30 (1)	0.72	1.00
Ba II*	56	2.18	3.30 (1)	1.12	1.40
La II*	57	1.10	2.09 (1)	0.99	1.27
Ce II	58	1.58	2.56±0.11 (8)	0.98	1.26
Pr II	59	0.72	1.79 (1)	1.07	1.35
Nd II	60	1.42	2.21±0.17 (8)	0.79	1.07
Sm II	62	0.96	1.97±0.19 (4)	1.01	1.29
Eu II*	63	0.52	0.37 (1)	–0.15	0.13

* abundance is derived using spectrum synthesis calculations. The number inside the parenthesis shows the number of lines used for the abundance determination.
(a) Asplund *et al.* (2009).

TABLE 3.24: **Elemental abundances in HD 154276.**

Element	Z	solar $log\epsilon^a$	$log\epsilon$ (dex)	[X/H]	[X/Fe]
Li*	3	1.05	< 0.70	< −0.35	< −0.25
O	8	8.69	8.97(syn)	0.28	0.38
Na I	11	6.24	6.20 ± 0.05(3)	−0.04	0.06
Mg I	12	7.60	7.81 ± 0.06(3)	0.21	0.31
Al I	13	6.45	6.23 ± 0.08(2)	−0.22	−0.12
Si I	14	7.51	7.54 ± 0.05(5)	0.03	0.13
Ca I	20	6.34	6.22 ± 0.20(27)	−0.12	−0.02
Sc II*	21	3.15	3.25(1)	0.10	0.20
Ti I	22	4.95	5.02 ± 0.17(27)	0.07	0.17
Ti II	22	4.95	5.06 ± 0.21(18)	0.11	0.21
V I*	23	3.93	3.90(1)	−0.03	0.07
Cr I	24	5.64	5.51 ± 0.20(11)	−0.13	−0.03
Cr II	24	5.64	5.53± 0.07(5)	−0.11	−0.01
Mn I	25	5.43	5.17 ± 0.15(6)	−0.26	−0.16
Fe I	26	7.50	7.41 ± 0.13(150)	−0.09	-
Fe II	26	7.50	7.40± 0.14(15)	−0.10	-
Co I	27	4.99	4.85 ± 0.10(2)	−0.14	−0.04
Ni I	28	6.22	6.13 ± 0.15(19)	−0.09	0.01
Zn I	30	4.56	4.64 ± 0.00(2)	0.08	0.18
Sr I*	38	2.87	2.55(1)	−0.32	−0.22
Y II	39	2.21	2.18 ± 0.19(4)	−0.03	0.07
Zr I*	40	2.58	2.40(1)	−0.18	−0.08
Ru I*	44	1.75	< 2.55(1)	< 0.8	< 0.18
Ba II*	56	2.18	2.30 ± 0.15(3)	0.12	0.22
La II*	57	1.10	1.20(1)	0.10	0.20
Ce II	58	1.58	1.66±0.03(2)	0.08	0.18
Nd II*	60	1.42	1.72 ±0.12(2)	0.30	0.40
Sm II*	62	0.96	0.93(1)	−0.03	0.07

* abundance is derived using spectrum synthesis calculations. The number inside the parenthesis shows the number of lines used for the abundance determination.
(a) Asplund *et al.* (2009).

TABLE 3.25: **Elemental abundances in HD 238020.**

Element	Z	solar $log\epsilon^a$	$log\epsilon$ (dex)	[X/H]	[X/Fe]
C (C_2, 5165 Å)	6	8.43	7.75 (syn)	−0.68	0.00
C (CH, 4310 Å)	6	8.43	7.68 (syn)	−0.75	−0.07
O I	8	8.69	8.09 (syn)	−0.60	0.08
Na I	11	6.24	5.61±0.11 (4)	−0.63	0.05
Mg I	12	7.60	7.29±0.08 (4)	−0.31	0.37
Si I	14	7.51	6.31 (1)	−1.20	−0.52
Ca I	20	6.34	5.83±0.19 (21)	−0.51	0.17
Sc II*	21	3.15	2.47±0.15 (6)	−0.68	0.00
Ti I	22	4.95	4.45±0.11 (14)	−0.50	0.18
Ti II	22	4.95	4.40±0.20 (22)	−0.55	0.13
V I*	23	3.93	3.23 (1)	−0.70	−0.02
Cr I	24	5.64	4.98±0.12 (13)	−0.66	0.02
Cr II	24	5.64	5.01 (1)	−0.63	0.05
Mn I*	25	5.43	4.60±0.03 (3)	−0.83	−0.15
Fe I	26	7.50	6.83±0.15 (136)	−0.67	-
Fe II	26	7.50	6.82±0.16 (17)	−0.68	-
Co I	27	4.99	4.30±0.20 (4)	−0.69	−0.01
Ni I	28	6.22	5.60±0.21 (15)	−0.62	0.06
Cu I	29	4.19	3.89 (1)	−0.30	0.38
Zn I	30	4.56	3.75±0.04 (2)	−0.81	−0.13
Sr II	38	2.87	2.27 (1)	−0.60	0.08
Y II	39	2.21	1.27±0.12 (8)	−0.94	−0.26
Zr I	40	2.58	2.01±0.06 (2)	−0.57	0.11
Zr II	40	2.58	1.95±0.04 (2)	−0.63	0.05
Ba II*	56	2.18	1.75 (1)	−0.43	0.25
La II*	57	1.10	0.90 (1)	−0.20	0.48
Ce II	58	1.58	1.09±0.11 (7)	−0.49	0.19
Pr II	59	0.72	0.50±0.20 (2)	−0.22	0.46
Nd II	60	1.42	1.00±0.25 (12)	−0.42	0.26
Sm II	62	0.96	0.70±0.07 (4)	−0.26	0.42
Dy II	66	1.10	0.53 (1)	−0.57	0.11

* abundance is derived using spectrum synthesis calculations. The number inside the parenthesis shows the number of lines used for the abundance determination.
(a) Asplund *et al.* (2009).

TABLE 3.26: **Elemental abundances in and HE 0017+0055.**

Element	Z	solar $log\epsilon^a$	$log\epsilon$ (dex)	[X/H]	[X/Fe]
C (C_2, 5165 Å)	6	8.43	8.70 (syn)	0.27	2.73
C (C_2, 5635 Å)	6	8.43	8.71 (syn)	0.28	2.74
C (CH, 4310 Å)	6	8.43	8.73 (syn)	0.30	2.76
N (CN, 4215 Å)	7	7.83	8.20 (syn)	0.37	2.83
Ti I	22	4.95	3.13 (1)	−1.82	0.64
Ti II	22	4.95	3.14±0.05 (3)	−1.81	0.65
Cr I	24	5.64	2.68 (1)	−2.96	−0.50
Fe I	26	7.50	5.03±0.12 (21)	−2.47	-
Fe II	26	7.50	5.05±0.03 (3)	−2.45	-
Zn I	30	4.56	2.62 (1)	−1.94	0.52
Y II	39	2.21	0.33±0.08 (3)	−1.88	0.58
Zr II	40	2.58	1.67±0.20 (3)	−0.91	1.55
Ba II*	56	2.18	2.02 (1)	−0.16	2.30
La II*	57	1.10	1.10 (2)±0.20	0.0	2.46
Ce II	58	1.58	1.23±0.06 (2)	−0.35	2.11
Pr II	59	0.72	0.68 (1)	−0.04	2.42
Nd II	60	1.42	1.21±0.11 (4)	−0.21	2.25
Sm II	62	0.96	0.48±0.04 (2)	−0.48	1.98
Eu II*	63	0.52	0.20 (1)	−0.32	2.14
$^{12}C/^{13}C$ (C_2, 4740 Å) = 4.00					
$^{12}C/^{13}C$ (CN, 8005 Å) = 3.64					

* abundance is derived using spectrum synthesis calculations. The number inside the parenthesis shows the number of lines used for the abundance determination.

(a) Asplund *et al.* (2009).

TABLE 3.27: **Elemental abundances in HE 0308−1612.**

Element	Z	solar $log\epsilon^a$	$log\epsilon$ (dex)	[X/H]	[X/Fe]
C	6	8.43	8.48(syn)	0.05	0.78
N	7	7.83	7.25(syn)	−0.58	0.15
Na I*	11	6.24	5.85(1)	−0.39	0.34
Mg I	12	7.60	7.22± 0.01(2)	−0.38	0.35
Ca I	20	6.34	5.98± 0.18(5)	−0.36	0.37
Sc II*	21	3.15	2.95(1)	−0.2	0.53
Ti I	22	4.95	4.54± 0.15(5)	−0.41	0.32
Ti II	22	4.95	4.52(1)	−0.43	0.30
V I*	23	3.93	3.49(1)	−0.44	0.29
Cr I	24	5.64	4.53± 0.20(3)	−1.11	−0.39
Mn I*	25	5.43	4.99± 0.13(3)	−0.44	0.29
Fe I	26	7.50	6.78± 0.19(40)	−0.72	-
Fe II	26	7.50	6.77± 0.15(3)	−0.73	-
Ni I	28	6.22	5.81± 0.13(5)	−0.41	0.32
Zn I*	30	4.56	3.65(1)	−0.91	−0.19
Sr I	38	2.87	3.24(1)	0.37	1.10
Y II	39	2.21	2.61±0.09(4)	0.4	1.13
Ba II*	56	2.18	3.08(1)	0.9	1.63
La II*	57	1.10	1.80(1)	0.7	1.43
Ce II	58	1.58	2.56±0.08(3)	0.98	1.71
Pr II*	59	0.72	2.00(1)	1.28	2.01
Nd II	60	1.42	2.42±0.18(10)	1.0	1.73
Sm II	62	0.96	1.68± 0.14(2)	0.72	1.45
Eu II*	63	0.52	0.14(1)	−0.38	0.35

$^{12}C/^{13}C$ (CN, 8005 Å) = 15.6

* abundance is derived using spectrum synthesis calculations. The number inside the parenthesis shows the number of lines used for the abundance determination.

(a) Asplund *et al.* (2009).

TABLE 3.28: **Elemental abundances in HE 0319–0215.**

Element	Z	solar $log\epsilon^a$	$log\epsilon$ (dex)	[X/H]	[X/Fe]
C (C_2, 5165 Å)	6	8.43	8.23 (syn)	−0.20	2.37
C (C_2, 5635 Å)	6	8.43	8.29 (syn)	−0.14	2.43
C (CH, 4310 Å)	6	8.43	8.30 (syn)	−0.13	2.44
N (CN, 4215 Å)	7	7.83	7.33 (syn)	−0.50	2.07
Na I	11	6.24	4.62±0.12 (2)	−1.62	0.95
Mg I	12	7.60	5.51 (1)	−2.09	0.48
Ca I	20	6.34	4.49±0.21 (4)	−1.85	0.72
Ti I	22	4.95	3.16 (1)	−1.79	0.78
Ti II	22	4.95	3.30±0.12 (3)	−1.65	0.92
Fe I	26	7.50	4.92±0.10 (30)	−2.58	-
Fe II	26	7.50	4.94±0.05 (5)	−2.56	-
Y II	39	2.21	0.79±0.20 (2)	−1.42	1.15
Zr II	40	2.58	0.63 (1)	−1.95	0.62
Ba II*	56	2.18	1.49 ±0.12 (2)	−0.69	1.88
Ce II	58	1.58	0.93±0.02 (2)	−0.65	1.92
Pr II	59	0.72	0.03 (1)	−0.69	1.88
Nd II	60	1.42	0.74±0.22 (6)	−0.68	1.89
Sm II	62	0.96	0.19±0.13 (4)	−0.77	1.80
Eu II*	63	0.52	−1.20 (1)	−1.72	0.85

* abundance is derived using spectrum synthesis calculations. The number inside the parenthesis shows the number of lines used for the abundance determination.
(a) Asplund *et al.* (2009).

TABLE 3.29: **Elemental abundances in HE 0401−0138.**

	Z	solar $log\epsilon^{(a)}$	$log\epsilon$ (dex)	[X/H]	[X/Fe]
Li	3	1.05	< 0.80	< –0.25	< 3.20
C (CH, 4310Å)	6	8.43	5.27 (syn)	−3.16	0.29
O	8	8.69	< 6.80 (1)	< –1.89	< 1.56
Na I	11	6.24	3.07±0.19 (2)	−3.17	0.28
Mg I	12	7.60	5.01±0.12 (3)	−2.59	0.86
Ca I	20	6.34	3.41±0.02 (3)	−2.93	0.52
Sc II*	21	3.15	−0.05±0.05 (2)	−3.20	0.25
Ti I	22	4.95	1.84±0.09 (3)	−3.11	0.34
Ti II	22	4.95	1.99±0.23 (6)	−2.96	0.49
Cr I	24	5.64	2.14±0.08 (2)	−3.50	−0.05
Mn I*	25	5.43	1.27±0.03 (2)	−4.16	−0.71
Fe I	26	7.50	4.04±0.14 (33)	−3.46	-
Fe II	26	7.50	4.07±0.06 (4)	−3.43	-
Co I	27	4.99	1.76 (1)	−3.23	0.22
Ni I	28	6.22	2.89 (1)	−3.33	0.12
Sr II	38	2.87	−0.37 (1)	−3.24	0.21
Y II	39	2.21	−0.90 (1)	−3.11	0.34
Ba II*	56	2.18	−1.39±0.01 (2)	−3.57	−0.12
La II*	57	1.10	< −1.90±0.10 (2)	< −3.00	< 0.45
Ce II*	58	1.58	< −1.24±0.16 (2)	< −2.82	< 0.63
Pr II*	59	0.72	< −2.15±0.05 (2)	< −2.87	< 0.58
Nd II*	60	1.42	< −2.10±0.10 (2)	< −3.52	< –0.07
Sm II*	62	0.96	< −2.36 (1)	< −3.32	< 0.13
Eu II*	63	0.52	< −2.20±0.10 (2)	< −2.72	< 0.73

* abundance is derived using spectrum synthesis calculations. The number inside the parenthesis shows the number of lines used for the abundance determination.
(a) Asplund *et al.* (2009).

TABLE 3.30: **Elemental abundances in HE 0507–1653.**

Element	Z	solar $log\epsilon^a$	$log\epsilon$ (dex)	[X/H]	[X/Fe]
C (C_2, 5165 Å)	6	8.43	8.18 (syn)	−0.25	1.19
C (C_2, 5635 Å)	6	8.43	8.12 (syn)	−0.31	1.13
N (CN, 4215 Å)	7	7.83	7.80	−0.03	1.41
Na I	11	6.24	5.19±0.02 (3)	−1.05	0.39
Mg I	12	7.60	6.68±0.11 (3)	−0.92	0.52
Ca I	20	6.34	5.30±0.19 (8)	−1.04	0.40
Sc II*	21	3.15	1.73±0.03 (2)	−1.42	0.02
Ti I	22	4.95	3.88±0.11 (3)	−1.07	0.37
Ti II	22	4.95	3.85±0.23 (8)	−1.10	0.34
Cr I	24	5.64	4.21±0.15 (6)	−1.43	0.01
Mn I*	25	5.43	3.75 (1)	−1.68	−0.24
Fe I	26	7.50	6.04±0.11 (36)	−1.46	-
Fe II	26	7.50	6.08±0.08 (4)	−1.42	-
Co I	27	4.99	3.52 (1)	−1.47	−0.03
Ni I	28	6.22	4.76±0.18 (4)	−1.46	−0.02
Cu I	29	4.19	2.55 (1)	−1.64	−0.20
Zn I	30	4.56	3.21 (1)	−1.35	0.09
Y II	39	2.21	1.97±0.11 (6)	−0.24	1.20
Zr I	40	2.58	2.71±0.09 (2)	0.13	1.57
Zr II	40	2.58	2.77±0.21 (2)	0.19	1.63
Ba II*	56	2.18	2.80 ±0.10 (2)	0.62	2.06
La II*	57	1.10	1.60 (1)	0.50	1.94
Ce II	58	1.58	2.17±0.09 (9)	0.59	2.03
Pr II	59	0.72	1.25 (1)	0.53	1.97
Nd II	60	1.42	2.01±0.15 (11)	0.59	2.03
Sm II	62	0.96	1.60±0.15 (4)	0.64	2.08
Eu II*	63	0.52	0.11 ±0.01 (2)	−0.41	1.03

* abundance is derived using spectrum synthesis calculations. The number inside the parenthesis shows the number of lines used for the abundance determination.
(a) Asplund *et al.* (2009).

TABLE 3.31: **Elemental abundances in HE 0930–0018.**

Element	Z	solar $log\epsilon^a$	$log\epsilon$ (dex)	[X/H]	[X/Fe]
C (C_2, 5165 Å)	6	8.43	8.67 (syn)	0.24	1.63
C (C_2, 5635 Å)	6	8.43	8.70 (syn)	0.27	1.66
Na I	11	6.24	5.41±0.03 (2)	−0.83	0.56
Mg I	12	7.60	6.69 (1)	−0.91	0.48
Ca I	20	6.34	5.34±0.11 (6)	−1.00	0.39
Ti I	22	4.95	3.46±0.21 (7)	−1.49	−0.10
Ti II	22	4.95	3.45±0.20 (4)	−1.50	−0.11
V I*	23	3.93	2.66 (1)	−1.27	0.12
Cr I	24	5.64	3.74±0.16 (3)	−1.90	−0.51
Mn I*	25	5.43	3.15 (1)	−2.28	−0.89
Fe I	26	7.50	6.11±0.11 (19)	−1.39	-
Fe II	26	7.50	6.11±0.09 (3)	−1.39	-
Co I	27	4.99	3.49±0.12 (2)	−1.50	−0.11
Ni I	28	6.22	5.57±0.16 (3)	−0.65	0.74
Zn I	30	4.56	3.30 (1)	−1.26	0.13
Y II	39	2.21	1.52±0.18 (3)	−0.69	0.70
Zr I	40	2.58	1.57 (1)	−1.01	0.38
Ba II*	56	2.18	1.88 ±0.32 (2)	−0.30	1.09
La II*	57	1.10	0.80 (1)	−0.30	1.09
Ce II	58	1.58	1.53±0.13 (3)	−0.05	1.34
Pr II	59	0.72	0.41±0.09 (2)	−0.31	1.08
Nd II	60	1.42	0.96±0.14 (8)	−0.46	0.93
Sm II	62	0.96	0.55±0.20 (2)	−0.41	0.98

* abundance is derived using spectrum synthesis calculations. The number inside the parenthesis shows the number of lines used for the abundance determination.
(a) Asplund *et al.* (2009).

TABLE 3.32: **Elemental abundances in HE 1005–1439.**

	Z	solar $log\epsilon^{(a)}$	$log\epsilon$ (dex)	$\sigma_{log\epsilon}$	[X/H]	[X/Fe]	$\sigma_{[X/Fe]}$
C (CH, 4310 Å)	6	8.43	7.65 (syn)	0.23	−0.78	2.25	0.27
C (C_2, 5165 Å)	6	8.43	7.82 (syn)	0.22	−0.61	2.42	0.27
C (C_2, 5635 Å)	6	8.43	7.85 (syn)	0.21	−0.58	2.45	0.26
Na I	11	6.24	4.58±0.03 (2)	0.16	−1.66	1.37	0.22
Mg I	12	7.60	5.10±0.05 (4)	0.12	−2.50	0.53	0.19
Ca I	20	6.34	3.78±0.18 (10)	0.10	−2.56	0.47	0.18
Sc II	21	3.15	0.82±0.10 (2)	0.17	−2.33	0.70	0.23
Sc II*	21	3.15	0.75±0.00 (2)	0.15	−2.40	0.63	0.23
Ti I	22	4.95	2.27±0.17 (4)	0.14	−2.68	0.35	0.21
Ti II	22	4.95	2.23±0.20 (8)	0.12	−2.72	0.31	0.20
Cr I	24	5.64	2.59±0.15 (5)	0.17	−3.05	−0.02	0.23
Mn I	25	5.43	2.56±0.14 (2)	0.25	−2.87	0.16	0.29
Mn I*	25	5.43	2.13±0.03 (2)	0.23	−3.30	−0.27	0.28
Fe I	26	7.50	4.46±0.15 (45)	0.15	−3.04	-	-
Fe II	26	7.50	4.49±0.03 (5)	0.10	−3.01	-	-
Co I	27	4.99	2.20±0.07 (3)	0.13	−2.79	0.24	0.20
Ni I	28	6.22	3.40 (1)	0.23	−2.82	0.21	0.28
Sr II	38	2.87	0.10±0.22 (2)	0.27	−2.77	0.26	0.31
Y II	39	2.21	−0.40±0.27 (3)	0.18	−2.61	0.42	0.23
Ba II	56	2.18	0.64±0.27 (3)	0.28	−1.54	1.49	0.31
Ba II*	56	2.18	0.31±0.24 (3)	0.27	−1.87	1.16	0.31
La II	57	1.10	−0.61±0.12 (3)	0.13	−1.71	1.32	0.20
La II*	57	1.10	−0.68±0.06 (3)	0.11	−1.78	1.25	0.19
Ce II	58	1.58	−0.07±0.17 (3)	0.14	−1.65	1.38	0.21
Pr II	59	0.72	−0.76 (1)	0.22	−1.48	1.55	0.27
Nd II	60	1.42	−0.36±0.15 (4)	0.13	−1.78	1.25	0.20
Eu II*	63	0.52	−2.05±0.18 (2)	0.17	−2.57	0.46	0.22
Dy II	66	1.10	−1.21±0.19 (3)	0.15	−2.31	0.72	0.21
Er II	68	0.92	−1.05±0.20 (2)	0.17	−1.97	1.06	0.23
Hf II	72	0.85	−0.73±0.01 (2)	0.16	−1.58	1.45	0.18
Pb II*	82	1.75	0.70 (1)	0.11	−1.05	1.98	0.19

$^{12}C/^{13}C$ (C_2, 4740 Å) = 5.0

* abundance is derived using spectrum synthesis calculations. The number inside the parenthesis shows the number of lines used for the abundance determination.

(a) Asplund *et al.* (2009).

TABLE 3.33: **Elemental abundances in HE 1023–1504.**

Element	Z	solar $log\epsilon^a$	$log\epsilon$ (dex)	[X/H]	[X/Fe]
C (C_2, 5165 Å)	6	8.43	8.65 (syn)	0.22	1.88
C (C_2, 5635 Å)	6	8.43	8.72 (syn)	0.29	1.95
Na I	11	6.24	5.06 (1)	−1.18	0.48
Ca I	20	6.34	5.51±0.14 (3)	−0.83	0.83
Ti I	22	4.95	3.95±0.15 (3)	−1.00	0.66
Cr I	24	5.64	3.98±0.11 (2)	−1.66	0.00
Fe I	26	7.50	5.84±0.14 (20)	−1.66	-
Fe II	26	7.50	5.84±0.07 (2)	−1.66	-
Y II	39	2.21	1.67±0.21 (2)	−0.54	1.12
Zr II	40	2.58	2.23 (1)	−0.35	1.31
Ba II*	56	2.18	2.60 (1)	0.42	2.08
Ce II	58	1.58	2.42±0.19 (3)	0.84	2.50
Nd II	60	1.42	1.91±0.13 (5)	0.49	2.15
Sm II	62	0.96	1.24±0.14 (2)	0.28	1.94
Eu II*	63	0.52	−0.25 (1)	−0.77	0.89

* abundance is derived using spectrum synthesis calculations. The number inside the parenthesis shows the number of lines used for the abundance determination.
(a) Asplund *et al.* (2009).

TABLE 3.34: **Elemental abundances in HE 1153−0518.**

	Z	solar $log\epsilon^{(a)}$	$log\epsilon$ (dex)	[X/H]	[X/Fe]
Li	3	1.05	< 0.90	< –0.15	< 2.99
C (C_2, 5165 Å)	6	8.43	7.90 (syn)	−0.53	2.61
C (C_2, 5635 Å)	6	8.43	7.95 (syn)	−0.48	2.66
O	8	8.69	< 6.89 (syn)	< –1.80	< 1.34
Na I	11	6.24	5.03±0.02 (2)	−1.21	1.93
Mg I	12	7.60	5.57±0.02 (2)	−2.03	1.11
Ca I	20	6.34	3.86 (1)	−2.48	0.66
Sc II*	21	3.15	–0.07 (1)	−3.22	–0.08
Ti I	22	4.95	2.48 (1)	−2.47	0.67
Ti II	22	4.95	2.29±0.18 (4)	−2.66	0.48
Cr I	24	5.64	2.63 (1)	−3.01	0.13
Fe I	26	7.50	4.36±0.20 (29)	−3.14	-
Fe II	26	7.50	4.37±0.23 (2)	−3.13	-
Ni I	28	6.22	3.24 (1)	−2.98	0.16
Y II	39	2.21	−0.88 (1)	−3.09	0.05
Ba II*	56	2.18	–0.97±0.15 (3)	−3.15	–0.01
La II*	57	1.10	< –1.60 (1)	< −2.70	< 0.44

* abundance is derived using spectrum synthesis calculations. The number inside the parenthesis shows the number of lines used for the abundance determination.
(a) Asplund *et al.* (2009).

TABLE 3.35: **Elemental abundances in HE 1246−1344.**

	Z	solar $log\epsilon^{(a)}$	$log\epsilon$ (dex)	[X/H]	[X/Fe]
Li	3	1.05	< 0.30	< –0.75	< 2.75
C (CH, 4310Å)	6	8.43	4.95 (syn)	−3.48	0.02
O	8	8.69	< 6.58 (1)	<–2.11	< 1.39
Na I	11	6.24	4.27±0.02 (2)	−1.97	1.53
Mg I	12	7.60	4.83±0.20 (2)	−2.77	0.73
Ca I	20	6.34	3.35±0.14 (7)	−2.99	0.51
Sc II*	21	3.15	−0.10±0.14 (2)	−3.25	0.25
Ti I	22	4.95	1.84±0.05 (2)	−3.11	0.39
Ti II	22	4.95	1.86±0.10 (12)	−3.09	0.41
Cr I	24	5.64	1.87±0.17 (4)	−3.77	−0.27
Mn I*	25	5.43	1.12±0.08 (2)	−4.31	−0.81
Fe I	26	7.50	3.99±0.09 (43)	−3.51	-
Fe II	26	7.50	4.02±0.01 (2)	−3.48	-
Co I	27	4.99	1.62 (1)	−3.37	0.13
Ni I	28	6.22	2.80±0.09 (2)	−3.42	0.08
Sr II	38	2.87	−1.70±0.11 (2)	−4.57	−1.07
Y II	39	2.21	-	-	-
Ba II*	56	2.18	−2.80 (1)	−4.98	−1.48
La II*	57	1.10	< −1.90±0.10 (2)	< −3.00	< 0.50
Ce II*	58	1.58	< −1.58 (1)	< −3.16	< 0.34
Pr II*	59	0.72	< −1.82±0.10 (2)	< −2.54	< 0.96
Nd II*	60	1.42	< −2.05±0.05 (2)	< −3.47	< 0.03
Sm II*	62	0.96	< −1.87±0.24 (3)	< −2.83	< 0.67
Eu II*	63	0.52	< −2.35±0.15 (2)	< −2.87	< 0.63

* abundance is derived using spectrum synthesis calculations. The number inside the parenthesis shows the number of lines used for the abundance determination.
(a) Asplund *et al.* (2009).

TABLE 3.36: **Elemental abundances in HE 2144−1832.**

Element	Z	solar $log\epsilon^a$	$log\epsilon$ (dex)	[X/H]	[X/Fe]
C (C_2, 5165 Å)	6	8.43	8.65 (syn)	0.22	1.85
C (C_2, 5635 Å)	6	8.43	8.60 (syn)	0.17	1.80
C (CH, 4310 Å)	6	8.43	8.55 (syn)	0.12	1.75
N (CN, 4215 Å)	7	7.83	6.70 (syn)	−1.13	0.50
Na I	11	6.24	5.14±0.08 (3)	−1.10	0.53
Mg I	12	7.60	6.64±0.11 (2)	−0.96	0.67
Ca I	20	6.34	5.11±0.17 (8)	−1.23	0.40
Ti I	22	4.95	3.53±0.13 (6)	−1.42	0.21
Ti II	22	4.95	3.51±0.05 (3)	−1.44	0.19
V I*	23	3.93	2.36 (1)	−1.57	0.06
Cr I	24	5.64	3.89±0.18 (4)	−1.75	−0.12
Mn I*	25	5.43	3.20 (2)±0.0	−2.23	−0.60
Fe I	26	7.50	5.87±0.15 (27)	−1.63	-
Fe II	26	7.50	5.87±0.00 (2)	−1.63	-
Co I	27	4.99	3.42±0.03 (3)	−1.57	0.06
Ni I	28	6.22	5.00±0.16 (5)	−1.22	0.41
Zn I	30	4.56	2.85 (1)	−1.71	−0.08
Sr I*	38	2.87	1.90 (1)	−0.97	0.66
Y II	39	2.21	1.74±0.08 (3)	−0.47	1.16
Zr I	40	2.58	1.92±0.18 (3)	−0.66	0.97
Ba II*	56	2.18	2.04 (1)	−0.14	1.49
La II*	57	1.10	1.00 (1)	−0.10	1.53
Ce II	58	1.58	1.65±0.17 (6)	0.07	1.70
Pr II	59	0.72	0.81±0.17 (3)	0.09	1.72
Nd II	60	1.42	1.40±0.17 (7)	−0.02	1.61
Sm II	62	0.96	1.11±0.21 (3)	0.15	1.78
Eu II*	63	0.52	−0.10 (1)	−0.62	1.01

$^{12}C/^{13}C$ (C_2, 4740 Å) = 2.50

$^{12}C/^{13}C$ (CN, 8005 Å) = 2.50

* abundance is derived using spectrum synthesis calculations. The number inside the parenthesis shows the number of lines used for the abundance determination.

(a) Asplund *et al.* (2009).

TABLE 3.37: **Elemental abundances in HE 2339−0837.**

Element	Z	solar $log\epsilon^a$	$log\epsilon$ (dex)	[X/H]	[X/Fe]
C (C_2, 5165 Å)	6	8.43	8.73 (syn)	0.30	3.04
C (C_2, 5635 Å)	6	8.43	8.50 (syn)	0.07	2.81
Na I	11	6.24	5.04±0.03 (2)	−1.20	1.54
Mg I	12	7.60	7.03 (1)	−0.57	2.17
Ca I	20	6.34	4.09±0.14 (4)	−2.25	0.49
Ti II	22	4.95	2.62±0.15 (4)	−2.33	0.41
Cr I	24	5.64	2.56 (1)	−3.08	−0.34
Fe I	26	7.50	4.76±0.08 (19)	−2.74	-
Fe II	26	7.50	4.76±0.08 (4)	−2.74	-
Sr I*	38	2.87	1.45 (1)	−1.42	1.32
Y II	39	2.21	0.14±0.10 (3)	−2.07	0.67
Zr II	40	2.58	1.48 (1)	−1.10	1.64
Ba II*	56	2.18	1.65 (1)±0.15	−0.53	2.21
La II*	57	1.10	0.60 (1)	−0.50	2.24
Ce II	58	1.58	1.21±0.13 (3)	−0.37	2.37
Pr II	59	0.72	0.24±0.22 (2)	−0.48	2.26
Nd II	60	1.42	1.23±0.10 (5)	−0.19	2.55
Sm II	62	0.96	0.51±0.14 (3)	−0.45	2.29
Eu II*	63	0.52	−0.38 (1)	−0.90	1.84

$^{12}C/^{13}C$ (C_2, 4740 Å) = 7.00

* abundance is derived using spectrum synthesis calculations. The number inside the parenthesis shows the number of lines used for the abundance determination.

(a) Asplund *et al.* (2009).

TABLE 3.38: **Comparison of the abundances of our programme stars with the literature values.**

Star Name	[Fe/H]	[C/Fe]*	[N/Fe]	[Sr/Fe]	[Y/Fe]	[Zr/Fe]	[Ba II/Fe]	Ref
BD+75 348	−0.42	0.31	0.79	-	1.27	1.25	1.62	1
	−0.87	0.50	-	-	1.50	1.50	1.70	Z00
CD−27 14351	−2.71	2.98	1.88	1.74	1.97	2.21	1.82	1
	−2.62	2.89	1.89	1.73	1.99	-	1.77	K17
HD 147609	–0.28	0.38	-	1.51	1.07	1.00	1.40	1
	–0.45	-	-	1.32	1.57	1.56	1.57	AB06
	-	-	-	-	0.96	0.80	-	N94
HD 154276	–0.10	-	-	–0.22	0.07	–0.08	0.22	1
	–0.29	-	-	-	–0.07	-	–0.03	B14
HE 0017+0055	−2.46	2.74	2.83	-	0.58	1.55	2.30	1
	−2.40	2.17	2.47	-	0.50	1.60	> 1.90	J16
	−2.72	2.31	0.52	-	-	-	-	K11
HE 0319–0215	−2.57	2.41	2.07	-	1.15	0.62	1.88	1
	−2.42	2.12	0.92	-	-	-	-	K11
	−2.30	2.00	-	-	-	-	0.52	H16
	−2.90	2.47	2.47	-	0.63	0.35	1.75	K21

Table 3.38: *–continued*

Star Name	[Fe/H]	[C/Fe]*	[N/Fe]	[Sr/Fe]	[Y/Fe]	[Zr/Fe]	[Ba II/Fe]	Ref
HE 0401–0138	−3.45	0.29	-	0.21	0.34	-	–0.12	1
	–	0.24	-	0.11	0.05	-	–0.21	B05
HE 0507–1653	−1.44	1.16	1.41	-	1.20	1.63	2.06	1
	−1.38	1.29	0.80	-	-	-	1.89	A07
	−1.42	1.33**	1.20	-	-	-	-	S08
	−1.81	1.61	0.97	-	-	-	-	K11
	−1.32	-	-	-	-	-	1.56	Y13
	−1.35	1.22	1.02	1.08	1.08	1.47	1.77	K21
HE 1005–1439	−3.03	2.25	-	0.26	0.42	-	1.16	1
	−3.17	2.48		-	-	-	1.06	A07
	−3.09	-	-	-	-	-	1.17	Y13
	-	2.14**	-	-	-	-	-	S08
HE 1246–1344	−3.50	0.02	-	–1.07	-	-	–1.48	1
	–	–0.06	-	–1.25	-	-	-	B05
HE 2144−1832	−1.63	1.80	0.50	0.66	1.16	0.97	1.49	1
	−1.70	0.80	0.60	1.50	-	-	1.30	H16

** – Abundance is derived using [C I] line

TABLE 3.38: *–continued*

Star Name	[Fe/H]	[C/Fe]*	[N/Fe]	[Sr/Fe]	[Y/Fe]	[Zr/Fe]	[Ba II/Fe]	Ref
HE 2339−0837	−2.74	2.93	-	1.32	0.67	1.64	2.21	1
	−2.71	2.71	-	-	-	-	-	K11
Star Name	[La II/Fe]	[Ce II/Fe]	[Pr II/Fe]	[Nd II/Fe]	[Sm II/Fe]	[Eu II/Fe]		Ref
BD+75 348	1.92	1.81	1.87	1.63	1.54	0.70		1
	2.00	1.90	1.50	1.40	2.20	1.60		Z00
CD−27 14351	1.56	1.89	1.96	1.37	-	< 0.39		1
	1.57	2.63	-	1.26	-	1.65		K17
HD 147609	1.27	1.26	1.35	1.07	1.29	0.13		1
	1.63	1.64	1.22	1.32	1.09	0.74		AB06
	-	-	-	0.98	-	-		N94
HD 154276	0.20	0.18	-	0.40	0.07	-		1
	-	-	-	-	-	-		B14
HE 0017+0055	2.46	2.11	2.42	2.25	1.98	2.14		1
	2.40	2.00	-	2.20	1.90	2.30		J16
	-	-	-	-	-	-		K11

TABLE 3.38: *–continued*

Star Name	[Fe/H]	[C/Fe]*	[N/Fe]	[Sr/Fe]	[Y/Fe]	[Zr/Fe]	[Ba II/Fe]	Ref
HE 2339−0837	−2.74	2.93	-	1.32	0.67	1.64	2.21	1
	−2.71	2.71	-	-	-	-	-	K11
Star Name	[La II/Fe]	[Ce II/Fe]	[Pr II/Fe]	[Nd II/Fe]	[Sm II/Fe]	[Eu II/Fe]		Ref
HE 0319–0215	-	1.92	1.88	1.89	1.80	0.85		1
	-	-	-	-	-	-		K11
	-	-	-	-	-	-		H16
	1.70	1.75	1.81	1.74	1.49	1.31		K21
HE 0401–0138	< 0.45	< 0.63	< 0.58	< –0.07	< 0.13	< 0.73		1
	-	-	-	-	-	-		B05
HE 0507–1653	1.94	2.03	1.97	2.03	2.08	1.03		1
	-	-	-	-	-	-		A07
	-	-	-	-	-	-		S08
	-	-	-	-	-	-		K11
	-	-	-	-	-	-		Y13
	1.78	1.77	1.82	1.85	1.92	1.13		K21

TABLE 3.38: *–continued*

Star Name	[La II/Fe]	[Ce II/Fe]	[Pr II/Fe]	[Nd II/Fe]	[Sm II/Fe]	[Eu II/Fe]	-	Ref
HE 1005–1439	1.25	1.38	1.55	1.25	-	0.46	-	1
	-	-	-	-	-	-	-	A07
	-	-	-	-	-	-	-	Y13
	-	-	-	-	-	-	-	S08
HE 1246–1344	< 0.50	< 0.34	< 0.96	< 0.03	< 0.67	< 0.63	-	1
	-	-	-	-	-	-	-	B05
HE 2144−1832	1.53	1.70	1.72	1.61	1.78	1.01	-	1
	-	-	-	-	-	-	-	H16
HE 2339−0837	2.24	2.37	2.26	2.55	2.29	1.84	-	1
	-	-	-	-	-	-	-	K11

* − Abundance of carbon is the average abundance derived from different molecular bands.

References: 1. Our work, A07- Aoki *et al.* (2007), AB06- Allen and Barbuy (2006), B05- Barklem *et al.* (2005), B14- Bensby *et al.* (2014), H16- Hansen *et al.* (2016c), J16- Jorissen *et al.* (2016a), K11- Kennedy *et al.* (2011), K17- Karinkuzhi *et al.* (2017), K21- Karinkuzhi *et al.* (2021), N94- North *et al.* (1994), S08- Schuler *et al.* (2008), Y13- Yong *et al.* (2013), Z00- Začs *et al.* (2000).

Chapter 4

Formation Scenarios of CEMP-s and CEMP-r/s stars: identifying production mechanisms for CEMP-r/s stars*

4.1 Introduction

A comprehensive understanding of the formation scenarios and the formation sites for different classes of stars is indispensable to assimilate the underlying physical conditions of nucleosynthesis. As n-capture nucleosynthesis takes place in extreme conditions, it is pivotal to explore the possible formation sites for the stars showing enhancement of n-capture elements. A number of different scenarios describing the

*Main results of this work are published in Goswami and Goswami (2020) & Goswami *et al.* (2021).

origin of enhanced heavy elements on the surface chemical composition of CEMP-*s* and CEMP-*r/s* stars are available in the literature (Jonsell *et al.* 2006; Lugaro *et al.* 2009).

For *s*-process enrichment, a binary AGB nucleosynthesis model is considered where the star we observe (secondary) is in a binary configuration with an evolved star (primary). This primary star completes the AGB phase and becomes a white dwarf at the end of its evolution. During the evolutionary process, the object expels *s*-process enriched matter, which is then accreted by the secondary star. In addition, nucleosynthesis occurring in the inter-shell region of the secondary star may also contribute to both the light and the heavy *s*-process element enrichment when the synthesised material is brought to the surface via different processes like convective mixing (due to temperature gradient), non-convective processes like thermohaline mixing (due to density gradient) (Stancliffe *et al.* 2007), rotation mechanisms, and TDU.

Several proposed scenarios are also being put forward for the origin of the CEMP-*r/s* stars by several authors: i) the primary, after passing through the AGB phase, explodes as a type 1.5 supernova (Zijlstra 2004; Wanajo *et al.* 2006); ii) the enrichment of *r*-process elements is produced via an accretion-induced collapse (Cohen *et al.* 2003; Qian and Wasserburg 2003) and enriches the secondary; iii) a triple star system having a massive star is responsible for enriching the secondary star (Cohen *et al.* 2003); iv) a primordial origin (i.e. the environment, in which the CEMP-*r/s* star was born, was already enriched by *r*-process elements) (Bisterzo *et al.* 2011). Another nucleosynthesis process, invoked by Cowan and Rose (1977) is a *n*-capture regime at neutron densities intermediate between those for *s*-process and *r*-process, and now termed as intermediate (i)-process. Multiple stellar sites such as very metal-poor AGB stars (Campbell and Lattanzio 2008; Cristallo *et al.* 2009a; Campbell *et al.* 2010; Stancliffe *et al.* 2011), very late thermal pulse (VLTP) in post-AGB stars (Herwig *et al.* 2011), super-AGB stars (Doherty *et al.* 2015;

Jones *et al.* 2016), low-metallicity massive stars (Clarkson *et al.* 2018; Banerjee *et al.* 2018), and rapidly accreting white dwarfs (Denissenkov *et al.* 2017; Côté *et al.* 2018; Denissenkov *et al.* 2019) are expected to meet the conditions necessary for the *i*-process.

In the following, we have discussed these formation scenarios in the context of our programme stars. We note that our sample contains three CEMP-*r/s* stars and six CEMP-*s* stars (Table 3.6).

Long term radial velocity monitoring programmes (McClure 1983, 1984; McClure and Woodsworth 1990; Jorissen *et al.* 1998; Lucatello *et al.* 2005; Jorissen *et al.* 2016b; Hansen *et al.* 2016b; Jorissen *et al.* 2019) show that CH, Ba, CEMP-*s* and CEMP-*r/s* stars belong to binary systems with now invisible white dwarf companions. As discussed in Chapter 3, most of our programme stars show radial velocity variations. Jorissen *et al.* (2016b) confirmed the objects HD 145777, HE 0017+0055, HE 0507–1653 & HE 2144–1832 to be in binary systems with long periods. The object HE 0319–0215 is also confirmed as a binay by Hansen *et al.* (2016b). While CD–27 14351 shows radial velocity variations (Table 3.2), information on binarity is not available for HE 0930–0018, HE 1023–1504 & HE 2339−0837. We have examined in detail if *i*-process nucleosynthesis could explain the abundance pattern observed in the programme stars enhanced in both *s*- and *r*-process elements. We have also extended this study to eight more CEMP-*r/s* stars found in the literature.

4.2 Formation Scenario of CEMP-*s* stars

As in the cases of Ba and CH stars, CEMP-*s* stars show enhancement of *s*-process elements and are found to be in binary systems with white dwarf companions.

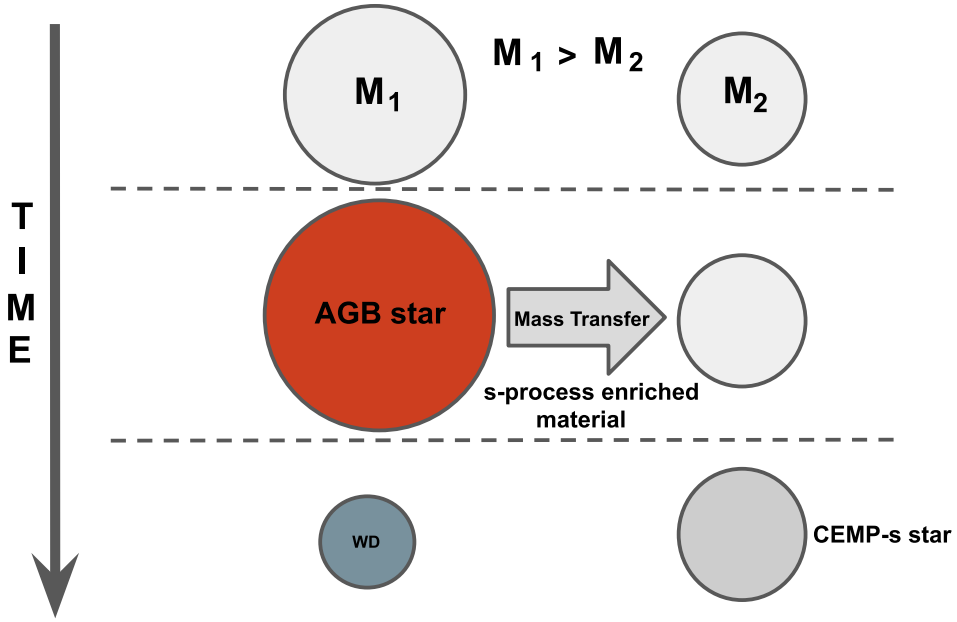

FIGURE 4.1: AGB mass-transfer in a binary system.

The widely accepted formation scenario for these stars is the AGB mass-transfer mechanism in a binary system. As shown in Figure 4.1, it is considered that these stars are formed in binary systems, where the slightly more massive star (the primary) evolves through the AGB phase faster than the companion (the secondary). In the AGB phase, the primary star produces *s*-process elements along with carbon and passes the newly synthesised material to the secondary via two prime mass-transfer mechanisms: wind accretion and Roche-lobe overflow (RLOF) (Abate *et al.* 2013). We observe the secondary star as Ba/CH/CEMP-*s* star. The observed enhancement of heavy elements in CD−27 14351, HD 145777, HE 0319–0215, HE 0507–1653, HE 0930–0018, HE 1023–1504 may be attributed to binary companions in such a binary system.

4.3 Formation Scenarios of CEMP-*r/s* stars

We have discussed in Chapter 1 that *s*- and *r*-process nucleosynthesis take place at different stellar sites with different physical conditions of neutron-densities and *n*-capture time-scales. The CEMP-*r/s* stars show enhancement of both *s*- and *r*-process elements and hence draw special attention regarding their formation and origin of the abundance peculiarities. Several formation scenarios have been proposed in the literature to explain the unusual abundance patterns of CEMP-*r/s* stars. Jonsell *et al.* (2006) and Lugaro *et al.* (2009) discussed a few scenarios to explain the origin of CEMP-*r/s* stars and found that none of them are conclusive and free from uncertainties (Abate *et al.* 2016). In the following we have discussed and critically examined the formation scenarios in the context of the CEMP-*r/s* stars in our sample.

4.3.1 Radiative Levitation

Radiative levitation is a process identified in hot stars (e.g. Przybylski's star), where due to the large photon absorption cross-sections of the partially ionized species of heavy elements, radiative pressure pushes the elements outwards, causing the abundances of the heavy elements in the atmospheres of the stars to appear higher than the solar abundances. This process was suggested as responsible for the formation of CEMP-*r/s* stars. However, Richard *et al.* (2002) and Matrozis and Stancliffe (2016) have found in their simulations that the radiative levitation process can take place in the main-sequence and main-sequence turn-off phases of hot stars due to their thin convective envelopes. CEMP (-*s* & -*r/s*) stars are generally observed to be subgiants or giants and the effect of radiative levitation is found to be negligible in giants and low-temperature objects. All the objects in our sample that we have found to be enhanced in both *s*- and *r*-process elements

are low-temperature (4160−4940 K) objects with log g values in the range 0.6 to 1.40 cgs units. Radiative levitation thus cannot be a process responsible for the observed overabundance of heavy elements in these stars. Cohen *et al.* (2003), Jonsell *et al.* (2006), and Abate *et al.* (2016) also discussed this scenario at length and rejected radiative levitation as a possible formation scenario of CEMP-*r/s* stars.

4.3.2 Self-pollution of a star formed from *r*-rich ISM

According to this scenario (Figure 4.2), a CEMP-*r/s* star is formed from an *r*-process material enriched ISM, which may happen because of an early supernova, and later self-contaminated by carbon and *s*-process materials in the AGB phase (Hill *et al.* 2000; Cohen *et al.* 2003; Jonsell *et al.* 2006). As suggested by Jonsell *et al.* (2006) and Abate *et al.* (2016), this hypothesis may be rejected based on the fact that the CEMP-*r/s* stars observed to date have not yet reached the AGB phase of evolution in order to undergo *s*-process nucleosynthesis. Although the stars that we have studied are giants, the absence of Tc lines and estimated low $^{12}C/^{13}C$ values suggested the extrinsic nature of the overabundance of *n*-capture elements. So, this scenario cannot explain the abundance peculiarities observed in our programme stars.

4.3.3 SN and AGB pollution of a star in triple system

In this scenario (Figure 4.3), a CEMP-*r/s* star can be the tertiary in a triple star system, where the most massive one evolves the fastest and undergoes supernova explosion making the other two stars *r*-rich. Then the more massive one among the rest of the two stars evolves through AGB phase and dumps carbon and *s*-process

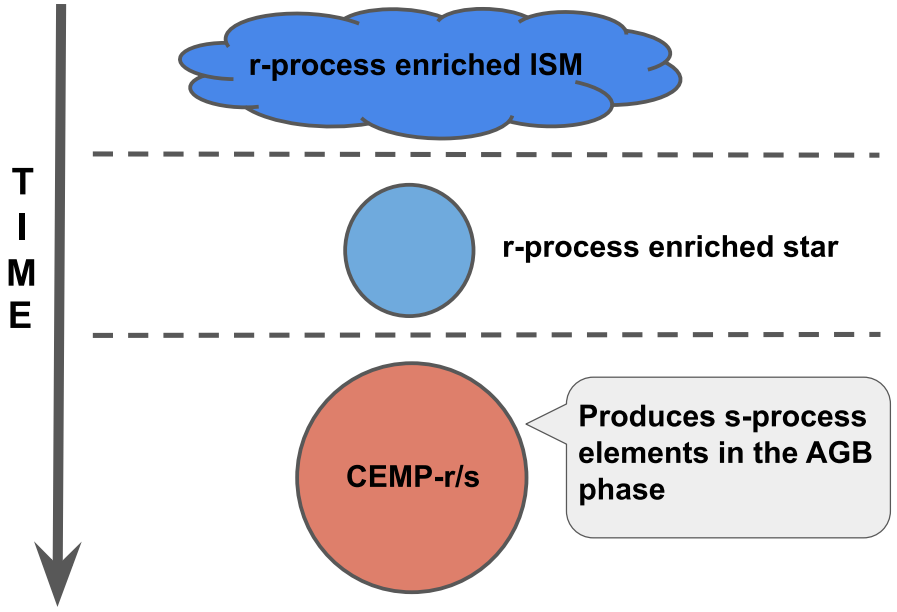

FIGURE 4.2: Self-pollution of a star formed from *r*-rich ISM.

elements in the other star, which we now observe as CEMP-*r/s* star (Cohen *et al.* 2003; Jonsell *et al.* 2006). This scenario is discarded because it seems highly unfeasible that the triple star system survives a SN explosion of such close proximity for further mass-transfer. Abate *et al.* (2016) also dismissed this hypothesis as they could not reproduce the observed frequency of CEMP-*r/s* stars among CEMP-*s* stars they studied.

4.3.4 AGB and 1.5 SN pollution of a star in a binary system

According to this scenario, as shown in Figure 4.4, a CEMP-*r/s* star is formed in a binary system, where the primary, evolving through AGB phase, first transfers carbon and *s*-process rich material to the secondary and subsequently transfers *r*-process rich material exploding as a type 1.5 supernova (Jonsell *et al.* 2006). A

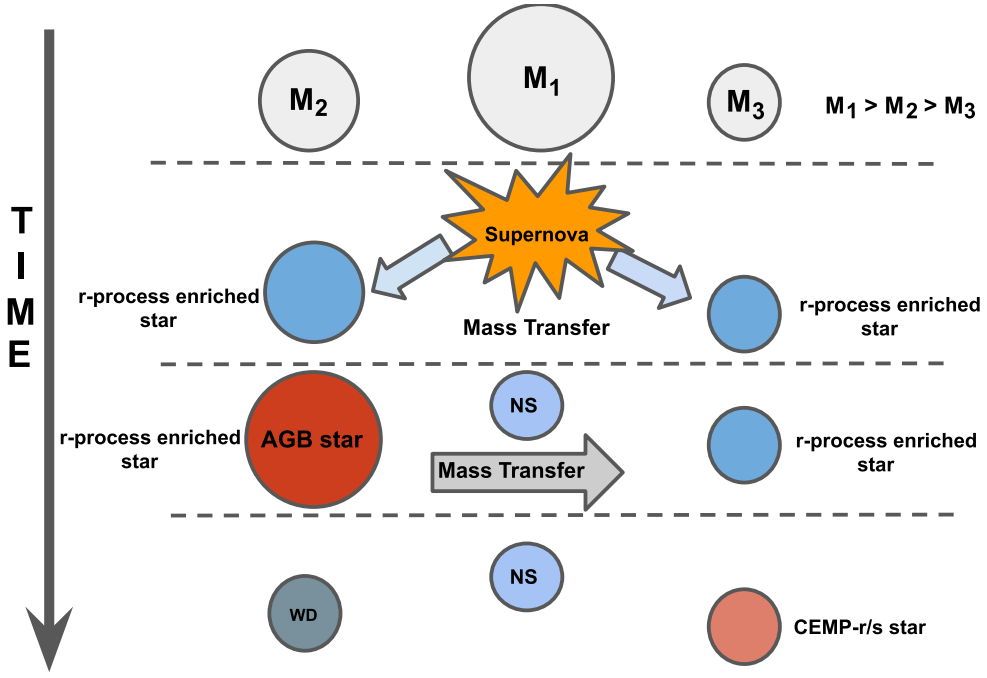

FIGURE 4.3: SN and AGB pollution of a star in triple system.

degenerate core of a high mass AGB star, due to low efficiency of mass-loss at low metallicity, can remain massive enough to exceed Chandrasekhar mass limit and explode (Zijlstra 2004). Iben and Renzini (1983) called such explosion processes as 'type 1.5 supernovae'. However, Nomoto *et al.* (1976), Iben and Renzini (1983), and Lau *et al.* (2008) found that Type 1.5 supernova disrupts the binary system as the primary star gets destroyed. So, Abate *et al.* (2016) rejected this hypothesis, as most of the CEMP-*r/s* stars belong to binary systems. Due to the same reason, this scenario is also not applicable to our programme stars.

4.3.5 AGB and accretion-induced collapse (AIC) pollution of a star in a binary system

This scenario, as shown in Figure 4.5, too considers a binary system, where the secondary is now seen as a CEMP-*r/s* star. Being the more massive among the

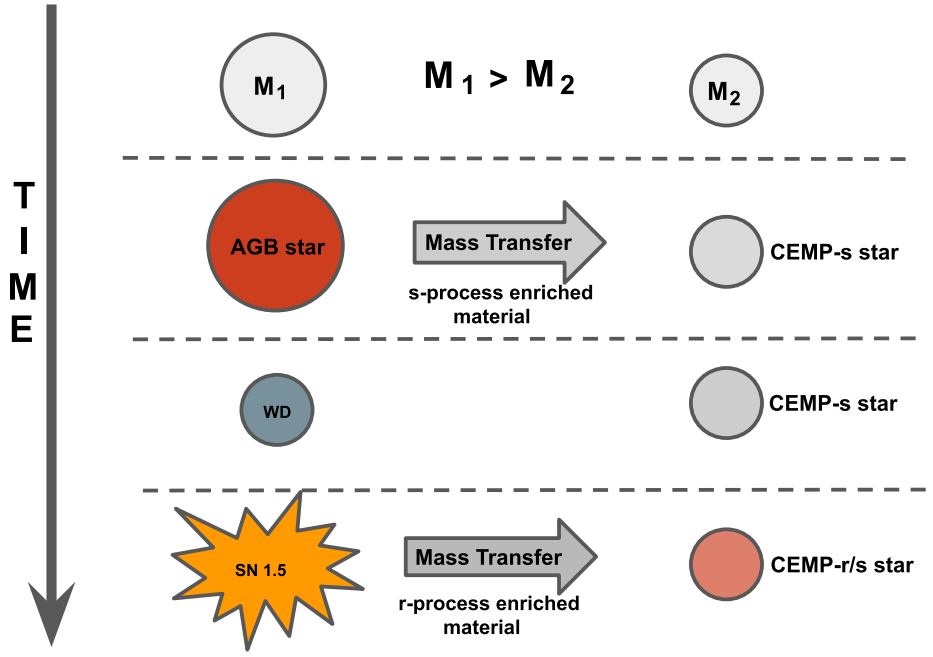

FIGURE 4.4: AGB and 1.5 SN pollution of a star in a binary system.

two, the primary evolves through the AGB phase and becomes a white dwarf transferring *s*-process rich elements to the companion at the end of its evolutionary phase. Gradually, the companion also evolves to a giant phase and transfers back material to the white dwarf triggering an accretion-induced collapse (AIC). The secondary gets polluted with *r*-process material produced due to the collapse (Cohen *et al.* 2003; Qian and Wasserburg 2003). This scenario has two major drawbacks- i) All the CEMP-*r/s* stars found to date are not in giant phases of evolution. In many cases, the observed CEMP-*r/s* stars are found to be at main-sequence turn-off stages, making the mass-accretion difficult for the white dwarf companion (Lugaro *et al.* 2009). Moreover, for this scenario to work effectively, a narrow orbital separation is necessary so that the stars remain close enough for the second phase of mass-transfer (Abate *et al.* 2016). Considering a narrow separation for the three phases of mass-transfer, Abate *et al.* (2016) calculated the expected frequency of CEMP-*r/s* stars, which did not match with the observed frequency. ii) It is quite unclear whether accretion induced collapse can really produce enough *r*-process material to match the abundance pattern observed in

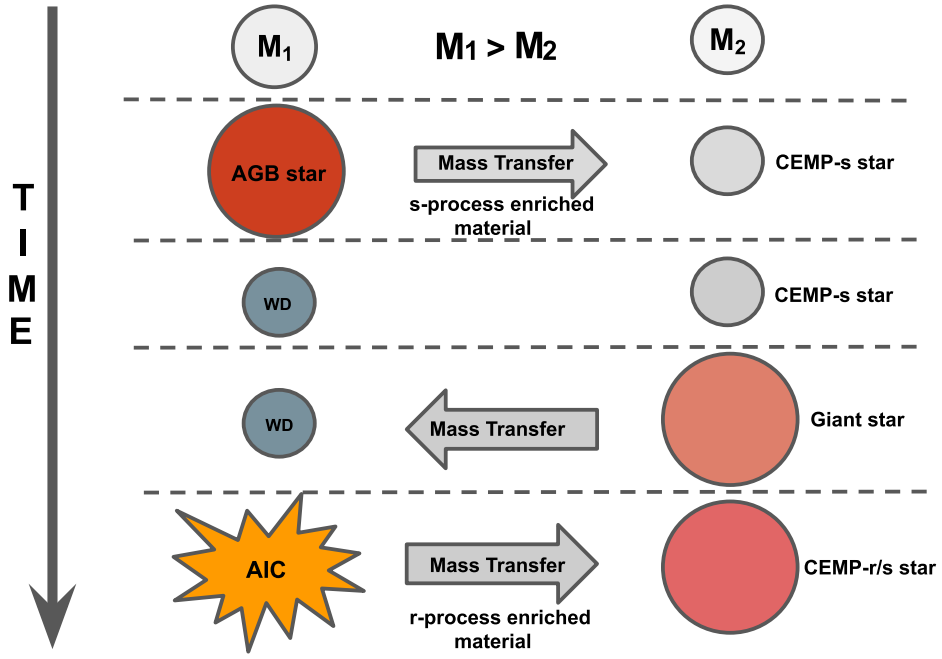

FIGURE 4.5: AGB and AIC pollution of a star in a binary system.

CEMP-*r/s* stars (Qian and Woosley 1996; Qian and Wasserburg 2003).

4.3.6 AGB-pollution of a star in binary system formed from *r*-rich ISM

In this scenario (Figure 4.6), a binary system is formed from ISM enriched in *r*-process elements, most likely due to early supernova. In the binary system, the more massive companion (primary) evolves faster and proceeds to AGB phase of evolution, where it undergoes *s*-process nucleosynthesis. Then, mass transfer during the AGB phase makes the secondary star enriched in *s*-process elements, which was already enriched with *r*-process elements (Hill *et al.* 2000; Cohen *et al.* 2003; Ivans *et al.* 2005; Jonsell *et al.* 2006; Bisterzo *et al.* 2011). Although Bisterzo *et al.* (2011, 2012) claim to reproduce, within the error bars, the observed [hs/ls] in CEMP-*r/s* and CEMP-*s* stars, there are several arguments that stand against this scenario. In particular, the correlation of the abundances of Ba and Eu cannot be

reproduced by the AGB models (Abate *et al.* 2016), and also that this scenario cannot explain the large fraction of CEMP-*r/s* stars among the CEMP-*s* stars (Jonsell *et al.* 2006; Lugaro *et al.* 2009).

The stars formed by AGB pollution in the binary system formed from *r*-rich ISM are termed as 'CEMP-*r+s* stars' (Frebel 2018; Gull *et al.* 2018).

Gull *et al.* (2018) reported a red giant CEMP star RAVE J094921.8−161722 ([Fe/H] = −2.2, [C/Fe] = 1.35) with a surprising elemental abundance pattern. The star exhibits an enhanced abundance of Pb, indicating *s*-process contribution and Th, which is produced in *r*-process nucleosynthesis. Gull *et al.* (2018) claimed that this object was the first bona fide CEMP-*r+s* star as its abundance pattern could be satisfactorily fitted only with AGB mass-transfer model taking into account initial *r*-process enhancement. Sbordone *et al.* (2020) reported the abundance analysis of the object GIU J190734.24-315102.1 located in the Sagittarius (Sgr) dwarf spheroidal (dSph) galaxy, and claimed that the abundance pattern could be best fitted only with a model considering AGB-pollution in a binary system pre-enriched with a neutron star–neutron star merger event. Due to its formation scenario this object may be referred to as a bona fide CEMP-*r+s* star.

The expected rate of occurrence of CEMP-*r+s* stars among metal-poor stars is $2\% - 3\%$ (Gull *et al.* 2018). With an occurrence rate of 3%, about two dozen *r*-II stars have been found to date (Gull *et al.* 2018), although why no other bona fide CEMP-*r+s* stars have yet been detected remains a puzzle (Frebel 2018).

4.3.7 Intermediate *n*-capture process (*i*-process)

Cowan and Rose (1977) found based on their simulations that a significantly high neutron flux (higher than that of *s*-process) can be produced by mixing different

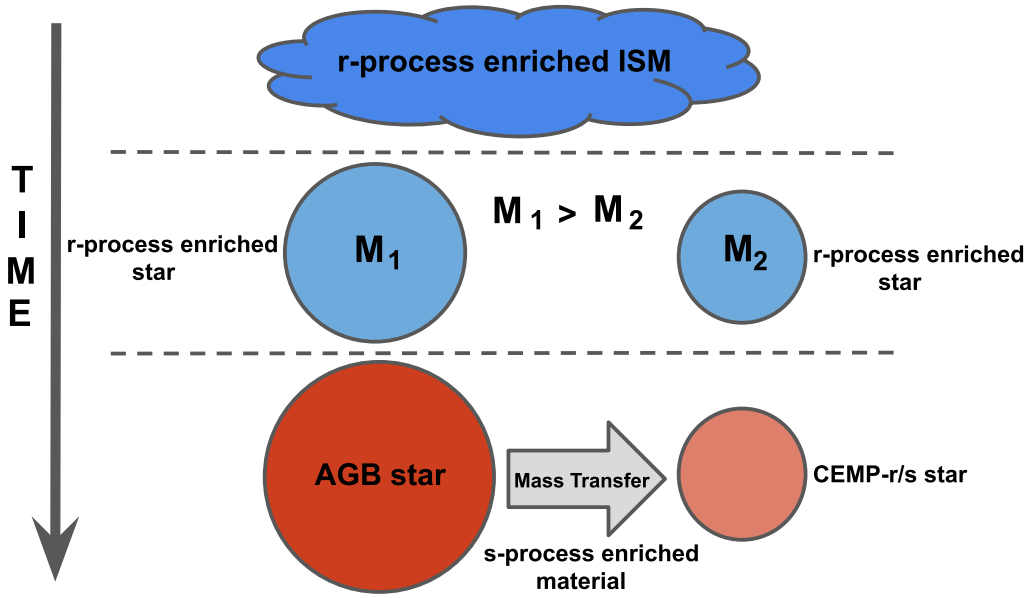

FIGURE 4.6: AGB-pollution of a star in binary system formed from r-rich ISM.

amounts of hydrogen-rich material into the intershell region of AGB stars (also known as proton ingestion episodes or PIEs), leading to the occurrence of a different type of n-capture nucleosynthesis in AGB stars. This nucleosynthesis process operating at a neutron-density ($n_n \sim 10^{15}$ cm^{-3}), which is intermediate to that of s- and r-process neutron densities (and hence called as 'i'-process) can produce both s- and r-process elements in a single stellar site (Dardelet *et al.* 2014; Hampel *et al.* 2016; Roederer *et al.* 2016; Hampel *et al.* 2019). Hampel *et al.* (2016) successfully reproduced the abundance distribution of 20 CEMP-r/s stars with the help of an i-process model. Although it is evident that the i-process can explain the abundance pattern seen in CEMP-r/s stars, the astrophysical sites of the i-process are not clearly understood. A variety of sites have been proposed where PIEs can take place, favouring the conditions for i-process nucleosynthesis. In the following Section (4.4) we will discuss this in detail.

4.4 The *i*-process nucleosynthesis

For *i*-process nucleosynthesis, we consider a formation scenario similar to that suggested for Ba, CH and CEMP-*s* stars (Figure 4.1). In the case of the formation scenario for *i*-process, the only difference is that the primary produces both *s*- and *r*-process elements in the AGB phase (unlike in the case of Ba, CH and CEMP-*s* stars where the primary produces only *s*-process elements in the AGB phase), and later pollutes the secondary with both *s*- and *r*-process elements. Recent simulations have shown that higher neutron densities of the order of 10^{12-15} cm^{-3} necessary for *i*-process are attained in very metal-poor AGB stars (Campbell and Lattanzio 2008; Cristallo *et al.* 2009a; Campbell *et al.* 2010; Stancliffe *et al.* 2011). The reactions ^{13}C(α, n)^{16}O and ^{22}Ne(α, n)^{25}Mg are the two neutron sources proposed to operate in AGB stars. The reaction ^{22}Ne(α, n)^{25}Mg that can produce a neutron-density of $\sim 10^{11-14}$ cm^{-3} needs a temperature of $\sim 3{\times}10^{8}$ K for activation, which is achieved only in intermediate-mass stars (M $\geq$ 3 M$\odot$) at the thermal pulse (TP) phase (Lugaro *et al.* 2012). As this phase is very short (a few days), in spite of high neutron-density, neutron exposure remains inefficient to produce the heavy-*s* process peak (Fishlock *et al.* 2014). The ^{13}C(α, n)^{16}O neutron source gets activated at a lower temperature ($\sim 1{\times}10^{8}$ K), and hence can operate in the interpulse phase of both low- and intermediate-mass AGB stars. Although this reaction can produce a neutron-density of $\sim 10^{7}$ cm^{-3}, the longer timescale ($\sim$10^{5} years) of the interpulse phase enables sufficient neutron exposure to produce the heavy-*s* peak. However, some authors (Masseron *et al.* 2010; Jorissen *et al.* 2016a) argue in favour of the ^{22}Ne(α, n)^{25}Mg reaction as the primary neutron source responsible for the production of the abundance peculiarity observed in CEMP-*r/s* stars.

The isotopic ratio of Mg could provide sufficient clues about the neutron source. The operation of ^{22}Ne(α, n)^{25}Mg reaction produces a large amount of ^{25}Mg, which in turn produces ^{26}Mg by *n*-capture. So, we can expect the ^{24}Mg : ^{25}Mg : ^{26}Mg ratio

to change from the terrestrial (79 : 10 : 11) value to a ratio with higher abundances of ^{25}Mg and ^{26}Mg (Scalo 1978). However, Zamora *et al.* (2004) attempted to determine Mg isotopic ratios from MgH bands in cool carbon stars and concluded that at optical wavelengths, it is not possible to derive the Mg isotopic ratios as the synthetic spectra are insensitive to variations of Mg isotopic ratios due to the presence of strong C_2 and CN molecular bands. Thus, the scope of finding a spectroscopic test to identify the neutron source responsible for the production of heavy elements in CEMP-*r/s* stars still remains open.

Another site proposed for the *i*-process nucleosynthesis, supporting binary mass-transfer scenario for the formation of CEMP-*r/s* stars, is the very late thermal pulse (VLTP) in post-AGB stars (Herwig *et al.* 2011). The abundance pattern of Sakurai's object (V4334 Sagittarii), a born-again giant, could not be reproduced by *s*-process yields. This object shows an overabundance of Rb, Sr, and Y that is two orders of magnitude higher than that of the second *s*-process peak (Asplund *et al.* 1999). Assuming proton ingestion into the He-shell convection zone, Herwig *et al.* (2011) carried out a 3D hydrodynamic simulation of a VLTP in a pre-white dwarf. They achieved a significantly high neutron-density (10^{15} cm^{-3}) and could successfully reproduce the abundance distribution of Sakurai's object. The post-AGB stars in the Large and Small Magellanic Clouds (LMC and SMC, respectively) are found to exhibit an unusual abundance pattern (van Winckel 2003). Lugaro *et al.* (2015) illustrated that the *s*-process cannot explain the abundance pattern of these stars and proposed that *i*-process might explain better the abundances of the heavy elements along with the measured low abundance of Pb. Later, Hampel *et al.* (2019) could satisfactorily fit the abundance patterns observed in seven Pb-poor post-AGB stars (including the post-AGB stars of LMC and SMC) with *i*-process models.

Simulations of super-AGB TP stars showed that proton ingestion into the convective He-burning shell is favoured following the production of *i*-process neutron-density (Doherty *et al.* 2015; Jones *et al.* 2016). Metal-poor massive stars (20 − 30 $M_{\odot}$) are also considered as *i*-process sites (Clarkson *et al.* 2018; Banerjee *et al.* 2018). A single CEMP-*r/s* star can form from the ISM contaminated by the *i*-process material ejected by metal-poor massive stars (Banerjee *et al.* 2018).

One more proposed site for *i*-process nucleosynthesis is rapidly accreting white dwarf (RAWDs) (Denissenkov *et al.* 2017; Côté *et al.* 2018; Denissenkov *et al.* 2019). Denissenkov *et al.* (2019) proposed that single CEMP-*r/s* stars could be the tertiary (with a wider orbit) in a triple star system, where it orbits a close binary with a RAWD. Later the tertiary escapes from the triple star system being polluted by *i*-process material from the RAWD when the RAWD explodes as a SNIa. Hampel *et al.* (2019) pointed out that due to the requirement of a particular sequence of events, population synthesis calculations can only decide the probability of the formation of CEMP-*r/s* stars from RAWDs.

Roederer *et al.* (2016) reported a metal-poor star HD 94028 with an underabundance of carbon ([C/Fe] = -0.06) and low Ba and Eu abundances. With the help of high-quality NUV spectra, they could estimate the abundances or upper limits of 64 species of 56 elements, including the species whose features are seen mostly in the NUV. Roederer *et al.* (2016) found that the star exhibits a supersolar [As/Ge] ratio, a solar [Se/As] ratio, and enhanced abundances of Mo and Ru. They could not reproduce this elemental pattern with any combination of *s*- and *r*-process, but an additional contribution from the *i*-process could fit the peculiar pattern. The contribution of *i*-process has also been observed in pre-solar grains in pristine meteorites (Fujiya *et al.* 2013; Liu *et al.* 2014). These observations indicate more than one astrophysical site for the *i*-process.

4.4.1 Identifying *i*-process nucleosynthesis as the possible source of the abundance pattern seen in CEMP-*r/s* stars of our sample

In order to examine whether the *i*-process model yields could reproduce the observed abundances of the CEMP-*r/s* stars, we have made a detailed comparison of the observed abundances of these stars with *i*-process model yields. At first, We briefly discuss here the theoretical works of Dardelet *et al.* (2014) and Hampel *et al.* (2016) that led to *i*-process model yields. These authors have calculated *i*-process model yields with slightly different approaches, but both the groups could successfully reproduce the observed abundance pattern of CEMP-*r/s* stars. Single-zone nuclear network calculations were used in both the studies. Assuming proton-ingestion from the H-rich envelope to the He pulse-driven convective zone (PDCZ) to be responsible for the generation of higher neutron-densities ($n_n \sim 10^{15}$ cm^{-3}) Dardelet *et al.* (2014) used a constant combined mass-fraction of C+H (= 0.7) in their simulations. They considered the termination time of the *i*-process as a free parameter for their calculations. On the other hand, Hampel *et al.* (2016) calculated the yields of the *n*-capture nucleosynthesis, assuming the nucleosynthesis to operate in the intershell region of an AGB star, at different constant neutron-densities starting from $n_n \sim 10^7$ cm^{-3} to 10^{15} cm^{-3}. Dardelet *et al.* (2014) assumed the temperature and density for the He PDCZ to be 2.0×10^8 K and 10^4 gcm^{-3} respectively. These physical input parameters are chosen so as to prevent the proton capture by ^{13}N and allow the ^{13}C(α, n)^{16}O reaction for neutron release. As a test, Hampel *et al.* (2016) tried to calculate the yields with a range of temperatures (1×10^8 K to 2.2×10^8 K) and densities (800 gcm^{-3} to 3200 gcm^{-3}), but, didn't see significant changes in the results. However, for the final simulations they adapted the parameters (T = 1.5×10^8 K and $\rho = 1600$ gcm^{-3}) of the intershell region of a low-metallicity (z = 10^{-4}), low-mass (M = 1 M$_\odot$) AGB star (Stancliffe *et al.* 2011). As initial abundances of the He PDCZ, Dardelet

et al. (2014) considered solar-abundances (except C and O), scaled down to z = 10^{-3}. The abundances of C and O are taken to be X(^{12}C)=0.5 and X(^{16}O)=0.05, which are typical abundances for the He PDCZ. Whereas Hampel *et al.* (2016) adapted the constituents of the intershell region from that of Abate *et al.* (2015). A high neutron exposure of $\tau \sim 495$ mb^{-1} is ensured by adjusting the run times of the models. Due to such high neutron exposures, the abundance pattern of heavy elements and the seed nuclei comes to an equilibrium, which makes the element-to-element ratio a function of constant neutron-density.

In the model of Dardelet *et al.* (2014), almost all of the ^{12}C isotope get transformed into ^{13}N during the first second of run-time. Then in 9.97 minutes, ^{13}N decays to form ^{13}C, which captures α to release neutrons with high neutron-densities through the reaction ^{13}C(α, n)^{16}O. The neutron exposure (τ) increases with time, reaching up to $10 - 50$ mb^{-1} and subsequently, the heavier elements are produced. This model could successfully reproduce the observed abundance pattern of three CEMP-*r/s* stars. On the other hand, Hampel *et al.* (2016) noticed that when the neutron exposure was kept switched on for lower neutron densities ($n_n \sim 10^7$ cm^{-3}), typical *s*-process abundance pattern is produced with stable peaks of ls (Sr, Y, Zr) and hs (Ba, La, Ce) elements. But with higher neutron-densities ($n_n = 10^{12} - 10^{15}$ cm^{-3}), both the peaks of ls and hs elements shift to lighter elements. In particular, a peak at ^{135}I is formed due to the *i*-process neutron-densities. Then, the neutron exposure is turned off for t = 10 Myr. During this time, it is noticed that unstable isotopes decay to produce stable isotopes at ls and hs peaks. The decay of ^{135}I produces ^{135}Ba. With increasing neutron densities, abundances of Ba and Eu are found to increase. This is how the abundance pattern gets modified due to *i*-process. Using this *i*-process model, Hampel *et al.* (2016) could successfully reproduce the observed abundance pattern of twenty CEMP-*r/s* stars, including the three previously reproduced by the *i*-process model of Dardelet *et al.* (2014).

We have used the recent model predictions ([X/Fe]) for neutron densities ranging

from $n_n \sim 10^9 - 10^{15}$ cm^{-3} (Hampel *et al.* 2016), and compared with the elemental abundance pattern of our sample of CEMP-*r/s* stars. We have followed the procedure discussed in Hampel *et al.* (2016) and used the equation-

$$X = X_i(1 - d) + X_{\odot}d, \tag{4.1}$$

where X_i is the model yield, $X_{\odot}$ is the solar-scaled abundance, and d is a dilution factor.

Figure 4.7 shows the best-fit models with appropriate neutron densities and corresponding dilution factors. It is seen that the *i*-process model with neutron densities of $n_n \sim 10^{13}$ cm^{-3}, 10^{15} cm^{-3}, and 10^{14} cm^{-3} closely fit the observed abundances of HE 2144−1832, HE 0017+0055, and HE 2339−0837, respectively. The best model fit for HD 145777 is found at a neutron-density of $n_n \sim 10^{10}$ cm^{-3}.

4.5 Identifying the formation mechanisms of literature CEMP-*r/s* stars

In order to understand the origin of the abundance patterns of heavy elements of stars, we have chosen a sample of eight stars that were previously reported as CEMP-*r/s* stars by various authors (Goswami *et al.* 2006; Goswami and Aoki 2010; Allen *et al.* 2012; Hansen *et al.* 2019; Purandardas *et al.* 2019). For these objects, in spite of several studies, the production mechanisms leading to the observed abundance pattern remained poorly understood. Hence, we have undertaken to examine if the *i*-process could explain the observed abundance patterns.

The objects are selected following CEMP stars criteria (i.e., [Fe/H] < -1, and

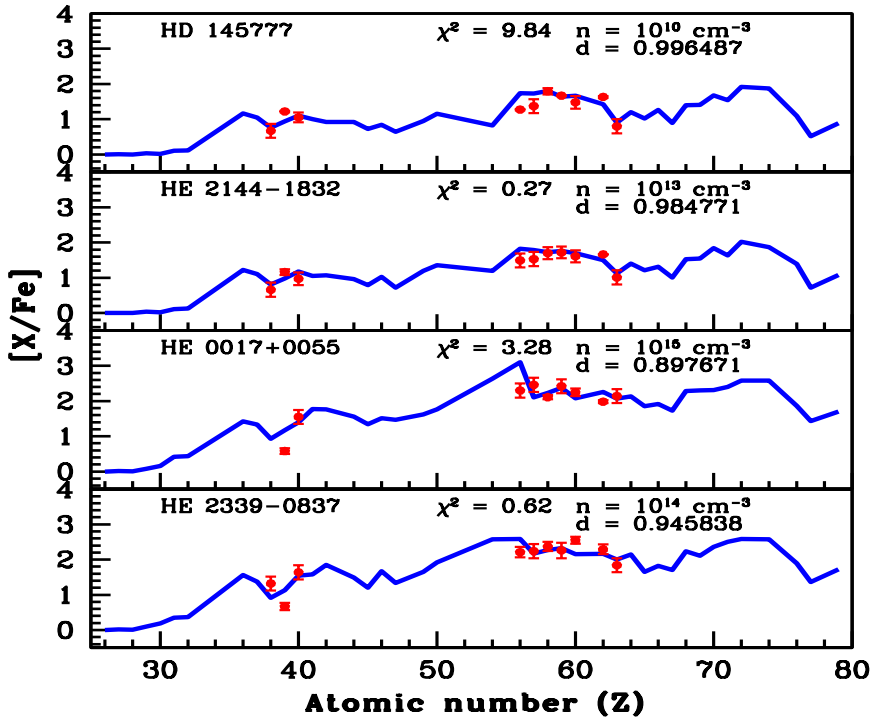

FIGURE 4.7: Best-fit *i*-process model (solid blue curve) for the three CEMP-*r/s* (HE 0017+0055, HE 2144–1832 and HE 2339–0837) stars and a CEMP-*s* (HD 145777) star. The points with error bars indicate the observed abundances.

[C/Fe] > 0.7), and have metallicity in the range $-1.70 <$ [Fe/H] < -2.70. The atmospheric parameters of the sample stars are presented in Table 4.1. The abundance ratios of *n*-capture elements and carbon with respect to Fe are presented in Table 4.2.

The object CD–28 1082 was found to be a CEMP-*r/s* star with [Ba/Fe] = 2.09, [Eu/Fe] = 2.07 and [Ba/Eu] = 0.02 with a $^{12}C/^{13}C$ ratio ~ 16 (Purandardas *et al.* 2019). The objects HE 0002−1037, HE 0059−6540 and HE 0151−6007 have been reported as CEMP-*r/s* stars by Hansen *et al.* (2019). These three objects exhibit abundances of Ba and Eu in the ranges $1.7 <$ [Ba/Fe] < 2.3 and $1.5 <$ [Eu/Fe] < 2.3 with [Ba/Eu] < 0.5 in each case. Hansen *et al.* (2019) estimated the $^{12}C/^{13}C$ ratio to be 24 and 1 for the objects HE 0002−1037 and HE 0059−6540 respectively. The kinematic analysis shows that all these four sample stars belong to the inner halo population in the Galaxy. Allen *et al.* (2012) classified the objects CS 29503−010

TABLE 4.1: **Atmospheric parameters of the literature CEMP-*r/s* stars.**

Star name	T_{eff} (K)	log g	ζ (km s^{-1})	[Fe/H]
CD−28 1082[1]	5200	1.90	1.42	−2.45
CS 29503−010[2]	6050	3.66	1.60	−1.70
CS 29528−028[2]	7100	4.27	1.20	−2.15
HD 209621[3]	4500	2.00	2.00	−1.93
HE 0002−1037[4]	5010	2.00	1.80	−2.40
HE 0059−6540[4]	5040	2.10	1.80	−2.20
HE 0151−6007[4]	4350	1.00	2.10	−2.70
HE 1305+0007[5]	4750	2.00	2.00	−2.01

1. Purandardas *et al.* (2019), *2*. Allen *et al.* (2012), *3*. Goswami and Aoki (2010), *4*. Hansen *et al.* (2019), *5*. Goswami *et al.* (2006).

and CS 29528−028 to be CEMP-*r/s* stars with [Ba/Fe] = 1.81 & 2.49 and [Eu/Fe] = 1.69 & 2.16 respectively on the basis of their analysis. Elemental abundances of two CEMP-*r/s* stars HE 1305+0007 and HD 209621 have been taken from Goswami *et al.* (2006) and Goswami and Aoki (2010) respectively. Tsuji *et al.* (1991) and Goswami *et al.* (2006) estimated $^{12}C/^{13}C$ ratio to be ~ 10 for both the objects HD 209621 and HE 1305+0007.

4.5.1 Comparison of the observed abundances of literature CEMP-*r/s* stars with *i*-process model predictions

The best fit models with appropriate neutron-densities and corresponding dilution factors are shown in Figure 4.8. The best fit neutron-density for each of the sample stars is adopted to be that value for which we got the minimum value of 'χ^2' (where χ^2 measures the differences between modelled and observed values).

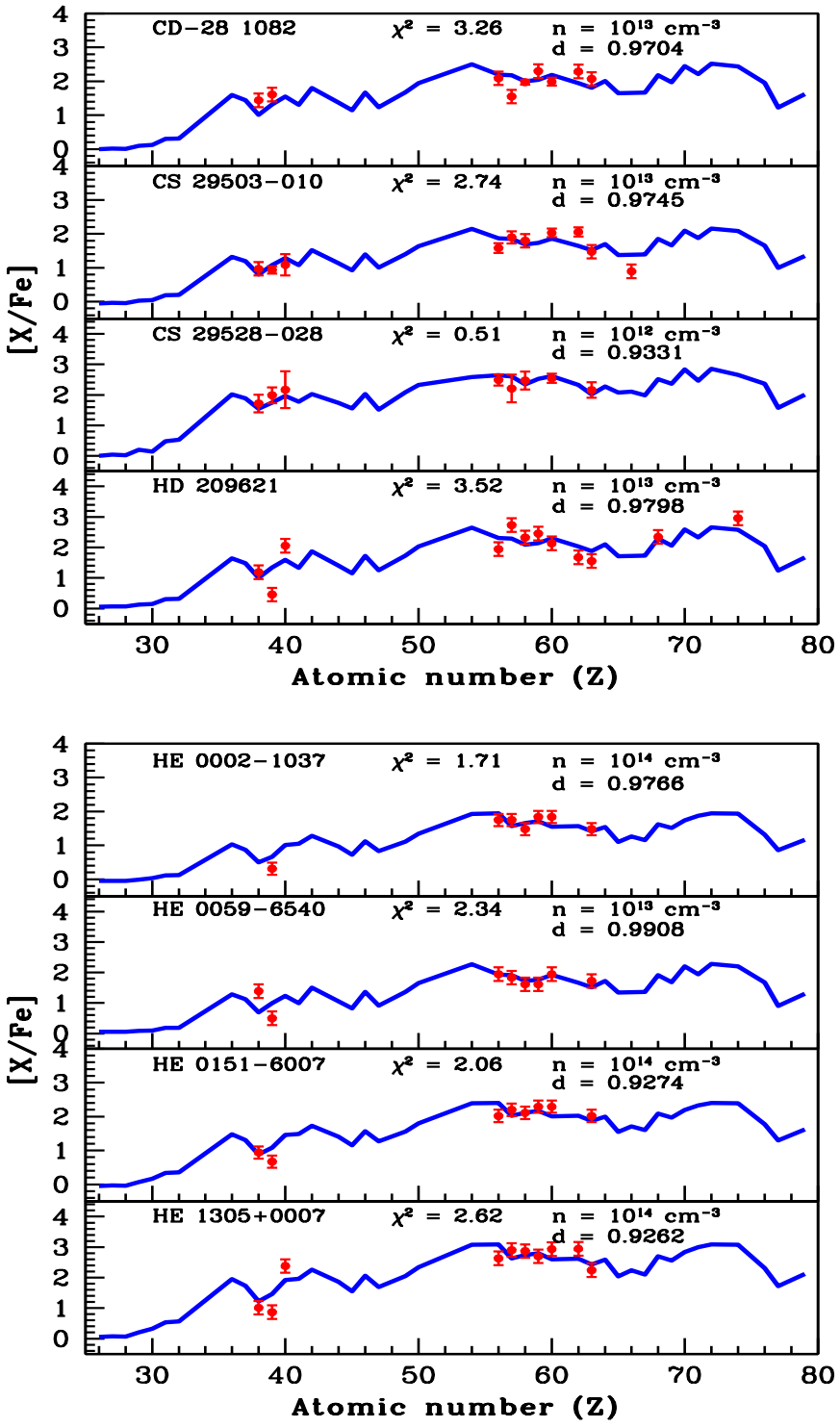

FIGURE 4.8: Best-fit *i*-process model (solid blue curve) for the literature sample of CEMP-*r/s* stars. The points with error bars indicate the observed abundances.

TABLE 4.2: **Abundance ratios of *n*-capture elements of the literature CEMP-*r/s* stars.**

Star name	[Fe/H]	[C/Fe]	[Sr/Fe]	[Y/Fe]	[Zr/Fe]	[Ba/Fe]	Ref
CD−28 1082	−2.45	2.19	1.44	1.61	-	2.09	1
CS 29503−010	−1.70	1.65	1.13	1.09	1.26	1.81	2
CS 29528−028	−2.15	2.76	1.72	1.99	2.17	2.49	2
HD 209621	−1.93	1.25	1.02	0.36	1.80	1.70	3
HE 0002−1037	−2.40	1.90	<1.00	0.40	-	2.00	4
HE 0059−6540	−2.20	1.40	1.20	0.40	-	1.70	4
HE 0151−6007	−2.70	1.70	1.10	0.80	-	2.30	4
HE 1305+0007	−2.01	1.84	0.86	0.73	2.09	2.32	5
Star name	[La/Fe]	[Ce/Fe]	[Pr/Fe]	[Nd/Fe]	[Sm/Fe]	[Eu/Fe]	Ref
CD−28 1082	1.55	1.97	2.30	1.99	2.29	2.07	1
CS 29503−010	2.16	2.05	-	2.31	2.34	1.69	2
CS 29528−028	2.21	2.47	-	2.54	-	2.16	2
HD 209621	2.41	2.04	2.16	1.87	1.46	1.35	3
HE 0002−1037	2.00	1.70	2.10	2.10	-	1.70	4
HE 0059−6540	1.60	1.40	1.40	1.70	-	1.50	4
HE 0151−6007	2.50	2.40	2.60	2.60	-	2.30	4
HE 1305+0007	2.56	2.53	2.38	2.59	2.60	1.97	5

References: 1. Purandardas *et al.* (2019), 2. Allen *et al.* (2012), 3. Goswami and Aoki (2010), 4. Hansen *et al.* (2019), 5. Goswami *et al.* (2006).

We have found that *i*-process models with neutron-densities of $n_n \sim 10^{12}$ cm^{-3} to 10^{14} cm^{-3} closely fit the observed abundances of the sample stars. We have obtained a neutron-density of $n_n \sim 10^{14}$ cm^{-3} for the star HE 1305+0007. Hampel *et al.* (2019) also stdied this object and reported similar neutron-density. In their *i*-process models Hampel *et al.* (2019) considered neutron-exposure (τ) as a free parameter along with dilution factor (d). Varying 'd' and 'τ' at different constant neutron-densities, they could fit the observed abundances of HE 1305+0007 and HD 209621 with models of neutron-densities, $n_n \sim 10^{14}$ cm^{-3} and 10^{13} cm^{-3}

respectively. We, too, got the best fit at $n_n \sim 10^{13}$ cm^{-3} for the object HD 209621 taking only 'd' as a free parameter with constant 'τ'.

4.6 Conclusions

In the context of the double enhancement (enhanced in both *s*- and *r*-process elements) seen in the CEMP-*r/s* stars, we have discussed different formation scenarios of CEMP-*r/s* stars. The absence of Tc lines and the low values of $^{12}C/^{13}C$ indicate the extrinsic nature of the programme stars. We have examined if *i*-process stellar yields could adequately explain the enhancement in both *s*- and *r*-process elements observed in the programme stars as well as in a selected sample of eight CEMP-*r/s* stars from literature. We have seen that *i*-process models of Hampel *et al.* (2016) can satisfactorily reproduce the observed overabundance of heavy elements in the CEMP-*r/s* stars. The *i*-process model (Hampel *et al.* 2016) with neutron-density, $n_n \sim 10^{13}$ cm^{-3}, $n_n \sim 10^{14}$ cm^{-3}, and $n_n \sim 10^{15}$ cm^{-3} give the best fit to the observed overabundance of heavy elements in the stars HE 2144−1832, HE 2339−0837 and HE 0017+0055 respectively. For HD 145777, in order to fit the observed abundances, an *i*-process model with neutron-density of 10^{10} cm^{-3} is needed. This is towards the higher limit of the neutron-density required for *s*-process nucleosynthesis. The *i*-process stellar yields required to fit the observed abundance patterns of the literature sample of eight stars are found to correspond to neutron-densities as high as 10^{12} cm^{-3} to 10^{14} cm^{-3}.

Chapter 5

Classification criteria of CEMP-s and CEMP-r/s stars: analysis of shortcomings and proposed improvements*

5.1 Introduction

In order to explain the nature of the emerging CEMP stars, Beers and Christlieb (2005) introduced for the first time four subclasses of CEMP stars using only two n-capture elements, Ba and Eu (due to the observational limitations). This scheme of classification is a guide to the community to use the unifying nomenclature and to facilitate further advances. However, since the classification of Beers and Christlieb (2005), various authors (Jonsell *et al.* 2006; Masseron *et al.* 2010;

*Main results of this work are published in Goswami *et al.* (2021).

Norris *et al.* 2010; Bisterzo *et al.* 2011; Bonifacio *et al.* 2015; Maeder and Meynet 2015; Yoon *et al.* 2016; Abate *et al.* 2016; Hansen *et al.* 2016c; Frebel 2018; Hansen *et al.* 2019; Skúladóttir *et al.* 2020) put forward different criteria for identification and classification of the CEMP stars. The ever-growing data sets and the advancement of theoretical predictions require further revisions of the classification schemes, and thus revisiting these classification schemes is extremely important and unavoidable.

Among the CEMP stars, distinguishing the CEMP-*s* and CEMP-*r/s* stars is crucial in order to understand the physical and nucleosynthetic processes responsible for the abundance patterns of the two subclasses. However, the object HD 145777 is found to fall into different subclasses when classified based on the different classification schemes put forward by different groups of authors. To remove the uncertainties and clear the confusion regarding its classification, we have revisited the classification schemes of CEMP-*s* and CEMP-*r/s* stars found in the literature. From a detailed investigation of different classifiers of CEMP stars, we have seen that none of the existing classification criteria could clearly distinguish the CEMP-*s* and CEMP-*r/s* stars. We have put forward a new classification scheme to distinguish the two subclasses.

5.2 Classification of CEMP-*s* and CEMP-*r/s* stars: a brief review

The subclasses of CEMP stars help us to uncover the processes by which the *n*-capture elements are produced. Depending upon the enhancement of elements produced by slow ('*s*') and rapid ('*r*') *n*-capture processes, CEMP stars are divided into different subclasses (Beers and Christlieb 2005; Jonsell *et al.* 2006; Masseron

et al. 2010; Abate *et al.* 2016; Frebel 2018; Hansen *et al.* 2019). The early sub-classification of CEMP class was given by Beers and Christlieb (2005):

- CEMP: [C/Fe] > 1.0;
- CEMP-*s*: [Ba/Fe] $> +1.0$, and [Ba/Eu] > 0.5 (characterised by enhancement of barium, which is an *s*-process indicator);
- CEMP-*r*: [Eu/Fe] $> +1.0$ (characterised by enhancement of europium, which is an *r*-process indicator);
- CEMP-*r/s*: $0.0 <$ [Ba/Eu] < 0.5 (enhanced in both barium and europium);
- CEMP-*no*: [Ba/Fe] < 0 (not enhanced in heavy elements).

Abate *et al.* (2016) adopted the following classification:

- CEMP: [C/Fe] > 1.0;
- CEMP-*s*: [Ba/Fe] $> +1.0$ and [Ba/Eu] > 0;
- CEMP-*r*: [Eu/Fe] $> +1.0$ and [Ba/Eu] ≤ 0;
- CEMP-*r/s*: [Eu/Fe] $> +1.0$, [Ba/Fe] $> +1.0$, and [Ba/Eu] > 0.0;
- CEMP-*no*: [Ba/Fe] ≤ 1.0 and [Eu/Fe] ≤ 1.0;

  These classification criteria for CEMP-*s* and CEMP-*r/s* stars are also adopted by Jonsell *et al.* (2006) and Masseron *et al.* (2010).

Frebel (2018) adopted the CEMP star definition of Aoki *et al.* (2007), and put forward a classification scheme for CEMP stars as follows:

- CEMP: [C/Fe] > 0.7 for $\log(L/L_{\odot}) \leq 2.3$ & [C/Fe] $\leq [3.0 - \log(L/L_{\odot})]$ for $\log(L/L_{\odot}) > 2.3$;
- *r* I: $0.3 \leq$ [Eu/Fe] $\leq +1.0$ and [Ba/Eu] < 0.0;
- *r* II: [Eu/Fe] $> +1.0$ and [Ba/Eu] < 0.0;
- r_{lim}: [Eu/Fe] < 0.3, [Sr/Ba] > 0.5, and [Sr/Eu] > 0.0;
- CEMP-*s*: [Ba/Fe] $> +1.0$, [Ba/Eu] $> +0.5$, [Ba/Pb] > -1.5;
- CEMP-*r+s*: $0.0 <$ [Ba/Eu] $< +0.5$ and $-1.0 <$ [Ba/Pb] < -0.5;
- CEMP-*i*: $0.0 <$ [La/Eu] < 0.6 and [Hf/Ir]$\sim$1.0 (some authors use the 'CEMP-*i*' nomenclature to indicate CEMP-*r/s* stars). The *r*-process enriched stars may or may not be carbon enhanced.

Hansen *et al.* (2019) recently gave a new classification scheme based on [Sr/Ba]:

- CEMP: [C/Fe] > 1.0;
- CEMP-*no*: [Sr/Ba] > 0.75;
- CEMP-*s*: $-0.5 <$ [Sr/Ba] < 0.75;
- CEMP-*r/s*: $-1.5 <$ [Sr/Ba] < -0.5;
- CEMP-*r*: [Sr/Ba] < -1.5.

We have seen that one of our programme stars, HD 145777, is classified as a CEMP-*r/s* star by three classification schemes (Beers and Christlieb 2005; Frebel 2018; Hansen *et al.* 2019) and as a CEMP-*s* star by the criteria discussed by Abate *et al.* (2016). Again, in Chapter 4, we have seen that for HD 145777, in order to fit the observed abundances, a model with neutron-density of 10^{10} cm^{-3} is needed. This is towards the higher limit of the neutron-density required for

s-process nucleosynthesis. So, we tried to figure out which of the classification schemes discussed above can distinguish CEMP-*s* and CEMP-*r/s* stars effectively. We have also examined if [hs/ls] can be used to classify CEMP-*s* and CEMP-*r/s* stars. As the difficulty lies in identiying the CEMP-*s* and CEMP-*r/s* stars, we focus on the classification schemes that concern these two subclasses.

5.3 Analysis of classifiers and a proposed improved classification scheme

Four objects in our sample, HD 145777, HE 0017+0055, HE 2144−1832, and HE 2339−0837, show overabundances of Ba and Eu along with other light-*s* and heavy-*s* elements. With $0 <$ [Ba/Eu] < 0.5, the objects fall in the category of CEMP-*r/s* stars if we follow the classification criteria of Beers and Christlieb (2005). But, according to the classification scheme of Abate *et al.* (2016), CEMP-*r/s* stars are those that have [Ba/Fe] and [Eu/Fe] values that are greater than unity. This criterion classifies HE 2144−1832 ([Ba/Fe] = 1.49 and [Eu/Fe] = 1.01), HE 0017+0055 ([Ba/Fe] = 2.30 and [Eu/Fe] = 2.14), and HE 2339−0837 ([Ba/Fe] = 2.21 and [Eu/Fe] = 1.84) as CEMP-*r/s* stars, and HD 145777 (with [Ba/Fe] = 1.27 and [Eu/Fe] = 0.80) as a CEMP-*s* star. All four of these objects fall in the category of CEMP-*r/s* stars if we use the criteria $0.0 <$ [La/Eu] < 0.6 given by Frebel (2018) for the CEMP-*i* subclass (we use the 'CEMP-*r/s*' nomenclature). We could not estimate the abundances of Hf, Ir, and Pb, hence the other criteria, namely [Hf/Ir] ~ 1.0 for the CEMP-*i* subclass and [Ba/Pb] > -1.5 for the CEMP-*s* subclass put forward by Frebel (2018), could not be used. However, the lower limit given on [Ba/Eu] (> 0.5) by Frebel (2018) for the CEMP-*s* subclass clearly indicates that these four stars cannot be classified as CEMP-*s* stars. If we use [Sr/Ba] as a classifier, as discussed in Hansen *et al.* (2019) with values [Sr/Ba] ~ -0.60, -0.83, and -0.89 respectively for HD 145777, HE 2144−1832, and

HE 2339−0837, they fall in the category of CEMP-*r/s* stars. As the abundance of Sr could not be estimated for the object HE 0017+0055, [Sr/Ba] could not be used to classify this object.

The objects CD−27 14351, HE 0319–0215, HE 0930–0018 and HE 1023–1504 are found to satisfy the criteria for the CEMP-*s* stars. Although based on a few classification criteria, the classification of HD 145777 and HE 0507–1653 remains uncertain; we have shown from a detailed analysis that these objects belong to CEMP-*s* stars.

5.3.1 Probing [hs/ls] as a classifier

It has been noted from various studies in the past (Bisterzo *et al.* 2011, 2012; Abate *et al.* 2015, 2016; Hampel *et al.* 2016) that [hs/ls] exhibit higher values for CEMP-*r/s* stars than that of CEMP-*s* stars. In this section we explore whether [hs/ls] can be used to distinguish CEMP-*r/s* and CEMP-*s* stars, and hence if this ratio can be used as a classifier. To accomplish this we carried out a literature survey and compiled data for 40 CEMP-*s* and 32 CEMP-*r/s* stars, and calculated [hs/ls], [Sr/Ba], and [Ba/Eu] for these stars on a homogeneous scale. We adopt the CEMP classifications of the literature objects given by the original studies and without any ambiguity. However, for some objects different groups have provided different atmospheric parameters and elemental abundances, and have assigned different classes to them. For instance, Allen *et al.* (2012) considered HE 0336+0113 to be a CEMP-*s* star, but Masseron *et al.* (2010) considered it a CEMP-*r/s* star. HE 0336+0113 exhibits [Eu/Fe] > 1.0 and shows the highest value of [Ba/Eu] ($=$ 1.45) among the CEMP stars (Cohen *et al.* 2006). Hampel *et al.* (2019), after comparing the object's observed abundances with *i*-process models, reported that the characteristic properties of HE 0336+0113 are more of *s*-process than *i*-process. This analysis prompted us to classify HE 0336+0113 as a CEMP-*s* star. Bisterzo

et al. (2011, 2012) studied most of the CEMP-*s* stars in Table 5.1 and explained their abundance peculiarities with the help of AGB models with initial masses of 1.3 − 2.0 M$\odot$. Except for SDSS J1349−0229, which is classified as a CEMP-*r/s* star (Behara *et al.* 2010), all other CEMP-*r/s* stars in Table 5.1 have been examined with *i*-process model predictions and their abundance patterns are well reproduced with *i*-process model yields (Hampel *et al.* 2016, 2019; Goswami and Goswami 2020).

The elemental abundances of the objects reported by different authors differ from each other. As different authors use different codes, model atmospheres, and line lists for their abundance analyses, it is not surprising to see the differences in their results; however, it is not an easy task to select one analysis over the others. Thus, for the objects for which the elemental abundance results from several different groups are available, we take the mean value of [Fe/H] and, similarly, the mean abundance for each element. For these cases, we use the mean [X/Fe] to calculate [hs/ls], [Sr/Ba], and [Ba/Eu]. To calculate [ls/Fe], we take the mean of the abundances of light-*s* elements (Sr, Y, Zr); similarly, the abundances of heavy-*s* elements (Ba, La, Ce, Nd) are averaged out to calculate [hs/Fe]. We do not consider the two second peak *s*-process elements Pr and Sm, as *r*-process contributes more than *s*-process to the isotopic abundances of these elements (Arlandini *et al.* 1999). Bisterzo *et al.* (2012) noted that light-*s* elements when plotted against each other show large scatter. Heavy-*s* elements also show scatter for some objects, although not as large. In order to reduce the systematic error, we calculated [ls/Fe] and [hs/Fe] only for those stars for which abundance estimates are available at least for two light *s*-process and two heavy *s*-process elements. To calculate [ls/Fe] and [hs/Fe], we also excluded those elements for which only the upper limit of abundance is mentioned in the literature. Table 5.1 presents the list of objects and their elemental abundance ratios of C, N, and heavy elements used for this analysis. Our estimates of [hs/ls] are also presented in this table. Estimates of [hs/ls], when plotted with respect to [Fe/H], show a large scatter (Figure 5.1(b)).

The use of different sets of elemental abundances instead of using a consistent set of elements for hs and ls abundances may also contribute to this observed scatter. Nevertheless, it is not always possible to have the same set of hs and ls elements for all stars, and using a consistent set of elements will tremendously affect the number of stars used to carry out the test. As metallicity decreases, the neutron-to-iron seed ratio increases and hence heavier elements are synthesised to a greater extent (i.e. [hs/ls] increases as metallicity decreases (Gallino *et al.* 1998a)). In Figure 5.1(b) we can clearly see this trend for both CEMP-*s* (black filled squares) and CEMP-*r/s* (red filled circles) stars. However, even though they have the same metallicity range, we note that the CEMP-*r/s* stars exhibit higher values of [hs/ls] than the CEMP-*s* stars (Bisterzo *et al.* 2011, 2012). This implies that neutron-density has to be higher for the formation of CEMP-*r/s* stars than of CEMP-*s* stars. Similarly, in Figure 5.1(d), we can see that the mean abundances of ls elements have the same range in the cases of CEMP-*s* and CEMP-*r/s* stars, but in CEMP-*r/s* stars the hs elements are more enhanced than in CEMP-*s* stars. This indicates that the heavy elements observed in CEMP-*r/s* stars are synthesised with a higher neutron-density than those in CEMP-*s* stars. This is because the higher neutron-density can easily overcome the barrier ($\tau \sim 0.05$ mb^{-1}) at the magic neutron number 50 (the ls peak) and effectively produces the hs peak at the magic neutron number 82. As seen from Figure 5.1(c), [Eu/Fe] increases with [hs/Fe], showing a tight correlation between [Eu/Fe] and [hs/Fe]. This correlation between heavy-*s* elements and Eu observed in the CEMP-*r/s* stars can only be explained with the help of a formation mechanism where both the *s*-process and *r*-process elements are produced in a single stellar site, which provides much support for *i*-process as a possible formation mechanism for CEMP-*r/s* stars. As [hs/ls] does not depend upon the dilution of the AGB processed material on the companion star, using a sample of CEMP-*s* and CEMP-*r/s* stars from the literature, we examined whether this ratio could be used to distinguish between CEMP-*s* and CEMP-*r/s* stars. We find that CEMP-*s* stars peak at around [hs/ls]$\sim$0.65 with a standard deviation of 0.35, and CEMP-*r/s* stars peak at [hs/ls]$\sim$1.06 with

a standard deviation of 0.32. However, even though they peak at different values of [hs/ls], we see an overlap of CEMP-*s* and CEMP-*r/s* stars in the range $0.0 <$ [hs/ls] < 1.5 (Figure 5.1(a) and 5.1(b)). Hence, [hs/ls] cannot be used as a useful classifier for CEMP-*s* and CEMP-*r/s* stars. In Figure 5.1(d) all the CEMP-*r/s* stars lie above the solid black line at [hs/Fe]$\sim$1.4; however, a limiting value of [hs/Fe] ≤ 1.4 also cannot be used as a classifier as many CEMP-*s* stars also exhibit [hs/Fe] ≥ 1.4.

5.3.2 [Sr/Ba] as a classifier

We first discuss the most recent classifier, [Sr/Ba]. When we plot [Sr/Ba] versus [Fe/H] (Figure 5.2(a)), we can see that there is a clear overlap of CEMP-*s* and CEMP-*r/s* stars with respect to [Sr/Ba] (as seen in the case of [hs/ls]) in the range $-1.6 <$ [Sr/Ba] < -0.5. In Figure 5.2(a) and 5.2(b) the grid formed by the dashed black lines and the grid formed by the dotted red lines represent the region of CEMP-*s* and CEMP-*r/s* stars, respectively, put forward by the classification scheme of Hansen *et al.* (2019). In Figure 5.2(b), it is seen that a few CEMP stars (Table 5.1) with an underabundance of Eu ([Eu/Fe] < 1.0) also fall in the region defined for CEMP-*r/s* stars. The number difference of CEMP-*s* stars in Figure 5.2(a) and 5.2(b) falling in the CEMP-*r/s* region indicates that many CEMP stars with the absence of Eu also fall in the category of CEMP-*r/s* stars by this classification criterion. We cannot separate CEMP-*s* and CEMP-*r/s* stars with the help of the [Sr/Ba] criterion (Hansen *et al.* 2019), and hence it cannot be used effectively. However, as mentioned by Hansen *et al.* (2019), this criterion may be useful to roughly distinguish between the different CEMP subclasses in low-resolution, low S/N large surveys as absorption lines of Eu are much weaker than Sr.

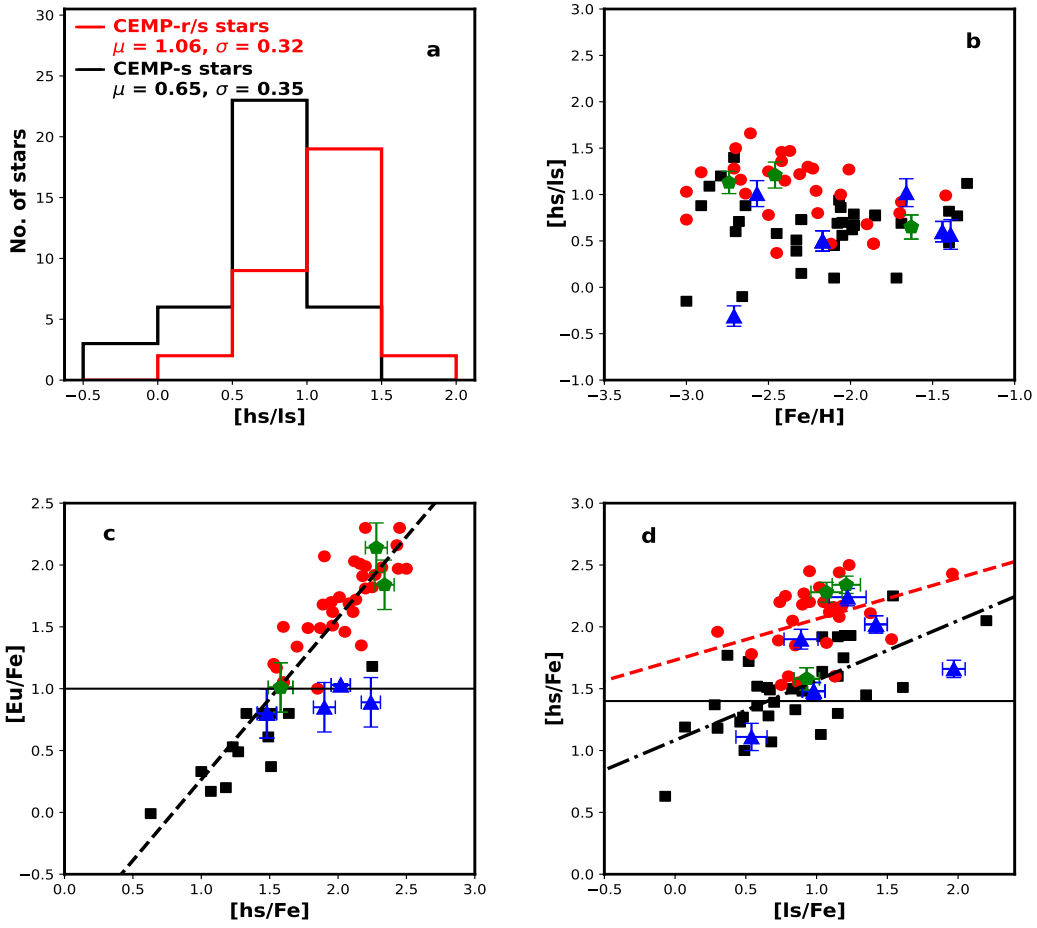

FIGURE 5.1: Filled red circles represent CEMP-*r/s* stars, filled black squares represent CEMP-*s* stars, filled blue triangles and filled green pentagons represent CEMP-*s* and CEMP-*r/s* stars of this work. In panel (a), μ and σ represent mean and standard deviation of [hs/ls] respectively for CEMP-*s* and CEMP-*r/s* stars. In panel (c), short dashed black line represents correlation between [hs/Fe] and [Eu/Fe] for CEMP-*s* and CEMP-*r/s* stars. In panel (d), dash-dotted black line and dashed red line represent correlation between [hs/Fe] and [ls/Fe] for CEMP-*s* and CEMP-*r/s* stars respectively.

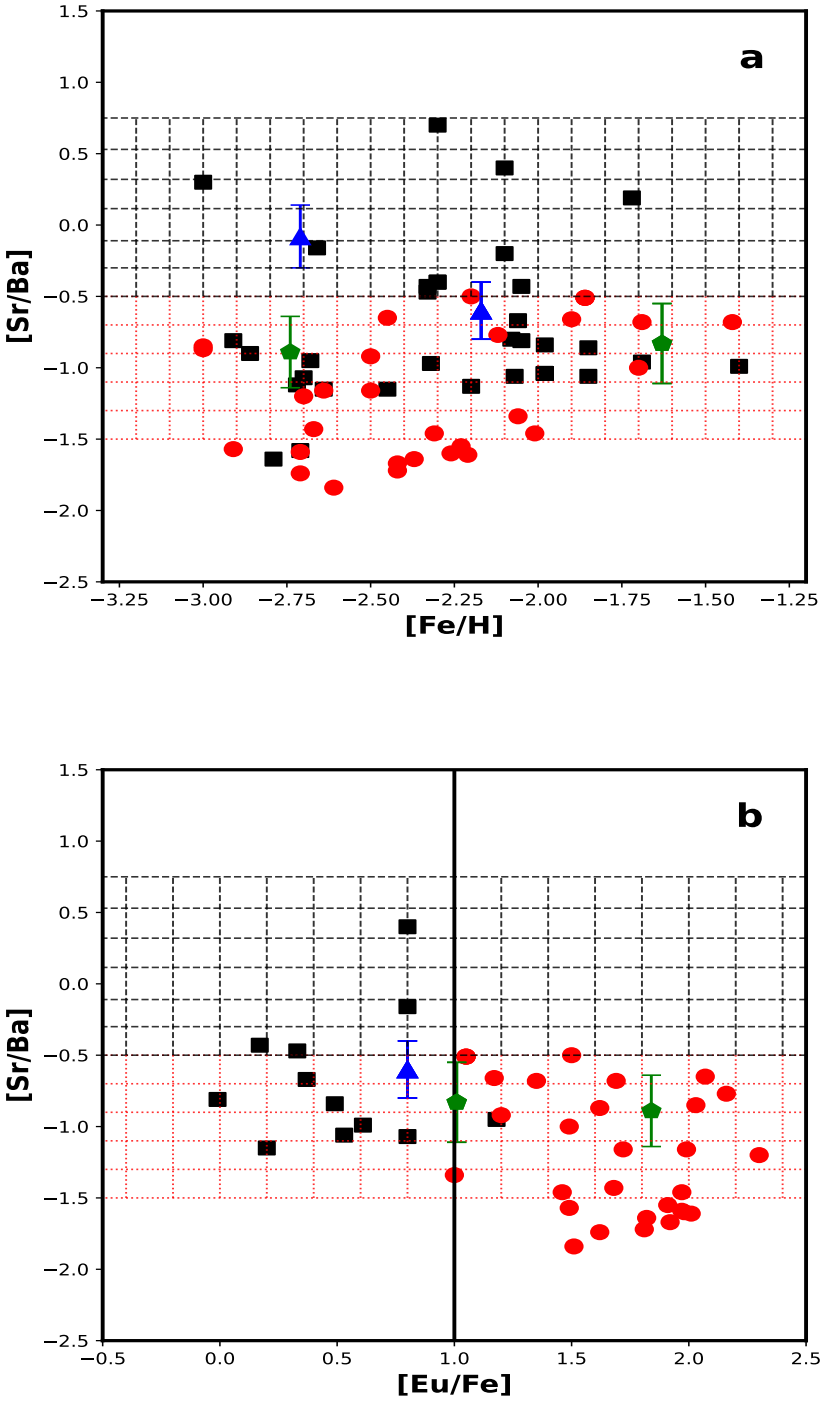

FIGURE 5.2: Filled red circles represent CEMP-*r/s* stars, filled black squares represent CEMP-*s* stars, filled blue triangles and filled green pentagons represent CEMP-*s* and CEMP-*r/s* stars of this work respectively. The grid formed by dashed black lines represent the region of CEMP-*s* stars and the grid formed by the dotted red lines represent the region of CEMP-*r/s* stars put forward by Hansen *et al.* (2019). In panel (b), solid black line at [Eu/Fe] = 1.0 separates the CEMP-*s* and CEMP-*r/s* stars according to the classification criteria adopted by Abate *et al.* (2016).

5.3.3 [Ba/Eu] as a classifier

In Figure 5.3(a) and 5.3(b) the grid formed by the dotted red lines bound the region ($0.0 <$ [Ba/Eu] < 0.5) allowed by Beers and Christlieb (2005) for CEMP-*r/s* stars. Although most of the CEMP-*r/s* stars (filled red circles), including our programme stars (filled green pentagons), reside inside the region, some fall outside the boundary. Abate *et al.* (2016) did not put an upper limit to [Ba/Eu] for CEMP-*s* and CEMP-*r/s* stars, so this criterion could be used more effectively (HE 0336+0113 and HE 0507–1653 are the only outliers). According to this criterion, CEMP-*r/s* stars are a subclass of CEMP-*s* stars and the criterion [Eu/Fe] > 1.0 separates the CEMP-*r/s* stars from the CEMP-*s* stars (Abate *et al.* 2016). Jonsell *et al.* (2006) and Masseron *et al.* (2010) also adopted the same classification scheme as Abate *et al.* (2016) to distinguish between CEMP-*s* and CEMP-*r/s* stars; however, their criteria to classify the other two subclasses (CEMP-*r* & CEMP-*no*) differ. Abundances of many of the CEMP-*r/s* stars, (e.g. CS 22881−036, CS 29497−030, HE 0143−0441, HE 2258−6358, and LP 625−44) having [Ba/Eu] > 0.5 are found to fit well with the *i*-process model (Hampel *et al.* 2016) of higher neutron-density ($n_n \sim 10^{14}$ cm^{-3}) (Hampel *et al.* 2019). This is in contrast to $0.0 <$ [Ba/Eu] < 0.5 of Beers and Christlieb (2005) for CEMP-*r/s* stars and also [Ba/Eu] > 0.5 of Frebel (2018) for CEMP-*s* stars.

5.3.4 [La/Eu] as a classifier

Unlike other classification schemes, Frebel (2018) used different sets of elements to classify CEMP-*s* and CEMP-*r/s* stars. While Ba, Eu and Pb are used in the case of CEMP-*s* stars, La, Eu, Hf, and Ir are used to classify CEMP-*r/s* stars. The abundances of Hf and Ir are usually derived from the absorption lines of Hf and Ir that are normally found in the NUV spectra. As we could not get the abundances

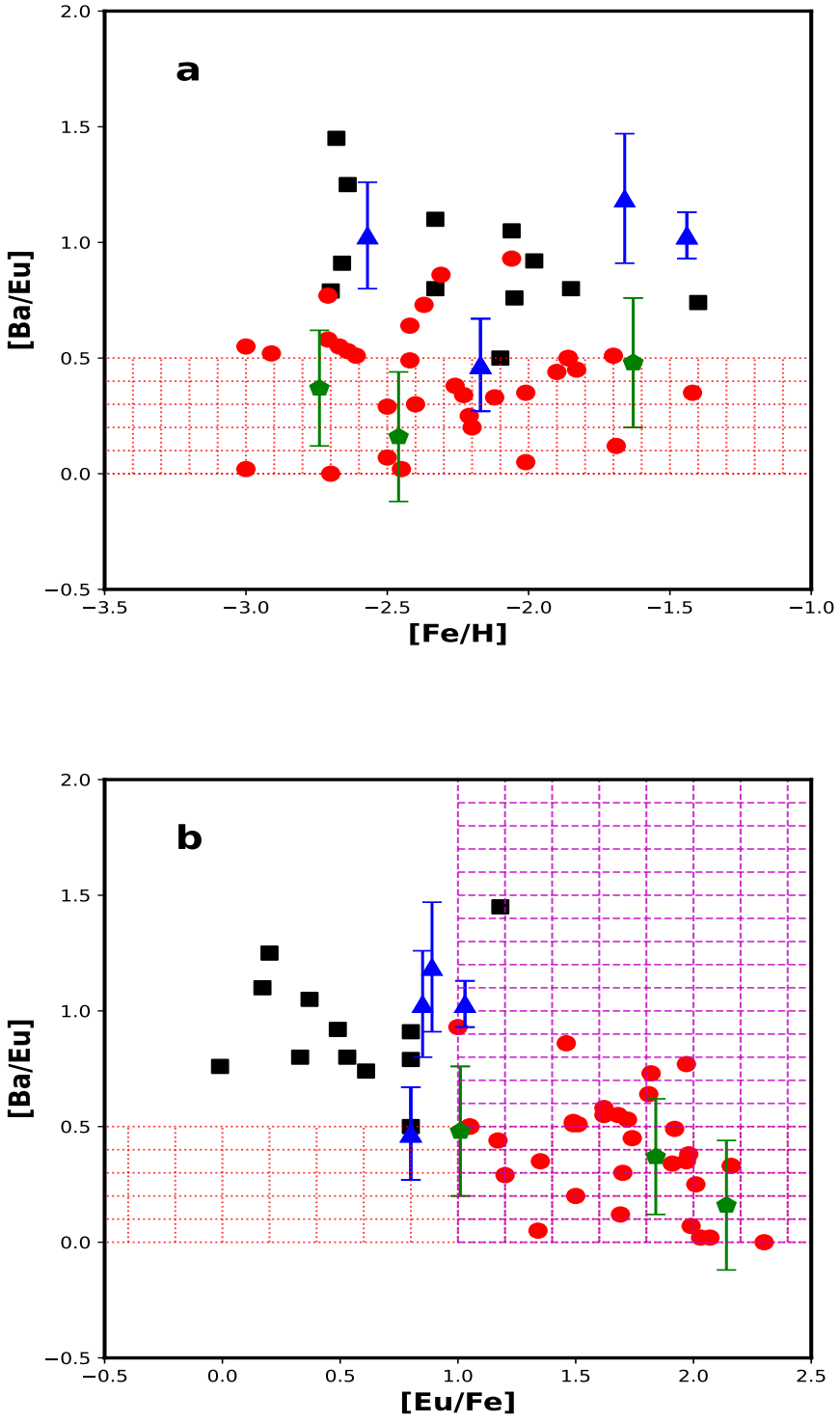

FIGURE 5.3: Filled red circles represent CEMP-*r/s* stars, filled black squares represent CEMP-*s* stars, filled blue triangles and filled green pentagons represent CEMP-*s* and CEMP-*r/s* stars of this work respectively. The grid formed by dotted red lines represent the region of CEMP-*r/s* stars put forward by Beers and Christlieb (2005). The grid formed by dashed magenta lines represent the region of CEMP-*r/s* stars put forward by Abate *et al.* (2016).

for these two elements in the literature, the criterion [Hf/Ir] $\sim$ 1.0 could not be tested with our compiled data. Theoretical validation of this criterion can be found in Table 4 of Hampel *et al.* (2016). In Figure 5.4(a), two CEMP-*r/s* stars are found to lie outside the region (the grid formed by dotted red lines) defined by 0.0 < [La/Eu] < 0.6, and two CEMP-*s* stars are located near the upper boundary ([La/Eu] $\sim$ 0.6) of the region.

5.3.5 [La/Ce] as a classifier

As models with higher neutron-densities are required to reproduce the observed overabundance of heavy elements in the CEMP-*r/s* stars, the possibility of ^{22}Ne(α, n)^{25}Mg being the primary neutron source cannot be discarded as it can produce a higher neutron-density than the ^{13}C(α, n)^{16}O reaction. Masseron *et al.* (2010) discussed the requirement of the ^{22}Ne(α, n)^{25}Mg neutron source for the production of heavy elements in CEMP-*r/s* stars on the basis of [La/Ce]. In general, [La/Ce] gives higher values in CEMP-*r/s* stars, which is possible only when ^{22}Ne(α, n)^{25}Mg operates. We have found [La/Ce] > 0.0 only in HE 0017+0055 among our programme stars. Jorissen *et al.* (2016a) also recorded a positive value for [La/Ce] for this object. In the case of the other two CEMP-*r/s* stars (HE 2144−1832 and HE 2339−0837), [La/Ce] is found to be negative. In the literature, such negative values are seen in a few other CEMP-*r/s* stars as well (Table 5.1). Furthermore, from the simulations of Hampel *et al.* (2016) at higher neutron-densities ($n_n \sim 10^{12-15}$ cm^{-3}), it can be seen that [La/Ce] does not yield a positive value for all the neutron-densities (see Table 4 of Hampel *et al.* 2016). For $n_n \sim 10^{12}$ and 10^{13} cm^{-3} [La/Ce] gives positive values, but for $n_n \sim 10^{14}$ and 10^{15} cm^{-3} [La/Ce] < 0. So we propose that [La/Ce] needs to be reconsidered as an indicator of neutron source.

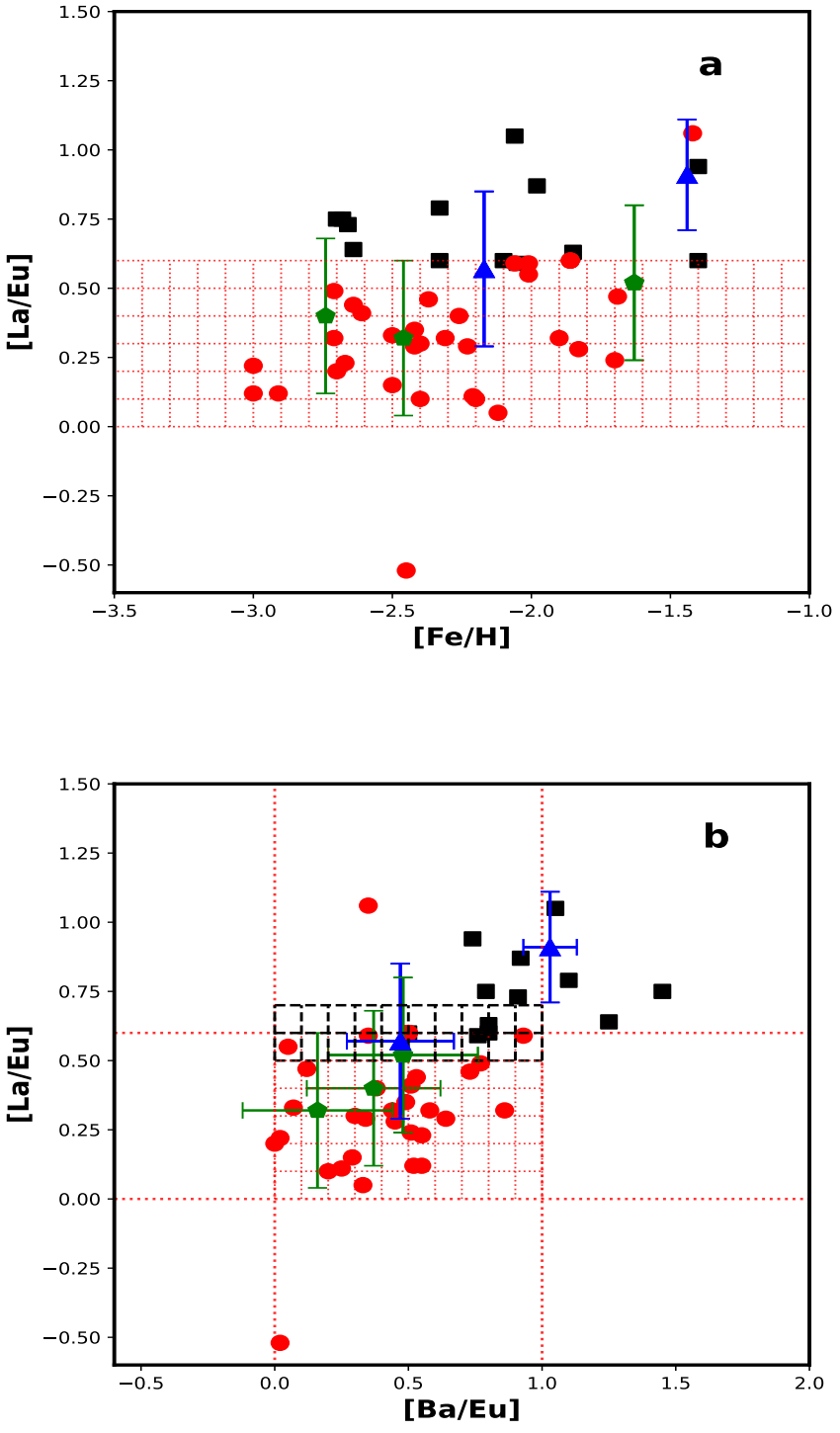

FIGURE 5.4: Filled red circles represent CEMP-*r/s* stars, filled black squares represent CEMP-*s* stars, filled blue triangles and filled green pentagons represent CEMP-*s* and CEMP-*r/s* stars of this work respectively. In panel (a), the grid formed by dotted red lines represent the region of CEMP-*r/s* stars put forward by Frebel (2018). In panel (b), we can see that except two, all the CEMP-*r/s* stars fall inside the grid formed by dotted red lines bound by $0.0 < [\mathrm{La/Eu}] < 0.6$ and $0.0 < [\mathrm{Ba/Eu}] < 1.0$. The grid formed by black dashed lines bound by $0.5 < [\mathrm{La/Eu}] < 0.7$ represent the uncertain region in the upper boundary of the classification put forward by Frebel (2018) for CEMP-*r/s* stars.

5.3.6 [As/Ge] and [Se/Ge] as classifiers

Roederer *et al.* (2016) suggested that supersolar [As/Ge] and solar or subsolar [Se/Ge] could indicate the operation of *i*-process. Although, due to the lack of high-quality NUV spectra, the abundances of these elements (As, Se, Ge) are currently limited, in the future the *n*-capture elements found in the NUV region are likely to play important roles in characterising the *i*-process. This will also help to validate the claim that [As/Ge] and [Se/Ge] could be used as classifiers of *i*-process.

5.3.7 An improved classification scheme

Frebel (2018) kept provisions for future adjustments to the classifying criteria. In Figure 5.4(b), except for two stars (CD−28 1082 and HD 209621), all the CEMP-*r/s* stars fall inside the region (the grid formed by the dotted red lines) bound by $0.0 < \text{[La/Eu]} < 0.6$ and $0.0 < \text{[Ba/Eu]} < 1.0$. As a few CEMP-(*s* & *r/s*) stars also fall very close to the upper boundary, we can put uncertainty on the upper limit of [La/Eu] (i.e. $\text{[La/Eu]} < 0.6 \pm 0.1$). We suggest that an object satisfying the criteria $0.0 < \text{[Ba/Eu]} < 1.0$ and $0.0 < \text{[La/Eu]} < 0.5$ can be classified as a CEMP-*r/s* star; however, if $\text{[La/Eu]} = 0.6 \pm 0.1$ the condition [Eu/Fe] > 1.0 also needs to be satisfied for the star to be a CEMP-*r/s* star. The two outliers exhibit differences in the range 0.5−0.7 dex between the abundances of La and the other hs elements. In Figure 5.3(b) we can see that a CEMP-*s* star HE 0336+0113, which is Eu (> 1.0) enhanced with very high value for [Ba/Eu] (=1.45), falls in the region allowed for CEMP-*r/s* stars. The upper limit of [Ba/Eu] (< 1.0) is chosen so as to avoid misclassifying such stars as CEMP-*r/s* stars.

The difficulty in drawing sharp boundaries to distinguish CEMP-*s* and CEMP-*r/s*

stars is clearly visible in all the classifiers. Moreover, the smooth transition of CEMP-*s* and CEMP-*r/s* stars, as seen in Figure 5.1(c), may indicate that *s*- and *i*-process neutron densities are not distinctly different and have a continuous range from $n_n \sim 10^7$ to 10^{15} cm^{-3}.

5.4 Conclusions

We have seen that the existing classification schemes of CEMP stars failed to classify the object HD 145777 uniquely. This compelled us to revisit the classification criteria. With the help of a sample of 72 CEMP-*s* and CEMP-*r/s* stars from the literature, we have critically analysed the different criteria used by various authors for CEMP-*s* and CEMP-*r/s* stars. We have found that the set of criteria adopted by Abate *et al.* (2016) is most suitable and fits well with the literature data. The criterion $0.0 <$ [La/Eu] < 0.6 put forward by Frebel (2018) to classify CEMP-*r/s* stars is also found to be suitable with a slight modification to the upper limit. As [hs/ls] gives higher values for CEMP-*r/s* stars than CEMP-*s* stars, we have examined whether [hs/ls] can be used as a classifier. We have found that CEMP-*s* and CEMP-*r/s* stars peak at different values of [hs/ls]. However, we have noticed that there is an overlap of [hs/ls] values in the range 0 to 1.5. Hence it is not possible to distinguish the CEMP-*s* and CEMP-*r/s* stars based on this ratio alone. We proposed, the best criteria to distinguish the CEMP-*s* and CEMP-*r/s* stars as:

- CEMP: [C/Fe] ≥ 0.7
- CEMP-*r/s*: [Ba/Fe] ≥ 1.0, [Eu/Fe] ≥ 1.0
    i) $0.0 \leq$ [Ba/Eu] ≤ 1.0 and/or $0.0 \leq$ [La/Eu] ≤ 0.7;
- CEMP-*s*: [Ba/Fe] ≥ 1.0

i.) [Eu/Fe] < 1.0, [Ba/Eu] > 0.0 and/or [La/Eu] > 0.5;

ii.) [Eu/Fe] ≥ 1.0, [Ba/Eu] > 1.0 and/or [La/Eu] > 0.7.

TABLE 5.1: **CEMP-*s* and CEMP-*r/s* stars from literature: 1. Aoki *et al.* (2001), 2. Aoki *et al.* (2002), 3. Aoki *et al.* (2008), 4. Barbuy *et al.* (2005), 5. Barklem *et al.* (2005), 6. Behara *et al.* (2010), 7. Cohen *et al.* (2003), 8. Cohen *et al.* (2006), 9. Karinkuzhi and Goswami (2014), 10. Goswami *et al.* (2006), 11. Hill *et al.* (2000), 12. Ishigaki *et al.* (2010), 13. Ivans *et al.* (2005), 14. Johnson and Bolte (2002), 15. Johnson and Bolte (2004), 16. Jonsell *et al.* (2005), 17. Jonsell *et al.* (2006), 18. Lucatello *et al.* (2003), 19. Purandardas *et al.* (2019), 20. Preston and Sneden (2001), 21. Pereira and Drake (2009), 22. Sivarani *et al.* (2004), 23. Van Eck *et al.* (2003), 24. Zacs *et al.* (1998), 25. Zhang *et al.* (2009), 26. Jorissen *et al.* (2016a), 27. this work, 28. Goswami and Aoki (2010), 29. Liu *et al.* (2012), 30. Allen *et al.* (2012), 31. Hansen *et al.* (2019), 32. mean of the presented data, 33. Burris *et al.* (2000) 34. Vanture (1992), 35. Masseron *et al.* (2010), 36. Placco *et al.* (2013).**

CEMP-*s* stars																				
Star Name	[Fe/H]	[C/Fe]	[N/Fe]	[C/N]	[Sr/Fe]	[Y/Fe]	[Zr/Fe]	[Ba/Fe]	[La/Fe]	[Ce/Fe]	[Nd/Fe]	[Sm/Fe]	[Eu/Fe]	[Pb/Fe]	[ls/Fe]	[hs/Fe]	[hs/ls]	[Ba/Eu]	[Sr/Ba]	Ref
BD+04 2466	-1.99	1.17	1.10	0.07	-	0.52	0.79	1.49	1.20	1.07	1.35	-	-	1.92	0.66	1.28	0.62	-	-	32
	-1.92	1.17	1.10	0.07	-	0.47	0.79	1.70	1.20	1.07	1.35	-	-	1.92	-	-	-	-	-	21
	-2.10	-	-	-	-	0.54	-	1.36	-	-	-	-	-	-	-	-	-	-	-	12
	-1.92	-	-	-	-	0.55	-	1.31	-	-	-	-	-	-	-	-	-	-	-	25
	-2.00	-	-	-	-	-	-	1.60	-	-	-	-	-	-	-	-	-	-	-	33
BD-01 2582	-2.25	-	-	-	-	-	-	1.50	-	-	-	-	-	-	-	-	-	-	-	33
BS 16077-0077[d,e]	-2.05[a]	2.25	-	-	-0.06	-0.12	-0.02	0.75	0.58	0.60	0.60	-	-0.01	-	-0.07	0.63	0.70	0.76	-0.81	30
CD-38 2151	-1.72	1.50	1.40	0.10	1.16	0.44	1.50	0.97	1.09	1.30	1.17	1.07	-	-	1.03	1.13	0.10	-	0.19	32
	-2.03	1.50	1.40	0.10	1.16	0.57	2.00	0.97	0.88	1.24	1.34	1.53	-	-	-	-	-	-	-	19
	-1.40	-	-	-	-	0.30	1.00	-	1.30	1.35	1.00	0.61	-	-					-	34
CS 22880-074[d]	-1.85	1.41	0.05	1.36	0.27	0.38	0.73	1.33	1.16	1.22	1.20	-	0.53	1.90	0.46	1.23	0.77	0.80	-1.06	32
	-1.76	1.51	0.20	1.31	0.14	0.60	0.73	1.34	1.24	-	-	-	0.55	-	-	-	-	-	-	20
	-1.93	1.30	-0.10	1.40	0.39	0.16	-	1.31	1.07	1.22	1.20	-	0.50	1.90	-	-	-	-	-	2
CS 22942-019	-2.66	2.10	0.50	1.60	1.55	1.58	1.69	1.71	1.53	1.54	1.26	1.64	0.80	≤1.60	1.61	1.51	-0.10	0.91	-0.16	32
	-2.67	2.20	0.70	1.50	1.40	-	-	1.50	1.85	-	-	-	0.80	-	-	-	-	-	-	20
	-2.64	2.00	0.30	1.70	1.70	1.58	1.69	1.92	1.20	1.54	1.26	1.64	0.79	≤1.60	-	-	-	-	-	2
CS 22949-008[d]	-2.45[a]	2.00	-	-	-0.17	1.25	1.61	0.98	-	1.49	1.98	0.61	-	-	0.90	1.48	0.58	-	-1.15	30

a − [Fe/H] is from Fe I lines, *b* − Average abundance from neutral and ionised species, *c* − Outliers of the classifier of Beers and Christlieb (2005), *d* − Outliers of the classifier of Hansen *et al.* (2019), *e* − Outliers of the classifier of Frebel (2018), *f* − Outlier of the classifier of Abate *et al.* (2016).

TABLE 5.1: *–continued*

CEMP-*s* stars																				
Star Name	[Fe/H]	[C/Fe]	[N/Fe]	[C/N]	[Sr/Fe]	[Y/Fe]	[Zr/Fe]	[Ba/Fe]	[La/Fe]	[Ce/Fe]	[Nd/Fe]	[Sm/Fe]	[Eu/Fe]	[Pb/Fe]	[ls/Fe]	[hs/Fe]	[hs/ls]	[Ba/Eu]	[Sr/Ba]	Ref
CS 29512-073[d]	-2.06[a]	1.40	-	-	0.75[b]	0.60	0.59	1.42	1.42	1.63	1.57	1.88	0.37	-	0.65	1.51	0.86	1.05	-0.67	30
CS 30301-015[d]	-2.64	1.60	0.60	1.00	0.30	0.29	-	1.45	0.84	1.16	1.25	0.85	0.20	1.70	0.30	1.18	0.88	1.25	-1.15	2
G 18-24	-1.62	-	-	-	-	0.58	-	1.17	-	-	-	-	-	-	-	-	-	-	-	12
G 24-25[d]	-1.40	1.03	-	-	0.36[b]	0.70	0.95[b]	1.35	1.55	1.59	1.47	1.40	0.61	1.68	0.67	1.49	0.82	0.74	-0.99	29
HD 5223	-2.05	1.57	-	-	1.39	0.63	1.57	1.82	1.76	1.87	1.54	1.68	-	< 2.21	1.19	1.75	0.56	-	-0.43	10
HD 30443[d]	-1.69	1.68	0.40	1.28	0.74	1.37	1.60	1.70	-	1.62	2.47	2.24	-	-	1.24	1.93	0.69	-	-0.96	19
HD 196944	-2.33	1.31	1.30	0.01	0.84	0.57	0.63	1.27	0.96	1.20	0.83	0.69	0.17	2.00	0.68	1.07	0.39	1.10	-0.43	32
	-2.45	1.42	-	-	-	0.58	-	1.56	-	1.49	0.94	-	-	-	-	-	-	-	-	24
	-2.25	1.20	1.30	-0.10	0.84	0.56	0.66	1.10	0.91	1.01	0.86	0.78	0.17	1.90	-	-	-	-	-	2
	-2.23	-	-	-	-	-	-	1.14	-	-	-	-	-	-	-	-	-	-	-	16
	-2.40	-	-	-	-	-	0.60	-	1.00	1.10	0.70	0.60	-	2.10	-	-	-	-	-	23
HD 198269	-1.40	-	-	-	-	0.50	1.20	-	1.40	1.60	1.00	0.90	0.80	-	0.85	1.33	0.48	-	-	34
HD 201626	-1.35	-	-	-	-	1.00	1.30	2.12	1.68	1.90	1.97	1.57	-	-	1.15	1.92	0.77	-	-	32
	-1.39	-	-	-	-	-	-	2.12	1.76	1.89	2.24	1.63	-	-	-	-	-	-	-	9
	-1.30	-	-	-	-	1.00	1.30	-	1.60	1.90	1.70	1.50	-	-	-	-	-	-	-	34
HE 0012-1441	-2.52[a]	1.59	0.64	0.95	-	-	-	1.15	-	-	-	-	-	< 1.92	-	-	-	-	-	8
HE 0024-2523[d]	-2.72[a]	2.60	2.10	0.50	0.34	<0.91	<1.22	1.46	1.80	-	-	-	<1.10	3.30	-	1.63	-	-	-1.12	18
HE 0202-2204[d]	-1.98	1.16	-	-	0.57	0.41	0.47	1.41	1.36	1.30	1.02	1.03	0.49	-	0.48	1.27	0.79	0.92	-0.84	5
HE 0231-4016[d]	-2.08	1.36	-	-	0.67	0.72	-	1.47	1.22	1.53	1.35	-	-	-	0.70	1.39	0.69	-	-0.80	5
HE 0253-6024	-2.10	1.30	0.20	1.10	1.50	0.80	-	1.70	1.50	1.20	2.00	-	<1.00	-	1.15	1.60	0.45	-	-0.20	31
HE 0317-4705	-2.30	1.40	0.40	1.00	1.70	0.60	-	1.00	1.40	1.50	1.30	-	<1.00	-	1.15	1.30	0.15	-	0.70	31
HE 0336+0113[f]	-2.68[a]	2.25	1.60	0.65	1.68	1.40	-	2.63	1.93	2.30	2.12	-	1.18	<2.28	1.54	2.25	0.71	1.45	-0.95	8
HE 0430-4404[d]	-2.07	1.44	-	-	0.56	0.60	-	1.62	1.41	-	-	-	-	-	0.58	1.52	0.94	-	-1.06	5
HE 1031-0020[d]	-2.86[a]	1.63	2.48	-0.85	0.31	0.25	-	1.21	1.16	1.40	1.72	-	<0.87	2.66	0.28	1.37	1.09	-	-0.90	8
HE 1135+0139	-2.33	1.19	-	-	0.66	0.36	0.46	1.13	0.93	1.17	0.77	-	0.33	-	0.49	1.00	0.51	0.80	-0.47	5
HE 1152-0355	-1.29	0.58	-	-	-	0.14	0.00	1.58	1.57	-	0.43	0.87	-	-	0.07	1.19	1.12	-	-	10
HE 1430-1123[d]	-2.71	1.84	-	-	0.24	0.50	-	1.82	-	-	1.72	-	-	-	0.37	1.77	1.40	-	-1.58	5
HE 1434-1442	-2.39[a]	1.95	1.40	0.55	-	0.37	-	1.23	-	-	1.70	-	-	2.18	-	1.47	-	-	-	8
HE 1443+0113	-2.07[a]	1.84	-	-	-	-	-	1.40	-	-	-	-	-	-	-	-	-	-	-	8
HE 1509-0806[d]	-2.91[a]	1.98	2.23	-0.25	1.12	0.95	-	1.93	1.67	1.89	2.18	-	<0.93	2.61	1.04	1.92	0.88	-	-0.81	8

TABLE 5.1: *–continued*

CEMP-*s* stars																				
Star Name	[Fe/H]	[C/Fe]	[N/Fe]	[C/N]	[Sr/Fe]	[Y/Fe]	[Zr/Fe]	[Ba/Fe]	[La/Fe]	[Ce/Fe]	[Nd/Fe]	[Sm/Fe]	[Eu/Fe]	[Pb/Fe]	[ls/Fe]	[hs/Fe]	[hs/ls]	[Ba/Eu]	[Sr/Ba]	Ref
HE 2138-3336[d]	-2.79	2.43	1.66	0.77	0.27	0.48	0.81	1.91	1.60	1.81	1.57	1.53	<1.09	3.84	0.52	1.72	1.20	-	-1.64	36
HE 2150-0825[d]	-1.98	1.35	-	-	0.66	0.85	0.97	1.70	1.41	1.48	1.42	-	-	-	0.83	1.50	0.67	-	-1.04	5
HE 2158-0348[d]	-2.70[a]	1.87	1.52	0.35	0.52	0.87	1.74	1.59	1.55	1.89	1.51	<2.40	0.80	2.60	1.04	1.64	0.60	0.79	-1.07	8
HE 2158-5134	-3.00	2.60	0.80	1.80	2.60	1.80	-	2.30	<2.00	<2.20	1.80	-	-	-	2.20	2.05	-0.15	-	0.30	31
HE 2227-4044[d]	-2.32	1.67	-	-	0.41	-	-	1.38	1.28	-	-	-	-	-	-	1.33	-	-	-0.97	5
HE 2232-0603[d]	-1.85[a]	1.22	0.47	0.75	0.55	0.60	-	1.41	1.23	1.45	-	-	-	1.55	0.58	1.36	0.78	-	-0.86	8
HE 2240-0412[d]	-2.20	1.35	-	-	0.24	-	-	1.37	-	-	-	-	-	-	-	-	-	-	-1.13	5
HE 2258-4427	-2.10	1.40	-0.10	1.50	1.70	1.00	-	1.30	1.40	1.60	1.50	-	0.80	-	1.35	1.45	0.10	0.50	0.40	31
HE 2339-4240	-2.30	1.70	0.60	1.10	1.60	0.80	-	2.00	2.00	1.70	2.00	-	-	-	1.20	1.93	0.73	-	-0.40	31
CEMP-*r/s* stars																				
Star Name	[Fe/H]	[C/Fe]	[N/Fe]	[C/N]	[Sr/Fe]	[Y/Fe]	[Zr/Fe]	[Ba/Fe]	[La/Fe]	[Ce/Fe]	[Nd/Fe]	[Sm/Fe]	[Eu/Fe]	[Pb/Fe]	[ls/Fe]	[hs/Fe]	[hs/ls]	[Ba/Eu]	[Sr/Ba]	Ref
BS 16080-175[e]	-1.86	1.75	<0.80	-	1.04	1.07	1.29	1.55	1.65	-	-	-	1.05	2.60	1.13	1.60	0.47	0.50	-0.51	30
BS 17436-058	-1.90	1.50	1.25	0.25	0.95	0.73	0.93	1.61	1.49	-	-	-	1.17	2.26	0.87	1.55	0.68	0.44	-0.66	30
CD-28 1082[e]	-2.45	2.19	2.73	-0.54	1.44	1.61	-	2.09	1.55	1.97	1.99	2.29	2.07	-	1.53	1.90	0.37	0.02	-0.65	19
CS 22183-015[c,d]	-2.91	2.13	1.78	0.35	0.44	0.50	0.68	2.01	1.61	1.72	1.78	-	1.49	2.99	0.54	1.78	1.24	0.52	-1.57	32
	-2.75[a]	1.92	1.77	0.15	0.34	0.52	-	2.04	1.70	1.88	1.91	-	1.70	2.79	-	-	-	-	-	8
	-3.12	-	-	-	-	0.45	0.62	2.09	1.59	1.55	1.65	-	1.39	3.17	-	-	-	-	-	14
	-2.85	2.34	1.79	0.55	0.54	0.54	0.74	1.89	1.53	-	-	-	1.37	3.00	-	-	-	-	-	30
CS 22881-036[c]	-2.06	1.96	1.00	0.96	0.59	1.01	0.95	1.93	1.59	-	2.04	-	1.00	-	0.85	1.85	1.00	0.93	-1.34	20
CS 22887-048[c]	-1.70	1.84	<1.29	-	1.00	0.99	1.23	2.00	1.73	-	-	-	1.49	3.40	1.07	1.87	0.80	0.51	-1.00	30
CS 22898-027[d]	-2.23	2.16	1.11	1.05	0.70	0.76	1.23	2.25	2.20	2.13	2.12	2.08	1.91	2.87	0.90	2.18	1.28	0.34	-1.55	32
	-2.15	1.95	1.20	0.75	0.60	0.95	1.39	2.27	2.28	-	2.00	-	1.94	-	-	-	-	-	-	20
	-2.30	2.34	1.24	1.10	0.59	0.60	1.28	2.26	2.19	-	-	-	1.91	2.89	-	-	-	-	-	30
	-2.25	2.20	0.90	1.30	0.92	0.73	1.01	2.23	2.13	2.13	2.23	2.08	1.88	2.84	-	-	-	-	-	2
CS 22948-027	-2.50	2.19	1.55	0.64	0.90	1.00	-	2.06	2.32	2.20	2.22	-	1.99	2.72	0.95	2.20	1.25	0.07	-1.16	32
	-2.47	2.43	1.75	0.68	0.90	1.00	-	2.26	2.32	2.20	2.22	-	1.88	2.72	-	-	-	-	-	4
	-2.57	2.10	1.10	1.00	-	-	-	1.67	-	-	-	-	-	-	-	-	-	-	-	20
	-2.47[a]	2.05	1.80	0.25	0.90	1.00	-	2.26	2.32	2.20	2.22	-	2.10	-	-	-	-	-	-	11

TABLE 5.1: *–continued*

CEMP-*r/s* stars																				
Star Name	[Fe/H]	[C/Fe]	[N/Fe]	[C/N]	[Sr/Fe]	[Y/Fe]	[Zr/Fe]	[Ba/Fe]	[La/Fe]	[Ce/Fe]	[Nd/Fe]	[Sm/Fe]	[Eu/Fe]	[Pb/Fe]	[ls/Fe]	[hs/Fe]	[hs/ls]	[Ba/Eu]	[Sr/Ba]	Ref
CS 29497-034	-3.00	2.61	2.16	0.45	1.20	0.97	-	2.05	2.25	2.00	2.16	-	2.03	2.95	1.09	2.12	1.03	0.02	-0.85	32
	-2.90	2.63	2.38	0.25	1.00	1.10	-	2.03	2.12	1.95	2.09	-	1.80	2.95	-	-	-	-	-	4
	-2.90[a]	2.50	2.30	0.20	1.00	1.10	-	2.03	2.12	1.95	2.09	-	2.25	-	-	-	-	-	-	11
	-3.20	2.70	1.80	0.90	1.60	0.70	-	2.10	2.50	2.10	2.30	-	-	-	-	-	-	-	-	31
CS 29497-030[c]	-2.64	2.43	2.00	0.43	1.09	0.84	1.42	2.25	2.16	2.12	2.00	-	1.72	3.60	1.12	2.13	1.01	0.53	-1.16	32
	-2.57	2.47	2.12	0.35	1.34	0.97	1.40	2.32	2.22	2.10	2.14	-	1.99	3.65	-	-	-	-	-	13
	-2.70	2.38	1.88	0.50	0.84	0.71	1.43	2.17	2.10	2.14	1.85	-	1.44	3.55	-	-	-	-	-	22
CS 29503-010	-1.69[a]	1.65	-	-	1.13[b]	1.09	1.26	1.81	2.16	2.05	2.31	2.34	1.69	-	1.16	2.08	0.92	0.12	-0.68	30
CS 29526-110[d]	-2.21	2.22	1.40	0.82	0.65	1.32	1.39	2.26	2.12	2.15	2.10	-	2.01	3.23	1.12	2.16	1.04	0.25	-1.61	32
	-2.07	2.07	-	-	0.77	1.34	1.26	2.39	2.09	-	-	-	-	3.16	-	-	-	-	-	3
	-2.38	2.20	1.40	0.80	0.88	-	1.11	2.11	1.69	2.01	2.01	-	1.73	3.30	-	-	-	-	-	2
	-2.19[a]	2.38	-	-	0.29	1.29	1.79	2.29	2.57	2.29	2.19	-	2.28	-	-	-	-	-	-	30
CS 29528-028	-2.12[a]	2.76	-	-	1.72[b]	1.99	2.17	2.49	2.21	2.47	2.54	-	2.16	-	1.96	2.43	0.47	0.33	-0.77	30
CS 31062-050[c,d]	-2.37	1.91	1.20	0.71	0.91	0.48	0.94	2.55	2.28	2.06	2.12	2.06	1.82	2.86	0.78	2.25	1.47	0.73	-1.64	32
	-2.41	1.82	-	-	-	0.48	0.85	2.80	2.12	2.02	1.99	1.96	1.79	2.81	-	-	-	-	-	15
	-2.32	2.00	1.20	0.80	0.91	-	1.02	2.30	2.44	2.10	2.24	2.15	1.84	2.90	-	-	-	-	-	2
HD 187861	-2.01	2.02	2.18	-0.16	-	0.00	-	1.39	1.89	1.69	1.80	0.70	1.34	2.86	-	1.70	-	0.05	-	32
	-1.65	-	-	-	-	0.00	-	-	2.05	2.00	1.80	0.70	-	-	-	-	-	-	-	34
	-2.36	2.02	2.18	-0.16	-	-	-	1.39	1.73	1.37	-	-	1.34	2.86	-	-	-	-	-	35
HD 209621[e]	-1.42	1.25	-	-	1.02	0.73	1.80	1.70	2.41	2.42	2.14	1.46	1.35	1.88	1.18	2.17	0.99	0.35	-0.68	32
	-1.93	1.25	-	-	1.02	0.36	1.80	1.70	2.41	2.04	1.87	1.46	1.35	1.88	-	-	-	-	-	28
	-0.90	-	-	-	-	1.10	-	-	-	2.80	2.40	-	-	-	-	-	-	-	-	34
HD 224959	-1.83	1.77	1.88	-0.11	-	0.80	-	2.19	2.02	2.01	1.80	1.40	1.74	3.06	-	2.01	-	0.45	-	32
	-1.60	-	-	-	-	0.80	-	-	2.00	2.10	1.80	1.40	-	-	-	-	-	-	-	34
	-2.06	1.77	1.88	-0.11	-	-	-	2.19	2.03	1.91	-	-	1.74	3.06	-	-	-	-	-	35
HE 0002-1037	-2.40	1.90	1.00	0.90	<1.00	0.40	-	2.00	2.00	1.70	2.10	-	1.70	-	-	1.95	-	0.30	-	31
HE 0017+0055	-2.40	2.17	2.47	-0.30	-	0.50	1.60	> 1.90	2.40	2.00	2.20	1.90	2.30	-	1.05	2.20	1.15	-	-	26
HE 0059-6540	-2.20	1.30	1.20	0.10	1.20	0.40	-	1.70	1.60	1.40	1.70	-	1.50	-	0.80	1.60	0.80	0.20	-0.50	31
HE 0131-3953[c,d]	-2.71	2.45	-	-	0.46	-	-	2.20	1.94	1.93	1.76	-	1.62	-	-	1.96	-	0.58	-1.74	5
HE 0143-0441[c]	-2.31[a]	1.98	1.73	0.25	0.86	0.59	1.05	2.32	1.78	1.93	2.17	-	1.46	3.11	0.83	2.05	1.22	0.86	-1.46	8

TABLE 5.1: *–continued*

CEMP-*r/s* stars																				
Star Name	[Fe/H]	[C/Fe]	[N/Fe]	[C/N]	[Sr/Fe]	[Y/Fe]	[Zr/Fe]	[Ba/Fe]	[La/Fe]	[Ce/Fe]	[Nd/Fe]	[Sm/Fe]	[Eu/Fe]	[Pb/Fe]	[ls/Fe]	[hs/Fe]	[hs/ls]	[Ba/Eu]	[Sr/Ba]	Ref
HE 0151-6007	-2.70	1.40	0.20	1.20	1.10	0.80	-	2.30	2.50	2.40	2.60	-	2.30	-	0.95	2.45	1.50	0.00	-1.20	31
HE 0338-3945[d]	-2.42	2.10	1.55	0.55	0.74	0.78	1.20	2.41	2.27	2.19	2.20	2.25	1.92	3.10	0.91	2.27	1.36	0.49	-1.67	32
	-2.41	2.07	-	-	0.73	0.73	-	2.41	2.26	2.21	2.09	-	1.89	-	-	-	-	-	-	5
	-2.42	2.13	1.55	0.58	0.74	0.83	1.20	2.41	2.28	2.16	2.30	2.25	1.94	3.10	-	-	-	-	-	17
HE 1105+0027[c,d]	-2.42	2.00	-	-	0.73	0.75	-	2.45	2.10	-	2.06	-	1.81	-	0.74	2.20	1.46	0.64	-1.72	5
HE 1305+0007	-2.01	1.84	-	-	0.86	0.73	2.09	2.32	2.56	2.53	2.59	2.60	1.97	2.37	1.23	2.50	1.27	0.35	-1.46	10
HE 2148-1247[d]	-2.26	1.91	1.65	0.26	0.76	0.83	1.47	2.36	2.38	2.28	2.27	1.99	1.98	3.12	1.02	2.32	1.30	0.38	-1.60	7
HE 2258-6358[c]	-2.67	2.42	1.44	0.98	0.80	0.70	0.69	2.23	1.91	1.66	1.76	1.81	1.68	3.32	0.73	1.89	1.16	0.55	-1.43	36
LP 625-44[c,d]	-2.71	2.10	1.00	1.10	1.15	0.99	1.34	2.74	2.46	2.27	2.30	2.21	1.97	2.55	1.16	2.44	1.28	0.77	-1.59	1
LP 706-7[c,d]	-2.61	2.13	1.50	0.63	0.18	0.42	<1.16	2.02	1.92	1.99	1.90	<2.21	1.51	2.40	0.30	1.96	1.66	0.51	-1.84	32
	-2.53	2.14	-	-	0.08	-	-	2.08	1.92	-	-	-	-	2.53	-	-	-	-	-	3
	-2.55	2.10	1.20	0.90	0.30	0.59	-	1.98	2.02	2.12	1.79	-	1.62	2.40	-	-	-	-	-	2
	-2.74	2.15	1.80	0.35	0.15	0.25	<1.16	2.01	1.81	1.86	2.01	<2.21	1.40	2.28	-	-	-	-	-	1
SDSS J0912+0216	-2.50	2.17	1.75	0.42	0.57	0.61	1.08	1.49	1.35	2.17	1.12	2.60	1.20	2.33	0.75	1.53	0.78	0.29	-0.92	6
SDSS J1349-0229[c]	-3.00	2.82	1.60	1.22	1.30	1.29	1.56	2.17	1.74	2.63	1.91	2.35	1.62	3.09	1.38	2.11	0.73	0.55	-0.87	6
Our Work																				
Star Name	[Fe/H]	[C/Fe]	[N/Fe]	[C/N]	[Sr/Fe]	[Y/Fe]	[Zr/Fe]	[Ba/Fe]	[La/Fe]	[Ce/Fe]	[Nd/Fe]	[Sm/Fe]	[Eu/Fe]	[Pb/Fe]	[ls/Fe]	[hs/Fe]	[hs/ls]	[Ba/Eu]	[Sr/Ba]	Ref
HD 145777[c,d,e]	-2.17	2.43	0.67	1.76	0.67	1.22	1.05	1.27	1.37	1.79	1.48	1.63	0.80	-	0.98	1.48	0.50	0.47	-0.60	27
CD-27 14351	-2.71	2.98	1.88	1.10	1.74	1.97	2.21	1.82	1.56	1.89	1.37	-	<0.39	-	1.97	1.66	−0.31	> 1.43	-0.08	27
HE 0017+0055	-2.46	2.73	2.83	-0.10	-	0.58	1.55	2.30	2.46	2.11	2.25	1.98	2.14	-	1.07	2.28	1.21	0.16	-	27
HE 2144-1832	-1.63	1.85	0.50	1.35	0.66	1.16	0.97	1.49	1.53	1.70	1.61	1.78	1.01	-	0.93	1.58	0.65	0.48	-0.83	27
HE 2339-0837	-2.74	3.04	-	-	1.32	0.67	1.64	2.21	2.24	2.37	2.55	2.29	1.84	-	1.21	2.34	1.13	0.37	-0.89	27
HE 0319-0215	-2.57	2.41	2.07	0.34	-	1.15	0.62	1.88	-	1.92	1.89	1.80	0.85	-	0.89	1.90	1.01	1.03	-	27
HE 0507-1653[f]	-1.44	1.16	1.41	-0.25	-	1.20	1.57	2.06	1.94	2.03	2.03	2.08	1.03	-	1.39	2.02	0.63	1.03	-	27
HE 0930-0018	-1.39	1.65	-	-	-	0.70	0.38	1.09	1.09	1.34	0.93	0.98	-	-	0.54	1.11	0.57	-	-	27
HE 1023-1504	-1.66	1.92	-	-	-	1.12	1.31	2.08	-	2.50	2.15	1.94	0.89	-	1.22	2.24	1.02	1.19	-	27

Chapter 6

HE 1005–1439: observational evidences for a new site where *i*- and *s*-processes operate in succession*

6.1 Introduction

Understanding the diverse abundance patterns exhibited by different groups of CEMP stars that are believed to be associated with different formation mechanisms have been a challenge. In this chapter, we report an extremely metal-poor carbon-enhanced star, HE 1005–1439, whose surface chemical composition is found to be enriched with both *s*-process and *i*-process nucleosynthesis that forms a new class of object with a distinct abundance pattern. The peculiar abundance pattern, observed for the first time in a CEMP star, was investigated based on a

*Main results of this work are published in Goswami and Goswami (2022).

parametric-model-based analysis that revealed almost equal contributions from both the *s*-process and the *i*-process to its surface chemical composition. We examined various production mechanisms and formation scenarios for this object. A formation scenario involving effective proton ingestion episodes (PIEs) triggering *i*-process nucleosynthesis followed by *s*-process asymptotic giant branch (AGB) nucleosynthesis with limited third-dredge-up (TDU) episodes seems to be most promising for this type of object.

Literature surveys show that this object had been studied earlier by different groups (Aoki *et al.* 2007; Schuler *et al.* 2008; Yong *et al.* 2013; Caffau *et al.* 2017). However, these studies were limited by the number of elements for which abundances were estimated. As the abundances of the *n*-capture elements except Ba are not reported in the literature, we revisited the object and estimated the atmospheric parameters as well as abundances of ten light elements and twelve heavy elements. The derived abundances were then carefully investigated with an aim to understand the origin and formation mechanism(s) of the object.

6.2 Peculiarity of HE 1005–1439

Our analysis shows the object HE 1005–1439 to be an extremely metal-poor star with [Fe/H] = –3.03 in accordance with Aoki *et al.* (2007). Carbon and *n*-capture elements are found to be enhanced in the programme star. Following the classification criteria of CEMP stars that we have put forward and discussed in Chapter 5, the object is found to belong to the CEMP-*s* sub-group as illustrated in Figure 6.1(a). As shown in Figure 6.1(b), [hs/ls], the ratio of heavy-*s* process (hs) elements (Ba, La, Ce, and Nd) to the light-*s* process (ls) elements (Sr and Y), is $\sim$ 0.92. In Goswami *et al.* (2021) it was shown that [hs/ls] peaks at a value 1.06

for CEMP-*r/s* stars. This value is quite close to the [hs/ls] value estimated for HE 1005–1439 indicating that the object could be a possible CEMP-*r/s* star.

Using the *s*-process yields calculated using the FRUITY[†] model (Straniero *et al.* 2006; Cristallo *et al.* 2009b, 2011, 2015) at the same metallicity (z=0.00002) of the programme star, and considering different masses, we were not able to reproduce the observed abundance pattern of heavy elements. In Figure 6.2(a), we show a comparison of the observed elemental abundances with the AGB model yields (normalised to the La abundance of HE 1005–1439), calculated for M = 1.3 $M_{\odot}$ and M = 2.0 $M_{\odot}$. As can be seen in the top panel of the residual plot of Figure 6.2(d), the *s*-process AGB models over-produce the light *s*-process elements Sr and Y, under-produce the elements Pr, Er, and Hf, and over-produce the third *s*-process peak element Pb.

We have also examined if the observed abundance pattern could be reproduced with the *i*-process model yields of Hampel *et al.* (2016). In Figure 6.2(b), we show a comparison of the *i*-process model yields of Hampel *et al.* (2016) (normalised to the La abundance of HE 1005–1439), calculated for $n_n = 10^{12}$ cm^{-3} and $n_n = 10^{14}$ cm^{-3}, with the observed elemental abundance pattern of the programme star. We found that the *i*-process model yields (Hampel *et al.* 2016) alone at neutron-densities $n_n = 10^{12}$ – 10^{15} cm^{-3} cannot satisfactorily reproduce the observed abundance pattern of the programme star. We can see from the middle panel of residual plot (Figure 6.2(d)) that the *i*-process model with $n_n = 10^{12}$ cm^{-3} fits the light *s*-process elements Sr and Y satisfactorily but under-produces Ce and Pr. The *i*-process model with $n_n = 10^{14}$ cm^{-3} is also found to under produce the light *s*-process elements Sr and Y and over-produce Ba, Eu, and Er. The peculiar abundance pattern observed in HE 1005–1439, which could not be explained either by *s*-process AGB nucleosynthesis or by the *i*-process alone, prompted us to

[†]`http://fruity.oa-teramo.inaf.it/`

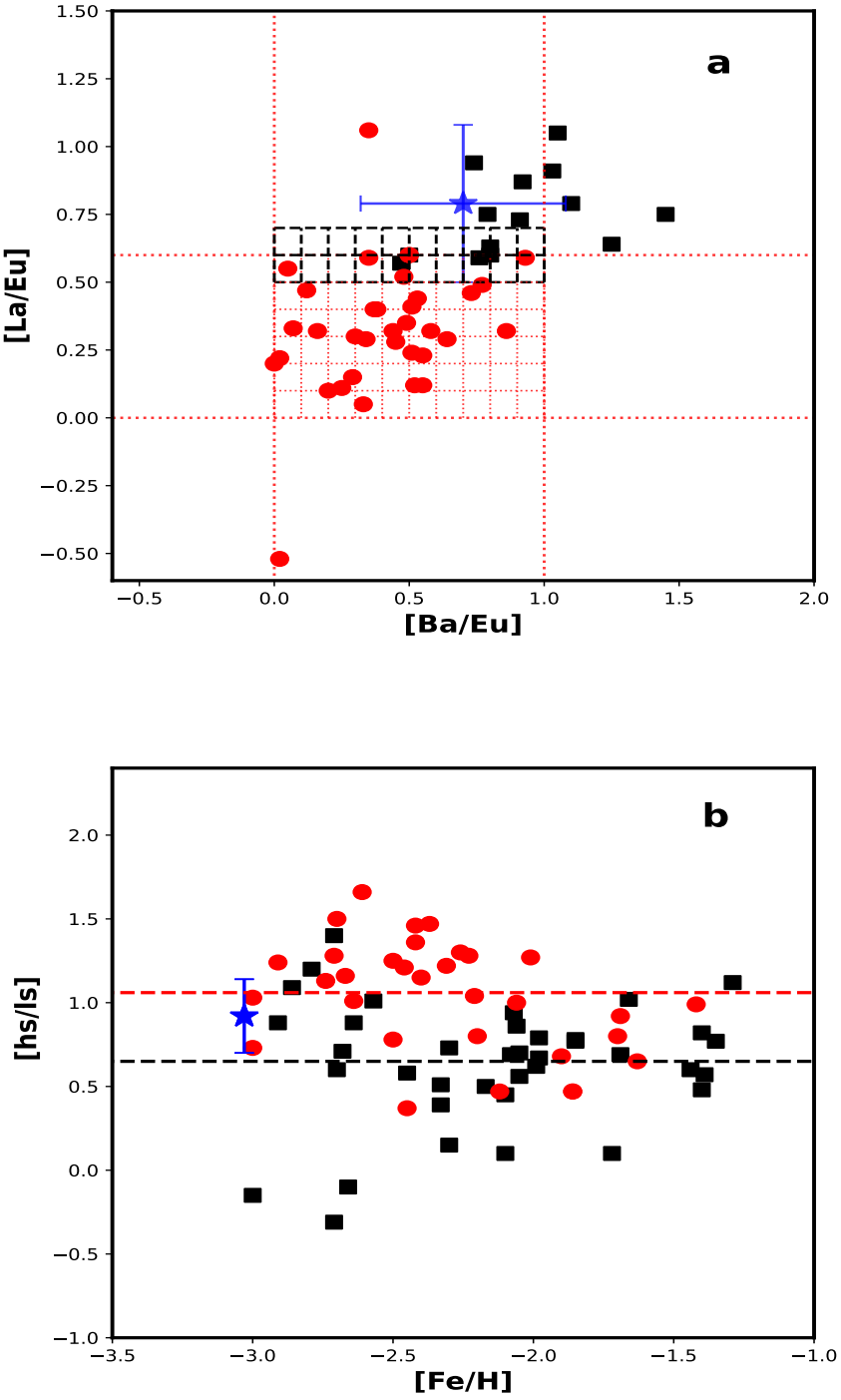

FIGURE 6.1: Filled red circles and filled black squares respectively represent literature CEMP-*r/s* and CEMP-*s* stars, and the blue star represents the object HE 1005–1439. *panel a:* Grid formed by the dotted red lines bound by $0.0 <$ [La/Eu] < 0.6 and $0.0 <$ [Ba/Eu] < 1.0 indicates the region defined for CEMP-*r/s* stars by our classification scheme (Chapter 5). The grid formed by the black dashed lines bound by $0.5 <$ [La/Eu] < 0.7 represents the region where [Eu/Fe] > 1.0 classifies the stars as CEMP-*r/s* and [Eu/Fe] < 1.0 classifies the stars as CEMP-*s*. *panel b:* Red dashed line at [hs/ls] $= 1.06$ and the black dashed line at [hs/ls] $= 0.65$ represent the peaks of [hs/ls] for CEMP-*r/s* and CEMP-*s*, respectively.

explore alternate production mechanisms that might have influenced its surface chemical composition.

6.3 Parametric-model based study

We performed a parametric-model-based study to delineate the contributions of *s*-, *i*- and *r*-processes to the observed abundances of heavy elements of the object HE 1005–1439. We used *s*-process model yields of the FRUITY model at different masses (M = 1.3–2.0 $M_{\odot}$), the Solar System *r*-process residual pattern (stellar model) given in Arlandini *et al.* (1999), and *i*-process model yields of Hampel *et al.* (2016) at different neutron-densities ($n_n = 10^{12}$–10^{15} cm^{-3}). We have excluded the element Pb from the parametric-model based study as the *i*-process model yields of Pb are not reported by Hampel *et al.* (2016). We have normalised the elemental abundances of the models to the La abundance of HE 1005–1439. The observed elemental abundances of HE 1005–1439 are then fitted with the parametric-model function $\log \epsilon_j = C_s\ N_{sj} + C_i N_{ij} + C_r N_{rj}$, where N_{sj}, N_{ij}, and N_{rj} indicate the normalised abundance from the *s*-process, *i*-process, and *r*-process, respectively. Here, C_s, C_i, and C_r indicate the component coefficients corresponding to contributions from the *s*-process, *i*-process, and *r*-process, respectively. In order to find the best fit, we have calculated χ^2 for all the possible combinations of models of *s*-process (M = 1.3–2.0 $M_{\odot}$) and *i*-process (n = 10^{12}–10^{15} cm^{-3}) along with solar *r*-process residues. The minimum χ^2 is achieved for a combination of an *s*-process model with M = 2.0 $M_{\odot}$ and an *i*-process model with n = 10^{14} cm^{-3} with no contribution from the *r*-process. The parametric-model function gives an excellent fit to the light *s*-process elements Sr and Y and a satisfactory fit to the heavier *n*-capture elements. The best parametric-model fit shows that the contribution from both *s*- and *i*-process are similar ($Cs = 0.56$, $Ci = 0.44$) as shown in Figure 6.2(c) and the bottom panel of the residual plot (Figure 6.2(d)).

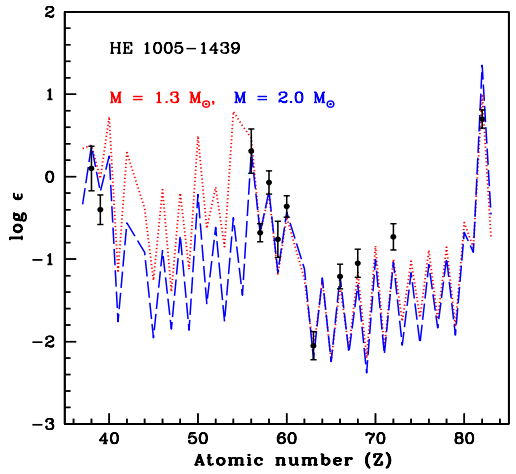

(a) *s*-process model fits for M = 1.3 $M_{\odot}$ & 2.0 $M_{\odot}$

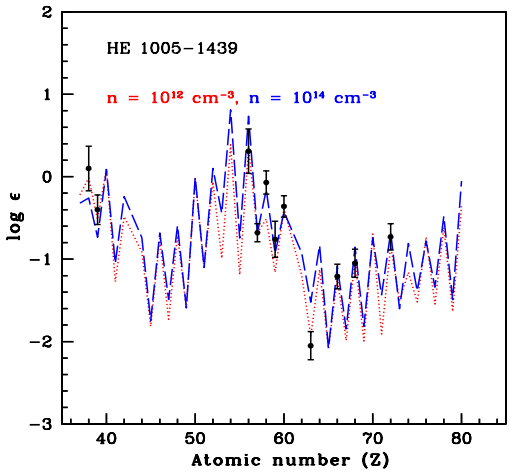

(b) *i*-process model fits for n = 10^{12} cm^{-3} & 10^{14} cm^{-3}

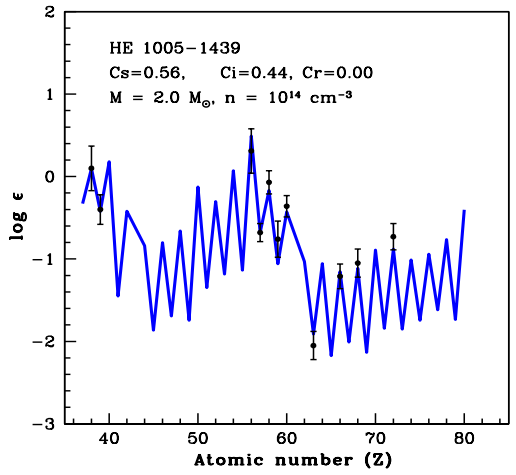

(c) Best-fit from parametric-model

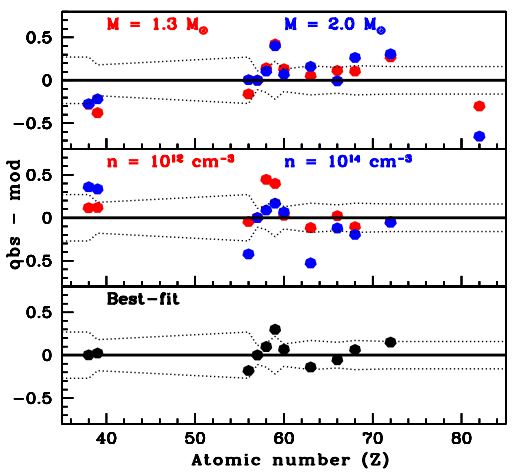

(d) Residual plot

FIGURE 6.2: Examples of theoretical model fits with the observed abundances of the star. In panels (a), (b), and (c), the points with error bars indicate the observed abundances.

6.4 Origin of HE 1005–1439: Possible formation scenarios

The parametric-model-based study clearly established that the surface chemical composition of HE 1005−1439 is influenced by almost equal contributions of *s*-process AGB nucleosynthesis and *i*-process nucleosynthesis. We have attempted to capture a formation scenario for this object involving a binary picture. Our assumption on binarity is profoundly based on the radial velocity variations observed in a few epochs. The low value of $^{12}C/^{13}C$ ($\sim$ 5.0) measured for HE 1005–1439 also points toward the extrinsic nature of carbon and hence the heavy elements in the star. In the intrinsic carbon stars (in the AGB phase), third-dredge-up (TDU) episodes bring ^{12}C and *s*-process material to the surface, and the $^{12}C/^{13}C$ ratio can have values more than 100 depending on the initial mass of the object (Karakas and Lattanzio 2014). However, in extrinsic carbon giants, such as HE 1005–1439, the $^{12}C/^{13}C$ ratio decreases due to the first dredge-up (FDU), which brings ^{13}C produced in the internal CNO cycle to the stellar atmosphere (Smith *et al.* 1993). Attributing the *s*-process contribution to the AGB mass-transfer scenario in the binary system, we carefully examined if any of the proposed formation scenarios of *i*-process nucleosynthesis available in literature could explain the *i*-process contribution in the observed abundance pattern of HE 1005−1439.

6.4.1 Investigation of the existing formation scenarios

We have investigated if the very late thermal pulse (VLTP) scenario proposed to explain the peculiar abundance pattern of the Sakurai object (V4334 Sagittarii) by Herwig *et al.* (2011) could explain the abundance peculiarities of HE 1005−1439. However, a characteristic property of VLTP in a pre-white dwarf stage of producing

light *s*-process elements is about 2 dex more than that of heavy *s*-process elements. This condition is not found to be satisfied in the case of HE 1005−1439.

Low-metallicity or zero-metallicity massive (20–30 $M_{\odot}$) stars (Banerjee *et al.* 2018) and super-AGB stars (9–11 $M_{\odot}$) (Jones *et al.* 2016) can pollute the ISM with *i*-process yields. However, an AGB mass-transfer scenario in a binary system formed from the *i*-process-enriched ISM also cannot explain the peculiar abundance pattern observed in HE 1005–1439 due to its inadequacy to describe the low observed Pb abundance in this object. As shown in Figure 6.2(a) and the top panel of Figure 6.2(d), the observed Pb abundance of HE 1005–1439 is about 0.30–0.60 dex lower than the prediction of the FRUITY model (Cristallo *et al.* 2009b, 2016) at [Fe/H] $\sim$ –3.0. Pb is the main product of the *s*-process in AGB stars at low metallicities (Cristallo *et al.* 2009b). The low Pb abundance of HE 1005–1439 is also found difficult to explain by the scenario of pre-enrichment of ISM with *i*-process material or a scenario involving any external source of *i*-process material such as rapidly accreting white dwarfs (Denissenkov *et al.* 2019). This is because in these cases, Pb would be more than (if the *i*-process neutron exposure (τ) of the progenitor is sufficient to produce enough Pb) or at a similar level to the *s*-process prediction, but it would not be less, as Pb is not destroyed in β-decay.

6.4.2 A proposed new scenario

We propose that the surface chemical composition of HE 1005–1439 may be attributed to mass-transfer from a now extinct AGB companion with both *s*- and *i*-process nucleosynthesis occurring under suitable conditions during its evolution at different thermal pulses. Such a formation scenario may not be unlikely as many studies on the evolution of AGB stars have shown that neutron-densities required for the *s*-process and the *i*-process can be achieved in the intershell region

with the help of the partial mixing of protons in the radiative conditions (Herwig 2000; Denissenkov and Tout 2003; Herwig *et al.* 2003; Cristallo *et al.* 2009b, 2011; Piersanti *et al.* 2013; Karakas and Lattanzio 2014) and efficient PIEs in the convective conditions (Hollowell *et al.* 1990; Fujimoto *et al.* 2000; Iwamoto *et al.* 2004; Campbell and Lattanzio 2008; Lau *et al.* 2009; Cristallo *et al.* 2009a, 2016; Choplin *et al.* 2021), respectively.

In a study conducted by Cristallo *et al.* (2009a) on the AGB evolution of a 1.5 $M_{\odot}$ model with [Fe/H] = –2.45 and without any α enhancement, it was found that a strong PIE is followed by a deep TDU. Due to the PIE, H-burning occurring in high-temperature convective conditions creates a huge amount of ^{13}C, which leads to an efficient neutron production with neutron-densities of the order of 10^{15} cm^{-3}. The study also noted that the convective He-shell splits into two sub-shells when the energy released by proton capture reactions slightly exceeds the energy production at the base of the convective shell. In the lower sub-shell, the ^{13}C (α, n) ^{16}O reaction produces *i*-process neutron-density and the nucleosynthesis path goes away from the valley of β stability producing a very high local [hs/ls] ratio. The upper sub-shell, where the CNO cycle is the main energy source, is later engulfed by the envelope. After that, a standard TP-AGB phase follows with repetitive TPs and TDUs, and *s*-process nucleosynthesis occurs. The number of expected stars experiencing PIEs is found to be significantly reduced if α-element enhancement is introduced (Cristallo *et al.* 2016).

Cristallo *et al.* (2009a) noted that the minimum mass of the models to experience TDU is significantly lowered by PIEs. Their model, after the PIE, encounters 25 additional TDU episodes, each of which is followed by radiative burning of the ^{13}C pocket. Although the final abundance pattern is found to be a combination of *i*- and *s*-processes, excessive *s*-process nucleosynthesis after the PIE would remove the trace of the *i*-process and thus reduce the [hs/ls] ratio.

In a recent study on the evolution of a 1 $M_{\odot}$ object at low metallicity ([Fe/H] = –2.5), Choplin *et al.* (2021) noticed three convective instabilities occurring at the beginning of the TP-AGB phase. The main PIE occurs during the third instability, which produces high neutron-densities of about 4.3×10^{14} $cm^{-3,}$ and a rich *i*-process nucleosynthesis occurs. We note that although they are of similar metallicities, while in the model of Choplin *et al.* (2021) no further TPs were possible after the main PIE, in that of Cristallo *et al.* (2009a) 25 TPs after the PIE masked the contribution of the *i*-process and resulted in an *s*-process surface abundance pattern.

We propose that a model that undergoes PIEs during the beginning of the TP-AGB phase (producing an *i*-process abundance pattern) followed by limited TPs (producing an *s*-process abundance pattern) is likely to explain the abundance peculiarity of HE 1005–1439. This scenario would also explain the low-Pb abundance observed in this object. The abundance of Pb depends on the time-integrated neutron exposure (τ). Hampel *et al.* (2019) have shown that with the increase of neutron-density, the neutron exposure (τ) required for Pb production increases. Therefore, a low Pb abundance may indicate that due to the operation of both *i*- and *s*-processes in succession, neither of the processes received sufficient exposure time to produce enough Pb expected at [Fe/H] $\sim$ –3.0.

6.5 Conclusions

A detailed, high-resolution spectroscopic study of the EMP star HE 1005–1439 revealed a peculiar abundance pattern different from those typically exhibited by CEMP stars. While the CEMP stars' classification criteria place the object in the CEMP-*s* group, the value of [hs/ls] $\sim$ 0.9 is closer to the value (1.06) at which CEMP-*r/s* stars peak. The abundance pattern could not be reproduced either by

the *s*-process or the *i*-process model predictions alone. However, a parametric-model based analysis clearly indicated that similar contributions from both the *s*- and the *i*-process might have resulted in the observed abundance pattern of HE 1005–1439. We propose that the origin of the observed peculiar abundance pattern may be attributed to mass transfer from a now-extinct AGB companion where both *i*- and *s*-process nucleosynthesis took place during various stages of the AGB evolution with PIEs triggering *i*-process followed by *s*-process AGB nucleosynthesis with a few TDU episodes.

Several uncertainties such as initial mass, metallicity, treatment of opacities, nuclear rates, and mixing mechanisms affect the theoretical understanding of AGB stars. The observational constraints derived from HE 1005–1439 and the proposed scenario might provide a link for a better understanding of the interplay between PIEs and the partial mixing of protons in the intershell region. This may also throw light into the conditions that result in a pure *s*- or *i*-process surface abundance pattern in low-mass, low-metallicity AGB stars. The proposed scenario would also be helpful in explaining the overlap of [hs/ls] ratio in CEMP-*s* and CEMP-*r/s* stars (Figure 5.1(a) of Chapter 5) and the smooth transition of elemental abundances from the CEMP-*s* to CEMP-*r/s* regime (Figure 5.1(c) of Chapter 5).

Chapter 7

Investigating the role of the initial mass of the progenitor AGBs in formation scenarios*

7.1 Introduction

The "mass" of a star plays a crucial role in its structure, evolution and final fate. In order to understand the role of "mass" in the formation scenarios of Ba stars, in this chapter, we have studied in detail the mass distribution of Ba stars and their progenitor AGBs. The mass distribution of the progenitor AGBs of CEMP-*s* stars is also studied. We have estimated the masses of the Ba stars and the masses of the primary companions of both the Ba and CEMP-*s* stars. We have compiled a large data set taking 205 Ba stars from the literature and estimated their masses using HR diagram. Adding to this data set, the five Ba from our sample, we have studied

*Main results of this work are accepted for publication in the Astronomical Journal (AJ), 2022.

the mass distribution of Ba stars. We have also estimated the initial masses of the companion AGBs of the programme stars with the help of a parametric model-based analysis using FRUITY models. The same analysis is used to estimate the masses of the companion AGBs of 159 Ba and 36 CEMP-*s* stars found in the literature.

As discussed in Chapters 1 & 4 the formation scenario of CEMP-*s* and Ba stars is similar. Both the types of stars (secondary) are extrinsic in nature, and they get the *s*-process rich material through mass-transfer from a more massive companion (primary), which evolves faster and produces *s*-process elements in the AGB phase.

Warner (1965) classified the Ba stars with Ba index 1 – 5 based on the strength of Ba II 4554 Å line. Ba1 and Ba5 signify stars showing the weakest and the strongest Ba lines, respectively. Several authors (Lu 1991; Jorissen *et al.* 1998; Yang *et al.* 2016; Escorza *et al.* 2017) used this Ba index to classify the Ba stars into two groups: mild Ba stars and strong Ba stars. The overabundance of *n*-capture elements is higher in strong Ba stars than that of mild Ba stars. Lower enhancement of heavy elements in mild Ba stars is explained by two plausible formation scenarios- i) a longer orbital period of the binary system and ii) relatively weaker neutron exposure in the AGB companion that pollutes the star (Yang *et al.* 2016).

In this chapter, we have presented, i) a brief review of the classification schemes of Ba and CEMP-*s* stars (Section 7.2), ii) classification of the programme stars under this study (Section 7.3), iii) determination of masses of the programme stars (Section 7.4), iv) determination of masses of the primary companions (AGB progenitors) of the programme stars (Section 7.5), v) a comprehensive discussion on the mass distributions of Ba stars and their AGB progenitors; and the mass distribution of the AGB progenitors of CEMP-*s* stars (Section 7.6) and vi) formation scenarios of mild and strong Ba stars (Section 7.7). Section 7.8 draws the

conclusions.

7.2 Classification schemes of the mild/strong Ba and CEMP-*s* stars: a brief review

7.2.1 Ba stars

Ba stars are first identified by Bidelman and Keenan (1951). Several authors (Pilachowski 1977; Sneden *et al.* 1981; Lu 1991; Jorissen *et al.* 1998; Yang *et al.* 2016; de Castro *et al.* 2016; Escorza *et al.* 2017; Jorissen *et al.* 2019) have put forward classification criteria to distinguish the mild and strong Ba stars. Pilachowski (1977) reported abundance analysis of seven Ba stars and demonstrated that the mild Ba stars show [s/Fe] $\geq$ 0.50, where [s/Fe] implies the average abundance of the available *s*-process elements. Sneden *et al.* (1981) suggested that the limiting values of [s/Fe] for mild Ba stars and classical (strong) Ba stars are 0.21 and 0.73 respectively. Using the Ba indices given by Warner (1965), Lu (1991) classified the Ba stars with Ba indices 0.3 – 1.5 as mild Ba stars and those with indices 2 – 5 as strong Ba stars. Jorissen *et al.* (1998) classified the stars with Ba index $\leq$ 2 as mild and Ba indices = 3 – 5 as strong Ba stars. Escorza *et al.* (2017) considered stars with Ba indices 1 and 2 as mild Ba stars and 3 – 5 as strong Ba stars. However, avoiding the use of Ba indices, Yang *et al.* (2016) used [Ba/Fe] as an indicator to distinguish the two groups. They considered stars with [Ba/Fe] $>$ 0.60 as strong Ba stars and stars with 0.17 $<$ [Ba/Fe] $<$ 0.54 as mild Ba stars. de Castro *et al.* (2016) used [s/Fe] $\geq$ 0.25 as a distinguishing value between normal giants and Ba stars. Jorissen *et al.* (2019) reported that [La/Fe] and [Ce/Fe] for strong Ba stars are greater than equal to unity, and that mild Ba stars always show [Ce/Fe] $\geq$ 0.2.

In this study, we use a similar criteria as that of Yang *et al.* (2016). We note that for many objects that are known as Ba stars in literature, the abundances of Ba are not reported due to the saturation of strong Ba lines in the spectra of Ba stars. We have used [hs/Fe] to differentiate the mild and strong Ba stars, where hs (heavy-*s*) represents Ba, La, Ce and Nd. We have not used Pr and Sm in the calculations of [hs/Fe], as the *r*-process contributes more to these two elements than that of *s*-process. We have considered stars with [hs/Fe] > 0.60 as strong Ba stars and stars with $0.17 <$ [hs/Fe] < 0.60 as mild Ba stars. We have discarded the possibility of using [s/Fe] as a classifier because [s/Fe] contains not only Pr and Sm, but also the ls elements Sr, Y, and Zr, and the *s*-process AGB models also cannot reproduce the ls elements satisfactorily. The ls elements are believed to have contributions from several different sources.

7.2.2 CEMP-*s* stars

CEMP stars are metal-poor stars ([Fe/H] < -1.0) with [C/Fe] > 0.7. Several classification schemes have been proposed in the literature (Beers and Christlieb 2005; Jonsell *et al.* 2006; Masseron *et al.* 2010; Abate *et al.* 2016; Frebel 2018; Hansen *et al.* 2019) to identify the CEMP-*s* stars from the different subclasses of CEMP stars. However, as discussed in Chapter 5, it is difficult to distinguish the CEMP-*s* and CEMP-*r/s* stars based on these classification schemes. In this Chapter, we have followed the classification scheme that we have put forward and discussed in Chapter 5. In particular, the CEMP-*s* stars are those that satisfy the conditions-

- CEMP-*s*: [C/Fe]$\geq$0.7, [Ba/Fe]$\geq$1.0

  i.) [Eu/Fe]$<$1.0, [Ba/Eu]$>$0.0 and/or [La/Eu]$>$0.5

ii.) [Eu/Fe]≥1.0, [Ba/Eu]>1.0 and/or [La/Eu]>0.7

7.3 Classification of the sample of Ba and CEMP-*s* stars

7.3.1 BD+75 348, BD+09 3019, HD 147609, HD 154276, HD 238020

A visual inspection of these objects clearly shows strong spectral lines of Sr II 4077 Å and Ba II 4554 Å, the characteristic features of Ba stars. After a detailed abundance analysis, we have classified these objects as Ba stars. The [Fe/H] of these objects lies between –0.68 and –0.10. HD 147609 and BD+75 348, with [C/Fe] $\sim$ 0.38 & 0.31, respectively are not carbon enhanced stars, but they show enhancement in *n*-capture elements. The abundance of C could not be estimated for HD 154276. BD+09 3019, with [C/Fe] $\sim$ 0.77, shows enhancement in carbon, and the *n*-capture elements are also strongly enhanced in the star. The high value of [hs/Fe] ($>$ 0.60) put BD+75 348, BD+09 3019 and HD 147609 in the category of strong Ba stars. HD 154276 and HD 238020, on the other hand, show only mild enhancement in *n*-capture elements. With [hs/Fe] $>$ 0.17, we classify these objects as mild Ba stars.

7.3.2 CD–27 14351, HD 145777, HE 0319–0215, HE 0507–1653, HE 0930–0018, HE 1023–1504

These objects are metal-poor (MP) and very metal-poor (VMP) stars with metallicity in the range –1.39 <[Fe/H] < –2.71. All these stars are carbon enhanced ([C/Fe] > 0.7) and enriched in *n*-capture elements. All the stars fall in the category of CEMP-*s* stars following our classification criteria. Although [Eu/Fe] is greater than unity in HE 0507–1653 and the classification scheme of Abate *et al.* (2016) (Figure 7.1)(a) puts it in the category of CEMP-*r/s* stars based on [Ba/Eu] > 0.0, Figure 7.1(b) shows that this star is a CEMP-*s* star from our classification scheme. We tried to fit *i*-process models (Hampel *et al.* 2016) calculated for neutron-densities, $n_n \sim 10^9 - 10^{15}$ cm^{-3} to the observed abundance pattern of HE 0507–1653. We found that the model with $n_n = 10^9$ cm^{-3} gives the minimum χ^2 value. So, this star cannot be a CEMP-*r/s* star. However, we will discuss in Section 7.5 that *s*-process yields produced by an M = 2.0 $M_\odot$ AGB can satisfactorily reproduce the observed abundance pattern of the star, placing it in the CEMP-*s* category. This verifies the upper limit on [Ba/Eu] (> 1.0) for CEMP-*r/s* stars put forward by us in our classification scheme.

7.4 Masses of the Ba stars

The masses of the programme stars are estimated from the position of the stars on the HR diagram ($\log(L/L_\odot)$ versus $\log(T_{eff})$ plot). In order to estimate the luminosities of the stars using Equation 7.1, the visual magnitudes (V) of the stars are taken from SIMBAD, the parallaxes (π) are taken from *Gaia*[†], the interstellar extinction (A_v) values are calculated from the formula given in Chen *et al.* (1998),

[†]`https://gea.esac.esa.int/archive/`

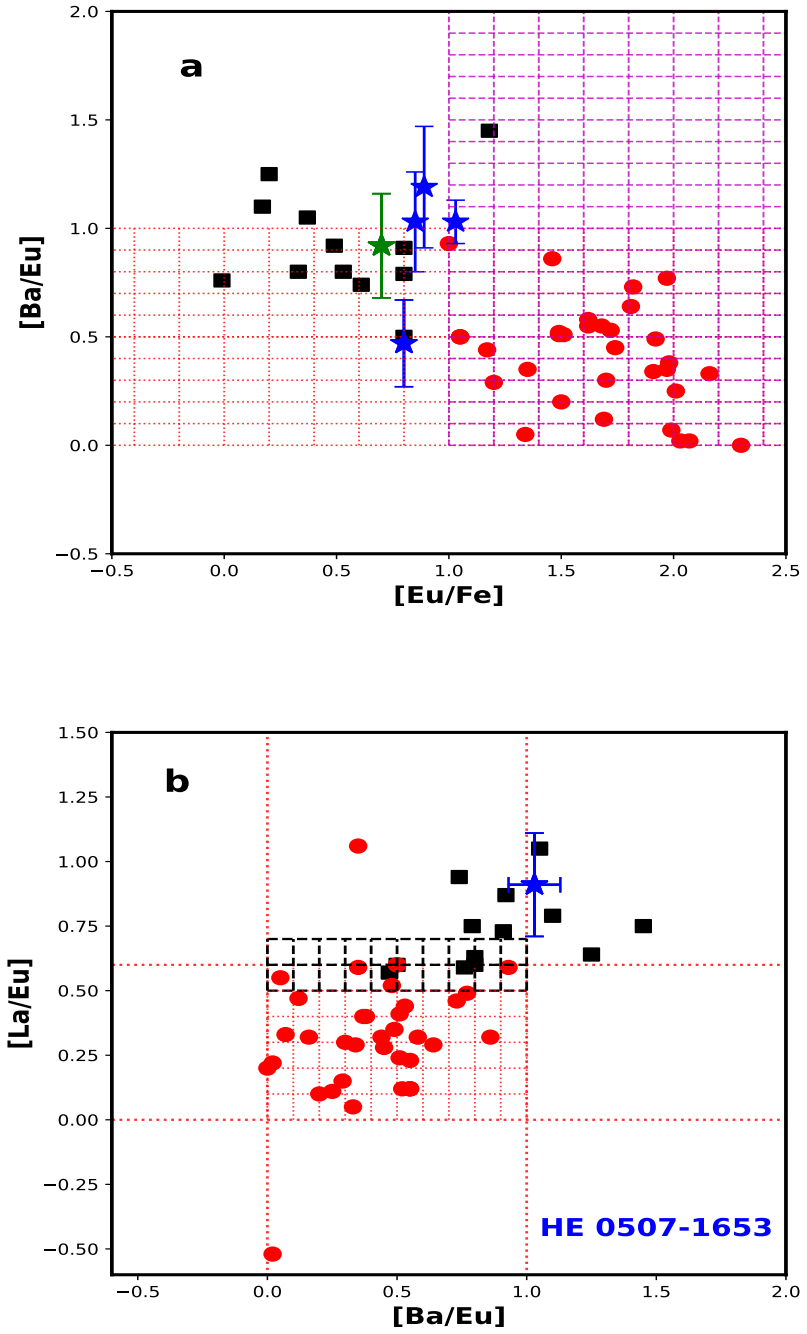

FIGURE 7.1: Filled red circles and filled black squares respectively represent literature CEMP-*r/s* and CEMP-*s* stars, the blue and the green stars represent the CEMP-*s* and Ba stars of this study. panel a: The grid formed by the dotted red lines represents the region of CEMP-*r/s* stars put forward by Beers and Christlieb (2005). The grid formed by the dashed magenta lines represents the region of CEMP-*r/s* stars put forward by Abate *et al.* (2016). panel b: Grid formed by the dotted red lines bound by $0.0 < [\mathrm{La/Eu}] < 0.6$ and $0.0 < [\mathrm{Ba/Eu}] < 1.0$ indicates the region defined for CEMP-*r/s* stars. The grid formed by the black dashed lines bound by $0.5 < [\mathrm{La/Eu}] < 0.7$ represents the region where $[\mathrm{Eu/Fe}] > 1.0$ classifies the stars as CEMP-*r/s* and $[\mathrm{Eu/Fe}] < 1.0$ classifies the stars as CEMP-*s*.

TABLE 7.1: **Observed abundance ratios and classifications of the Ba and CEMP-*s* stars.**

Star Name	[Fe/H]	[ls/Fe]	[hs/Fe]	[hs/ls]	[Eu/Fe]	[Ba/Eu]	[La/Eu]	Classification
BD+75 348	–0.42	1.26	1.75	0.49	0.70	0.92	1.22	Strong Ba star
BD+09 3019	–0.55	1.77	2.08	0.31	1.05	-	1.20	Strong Ba star
CD-27 14351	–2.71	1.97	1.66	–0.31	< 0.39	> 1.43	>1.17	CEMP-*s* star
HD 145777	–2.17	0.98	1.48	0.50	0.80	0.47	0.57	CEMP-*s* star
HD 147609	–0.28	1.19	1.25	0.06	0.13	1.27	1.14	Strong Ba star
HD 154276	–0.10	–0.08	0.25	0.33	-	-	-	Mild Ba star
HD 238020	–0.68	–0.04	0.30	0.34	-	-	-	Mild Ba star
HE 0319–0215	–2.57	0.89	1.90	1.01	0.85	1.03	-	CEMP-*s* star
HE 0507–1653	–1.44	1.39	2.02	0.63	1.03	1.03	0.91	CEMP-*s* star
HE 0930–0018	–1.39	0.54	1.11	0.57	-	-	-	CEMP-*s* star
HE 1023–1504	–1.66	1.22	2.24	1.02	0.89	1.19	-	CEMP-*s* star

the bolometric corrections (BC) are calculated using the empirical calibrations of Alonso *et al.* (1999).

$$log(L/L_{\odot}) = 0.4(M_{bol\odot} - V - 5 - 5log(\pi) + A_v - BC) \tag{7.1}$$

To estimate the mass of the stars, we have used the updated BASTI-IAC evolutionary tracks[‡] (Hidalgo *et al.* 2018) generated, including overshooting and diffusion, for the corresponding metallicities of the programme stars. For $\log(T_{eff})$, we have used our spectroscopic T_{eff} estimates. Figure 7.2(a) shows the evolutionary tracks corresponding to three Ba stars of our study. We could not determine the masses of the CEMP-*s* stars using the evolutionary tracks as they are not suitable for stars with enhanced carbon. As an illustration, in Figure 7.2(b) we have shown the evolutionary track corresponding to HE 0507–1653, a CEMP-*s* star. We can see that the star falls towards the right side of the evolutionary track. This is because the evolutionary tracks highly depend on the opacity in the stellar atmospheres, and the BASTI-IAC evolutionary tracks are not calculated considering

[‡]`http://basti-iac.oa-abruzzo.inaf.it/`

TABLE 7.2: **Masses of the Ba stars.**

Star Name	Parallax	A_v	BC	$\log(L/L_\odot)$	$\log T_{eff}$	Mass ($M_\odot$)
BD+75 348	1.6672	0.147608	–0.320606	1.83	3.684	1.20
BD+09 3019	0.4105	0.000000	–0.690934	2.62	3.625	1.00
HD 147609	4.301	0.04242	–0.35289	1.12	3.803	1.70
HD 154276	11.554	0.058009	–0.046765	0.164	3.764	1.00
HD 238020	2.4767	0.000000	–0.225678	1.81	3.712	2.20

high carbon abundances, which is one of the major sources of opacities for these objects (Marigo 2002). The use of the evolutionary tracks customised to the observed abundances of the stars is out of the scope of this thesis. The masses of the Ba stars including $\log(L/L_\odot)$ estimates, are presented in Table 7.2.

7.5 Initial masses of the binary companion (primary)

We have performed a parametric-model-based analysis, using AGB yields of the FRUITY[§] models (Straniero *et al.* 2006; Cristallo *et al.* 2009a, 2011, 2015) to estimate the initial masses of the companions of the programme stars. We have calculated the *s*-process yields, using FRUITY models, at different masses (1.3 – 6.0 $M_\odot$) corresponding to the metallicities of the programme stars. The observed abundances of the *n*-capture elements of a programme star are then fitted with the following parametric model function as discussed in Husti *et al.* (2009)–

$$\left[\frac{X}{Fe}\right] = log\left(10^{[X/Fe]^{ini}} \times (1 - 10^{-d}) + 10^{[X/Fe]^{AGB} - d}\right) \tag{7.2}$$

[§]`http://fruity.oa-teramo.inaf.it/`

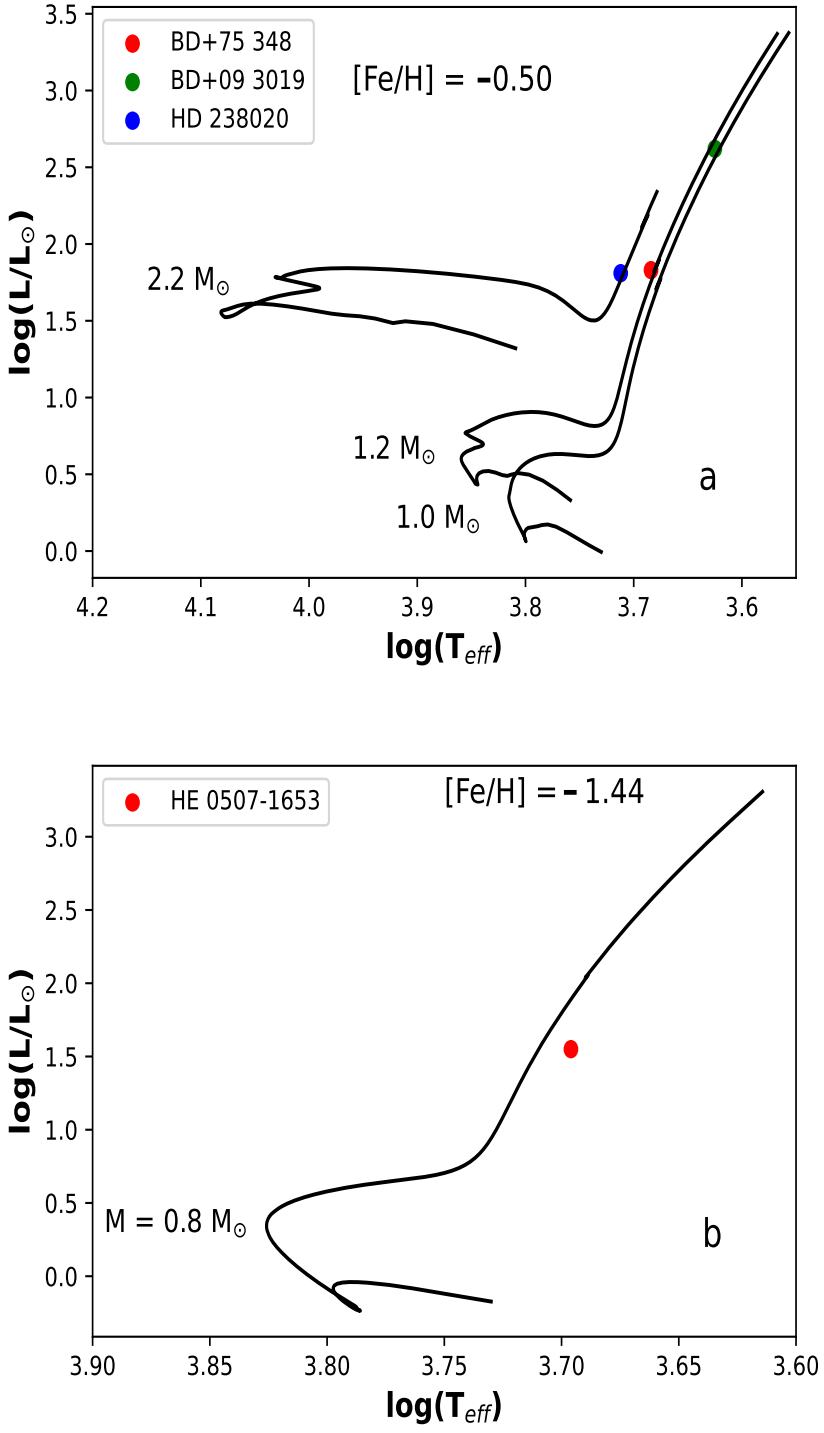

FIGURE 7.2: Hertzsprung-Russel diagram. Panel (a) shows evolutionary tracks for different masses at [Fe/H] ∼ -0.50. Red filled circle, green filled pentagon and blue filled triangle represent the positions of three Ba stars BD+75 348, BD+09 3019 and HD 238020 respectively. In panel (b), an evolutionary track for M = 0.8 $M_{\odot}$ at [Fe/H] = –1.44 is shown. The red filled circle represents a CEMP-*s* star HE 0507–1653.

where, $\left[\frac{X}{Fe}\right]$ is the abundance of the element X in the programme star, $[X/Fe]^{ini}$ is the initial abundance (before mass-transfer) of the element X in the programme star, $[X/Fe]^{AGB}$ is the AGB yield of the element X, d- the dilution factor is a free parameter. We find the model which gives the best fit to the observed abundances by varying d for each set of AGB model yields with different masses. In order to find the best fit, we have calculated χ^2 for each AGB model. The corresponding mass of the AGB model for which we get the minimum value of χ^2 is the required mass of the companion AGB of the programme star. The best-fit models with the AGB masses, corresponding dilution factors and minimum χ^2 values of the programme stars are shown in Figure 7.3.

7.6 Mass distribution of primary and secondary stars

The mass distribution of Ba stars has been previously studied by several groups (Han *et al.* 1995; Mennessier *et al.* 1997; Jorissen *et al.* 1998; Escorza *et al.* 2017; Jorissen *et al.* 2019). Using the same procedures discussed in Section 7.4 and Section 7.5, we have evaluated the mass distributions of Ba stars (secondary stars) and the primaries (companion AGBs) of both Ba and CEMP-*s* stars. For this analysis, we have selected a sample of 228 Ba stars and 36 CEMP-*s* stars from several sources in the literature. The atmospheric parameters and elemental abundances of the Ba stars are collected from Allen and Barbuy (2006), de Castro *et al.* (2016), Yang *et al.* (2016), Karinkuzhi *et al.* (2018), and Shejeelammal *et al.* (2020). We have calculated the [hs/Fe] values for the sample of 228 Ba stars and removed the ones having [hs/Fe] < 0.17. The lower limit (0.17) of [hs/Fe] ensures the selection of true Ba stars from the sample. The metallicity of the sample of Ba stars ranges from [Fe/H] = –1.11 to +0.23. In Table 7.3, we have presented the list of Ba stars

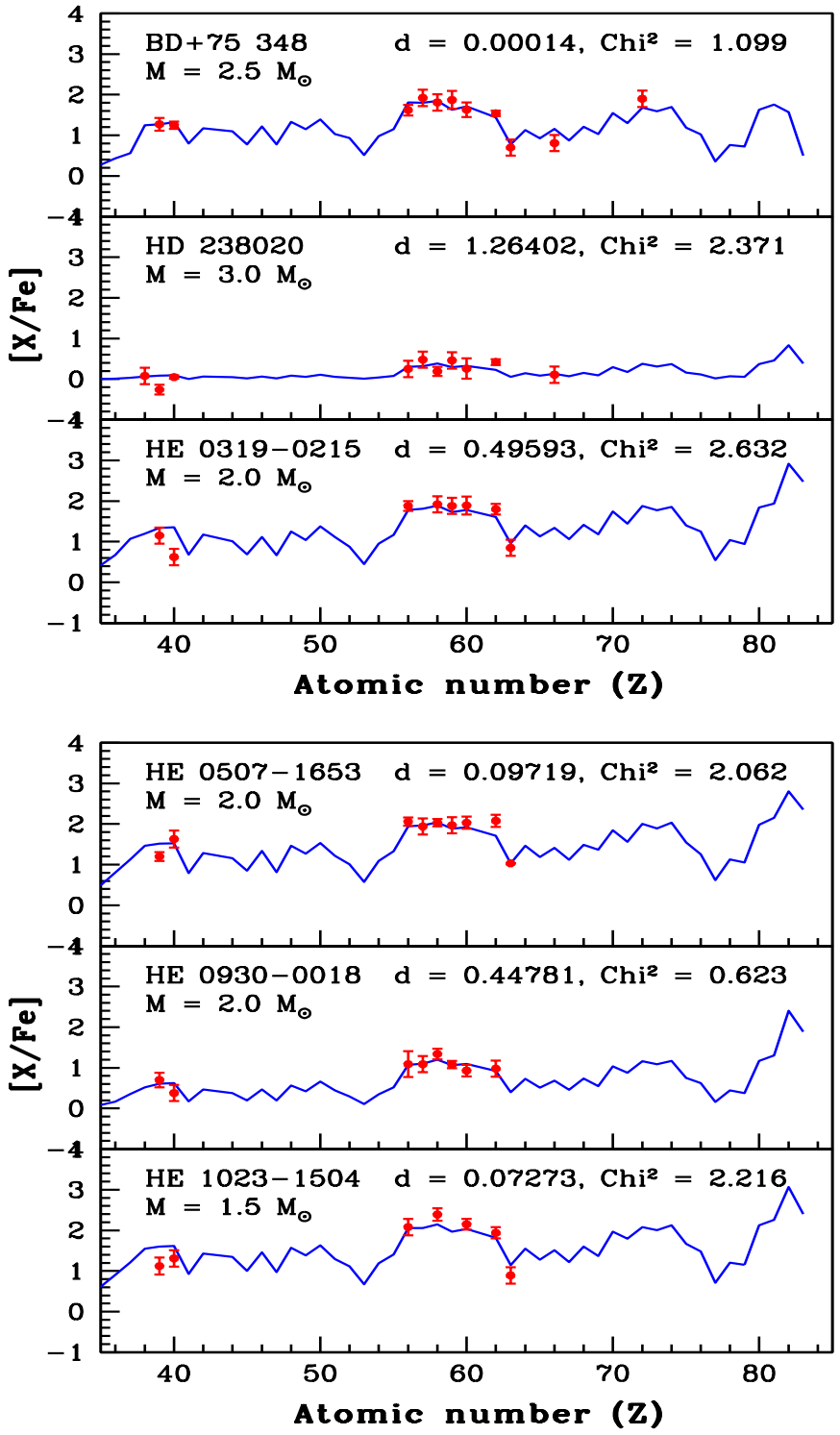

FIGURE 7.3: Best-fit parametric-models for a sample of two Ba (BD+75 348 & HD 238020) and four CEMP-*s* (HE 0319–0215, HE 0507–1653, HE 0930–0018 & HE 1023–1504) stars of this study. The points with error bars indicate the observed abundances.

used for this study. Column 6 of Table 7.3 gives the [hs/Fe] that we have calculated and column 13 shows the classification. The atmospheric parameters and elemental abundances of CEMP-*s* stars are taken from our previously compiled CEMP-*s* stars' list presented in Chapter 5 (Table 7.4). We could not estimate the masses of the sample of CEMP-*s* stars due to the inadequacy of the evolutionary tracks, as discussed in Section 7.4. We note that the method of deriving the masses of Ba and CEMP-*s* stars using evolutionary tracks in HR diagram is not free from certain drawbacks. In particular, the evolutionary tracks do not take care of the mass-transfer event taking place when the star was in the main-sequence stage.

7.6.1 Mass distribution of Ba stars

Han *et al.* (1995) from the theoretical analysis showed that the average mass of strong Ba stars is expected to be about 1.8 $M_{\odot}$. They found a different peak (1.7 $M_{\odot}$) when all the Ba stars, including mild and strong Ba stars, were considered. Mennessier *et al.* (1997) advocated that mild Ba stars are clump giants with 2.5 – 4.5 $M_{\odot}$ mass range, and these stars are a population of high and low mass objects dominated by high mass objects with a small tail of less massive objects. They found that strong Ba stars are giants in the mass range 1.0 – 3.0 $M_{\odot}$. Jorissen *et al.* (1998) also reported different mass values for mild and strong Ba stars. Considering the mass of the companion WD as 0.60 ± 0.04 $M_{\odot}$, they estimated the masses of mild and strong Ba stars to be 1.90 ± 0.20 and 1.50 ± 0.20, respectively. Escorza *et al.* (2017) derived the mass distribution of Ba stars using a large sample. In order to find the masses of the Ba stars, they generated the evolutionary tracks using *STAREVOL* at a metallicity [Fe/H] = –0.25. They don't see any difference in the mass distribution of mild and strong Ba stars, unlike the previous claims. They found that the mass distribution of Ba stars peaks at 2.5 $M_{\odot}$ with a tail at higher masses up to 4.5 $M_{\odot}$. Jorissen *et al.* (2019) also presented the mass distribution of the Ba stars they studied using a method similar to that of Escorza

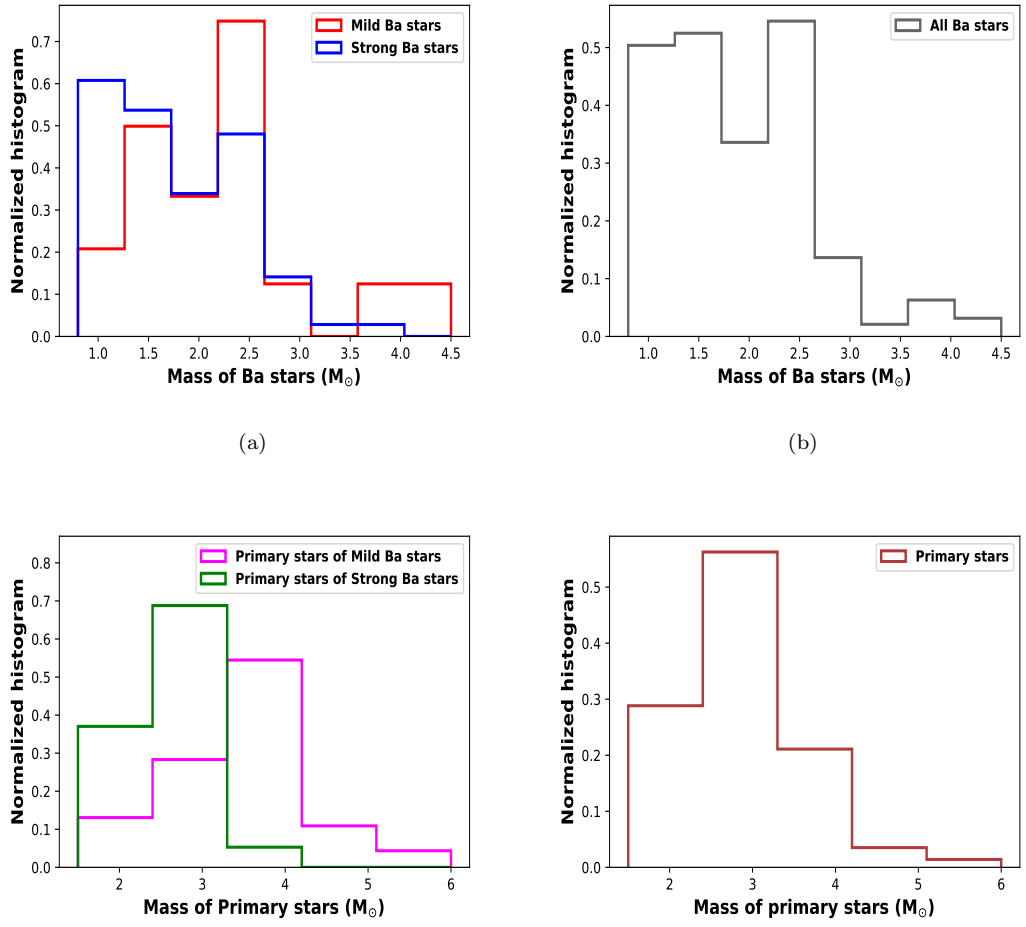

FIGURE 7.4: Mass distributions of Ba stars and their progenitor AGBs (primary stars). Panel (a) shows the mass distributions of mild and strong Ba stars. Panel (b) shows the mass distribution of both mild and strong Ba stars as a whole. Panel (c) shows the mass distributions of the primary stars of mild and strong Ba stars. Panel (d) shows the mass distribution of the primary stars of both mild and strong Ba stars as a whole.

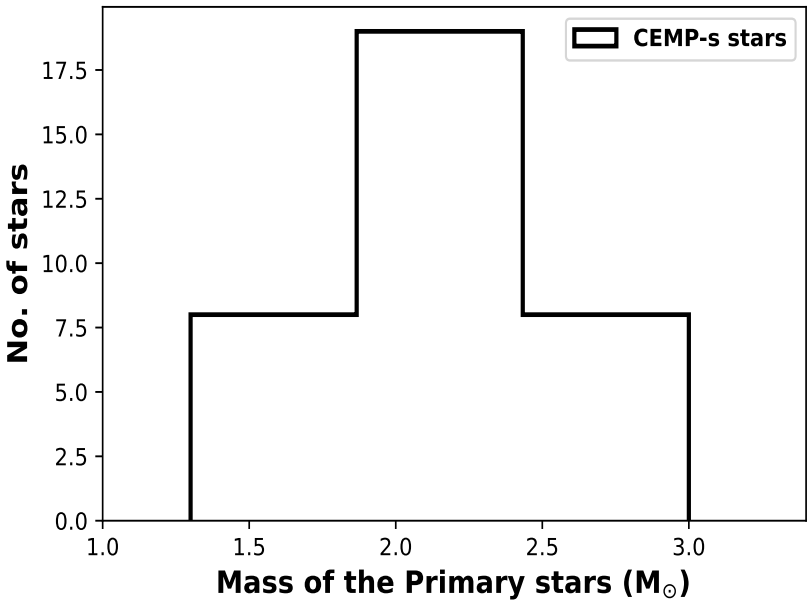

FIGURE 7.5: Mass distribution of the primary companions of the CEMP-*s* stars.

et al. (2017). However, Jorissen *et al.* (2019) have used the evolutionary tracks calculated at the metallicities of the individual stars as in order to get the accurate mass distribution, it is important to use the evolutionary tracks corresponding to the metallicities of the respective stars. Jorissen *et al.* (2019) found that the mass of Ba stars range from 1.0 – 3.0 $M_{\odot}$ with a tail up to 5 $M_{\odot}$. This tail is comprised of mild Ba stars, mostly of [Fe/H] $\geq$ –0.1.

Following the procedure described in Section 7.4 we have estimated the masses of the sample of Ba stars. We have used the BASTI-IAC evolutionary tracks at eleven different metallicities, [Fe/H] = +0.16, +0.05, –0.05, –0.15, –0.25, –0.35, –0.45, –0.55, –0.63, –0.72, –0.95 covering the metallicity range of the sample. We could estimate the masses of 205 Ba stars in total, out of which 52 are mild Ba stars, and 153 are strong Ba stars. The derived masses of the Ba stars are presented in Column 8 of Table 7.3. We found that the mild and strong Ba stars occupy the same mass range, with the tails of strong and mild Ba stars going to 4.0 M⊙ and 4.5 M⊙ respectively (Figure 7.4(a)). As an example, we have shown

in Figure 7.6(a) the positions of the sample of Ba stars in the HR diagram with evolutionary tracks of different masses at [Fe/H] = –0.25. Figure 7.4(b) shows the whole sample of Ba stars without distinguishing between mild and strong Ba stars. We found that the mass distribution of the Ba stars cannot be explained by a single Gaussian distribution. Rather, the Ba stars are distributed throughout the mass range in a disorderly manner. While Escorza *et al.* (2017) found the masses of the Ba stars to peak at 2.5 $M_{\odot}$, in our case, we found the average value of the distribution to be at 1.9 $M_{\odot}$. It is to be noted that Escorza *et al.* (2017) observed a lack of Ba stars in the mass range 1.0 – 2.0 $M_{\odot}$. But, neither our study nor the study by Jorissen *et al.* (2019) confirms that observation. The difference seen in this study and the study by Escorza *et al.* (2017) may come from two main sources. Firstly, the evolutionary tracks used in both studies are different. While Escorza *et al.* (2017) used STAREVOL code (not publicly available) to generate the evolutionary tracks, we have used the BASTI-IAC evolutionary tracks. Secondly, while Escorza *et al.* (2017) estimated the masses using the evolutionary tracks of a single [Fe/H] (=–0.25), our estimation is based on eleven different metallicities close to the metallicities of the sample stars. For instance, Figure 7.6(b) shows how different the evolutionary track of a particular mass could be at different metallicities.

7.6.2 Mass distribution of primary stars

We have estimated the masses of the companion AGBs of the sample of Ba and CEMP-*s* stars following the same procedure described in Section 7.5. For this study, we assume that the enhancement of *n*-capture elements in all these stars is due to a mass-transfer event in a binary system where the slightly massive companion (primary star) evolves through the AGB phase, produces *n*-capture elements and transfers the elements to the secondary star, which alters the surface

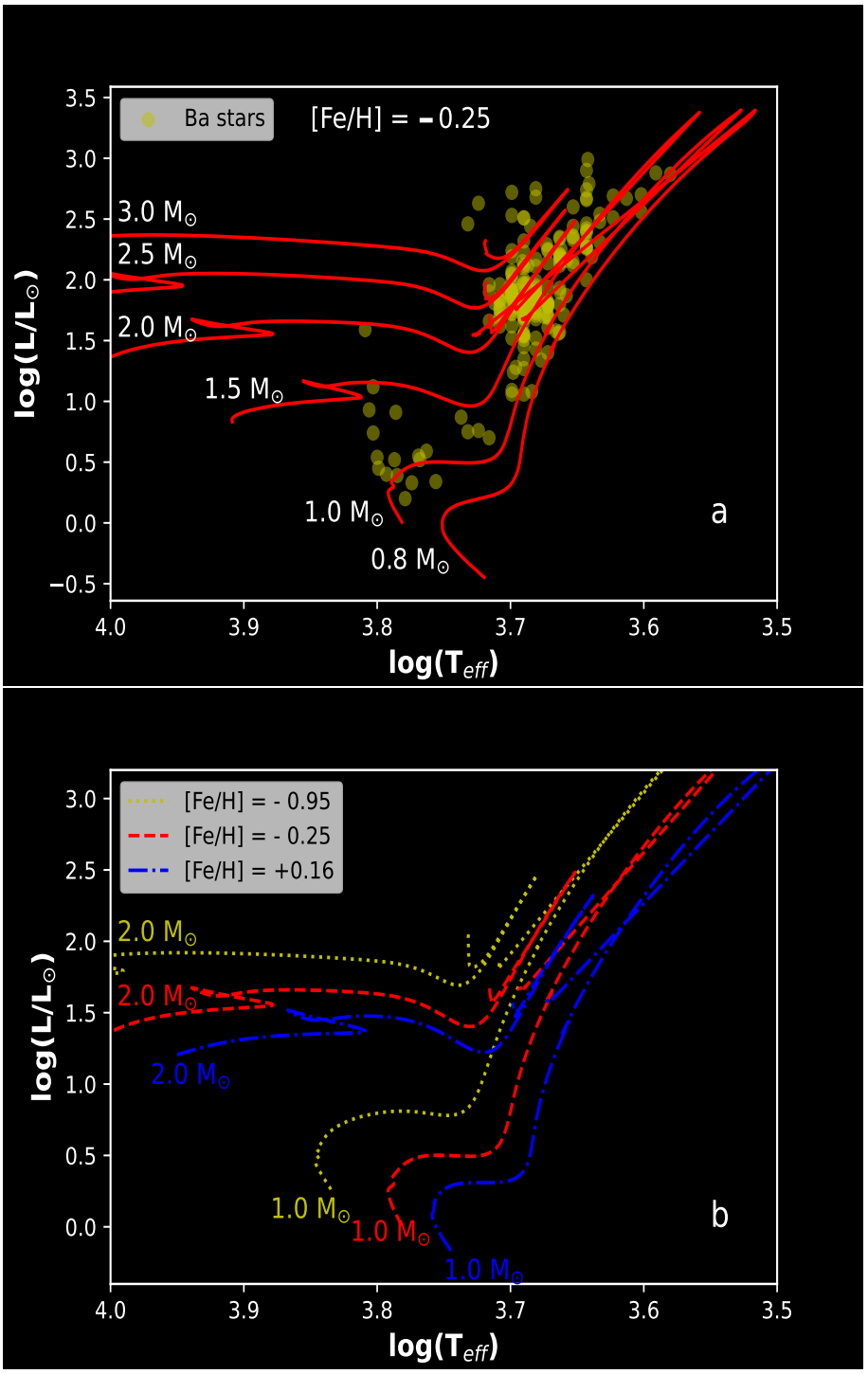

FIGURE 7.6: Hertzsprung-Russel diagram. Panel (a) shows evolutionary tracks for different masses at [Fe/H] = -0.25. Yellow points represent the positions of the Ba stars compiled from the literature. In panel (b), we have compared the evolutionary tracks for M = 1.0 $M_{\odot}$ & 2.0 $M_{\odot}$ at three different metallicities [Fe/H] = –0.95, –0.25 and +0.16.

composition of the secondary star significantly. If the uncertainty in abundance for a particular element is not reported in the literature, we considered the uncertainty to be 0.2 dex. The number of *n*-capture elements for which abundance estimates are available in the literature range from 4 to 14 (column 12 of Table 7.3 and column 8 of Table 7.4).

7.6.2.1 *Determination of the masses of the primary companions of Ba Stars:*

We could estimate the masses of the primary companions of 158 Ba stars. Out of these, 52 are mild Ba stars, and 106 are strong Ba stars. We have divided the sample of Ba stars into seven groups based on the metallicities of the stars and used FRUITY models at z = 0.020, 0.014, 0.010, 0.008, 0.006, 0.003, 0.002. We have presented the initial masses of the primary stars (M^{ini}_{AGB}), χ^2, dilution factor (d) and the number of elements used for the analysis (N) in columns 9, 10, 11 and 12, respectively of Table 7.3. When we plot the histograms of primary companions' masses for mild and strong Ba stars separately, we can clearly see two peaks (Figure 7.4(c)). The mass range of primaries for mild Ba stars ($1.5 < M_{\odot} < 6.0$) is greater than that ($1.5 < M_{\odot} < 4.0$) of strong Ba stars. The masses of primaries of strong Ba stars peak at 2.5 $M_{\odot}$ with a standard deviation of 0.51 $M_{\odot}$ and that of mild Ba stars peak at 3.7 $M_{\odot}$ with a standard deviation of 1.03 $M_{\odot}$. If we consider the Ba star sample as a whole, including both mild and strong Ba stars, then the mass distribution of the primaries of Ba stars is found to peak at 2.9 $M_{\odot}$ with a standard deviation of 1.15 $M_{\odot}$ (Figure 7.4(d)).

7.6.2.2 *Determination of the masses of the primary companions of CEMP-s Stars:*

The metallicities of the sample of CEMP-*s* stars range from [Fe/H] = –3.00 to –1.29. We have divided the sample into five groups based on the metallicities of the stars. We have used FRUITY models at z= 0.001, 0.0003, 0.0001, 0.00005, 0.00002. We have presented the initial masses of the primary stars (M^{ini}_{AGB}), χ^2, dilution factor (d) and the number of elements used for the analysis (N) in columns 5, 6, 7 and 8, respectively of Table 7.4. The primary mass distribution of CEMP-*s* stars is found to peak at 2.04 $M_{\odot}$ with a standard deviation of 0.49 $M_{\odot}$.

7.7 Formation scenarios of mild and strong Ba stars: a brief review

de Castro *et al.* (2016) considered that mild Ba stars are formed from the ISM mildly enhanced with *s*-process elements. However, this formation scenario can be discarded as studies of Jorissen *et al.* (1998, 2019) have shown that both mild and strong Ba stars are formed in binary systems and AGB mass-transfer is responsible for the enhanced abundances of heavy elements. From theoretical analysis, Han *et al.* (1995) showed that while most mild Ba stars are formed from the wind accretion and wind exposure channels, the strong Ba stars are formed from the wind accretion, wind exposure and stable Roche lobe overflow (RLOF) channels. Yang *et al.* (2016) discussed two possible formation scenarios for the formation of mild Ba stars- i) the mild enhancement could be explained by weaker neutron exposure in the progenitor AGB and/or ii) less accretion efficiency due to a longer orbital period which means larger distance between the binary companions. However, from long term radial velocity monitoring programs Jorissen *et al.* (1998,

2019) have shown that mild Ba stars are not limited to long period systems only. The orbital periods of strong Ba stars are generally shorter than that of mild Ba stars, but there is no tight correlation. In fact, there is a clear overlap in the orbital periods of these two subclasses. From Table 8 of Jorissen *et al.* (2019), we can see that the period ranges of mild and strong Ba stars are 80 – 22065 days and 185.7 – 8523 days, respectively. So, a scenario having a longer orbital period cannot explain the formation of a mild Ba star. However, we note that the ranges of both orbital periods and progenitor masses of mild Ba stars are larger than that of strong Ba stars.

The difference in the mass peaks of primaries for mild and strong Ba stars (Figure 7.4(c)) indicates that companions of mild Ba stars are more massive than those of strong Ba stars. This is not surprising because, from Figure 7.7(a), it can be seen that massive (e.g. 4, 5, 6 $M_{\odot}$) AGBs yield less than the low-mass AGBs with the same dilution factor. So, we can say that the dominant factor controlling the abundance peculiarities of Ba stars is the initial mass of the companion. Mass-transfer from 4.0 – 6.0 $M_{\odot}$ AGB companions can describe the formation of mild Ba stars. The WD masses of $\sim$ 1.0 $M_{\odot}$ around Ba stars also point towards a massive (5 $M_{\odot}$) companion AGB (Jorissen *et al.* 2019). However, there is an overlap from 1.3 – 4.0 $M_{\odot}$ in the case of primary masses of mild and strong Ba stars. In this mass range, the metallicity of the system and dilution (hence the distance of the binary companions) play crucial roles in the formation of mild Ba stars. In Figure 7.8, we have seen that the mild Ba stars are distributed towards higher metallicities than that of strong Ba stars. Figure 7.7(b) shows the metallicity dependence of the AGB models. At higher metallicities, *s*-process efficiency decreases, and hence AGB yields decrease.

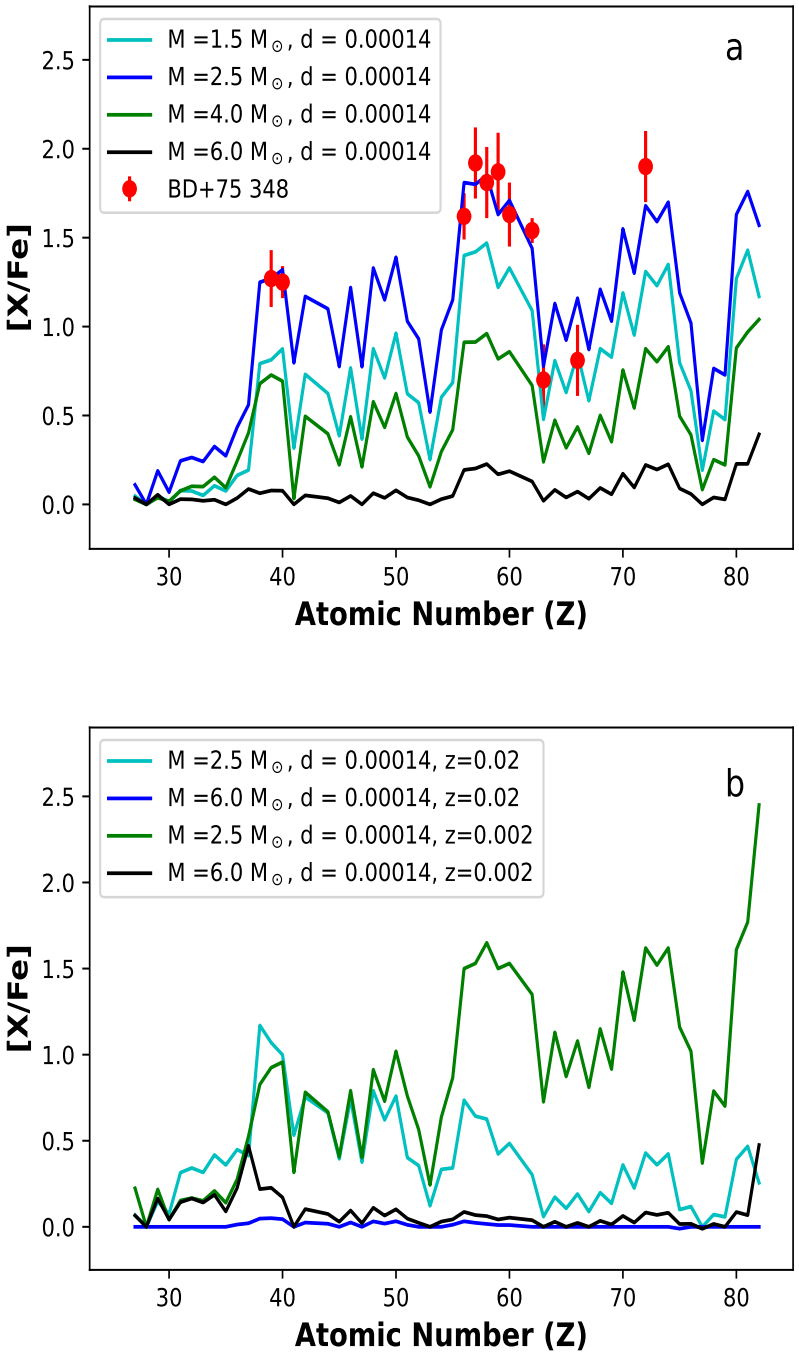

FIGURE 7.7: Panel a: Comparison of the *s*-process AGB model yields obtained at z = 0.006 for different masses using the same dilution factor (d). The points with error bars indicate the observed abundances of BD+75 348. Panel b: Comparison of the *s*-process AGB model yields obtained at two metallicities z = 0.02 and z = 0.002 for two masses M = 2.5 & 6.0 $M_{\odot}$ using the same dilution factor (d).

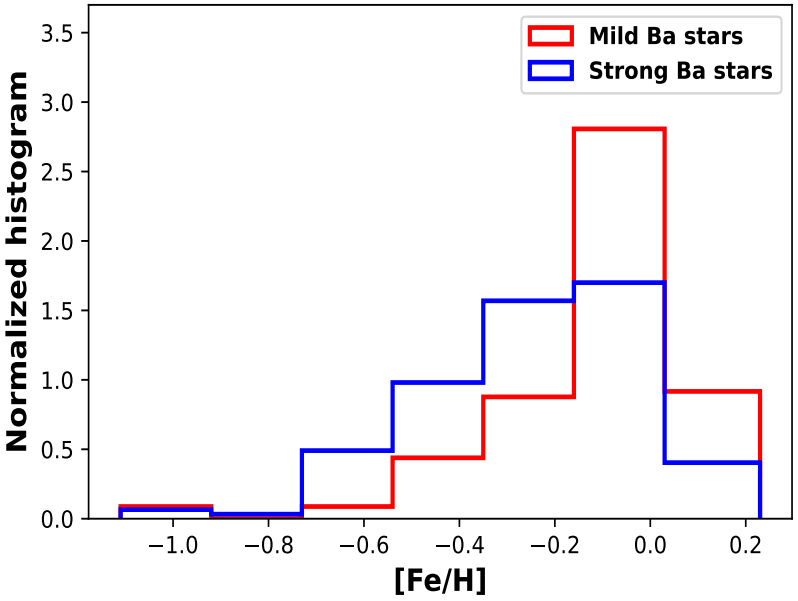

FIGURE 7.8: Metallicity distribution of the sample of mild and strong Ba stars.

7.8 Conclusions

We have conducted a detailed spectroscopic analysis of Ba and CEMP-*s* stars in our sample based on high-quality, high-resolution spectra. Out of the five Ba stars, we have classified three stars (BD+09 3019, BD+75 348 and HD 147609) as strong Ba stars and two stars (HD 154276 & HD 238020) as mild Ba stars. The stars (CD–27 14351, HD 145777, HE 0319–0215, HE 0507–1653, HE 0930–0018 and HE 1023–1504) are classified as CEMP-*s* stars. It is to be noted that HE 0507–1653 shows [Eu/Fe] $>$ 1.0 and according to the classification criteria of Abate *et al.* (2016) this star belongs to the category of CEMP-*r/s* stars, but the classification criteria that we proposed in Chapter 5 place this star in the CEMP-*s* subclass. While we could not get a reasonable fit for this object with *i*-process models with higher ($\geq 10^{12-15}$ cm^{-3}) neutron-densities, *s*-process AGB model with initial mass 2.0 M$\odot$ satisfactorily reproduces the observed abundance pattern. This star verifies our classification criteria.

We have derived the mass distribution of Ba stars and found that a single Gaussian cannot describe the mass distribution. The average mass of the distribution is found to be 1.9 $M_{\odot}$ with the tails of strong and mild Ba stars going up to 4.0 M⊙ and 4.5 M⊙ respectively. We confirm the previous claim by Escorza *et al.* (2017) that mild and strong Ba stars occupy the same mass range, but we do not confirm their claim that there is a lack of Ba stars in the mass range 1.0 – 2.0 $M_{\odot}$. Using a parametric-model-based analysis, we have derived the mass distributions of the AGB progenitors of the Ba and CEMP-*s* stars. To the best of our knowledge, this is the first attempt to derive the initial mass distribution of the primary companions of these stars. We found that the mass distributions of the progenitor AGBs of the mild and the strong Ba stars peak at different values. The peaks of the progenitor mass distributions of mild and strong Ba stars are at 3.7 $M_{\odot}$ and 2.5 $M_{\odot}$ respectively. We can, therefore, say that the initial mass of the companion AGB is the dominant factor controlling the heavy elements' enhancement in mild Ba stars. However, we cannot neglect the orbital periods and metallicities of the binary systems as a clear overlap can be seen in the progenitor mass distributions and orbital periods of mild and strong Ba stars. The mass distribution of progenitor AGBs of CEMP-*s* stars peak at 2.04 $M_{\odot}$ with a standard deviation of 0.49 $M_{\odot}$.

TABLE 7.3: **Masses of the Ba stars and initial masses of their AGB companions.**

Star Name	T_{eff} (K)	logg (cgs)	[Fe/H]	[ls/Fe]	[hs/Fe]	[hs/ls]	M_{Ba} ($M_\odot$)	M^{ini}_{AGB} ($M_\odot$)	χ^2	dil	N	Type	Ref
BD-01302	4200	1.10	-0.64	-0.14	0.17	0.310	-	1.5	0.67	1.85697	5	m	2
BD-18821	5000	2.30	-0.27	0.70	1.27	0.570	2.30	3.0	1.92	0.18030	5	s	2
BD-083194	4900	3.00	-0.10	0.95	1.52	0.570	2.00	-	-	-	5	s	2
BD-094337	4800	2.60	-0.24	1.31	1.50	0.190	1.80	2.5	0.26	0.42156	5	s	2
BD-142678	5200	3.10	0.01	0.94	0.94	0.010	3.00	-	-	-	5	s	2
BD+092384	4900	2.50	-0.98	0.57	0.88	0.310	0.80	3.0	0.90	0.46181	5	s	2
BD+185215	6300	4.20	-0.53	1.12	1.15	0.020	0.90	2.5	2.51	0.58244	14	s	1
CD-38585	4800	2.60	-0.52	1.00	1.54	0.540	0.80	2.0	0.41	0.17203	5	s	2
CD-267844	5100	2.80	0.02	0.55	0.39	-0.160	2.50	3.0	0.32	0.38827	5	m	2
CD-272233	4700	2.40	-0.25	0.81	1.10	0.290	1.20	2.0	0.85	0.24246	5	s	2
CD-298822	5100	2.80	0.04	0.94	1.15	0.220	3.00	-	-	-	5	s	2
CD-308774	4900	2.30	-0.11	0.50	0.43	-0.070	2.30	3.0	0.73	0.62088	5	m	2
CD-309005	4700	2.30	0.05	0.66	0.73	0.070	2.80	3.0	2.30	0.04737	5	s	2
CD-346139	4900	2.20	-0.07	0.63	0.66	0.030	3.00	-	-	-	5	s	2
CD-347430	4900	2.60	0.01	0.59	0.52	-0.080	2.40	3.0	0.72	0.25785	5	m	2
CD-463977	4900	2.60	-0.10	0.68	0.67	-0.010	2.20	-	-	-	5	s	2
CD-538144	4800	2.30	-0.19	0.81	1.16	0.340	1.70	2.5	3.21	0.02395	5	s	2
CD-611941	4800	2.40	-0.20	0.71	1.26	0.560	2.20	-	-	-	5	s	2

References: 1. Allen and Barbuy (2006), 2. de Castro *et al.* (2016). 3. Yang *et al.* (2016), 4. Karinkuzhi *et al.* (2018), 5. Shejeelammal *et al.* (2020), 6. This work

TABLE 7.3: *–continued*

Star Name	T_{eff} (K)	logg (cgs)	[Fe/H]	[ls/Fe]	[hs/Fe]	[hsls]	M_{Ba} ($M_\odot$)	M^{ini}_{AGB} ($M_\odot$)	χ^2	dil	N	Type	Ref
CPD-621013	5100	2.60	-0.08	0.72	0.94	0.220	2.60	-	-	-	5	s	2
CPD-644333	4900	2.60	-0.10	1.12	1.78	0.660	1.50	-	-	-	5	s	2
HD 107	6440	4.10	-0.36	0.49	0.59	0.100	2.60	-	-	-	13	m	1
HD 749	4610	2.80	0.17	0.84	1.09	0.250	1.30	-	-	-	14	s	1, 2
HD 4084	4800	2.80	-0.42	0.85	0.89	0.040	1.20	2.5	1.76	0.78980	5	s	2
HD 5322	4800	1.70	-0.18	0.03	0.21	0.180	4.50	5.0	0.27	0.10268	5	m	2
HD 5424	4728	2.50	-0.43	1.28	1.84	0.560	1.00	2.5	5.80	0.01784	16	s	1, 2, 4
HD 5825	5000	2.70	-0.48	0.75	1.11	0.360	2.20	2.5	0.48	0.67253	5	s	2
HD 8270	5940	4.20	-0.42	0.93	0.92	-0.010	0.90	4.0	1.74	0.08759	14	s	1
HD 11353	4592	2.10	0.04	-	0.38	-	2.50	4.0	2.03	0.49563	4	m	3
HD 11658	4699	2.60	0.00	-0.14	0.22	0.360	1.60	4.0	1.51	1.90483	5	m	3
HD 12392	4987	3.40	-0.38	1.12	1.43	0.310	1.10	2.5	2.32	0.12114	11	s	1, 2, 4
HD 13551	5870	4.00	-0.24	0.75	0.75	-0.010	1.00	2.5	0.80	0.72091	14	s	1
HD 13787	4966	2.90	0.00	0.35	0.54	0.190	2.40	4.0	1.22	0.09316	5	m	3
HD 15589	4900	3.10	-0.27	0.94	1.61	0.670	1.40	-	-	-	5	s	2
HD 16458	4550	1.80	-0.64	1.21	1.46	0.250	1.00	2.5	8.08	0.14053	11	s	4
HD 17067	4200	1.10	-0.61	0.83	1.33	0.500	1.00	2.5	3.66	0.38338	5	s	2
HD 18182	4900	2.40	-0.17	0.42	0.30	-0.120	2.00	3.0	0.10	0.78827	5	m	2
HD 18361	4900	2.60	0.01	0.49	0.36	-0.130	2.40	4.0	0.02	0.06940	5	m	2

TABLE 7.3: *–continued*

Star Name	T_{eff} (K)	logg (cgs)	[Fe/H]	[ls/Fe]	[hs/Fe]	[hsls]	M_{Ba} ($M_\odot$)	M^{ini}_{AGB} ($M_\odot$)	χ^2	dil	N	Type	Ref
HD 18418	4845	2.40	-0.29	0.12	0.67	0.550	3.00	4.0	0.80	0.22111	5	s	3
HD 20394	5100	2.90	-0.22	1.07	1.43	0.360	2.30	2.5	1.18	0.04319	5	s	2
HD 20644	4115	1.20	-0.12	-	0.59	-	-	1.5	1.49	0.17501	4	m	3
HD 21682	5200	2.80	-0.48	0.52	0.88	0.360	2.40	2.5	0.02	0.94319	5	s	2
HD 21989	4400	1.80	-0.14	0.54	0.68	0.140	1.60	2.0	0.98	0.35407	5	s	2
HD 22285	4900	2.30	-0.60	0.97	1.32	0.350	1.30	2.5	1.15	0.33086	5	s	2
HD 22589	5400	3.30	-0.27	0.91	0.59	-0.320	1.40	2.5	1.77	0.84988	14	m	1
HD 22772	4800	2.40	-0.17	0.84	0.99	0.150	1.10	3.0	1.12	0.01119	5	s	2
HD 24035	4750	2.20	-0.51	1.75	1.61	-0.140	0.80	-	-	-	-	s	5
HD 26886	5000	2.50	-0.30	0.47	0.72	0.250	2.30	3.0	0.01	0.71536	5	s	2
HD 27271	5022	2.90	-0.07	0.87	0.77	-0.100	2.60	3.0	11.25	0.00100	12	s	1, 4
HD 28159	3900	2.00	-0.50	0.25	0.40	0.140	0.80	5.0	12.82	0.10815	12	m	4
HD 29370	4800	2.10	-0.25	0.77	1.21	0.440	1.80	2.0	1.70	0.18502	5	s	2
HD 29685	4900	2.70	-0.07	0.57	0.66	0.090	1.40	3.0	1.87	0.16276	5	s	2
HD 30240	5100	2.70	0.02	0.70	0.72	0.020	2.80	3.0	1.60	0.03818	5	s	2
HD 30554	4800	2.50	-0.12	0.69	0.92	0.230	1.50	2.0	1.26	0.10176	5	s	2
HD 31308	4865	2.80	0.16	-	0.31	-	3.00	4.0	1.93	0.49622	4	m	3
HD 31487	4960	3.10	-0.04	1.28	1.58	0.300	2.60	-	-	-	11	s	4
HD 31812	5100	2.60	-0.07	0.66	0.53	-0.130	2.50	3.0	0.52	0.20328	5	m	2
HD 32712	4550	2.50	-0.25	0.63	1.52	0.890	1.00	2.5	15.82	0.03205	11	s	5

TABLE 7.3: *–continued*

Star Name	T_{eff} (K)	logg (cgs)	[Fe/H]	[ls/Fe]	[hs/Fe]	[hsls]	M_{Ba} ($M_\odot$)	M^{ini}_{AGB} ($M_\odot$)	χ^2	dil	N	Type	Ref
HD 32901	4400	1.60	-0.44	0.29	0.92	0.630	0.80	3.0	0.52	0.63315	5	s	2
HD 33709	5000	2.10	-0.20	0.36	0.45	0.090	4.00	-	-	-	5	m	2
HD 35993	5100	2.90	-0.05	0.91	1.22	0.310	2.40	-	-	-	5	s	2
HD 36650	4880	2.40	-0.02	0.62	0.84	0.210	1.90	3.0	2.61	0.18718	5	s	5
HD 38488	4400	2.00	0.05	0.83	0.98	0.140	2.30	-	-	-	5	s	2
HD 39778	5000	2.50	-0.12	0.78	0.98	0.200	2.40	-	-	-	5	s	2
HD 40430	4900	2.50	-0.23	0.67	0.85	0.180	2.20	3.0	0.14	0.48739	5	s	2
HD 41701	5000	2.60	0.02	0.35	0.39	0.040	2.60	4.0	0.53	0.14309	5	m	2
HD 42700	4800	2.20	-0.25	0.09	0.22	0.130	1.70	6.0	0.07	0.09376	5	m	2
HD 43232	4386	1.40	-0.03	0.12	0.46	0.340	4.00	-	-	-	5	m	3
HD 43389	4000	2.00	-0.38	0.50	1.49	0.980	-	2.0	10.18	0.18226	12	s	2, 4
HD 45483	4800	2.20	-0.14	0.65	0.61	-0.040	1.80	2.0	0.32	0.35138	5	s	2
HD 46407	4854	2.20	-0.36	1.31	1.58	0.280	1.40	-	-	-	11	s	4
HD 48565	5860	4.00	-0.62	1.06	1.40	0.340	1.30	2.5	1.50	0.41230	14	s	1
HD 48814	4800	2.30	-0.07	0.39	0.28	-0.110	2.00	4.0	0.18	0.22345	5	m	2
HD 49017	5100	2.80	0.02	0.09	0.35	0.260	2.80	4.0	1.17	0.45773	5	m	2
HD 49641	4400	1.50	-0.30	0.71	1.29	0.580	2.20	3.0	0.15	0.08592	7	s	2, 3
HD 49661	5000	2.40	-0.13	0.15	0.33	0.180	2.40	4.0	0.31	0.29285	5	m	2
HD 49778	5000	2.30	-0.22	0.16	0.37	0.210	4.50	5.0	0.04	0.06051	5	m	2
HD 50075	4900	2.50	-0.16	0.63	0.97	0.340	2.40	-	-	-	5	s	2

TABLE 7.3: *–continued*

Star Name	T_{eff} (K)	logg (cgs)	[Fe/H]	[ls/Fe]	[hs/Fe]	[hsls]	M_{Ba} ($M_\odot$)	M^{ini}_{AGB} ($M_\odot$)	χ^2	dil	N	Type	Ref
HD 50082	4789	2.40	-0.32	1.06	1.50	0.440	1.40	2.5	3.55	0.13084	12	s	4
HD 50843	4700	2.30	-0.31	0.21	0.65	0.440	0.90	4.0	0.28	0.17401	5	s	2
HD 51959	5000	3.20	-0.10	0.69	0.89	0.200	1.20	2.0	1.05	0.12993	5	s	2
HD 53199	5000	2.30	-0.23	0.69	0.92	0.230	2.10	-	-	-	6	s	2
HD 58121	4600	1.80	-0.01	0.33	0.44	0.100	2.50	4.0	1.66	0.07038	7	m	2, 3
HD 58368	5000	2.60	0.04	0.72	0.91	0.190	2.50	-	-	-	5	s	2, 3
HD 59852	5000	2.20	-0.22	0.34	0.37	0.030	2.60	-	-	-	5	m	2
HD 60197	3800	2.00	-0.60	0.96	1.21	0.240	-	2.5	9.78	0.04846	12	s	4
HD 61332	4700	2.10	0.07	0.41	0.49	0.080	2.50	4.0	0.68	0.01184	5	m	2
HD 62017	5000	1.80	-0.32	0.72	0.80	0.080	2.80	3.0	0.64	0.53949	5	s	2
HD 64425	4900	2.40	0.06	0.86	1.06	0.200	2.10	-	-	-	5	s	2
HD 66216	4588	2.40	0.23	-	0.31	-	-	4.0	0.57	0.49628	4	m	3
HD 66291	4600	1.50	-0.31	0.66	0.87	0.220	-	2.5	0.51	0.75217	5	s	2
HD 67036	4300	1.50	-0.41	0.92	1.24	0.320	1.10	2.5	2.42	0.51454	5	s	2
HD 71458	4600	2.20	-0.03	0.59	0.77	0.170	2.10	3.0	2.88	0.06749	5	s	2
HD 74950	4200	1.20	-0.21	0.60	0.88	0.280	1.30	2.0	0.87	0.48814	5	s	2
HD 76225	6110	3.80	-0.31	1.17	1.10	-0.070	1.20	2.5	1.10	0.49086	14	s	1
HD 81797	4034	1.20	0.01	0.15	0.50	- 0	-	4.0	2.80	0.37459	4	m	3
HD 82221	4400	1.60	-0.21	0.84	0.92	0.080	1.30	3.0	0.46	0.24681	5	s	2
HD 83548	5000	2.40	0.03	0.70	0.77	0.070	3.50	-	-	-	5	s	2

TABLE 7.3: *–continued*

Star Name	T_{eff} (K)	logg (cgs)	[Fe/H]	[ls/Fe]	[hs/Fe]	[hsls]	M_{Ba} ($M_\odot$)	M^{ini}_{AGB} ($M_\odot$)	χ^2	dil	N	Type	Ref
HD 84610	4900	2.50	0.00	0.59	0.59	-0.000	2.30	3.0	1.48	0.19780	5	m	2
HD 84678	4600	1.70	-0.13	1.15	1.77	0.620	1.90	-	-	-	5	s	2
HD 87080	5460	3.70	-0.44	1.15	1.63	0.480	1.40	2.0	1.08	0.16062	14	s	1
HD 88035	4900	2.40	-0.10	0.83	1.31	0.480	2.60	-	-	-	5	s	2
HD 88495	4900	3.00	-0.11	0.67	0.66	-0.010	1.00	2.0	0.21	0.30187	5	s	2
HD 88562	4000	2.00	-0.53	0.90	1.21	0.300	0.80	2.5	6.92	0.53838	12	s	4
HD 88927	4600	2.30	0.02	0.41	0.24	-0.160	1.20	4.0	0.12	0.23975	5	m	2
HD 89175	4900	2.10	-0.55	1.03	1.88	0.850	1.30	2.5	2.06	0.04801	5	s	2
HD 89638	4900	2.40	-0.19	0.46	0.68	0.220	1.80	2.0	1.04	0.40945	5	s	2
HD 89948	6010	4.30	-0.30	1.01	0.82	-0.190	0.90	2.5	1.97	0.78790	14	s	1
HD 90127	4600	2.20	-0.40	0.70	0.93	0.230	1.00	2.5	0.88	0.82555	7	s	2, 3
HD 90167	5000	2.60	-0.04	0.51	0.31	-0.200	2.60	4.0	0.05	0.09771	5	m	2
HD 91208	5100	3.00	0.05	0.77	0.77	-0.000	2.40	2.5	1.72	0.01872	5	s	2
HD 91979	4900	2.70	-0.11	0.73	0.92	0.180	1.20	2.0	0.90	0.08348	5	s	2
HD 92545	6210	4.00	-0.12	0.69	0.69	0.010	1.10	2.0	0.69	0.29535	14	s	1
HD 92626	4800	2.30	-0.15	1.10	1.98	0.880	2.50	-	-	-	5	s	2
HD 94518	5700	3.90	-0.55	0.66	0.86	0.200	0.80	1.5	9.91	0.21671	9	s	5
HD 95193	5000	2.70	0.04	0.61	0.54	-0.070	2.60	3.0	1.16	0.20525	7	m	2, 3
HD 95345	4500	1.80	-0.16	0.01	0.23	0.220	1.50	5.0	0.54	0.11124	5	m	2
HD 100503	4000	2.00	-0.72	1.18	1.67	0.490	-	2.0	6.43	0.00100	12	s	4

TABLE 7.3: *–continued*

Star Name	T_{eff} (K)	logg (cgs)	[Fe/H]	[ls/Fe]	[hs/Fe]	[hsls]	M_{Ba} ($M_\odot$)	M^{ini}_{AGB} ($M_\odot$)	χ^2	dil	N	Type	Ref
HD 102762	4400	1.70	-0.17	0.85	1.51	0.650	2.30	-	-	-	5	s	2
HD 102762	4400	1.70	-0.17	0.85	1.51	0.650	2.30	-	-	-	5	s	2
HD 107264	4500	1.50	-0.19	0.74	1.23	0.480	2.60	-	-	-	5	s	2
HD 107270	5400	2.70	0.05	0.69	0.32	-0.370	4.00	-	-	-	5	m	2
HD 107541	5000	3.20	-0.63	1.44	2.07	0.630	0.80	-	-	-	5	s	2
HD 107574	6400	3.60	-0.55	0.84	1.19	0.350	1.10	2.5	1.66	0.65343	14	s	1
HD 109061	4700	2.00	-0.56	0.56	0.75	0.190	0.90	4.0	0.16	0.19367	5	s	2
HD 110483	4900	2.60	-0.04	0.78	1.17	0.390	1.90	-	-	-	5	s	2
HD 110591	4700	1.80	-0.56	0.41	0.86	0.450	0.90	2.0	0.38	0.91031	5	s	2
HD 111315	4900	2.00	0.04	0.47	0.62	0.150	3.50	-	-	-	5	s	2
HD 113195	4700	2.10	-0.15	0.57	0.47	-0.100	1.40	2.0	0.11	0.50865	5	m	2
HD 113291	4700	2.60	-0.02	1.04	1.24	0.200	2.60	-	-	-	5	s	2
HD 114678	5200	2.80	-0.50	1.04	1.40	0.360	1.90	2.5	0.37	0.35642	5	s	2
HD 115277	4800	2.40	-0.03	0.52	0.29	-0.230	1.80	3.0	0.09	0.50414	5	m	2
HD 116869	4892	2.60	-0.44	0.87	1.19	0.320	1.40	2.5	3.63	0.59315	15	s	1, 2, 4
HD 119185	4800	2.00	-0.43	0.26	0.53	0.270	1.30	2.5	0.05	1.39963	5	m	2
HD 119650	4500	1.60	-0.10	0.29	0.28	-0.010	2.00	4.0	0.19	0.25877	5	m	2
HD 120571	4600	1.70	-0.39	0.42	0.83	0.410	2.00	-	-	-	5	s	2
HD 120620	4831	3.00	-0.30	1.41	1.66	0.250	0.80	-	-	-	11	s	2, 4
HD 121447	4000	1.00	-0.90	1.38	2.13	0.750	0.80	-	-	-	-	s	4

TABLE 7.3: *–continued*

Star Name	T_{eff} (K)	logg (cgs)	[Fe/H]	[ls/Fe]	[hs/Fe]	[hsls]	M_{Ba} ($M_\odot$)	M^{ini}_{AGB} ($M_\odot$)	χ^2	dil	N	Type	Ref
HD 122687	5000	2.60	-0.07	0.86	1.22	0.350	2.50	-	-	-	5	s	2
HD 123396	4360	1.40	-0.99	0.64	1.23	0.600	0.80	2.0	3.93	0.54064	14	s	1, 2
HD 123585	6350	4.20	-0.48	1.27	1.64	0.370	1.20	2.5	1.02	0.18789	14	s	1
HD 123701	5000	2.50	-0.44	0.83	1.30	0.470	1.70	2.0	0.64	0.40272	5	s	2
HD 123949	4378	1.80	-0.31	1.08	1.44	0.360	-	2.5	4.02	0.13418	11	s	4
HD 126313	4900	2.20	-0.10	0.76	1.21	0.460	4.00	-	-	-	5	s	2
HD 130255	4400	1.50	-1.11	0.34	0.42	0.080	-	4.0	0.27	0.47583	5	m	2
HD 131670	4700	2.20	-0.04	0.61	0.74	0.130	1.60	3.0	3.23	0.06881	5	s	2
HD 134698	4500	1.70	-0.52	0.57	0.53	-0.050	0.90	4.0	0.50	0.37469	5	m	2
HD 136636	4900	2.50	-0.04	0.91	1.29	0.390	1.70	-	-	-	5	s	2
HD 139266	4300	1.50	-0.27	0.78	1.17	0.390	1.60	2.0	2.43	0.20975	5	s	2
HD 139409	4700	2.10	-0.51	0.57	0.46	-0.110	0.80	4.0	0.95	0.43531	5	m	2
HD 142491	4800	2.00	0.02	0.02	0.26	0.240	4.50	-	-	-	5	m	2
HD 142751	4600	2.00	-0.10	0.72	0.78	0.060	1.80	2.0	0.74	0.18853	5	s	2
HD 143899	5000	2.50	-0.27	0.71	0.84	0.120	1.60	3.0	0.29	0.36915	5	s	2
HD 147136	4900	2.20	-0.01	-0.03	0.25	0.280	2.80	4.0	0.95	0.81585	5	m	2
HD 147884	5100	3.00	-0.09	0.90	0.90	0.010	2.50	-	-	-	5	s	2
HD 148177	4400	1.60	-0.15	0.69	0.78	0.090	2.50	2.0	1.32	0.20523	5	s	2
HD 148892	5000	2.30	-0.15	0.73	0.87	0.140	2.80	-	-	-	5	s	2

TABLE 7.3: *–continued*

Star Name	T_{eff} (K)	logg (cgs)	[Fe/H]	[ls/Fe]	[hs/Fe]	[hsls]	M_{Ba} ($M_\odot$)	M^{ini}_{AGB} ($M_\odot$)	χ^2	dil	N	Type	Ref
HD 150862	6310	4.60	-0.10	1.00	0.68	-0.320	1.10	3.0	0.75	0.19437	14	s	1
HD 154430	4200	1.20	-0.36	0.95	1.55	0.600	-	2.0	2.20	0.01517	5	s	2
HD 162806	4500	1.70	-0.26	0.72	1.11	0.390	1.80	2.0	0.28	0.10093	5	s	2
HD 168214	5300	3.20	-0.08	0.99	0.88	-0.110	1.50	-	-	-	5	s	2
HD 168560	4400	1.60	-0.13	0.42	0.65	0.240	1.70	2.0	1.42	0.45179	5	s	2
HD 168791	4400	1.70	-0.23	0.79	1.07	0.290	2.80	3.0	1.90	0.27214	5	s	2
HD 169106	4900	2.20	0.01	0.41	0.35	-0.050	4.00	-	-	-	5	m	2
HD 176105	4500	1.60	-0.14	0.46	0.49	0.030	1.90	2.0	0.19	0.56867	5	m	2
HD 177192	4700	1.70	-0.17	0.65	0.48	-0.170	1.20	2.0	0.31	0.44651	5	m	2
HD 178717	3800	1.00	-0.52	0.89	0.89	-0.010	0.80	2.5	5.88	0.76176	12	s	4
HD 179832	4780	2.70	0.23	0.52	0.43	-0.100	-	4.0	43.14	0.19279	11	m	5
HD 180622	4600	2.20	0.03	0.51	0.39	-0.120	1.50	4.0	0.29	0.03012	5	m	2
HD 180996	4900	2.60	0.06	0.55	0.49	-0.060	2.10	3.0	0.72	0.31511	5	m	2
HD 182300	5000	2.70	0.06	0.84	1.10	0.260	2.60	-	-	-	5	s	2
HD 183915	4500	1.60	-0.39	0.78	1.58	0.800	1.70	2.0	0.07	0.09492	5	s	2
HD 184001	5000	2.50	-0.21	0.60	0.61	0.010	2.20	2.5	0.04	0.81789	5	s	2
HD 187308	4900	2.50	-0.08	0.65	0.70	0.060	2.10	3.0	1.93	0.08263	5	s	2
HD 187762	4800	2.40	-0.30	0.23	0.54	0.310	1.50	-	-	-	5	m	2
HD 188985	6090	4.30	-0.30	1.08	1.16	0.070	0.90	2.5	0.71	0.46841	14	s	1

TABLE 7.3: *–continued*

Star Name	T_{eff} (K)	logg (cgs)	[Fe/H]	[ls/Fe]	[hs/Fe]	[hsls]	M_{Ba} ($M_\odot$)	M^{ini}_{AGB} ($M_\odot$)	χ^2	dil	N	Type	Ref
HD 193530	4400	1.60	-0.17	0.66	0.84	0.180	1.80	2.0	1.77	0.17296	5	s	2
HD 196445	4400	1.40	-0.19	0.99	1.42	0.430	1.90	-	-	-	5	s	2
HD 199435	5000	2.60	-0.39	0.86	1.46	0.590	1.70	3.0	0.02	0.09638	5	s	2
HD 199939	4710	2.40	-0.22	1.39	1.84	0.450	2.30	-	-	-	11	s	4
HD 200063	4100	1.10	-0.34	0.75	1.05	0.300	1.20	3.0	0.83	0.33877	5	s	2
HD 200995	4600	2.10	-0.03	0.60	0.82	0.220	2.10	3.0	3.55	0.02106	5	s	2
HD 201657	4700	2.20	-0.34	0.85	1.54	0.690	1.30	2.0	0.06	0.09499	5	s	2
HD 201824	4900	2.30	-0.33	0.89	1.47	0.580	1.70	2.0	0.55	0.09220	5	s	2
HD 203137	3609	0.60	0.07	-0.00	0.56	0.560	-	4.0	2.63	0.45154	5	m	3
HD 204075	5300	1.50	0.06	1.10	0.86	-0.240	4.00	-	-	-	5	s	2
HD 204886	4600	2.10	0.04	0.66	0.94	0.280	2.20	-	-	-	5	s	2
HD 207277	4600	2.00	-0.13	0.60	0.94	0.340	2.00	-	-	-	5	s	2
HD 207585	5800	3.80	-0.39	1.29	1.66	0.370	1.00	-	-	-	9	s	5
HD 210030	4700	1.90	-0.03	0.35	0.34	-0.010	1.60	4.0	0.22	0.18726	6	m	2, 3
HD 210709	4630	2.40	-0.04	0.55	0.70	0.150	1.10	3.0	4.53	0.09912	5	s	1, 2
HD 210910	4570	2.70	0.04	0.04	0.32	0.280	1.30	4.0	2.39	0.81279	14	m	1
HD 210946	4800	2.10	-0.12	0.67	0.69	0.030	1.80	2.0	0.38	0.28203	5	s	2
HD 211173	4900	2.60	-0.17	0.58	0.75	0.170	1.60	2.0	19.22	0.02981	11	s	5
HD 211221	4800	2.30	-0.11	-0.10	0.18	0.280	1.60	6.0	0.68	0.00099	5	m	2

TABLE 7.3: *–continued*

Star Name	T_{eff} (K)	logg (cgs)	[Fe/H]	[ls/Fe]	[hs/Fe]	[hsls]	M_{Ba} ($M_\odot$)	M^{ini}_{AGB} ($M_\odot$)	χ^2	dil	N	Type	Ref
HD 211594	4900	2.40	-0.43	1.19	1.79	0.600	1.30	2.5	2.52	0.04023	5	s	2
MFU112	4900	2.40	-0.43	1.12	1.80	0.670	1.00	2.5	3.47	0.06293	5	s	2
MFU214	4800	2.40	0.00	0.45	0.20	-0.260	1.90	3.0	0.17	0.64404	5	m	2
MFU229	4900	2.60	-0.01	0.61	0.49	-0.120	2.20	3.0	0.49	0.26493	5	m	2
Our Work													
Star Name	T_{eff} (K)	logg (cgs)	[Fe/H]	[ls/Fe]	[hs/Fe]	[hsls]	M_{Ba} ($M_\odot$)	M^{ini}_{AGB} ($M_\odot$)	χ^2	dil	N	Type	Ref
HD 75 348	4840	2.00	-0.42	1.26	1.75	0.49	1.60	2.5	1.09	0.00014	11	s	6
BD+09 3019	4220	2.00	-0.60	1.77	2.08	0.31	0.80	-	-	-	10	s	6
HD 147609	6350	3.50	-0.28	1.19	1.25	0.060	1.40	2.5	1.41	0.08444	10	s	1, 5
HD 154276	5820	4.30	-0.10	-0.08	0.25	0.330	1.00	5.0	1.39	0.06317	8	m	5
HD 238020	5150	2.10	-0.68	-0.04	0.30	0.34	2.20	3.0	2.37	1.26402	10	m	6

TABLE 7.4: **Initial masses of the AGB companions of CEMP-*s* stars.**

Star Name	T_{eff} (K)	log$g$ (cgs)	[Fe/H]	M^{ini}_{AGB} ($M_\odot$)	χ^2	dil.	N
BD+04 2466	5100	1.80	-1.92	3.0	3.61	0.26884	7
BS 16077-0077	5900	3.19	-2.05	2.0	1.89	1.14484	9
CD-38 2151	4600	0.90	-2.03	3.0	6.52	0.14247	9
CS 22880-0074	5850	3.80	-1.93	3.0	2.74	0.34538	11
CS 22942-0019	5000	2.40	-2.64	1.3	5.30	0.55686	10
CS 22949-0008	6000	3.74	-2.45	2.0	7.42	0.87952	7
CS 29512-0073	5560	3.44	-2.06	2.0	1.03	0.08517	11
CS 30301-0015	4750	0.80	-2.64	1.5	1.96	1.30710	10
G 24-25	5828	3.86	-1.40	2.0	0.74	0.29380	12
HD 196944	5250	1.80	-2.25	3.0	0.45	0.60809	12
HD 198269	4800	1.30	-1.30	2.5	3.99	0.07653	9
HE 0024-2523	6625	4.30	-2.72	2.0	9.47	0.39594	4
HE 0202-2204	5280	1.65	-1.98	2.0	0.53	0.38639	9
HE 0231-4016	5972	3.59	-2.08	2.0	0.19	0.18554	6
HE 0253-6024	4640	1.20	-2.10	2.5	6.37	0.00567	7
HE 0317-4705	4730	1.30	-2.30	1.5	5.78	0.14257	7

TABLE 7.4: *–continued*

Star Name	T_{eff} (K)	log$g$ (cgs)	[Fe/H]	M^{ini}_{AGB} ($M_\odot$)	χ^2	dil.	N
HE 0336+0113	5700	3.50	-2.68	1.5	0.94	0.22047	7
HE 0430-4404	6214	4.27	-2.07	2.0	0.94	0.15989	4
HE 1031-0020	5080	2.20	-2.86	2.0	24.74	1.75142	7
HE 1135+0139	5487	1.80	-2.33	1.5	0.36	0.55062	8
HE 1152-0355	4000	1.00	-1.29	1.5	2.99	0.35113	6
HE 1430-1123	5915	3.75	-2.71	2.0	3.71	0.85928	4
HE 1434-1442	5420	3.15	-2.39	2.0	7.13	1.61944	4
HE 1509-0806	5185	2.50	-2.91	2.0	0.93	0.35547	7
HE 2138-3336	5850	3.60	-2.79	2.0	10.82	0.61524	11
HE 2150-0825	5960	3.67	-1.98	2.0	0.35	0.06557	7
HE 2158-0348	5215	2.50	-2.70	2.0	1.14	0.72601	9
HE 2158-5134	4950	1.90	-3.00	1.3	12.46	0.00100	5
HE 2240-0412	5750	3.50	-1.85	3.0	1.90	0.31705	6
HE 2258-4427	4560	1.00	-2.10	2.5	2.24	0.10845	8

TABLE 7.4: *–continued*

Our Work							
Star Name	T_{eff} (K)	log$g$ (cgs)	[Fe/H]	M^{ini}_{AGB} ($M_\odot$)	χ^2	dil.	N
CD-27 14351	4320	0.50	-2.71	1.3	8.02	0.24628	8
HD 145777	4160	0.90	-2.17	2.0	0.58	0.00111	10
HE 0319-0215	4650	0.50	-2.57	2.0	2.63	0.49593	8
HE 0507-1653	4970	2.20	-1.44	2.0	2.06	0.09719	9
HE 0930-0018	4190	2.65	-1.39	2.0	0.62	0.44781	8
HE 1023-1504	4440	0.50	-1.66	1.5	2.22	0.07273	7

Chapter 8

Conclusions & Future Work

8.1 Key Results of the thesis

- We have performed detailed high-resolution spectroscopic analyses for a selected sample of **twenty metal-poor stars**. We have presented the first time detailed abundance analysis for **twelve** objects. For the rest of the objects updates on abundance estimates of several key elements are presented based on high-quality, high-resolution spectra. We have identified one normal metal-poor star, three strong and two mild Ba stars, one CH star, six CEMP-*s* stars, three CEMP-*r/s* stars, three Extremely metal-poor stars, and one unique CEMP star that may be called as CEMP-*i/s* star.

- We have examined the existing classification schemes of CEMP-*s* and CEMP-*r/s* stars and found that none of the classifiers are effective in distinguishing the CEMP-*s* and CEMP-*r/s* stars. We have put forward a new classification scheme based on the abundances of Ba, La and Eu to differentiate the two subclasses. Our proposed modified classification criteria are-

- CEMP: [C/Fe] $\geq$ 0.7
- CEMP-*r/s*: [Ba/Fe] $\geq$ 1.0, [Eu/Fe] $\geq$ 1.0
  - i) 0.0 $\leq$ [Ba/Eu] $\leq$ 1.0 and/or 0.0 $\leq$ [La/Eu] $\leq$ 0.7;
- CEMP-*s*: [Ba/Fe] $\geq$ 1.0
  - i.) [Eu/Fe] $<$ 1.0, [Ba/Eu] $>$ 0.0 and/or [La/Eu] $>$ 0.5;
  - ii.) [Eu/Fe] $\geq$ 1.0, [Ba/Eu] $>$ 1.0 and/or [La/Eu] $>$ 0.7.

- Our proposed classification scheme was validated by the detailed analysis of HE 0507–1653.

- Based on a parametric model-based analysis of the three CEMP-*r/s* stars in our sample, together with a collected sample of eight CEMP-*r/s* stars from literature, we have confirmed the claim made by a few recent studies that *i*-process is primarily responsible for the formation of CEMP-*r/s* stars.

- We have discovered an object HE 1005–1439 with a unique abundance pattern that has never been reported before. The star shows significant contamination from the products of both the *i*- and the *s*-processes. We have critically analysed many possible formation mechanisms, but none of them is found to explain the observed abundances without uncertainties. Based on our analysis, we have proposed a scenario involving a binary picture in which both the *i*- and the *s*-process nucleosynthesis occur in succession in the primary companion AGB star. The observational constraints derived from the object and the proposed scenario are expected to provide a link for a better understanding of the interplay between the PIEs and the partial mixing of protons in the intershell region. This may throw light into the conditions that result in a pure *s*- or *i*-process surface abundance pattern in low-mass, low-metallicity AGB stars. The proposed scenario would also be helpful in explaining the overlap of [hs/ls] ratio in CEMP-*s* and CEMP-*r/s* stars.

- We have derived the mass distribution for a large sample of Ba stars with stellar masses estimated from the HR diagram. We found that i) mild and strong Ba stars occupy the same mass range, ii) the mass distribution cannot be represented by a single Gaussian, iii) the average value of the distribution is found to be at 1.9 $M_{\odot}$.

- A comprehensive study on the mass distribution of the primary companion AGBs of Ba and CEMP-*s* stars is still lacking. Using FRUITY models with a parametric-model based study, we have derived the masses of the primary companions (AGBs) of a large sample of known Ba and CEMP-*s* stars. We found that the primary mass distributions of mild and strong Ba stars peak at different values. While the primary stars' mass distribution of mild Ba stars peaks at 3.7 $M_{\odot}$, for the strong Ba stars, the peak appears at 2.5 $M_{\odot}$. This gives enough evidence to conclude that masses of the AGB companions play a dominant role in the formation of mild and strong Ba stars. The mass distribution of primary stars for CEMP-*s* stars is found to peak at 2.04 $M_{\odot}$.

8.2 Ongoing/Future Work

- Detailed studies on different types of CEMP stars still remain scanty. We plan to extend this study for a larger sample of CEMP-*s* and CEMP-*r/s* stars covering a wider range in metallicity using high-resolution spectroscopy.

- A larger homogeneous sample of these stars is expected to provide useful information regarding metallicity and mass dependence of *i*-process nucleosynthesis.

- We have discovered an object HE 1005–1439, where *i*- and *s*-processes can occur in succession. Attempts will be made to put tighter constraints in

terms of elemental abundances to understand the switching between *s*- and *i*-process nucleosynthesis in low-mass, low-metallicity AGB stars.

- We have shown that the mass of the companion AGBs plays a crucial role in the formation of the mild and the strong Ba stars. In future, we would like to investigate in detail the role of the metallicity and orbital period in the formation scenarios of Ba stars.

- We have observed a large sample of field metal-poor stars at low-resolution to identify the carbon enhanced stars. A follow-up study of these objects with high-resolution spectroscopy is expected to complement the above-mentioned studies. Our efforts will be to accomplish this in the near future.

TABLE 8.1: **Successful observing proposals.**

Sl. No.	Proposal Title	Proposal Code*	Instrument	Allotted nights	Clear nights	Investigators#
1.	Spectroscopy of potential CH star candidates	HCT-2017-C3-P05	HCT/HESP	4	4	AG (PI), PPG (Co-PI)
2.	Spectroscopy of potential CH star candidates	HCT-2018-C1-P01	HCT/HESP	3	3	AG (PI), PPG (Co-PI)
3.	Spectroscopy of potential CH star candidates	HCT-2018-C2-P02	HCT/HESP	2	2	AG (PI), PPG (Co-PI)
4.	Spectroscopy of potential CH star candidates	HCT-2018-C3-P52	HCT/HESP	3	2	AG (PI), PPG (Co-PI)
5.	Spectroscopy of potential CH star candidates	HCT-2019-C1-P61	HCT/HESP	3	1.5	AG (PI), PPG (Co-PI)
6.	Neutron-capture nucleosynthesis : observational constraints for i-process	HCT-2019-C2-P04	HCT/HESP	3	2	PPG (PI), AG (Co-PI)
7.	Spectroscopy of potential CH star candidates	HCT-2019-C2-P06	HCT/HESP	3	1	AG (PI), PPG (Co-PI)
8.	Neutron-capture nucleosynthesis : observational constraints for i-process	HCT-2019-C3-P24	HCT/HESP	4	2	PPG (PI), AG (Co-PI)
9.	Spectroscopy of potential CH star candidates	HCT-2019-C3-P26	HCT/HFOSC	3	2	AG (PI), PPG (Co-PI)
10.	Potential CEMP star candidates for neutron-capture nucleosynthesis	HCT-2020-C1-P08	HCT/HFOSC	3.5	2.5	PPG (PI), AG (Co-PI)
11.	Potential CEMP star candidates for neutron-capture nucleosynthesis	HCT-2020-C2-P08	HCT/HFOSC	3	2	PPG (PI), AG (Co-PI)
12.	Potential CEMP star candidates for neutron-capture nucleosynthesis	HCT-2020-C3-P15	HCT/HFOSC	4	4	PPG (PI), AG (Co-PI)
13.	Potential CEMP star candidates for neutron-capture nucleosynthesis	HCT-2021-C1-P03	HCT/HFOSC	4	2	PPG (PI), AG (Co-PI)
14.	Potential CEMP star candidates for neutron-capture nucleosynthesis	HCT-2021-C2-P17	HCT/HFOSC	2.5	2	PPG (PI), AG (Co-PI)
15.	Potential CEMP star candidates for neutron-capture nucleosynthesis	HCT-2021-C3-P33	HCT/HFOSC	4	4	PPG (PI), AG (Co-PI)
16.	Spectroscopy of carbon enhanced metal-poor stars: Optical and Near Infrared	HCT-2022-C1-P17	HCT/HESP HCT/HFOSC/TIRSPEC	3	2	PPG (PI), AG (Co-PI)
17.	Searching for evolutionary connection between CH and Ba stars using optical and IR spectroscopy	HCT-2022-C1-P02	HCT/HESP HCT/TIRSPEC	2	0	SJ (PI), PPG (Co-PI)

∗- C1: Cycle 1 (January–April); C2: Cycle 2 (May–August); C3: Cycle 3 (September–December)

#- AG: Aruna Goswami; PPG: Partha Pratim Goswami; SJ: Shejeelammal J.

Bibliography

Abate, C., Pols, O. R., Izzard, R. G., Mohamed, S. S. and de Mink, S. E., 2013, "Wind Roche-lobe overflow: Application to carbon-enhanced metal-poor stars", *Astron. Astrophys.*, **552**, A26. [DOI], [ADS], [arXiv:1302.4441 [astro-ph.SR]]

Abate, C., Pols, O. R., Karakas, A. I. and Izzard, R. G., 2015, "Carbon-enhanced metal-poor stars: a window on AGB nucleosynthesis and binary evolution. I. Detailed analysis of 15 binary stars with known orbital periods", *Astron. Astrophys.*, **576**, A118. [DOI], [ADS], [arXiv:1502.07759 [astro-ph.SR]]

Abate, C., Stancliffe, R. J. and Liu, Z.-W., 2016, "How plausible are the proposed formation scenarios of CEMP-r/s stars?", *Astron. Astrophys.*, **587**, A50. [DOI], [ADS], [arXiv:1601.00976 [astro-ph.SR]]

Abbott, B. P., Abbott, R., Abbott, T. D., Acernese, F., Ackley, K., Adams, C., Adams, T., Addesso, P., Adhikari, R. X. and et al. [LIGO Scientific Collaboration and Virgo Collaboration], 2017, "GW170817: Observation of Gravitational Waves from a Binary Neutron Star Inspiral", *Phys. Rev. Lett.*, **119**, 161 101. [DOI]URL: `https://link.aps.org/doi/10.1103/PhysRevLett.119.161101`

Allen, D. M. and Barbuy, B., 2006, "Analysis of 26 barium stars. I. Abundances", *Astron. Astrophys.*, **454**(3), 895–915. [DOI], [ADS], [arXiv:astro-ph/0604036 [astro-ph]]

Allen, D. M., Ryan, S. G., Rossi, S., Beers, T. C. and Tsangarides, S. A., 2012, "Elemental abundances and classification of carbon-enhanced metal-poor stars", *Astron. Astrophys.*, **548**, A34. [DOI], [ADS], [arXiv:1210.5009 [astro-ph.SR]]

Alonso, A., Arribas, S. and Martinez-Roger, C., 1996, "The empirical scale of temperatures of the low main sequence (F0V-K5V).", *Astron. Astrophys.*, **313**, 873–890. [ADS]

Alonso, A., Arribas, S. and Martínez-Roger, C., 1999, "The effective temperature scale of giant stars (F0-K5). II. Empirical calibration of T_{eff} versus colours and [Fe/H]", *Astron. Astrophys. Suppl.*, **140**, 261–277. [DOI], [ADS]

Amarsi, A. M., Lind, K., Asplund, M., Barklem, P. S. and Collet, R., 2016, "Non-LTE line formation of Fe in late-type stars - III. 3D non-LTE analysis of metal-poor stars", *Mon. Not. Roy. Astron. Soc.*, **463**(2), 1518–1533. [DOI], [ADS], [arXiv:1608.06390 [astro-ph.SR]]

Aoki, W., Ryan, S. G., Norris, J. E., Beers, T. C., Ando, H., Iwamoto, N., Kajino, T., Mathews, G. J. and Fujimoto, M. Y., 2001, "Neutron Capture Elements in s-Process-Rich, Very Metal-Poor Stars", *Astrophys. J.*, **561**, 346–363. [DOI], [ADS], [astro-ph/0107040]

Aoki, W., Beers, T. C., Christlieb, N., Norris, J. E., Ryan, S. G. and Tsangarides, S., 2007, "Carbon-enhanced Metal-poor Stars. I. Chemical Compositions of 26 Stars", *Astrophys. J.*, **655**, 492–521. [DOI], [ADS], [astro-ph/0609702]

Aoki, W., Beers, T. C., Sivarani, T., Marsteller, B., Lee, Y. S., Honda, S., Norris, J. E., Ryan, S. G. and Carollo, D., 2008, "Carbon-Enhanced Metal-Poor Stars. III. Main-Sequence Turnoff Stars from the SDSS SEGUE Sample", *Astrophys. J.*, **678**, 1351–1371. [DOI], [ADS], [arXiv:0801.4187]

Aoki, Wako, Ryan, Sean G., Norris, John E., Beers, Timothy C., Ando, Hiroyasu and Tsangarides, Stelios, 2002, "A Subaru/High Dispersion Spectrograph Study of Lead (Pb) Abundances in Eight s-Process Element-rich, Metal-poor Stars",

Astrophys. J., **580**(2), 1149–1158. [DOI], [ADS], [arXiv:astro-ph/0208020 [astro-ph]]

Arentsen, A., Starkenburg, E., Shetrone, M. D., Venn, K. A., Depagne, É. and McConnachie, A. W., 2019, "Binarity among CEMP-no stars: an indication of multiple formation pathways?", *Astron. Astrophys.*, **621**, A108. [DOI], [ADS], [arXiv:1811.01975 [astro-ph.SR]]

Arlandini, C., Käppeler, F., Wisshak, K., Gallino, R., Lugaro, M., Busso, M. and Straniero, O., 1999, "Neutron Capture in Low-Mass Asymptotic Giant Branch Stars: Cross Sections and Abundance Signatures", *Astrophys. J.*, **525**, 886–900. [DOI], [ADS], [astro-ph/9906266]

Asplund, M., Lambert, D. L., Kipper, T., Pollacco, D. and Shetrone, M. D., 1999, "The rapid evolution of the born-again giant Sakurai's object", *Astron. Astrophys.*, **343**, 507–518. [ADS], [arXiv:astro-ph/9811208 [astro-ph]]

Asplund, Martin, Grevesse, Nicolas, Sauval, A. Jacques and Scott, Pat, 2009, "The Chemical Composition of the Sun", *Ann. Rev. Astron. Astrophys.*, **47**(1), 481–522. [DOI], [ADS], [arXiv:0909.0948 [astro-ph.SR]]

Banerjee, Projjwal, Qian, Yong-Zhong and Heger, Alexander, 2018, "New Neutron-capture Site in Massive Pop III and Pop II Stars as a Source for Heavy Elements in the Early Galaxy", *Astrophys. J.*, **865**(2), 120. [DOI], [ADS], [arXiv:1711.05964 [astro-ph.SR]]

Barbuy, B., Spite, M., Spite, F., Hill, V., Cayrel, R., Plez, B. and Petitjean, P., 2005, "New analysis of the two carbon-rich stars CS 22948-27 and CS 29497-34: Binarity and neutron capture elements", *Astron. Astrophys.*, **429**, 1031–1042. [DOI], [ADS], [astro-ph/0409213]

Barklem, P. S., Christlieb, N., Beers, T. C., Hill, V., Bessell, M. S., Holmberg, J., Marsteller, B., Rossi, S., Zickgraf, F.-J. and Reimers, D., 2005, "The Hamburg/ESO R-process enhanced star survey (HERES). II. Spectroscopic analysis

of the survey sample", *Astron. Astrophys.*, **439**, 129–151. [DOI], [ADS], [astro-ph/0505050]

Bartkevicius, A., 1996, "A New Version of the Catalog of CH and Related Stars (CH95 Catalog)", *Baltic Astronomy*, **5**, 217–229. [DOI], [ADS]

Beers, T. C., Preston, G. W. and Shectman, S. A., 1985, "A search for stars of very low metal abundance. I.", *Astron. J.*, **90**, 2089–2102. [DOI], [ADS]

Beers, Timothy C. and Christlieb, Norbert, 2005, "The Discovery and Analysis of Very Metal-Poor Stars in the Galaxy", *Ann. Rev. Astron. Astrophys.*, **43**(1), 531–580. [DOI], [ADS]

Beers, Timothy C., Preston, George W. and Shectman, Stephen A., 1992, "A Search for Stars of Very Low Metal Abundance. II", *Astron. J.*, **103**, 1987. [DOI], [ADS]

Beers, Timothy C., Rossi, Silvia, Norris, John E., Ryan, Sean G. and Shefler, Thomas, 1999, "Estimation of Stellar Metal Abundance. II. A Recalibration of the Ca II K Technique, and the Autocorrelation Function Method", *Astron. J.*, **117**(2), 981–1009. [DOI], [ADS]

Behara, N. T., Bonifacio, P., Ludwig, H.-G., Sbordone, L., González Hernández, J. I. and Caffau, E., 2010, "Three carbon-enhanced metal-poor dwarf stars from the SDSS. Chemical abundances from CO^{5}BOLD 3D hydrodynamical model atmospheres", *Astron. Astrophys.*, **513**, A72. [DOI], [ADS], [arXiv:1002.1670 [astro-ph.SR]]

Bensby, T., Feltzing, S. and Lundström, I., 2003, "Elemental abundance trends in the Galactic thin and thick disks as traced by nearby F and G dwarf stars", *Astron. Astrophys.*, **410**, 527–551. [DOI], [ADS]

Bensby, T., Feltzing, S. and Lundström, I., 2004, "Oxygen trends in the Galactic thin and thick disks", *Astron. Astrophys.*, **415**, 155–170. [DOI], [ADS], [astro-ph/0310741]

Bensby, T., Feltzing, S. and Oey, M. S., 2014, "Exploring the Milky Way stellar disk. A detailed elemental abundance study of 714 F and G dwarf stars in the solar neighbourhood", *Astron. Astrophys.*, **562**, A71. [DOI], [ADS], [arXiv:1309.2631 [astro-ph.GA]]

Bergeat, J., Knapik, A. and Rutily, B., 2001, "The effective temperatures of carbon-rich stars", *Astron. Astrophys.*, **369**, 178–209. [DOI], [ADS]

Bethe, H. A., 1939, "Energy Production in Stars", *Physical Review*, **55**(5), 434–456. [DOI], [ADS]

Bidelman, William P., 1956, "The carbon stars—An astrophysical enigma", *Vistas in Astronomy*, **2**(1), 1428–1437. [DOI], [ADS]

Bidelman, William P. and Keenan, Philip C., 1951, "The Ba II Stars.", *Astrophys. J.*, **114**, 473. [DOI], [ADS]

Bisterzo, S., Gallino, R., Straniero, O., Cristallo, S. and Käppeler, F., 2011, "The s-process in low-metallicity stars - II. Interpretation of high-resolution spectroscopic observations with asymptotic giant branch models", *Mon. Not. Roy. Astron. Soc.*, **418**, 284–319. [DOI], [ADS], [arXiv:1108.0500 [astro-ph.SR]]

Bisterzo, S., Gallino, R., Straniero, O., Cristallo, S. and Käppeler, F., 2012, "The s-process in low-metallicity stars - III. Individual analysis of CEMP-s and CEMP-s/r with asymptotic giant branch models", *Mon. Not. Roy. Astron. Soc.*, **422**, 849–884. [DOI], [ADS], [arXiv:1201.6198 [astro-ph.SR]]

Bonifacio, P., Caffau, E., Spite, M., Limongi, M., Chieffi, A., Klessen, R. S., François, P., Molaro, P., Ludwig, H. G., Zaggia, S., Spite, F., Plez, B., Cayrel, R., Christlieb, N., Clark, P. C., Glover, S. C. O., Hammer, F., Koch, A., Monaco, L., Sbordone, L. and Steffen, M., 2015, "TOPoS . II. On the bimodality of carbon abundance in CEMP stars Implications on the early chemical evolution of galaxies", *Astron. Astrophys.*, **579**, A28. [DOI], [ADS], [arXiv:1504.05963 [astro-ph.GA]]

Bromm, Volker and Larson, Richard B., 2004, "The First Stars", *Ann. Rev. Astron. Astrophys.*, **42**(1), 79–118. [DOI], [ADS], [arXiv:astro-ph/0311019 [astro-ph]]

Bromm, Volker, Coppi, Paolo S. and Larson, Richard B., 2002, "The Formation of the First Stars. I. The Primordial Star-forming Cloud", *Astrophys. J.*, **564**(1), 23–51. [DOI], [ADS], [arXiv:astro-ph/0102503 [astro-ph]]

Brooke, J. S. A., Bernath, P. F., Schmidt, T. W. and Bacskay, G. B., 2013, "Line strengths and updated molecular constants for the C_2 Swan system", *Journal of Quantitative Spectroscopy and Radiative Transfer*, **124**, 11–20. [DOI], [ADS], [arXiv:1212.2102 [astro-ph.SR]]

Burbidge, E. Margaret, Burbidge, G. R., Fowler, William A. and Hoyle, F., 1957, "Synthesis of the Elements in Stars", *Reviews of Modern Physics*, **29**(4), 547–650. [DOI], [ADS]

Burris, D. L., Pilachowski, C. A., Armandroff, T. E., Sneden, C., Cowan, J. J. and Roe, H., 2000, "Neutron-Capture Elements in the Early Galaxy: Insights from a Large Sample of Metal-poor Giants", *Astrophys. J.*, **544**, 302–319. [DOI], [ADS], [astro-ph/0005188]

Busso, M., Gallino, R. and Wasserburg, G. J., 1999, "Nucleosynthesis in Asymptotic Giant Branch Stars: Relevance for Galactic Enrichment and Solar System Formation", *Ann. Rev. Astron. Astrophys.*, **37**, 239–309. [DOI], [ADS]

Caffau, E., Bonifacio, P., Starkenburg, E., Martin, N., Youakim, K., Henden, A. A., González Hernández, J. I., Aguado, D. S., Allende Prieto, C., Venn, K. and Jablonka, P., 2017, "The Pristine survey II: A sample of bright stars observed with FEROS", *Astronomische Nachrichten*, **338**(6), 686–695. [DOI], [ADS], [arXiv:1705.10280 [astro-ph.SR]]

Campbell, S. W. and Lattanzio, J. C., 2008, "Evolution and nucleosynthesis of extremely metal-poor and metal-free low- and intermediate-mass stars. I. Stellar yield tables and the CEMPs", *Astron. Astrophys.*, **490**(2), 769–776. [DOI], [ADS], [arXiv:0901.0799 [astro-ph.SR]]

Campbell, S. W., Lugaro, M. and Karakas, A. I., 2010, "Evolution and nucleosynthesis of extremely metal-poor and metal-free low- and intermediate-mass stars. II. s-process nucleosynthesis during the core He flash", *Astron. Astrophys.*, **522**, L6. [DOI], [ADS], [arXiv:1010.1987 [astro-ph.SR]]

Chamberlain, Joseph W. and Aller, Lawrence H., 1951, "The Atmospheres of A-Type Subdwarfs and 95 Leonis.", *Astrophys. J.*, **114**, 52. [DOI], [ADS]

Chen, B., Vergely, J. L., Valette, B. and Carraro, G., 1998, "Comparison of two different extinction laws with HIPPARCOS observations", *Astron. Astrophys.*, **336**, 137–149. [ADS], [arXiv:astro-ph/9805018 [astro-ph]]

Chiappini, C., 2013, "First stars and reionization: Spinstars", *Astronomische Nachrichten*, **334**(6), 595–604. [DOI], [ADS]

Choplin, A., Siess, L. and Goriely, S., 2021, "The intermediate neutron capture process. I. Development of the i-process in low-metallicity low-mass AGB stars", *Astron. Astrophys.*, **648**, A119. [DOI], [ADS], [arXiv:2102.08840 [astro-ph.SR]]

Christlieb, N., Green, P. J., Wisotzki, L. and Reimers, D., 2001, "The stellar content of the Hamburg/ESO survey II. A large, homogeneously-selected sample of high latitude carbon stars", *Astron. Astrophys.*, **375**, 366–374. [DOI], [ADS], [astro-ph/0106240]

Christlieb, N., Schörck, T., Frebel, A., Beers, T. C., Wisotzki, L. and Reimers, D., 2008, "The stellar content of the Hamburg/ESO survey. IV. Selection of candidate metal-poor stars", *Astron. Astrophys.*, **484**(3), 721–732. [DOI], [ADS], [arXiv:0804.1520 [astro-ph]]

Clarkson, O., Herwig, F. and Pignatari, M., 2018, "Pop III i-process nucleosynthesis and the elemental abundances of SMSS J0313-6708 and the most iron-poor stars", *Mon. Not. Roy. Astron. Soc.*, **474**(1), L37–L41. [DOI], [ADS], [arXiv:1710.01763 [astro-ph.SR]]

Cohen, J. G., Christlieb, N., Qian, Y.-Z. and Wasserburg, G. J., 2003, "Abundance Analysis of HE 2148-1247, A Star with Extremely Enhanced Neutron Capture Elements", *Astrophys. J.*, **588**, 1082–1098. [DOI], [ADS], [astro-ph/0301460]

Cohen, J. G., McWilliam, A., Shectman, S., Thompson, I., Christlieb, N., Melendez, J., Ramirez, S., Swensson, A. and Zickgraf, F.-J., 2006, "Carbon Stars in the Hamburg/ESO Survey: Abundances", *Astron. J.*, **132**, 137–160. [DOI], [ADS], [astro-ph/0603582]

Côté, Benoit, Denissenkov, Pavel, Herwig, Falk, Ruiter, Ashley J., Ritter, Christian, Pignatari, Marco and Belczynski, Krzysztof, 2018, "i-process Contribution of Rapidly Accreting White Dwarfs to the Solar Composition of First-peak Neutron-capture Elements", *Astrophys. J.*, **854**(2), 105. [DOI], [ADS], [arXiv:1712.07551 [astro-ph.SR]]

Cowan, J. J. and Rose, W. K., 1977, "Production of ^{14}C and neutrons in red giants.", *Astrophys. J.*, **212**, 149–158. [DOI], [ADS]

Cowan, John J. and Sneden, Christopher, 2006, "Heavy element synthesis in the oldest stars and the early Universe", *Nature*, **440**(7088), 1151–1156. [DOI], [ADS]

Cowan, John J., Sneden, Christopher, Lawler, James E., Aprahamian, Ani, Wiescher, Michael, Langanke, Karlheinz, Martínez-Pinedo, Gabriel and Thielemann, Friedrich-Karl, 2021, "Origin of the heaviest elements: The rapid neutron-capture process", *Reviews of Modern Physics*, **93**(1), 015002. [DOI], [ADS], [arXiv:1901.01410 [astro-ph.HE]]

Cristallo, S., Piersanti, L., Straniero, O., Gallino, R., Domínguez, I. and Käppeler, F., 2009a, "Asymptotic-Giant-Branch Models at Very Low Metallicity", *Publications of the Astronomical Society of Australia*, **26**(3), 139–144. [DOI], [ADS], [arXiv:0904.4173 [astro-ph.SR]]

Cristallo, S., Straniero, O., Gallino, R., Piersanti, L., Domínguez, I. and Lederer, M. T., 2009b, "Evolution, Nucleosynthesis, and Yields of Low-Mass Asymptotic

Giant Branch Stars at Different Metallicities", *Astrophys. J.*, **696**(1), 797–820. [DOI], [ADS], [arXiv:0902.0243 [astro-ph.SR]]

Cristallo, S., Piersanti, L., Straniero, O., Gallino, R., Domínguez, I., Abia, C., Di Rico, G., Quintini, M. and Bisterzo, S., 2011, "Evolution, Nucleosynthesis, and Yields of Low-mass Asymptotic Giant Branch Stars at Different Metallicities. II. The FRUITY Database", *Astrophys. J. Suppl.*, **197**(2), 17. [DOI], [ADS], [arXiv:1109.1176 [astro-ph.SR]]

Cristallo, S., Straniero, O., Piersanti, L. and Gobrecht, D., 2015, "Evolution, Nucleosynthesis, and Yields of AGB Stars at Different Metallicities. III. Intermediate-mass Models, Revised Low-mass Models, and the ph-FRUITY Interface", *Astrophys. J. Suppl.*, **219**(2), 40. [DOI], [ADS], [arXiv:1507.07338 [astro-ph.SR]]

Cristallo, S., Karinkuzhi, D., Goswami, A., Piersanti, L. and Gobrecht, D., 2016, "Constraints of the Physics of Low-mass AGB Stars from CH and CEMP Stars", *Astrophys. J.*, **833**(2), 181. [DOI], [ADS], [arXiv:1610.05475 [astro-ph.SR]]

Cutri, R. M., Skrutskie, M. F., van Dyk, S., Beichman, C. A., Carpenter, J. M., Chester, T., Cambresy, L., Evans, T., Fowler, J., Gizis, J., Howard, E., Huchra, J., Jarrett, T., Kopan, E. L., Kirkpatrick, J. D., Light, R. M., Marsh, K. A., McCallon, H., Schneider, S., Stiening, R., Sykes, M., Weinberg, M., Wheaton, W. A., Wheelock, S. and Zacarias, N., 2003, "VizieR Online Data Catalog: 2MASS All-Sky Catalog of Point Sources (Cutri+ 2003)", *VizieR Online Data Catalog*, II/246. [ADS]

Dardelet, L., Ritter, C., Prado, P., Heringer, E., Higgs, C., Sandalski, S., Jones, S., Denisenkov, P., Venn, K., Bertolli, M., Pignatari, M., Woodward, P. and Herwig, F., 2014, "i process and CEMP-s+r stars", in *XIII Nuclei in the Cosmos (NIC XIII)*, [ADS]

de Castro, D. B., Pereira, C. B., Roig, F., Jilinski, E., Drake, N. A., Chavero, C. and Sales Silva, J. V., 2016, "Chemical abundances and kinematics of barium stars", *Mon. Not. Roy. Astron. Soc.*, **459**(4), 4299–4324. [DOI], [ADS], [arXiv:1604.03031 [astro-ph.SR]]

Deng, Li-Cai, Newberg, Heidi Jo, Liu, Chao, Carlin, Jeffrey L., Beers, Timothy C., Chen, Li, Chen, Yu-Qin, Christlieb, Norbert, Grillmair, Carl J., Guhathakurta, Puragra, Han, Zhan-Wen, Hou, Jin-Liang, Lee, Hsu-Tai, Lépine, Sébastien, Li, Jing, Liu, Xiao-Wei, Pan, Kai-Ke, Sellwood, J. A., Wang, Bo, Wang, Hong-Chi, Yang, Fan, Yanny, Brian, Zhang, Hao-Tong, Zhang, Yue-Yang, Zheng, Zheng and Zhu, Zi, 2012, "LAMOST Experiment for Galactic Understanding and Exploration (LEGUE) — The survey's science plan", *Research in Astronomy and Astrophysics*, **12**(7), 735–754. [DOI], [ADS], [arXiv:1206.3578 [astro-ph.GA]]

Denissenkov, Pavel A. and Tout, Christopher A., 2003, "Partial mixing and formation of the ^{13}C pocket by internal gravity waves in asymptotic giant branch stars", *Mon. Not. Roy. Astron. Soc.*, **340**(3), 722–732. [DOI], [ADS]

Denissenkov, Pavel A., Herwig, Falk, Battino, Umberto, Ritter, Christian, Pignatari, Marco, Jones, Samuel and Paxton, Bill, 2017, "I-process Nucleosynthesis and Mass Retention Efficiency in He-shell Flash Evolution of Rapidly Accreting White Dwarfs", *Astrophys. J. Lett.*, **834**(2), L10. [DOI], [ADS], [arXiv:1610.08541 [astro-ph.SR]]

Denissenkov, Pavel A., Herwig, Falk, Woodward, Paul, Andrassy, Robert, Pignatari, Marco and Jones, Samuel, 2019, "The i-process yields of rapidly accreting white dwarfs from multicycle He-shell flash stellar evolution models with mixing parametrizations from 3D hydrodynamics simulations", *Mon. Not. Roy. Astron. Soc.*, **488**(3), 4258–4270. [DOI], [ADS], [arXiv:1809.03666 [astro-ph.SR]]

Doherty, Carolyn L., Gil-Pons, Pilar, Siess, Lionel, Lattanzio, John C. and Lau, Herbert H. B., 2015, "Super- and massive AGB stars - IV. Final fates - initial-to-final mass relation", *Mon. Not. Roy. Astron. Soc.*, **446**(3), 2599–2612. [DOI], [ADS], [arXiv:1410.5431 [astro-ph.SR]]

Eggen, O. J., Lynden-Bell, D. and Sandage, A. R., 1962, "Evidence from the motions of old stars that the Galaxy collapsed.", *Astrophys. J.*, **136**, 748. [DOI], [ADS]

Eichler, David, Livio, Mario, Piran, Tsvi and Schramm, David N., 1989, "Nucleosynthesis, neutrino bursts and γ-rays from coalescing neutron stars", *Nature*, **340**(6229), 126–128. [DOI], [ADS]

Eichler, M., Arcones, A., Kelic, A., Korobkin, O., Langanke, K., Marketin, T., Martinez-Pinedo, G., Panov, I., Rauscher, T., Rosswog, S., Winteler, C., Zinner, N. T. and Thielemann, F. K., 2015, "The Role of Fission in Neutron Star Mergers and Its Impact on the r-Process Peaks", *Astrophys. J.*, **808**(1), 30. [DOI], [ADS], [arXiv:1411.0974 [astro-ph.HE]]

Escorza, A., Boffin, H. M. J., Jorissen, A., Van Eck, S., Siess, L., Van Winckel, H., Karinkuzhi, D., Shetye, S. and Pourbaix, D., 2017, "Hertzsprung-Russell diagram and mass distribution of barium stars", *Astron. Astrophys.*, **608**, A100. [DOI], [ADS], [arXiv:1710.02029 [astro-ph.SR]]

Escorza, A., Karinkuzhi, D., Jorissen, A., Siess, L., Van Winckel, H., Pourbaix, D., Johnston, C., Miszalski, B., Oomen, G. M., Abdul-Masih, M., Boffin, H. M. J., North, P., Manick, R., Shetye, S. and Mikołajewska, J., 2019, "Barium and related stars, and their white-dwarf companions. II. Main-sequence and subgiant starss", *Astron. Astrophys.*, **626**, A128. [DOI], [ADS], [arXiv:1904.04095 [astro-ph.SR]]

Ezzeddine, Rana, Frebel, Anna and Plez, Bertrand, 2017, "Ultra-metal-poor Stars: Spectroscopic Determination of Stellar Atmospheric Parameters Using

Iron Non-LTE Line Abundances", *Astrophys. J.*, **847**(2), 142. [DOI], [ADS], [arXiv:1612.06309 [astro-ph.SR]]

Fishlock, Cherie K., Karakas, Amanda I., Lugaro, Maria and Yong, David, 2014, "Evolution and Nucleosynthesis of Asymptotic Giant Branch Stellar Models of Low Metallicity", *Astrophys. J.*, **797**(1), 44. [DOI], [ADS], [arXiv:1410.7457 [astro-ph.SR]]

Frebel, Anna, 2018, "From Nuclei to the Cosmos: Tracing Heavy-Element Production with the Oldest Stars", *Annual Review of Nuclear and Particle Science*, **68**(1), 237–269. [DOI], [ADS], [arXiv:1806.08955 [astro-ph.SR]]

Frebel, Anna and Surman, Rebecca, 2020, "Lifting the secrets of stardust", *Nature Astronomy*, **4**, 564–565. [DOI], [ADS]

Fujimoto, Masayuki Y., Ikeda, Yasufumi and Iben, Icko, Jr., 2000, "The Origin of Extremely Metal-poor Carbon Stars and the Search for Population III", *Astrophys. J. Lett.*, **529**(1), L25–L28. [DOI], [ADS]

Fujimoto, Shin-ichiro, Nishimura, Nobuya and Hashimoto, Masa-aki, 2008, "Nucleosynthesis in Magnetically Driven Jets from Collapsars", *Astrophys. J.*, **680**(2), 1350–1358. [DOI], [ADS], [arXiv:0804.0969 [astro-ph]]

Fujiya, Wataru, Hoppe, Peter, Zinner, Ernst, Pignatari, Marco and Herwig, Falk, 2013, "Evidence for Radiogenic Sulfur-32 in Type AB Presolar Silicon Carbide Grains?", *Astrophys. J. Lett.*, **776**(2), L29. [DOI], [ADS], [arXiv:1310.0485 [astro-ph.SR]]

Gaia Collaboration, Katz, D., Antoja, T., Romero-Gómez, M., Drimmel, R., Reylé, C., Seabroke, G. M., Soubiran, C., Babusiaux, C., Di Matteo, P. and et al., 2018, "Gaia Data Release 2. Mapping the Milky Way disc kinematics", *Astron. Astrophys.*, **616**, A11. [DOI], [ADS], [arXiv:1804.09380]

Gallino, R., Arlandini, C., Busso, M., Lugaro, M., Travaglio, C., Straniero, O., Chieffi, A. and Limongi, M., 1998a, "Evolution and Nucleosynthesis in Low-Mass Asymptotic Giant Branch Stars. II. Neutron Capture and the S-Process", *Astrophys. J.*, **497**, 388–403. [DOI], [ADS]

Gallino, Roberto, Arlandini, Claudio, Busso, Maurizio, Lugaro, Maria, Travaglio, Claudia, Straniero, Oscar, Chieffi, Alessandro and Limongi, Marco, 1998b, "Evolution and Nucleosynthesis in Low-Mass Asymptotic Giant Branch Stars. II. Neutron Capture and the S-Process", *Astrophys. J.*, **497**(1), 388–403. [DOI], [ADS]

Goswami, A., 2005, "CH stars at high Galactic latitudes", *Mon. Not. Roy. Astron. Soc.*, **359**, 531–544. [DOI], [ADS], [astro-ph/0507202]

Goswami, A. and Aoki, W., 2010, "HD 209621: abundances of neutron-capture elements*", *Mon. Not. Roy. Astron. Soc.*, **404**, 253–264. [DOI], [ADS], [arXiv:1002.4477 [astro-ph.SR]]

Goswami, Aruna, Aoki, Wako, Beers, Timothy C., Christlieb, Norbert, Norris, John E., Ryan, Sean G. and Tsangarides, Stelios, 2006, "A high-resolution spectral analysis of three carbon-enhanced metal-poor stars", *Mon. Not. Roy. Astron. Soc.*, **372**(1), 343–356. [DOI], [ADS], [arXiv:astro-ph/0608106 [astro-ph]]

Goswami, Aruna, Aoki, Wako and Karinkuzhi, Drisya, 2016, "Subaru/HDS study of CH stars: elemental abundances for stellar neutron-capture process studies", *Mon. Not. Roy. Astron. Soc.*, **455**(1), 402–422. [DOI], [ADS], [arXiv:1510.07814 [astro-ph.SR]]

Goswami, Partha Pratim and Goswami, Aruna, 2020, "i-Process nucleosynthesis: Observational evidences from CEMP stars", *JAA*, **41**(1), 47. [DOI], [ADS], [arXiv:2011.02419 [astro-ph.SR]]

Goswami, Partha Pratim and Goswami, Aruna, 2022, "The peculiar abundances of HE 1005-1439. A carbon-enhanced extremely metal-poor star contaminated

with products of both s- and i-process nucleosynthesis", *Astron. Astrophys.*, **657**, A50. [DOI], [ADS], [arXiv:2110.02559 [astro-ph.SR]]

Goswami, Partha Pratim, Rathour, Rajeev Singh and Goswami, Aruna, 2021, "Spectroscopic study of CEMP-(s & r/s) stars. Revisiting classification criteria and formation scenarios, highlighting i-process nucleosynthesis", *Astron. Astrophys.*, **649**, A49. [DOI], [ADS], [arXiv:2101.09518 [astro-ph.SR]]

Gratton, Raffaele, Sneden, Christopher and Carretta, Eugenio, 2004, "Abundance Variations Within Globular Clusters", *Ann. Rev. Astron. Astrophys.*, **42**(1), 385–440. [DOI], [ADS]

Gull, Maude, Frebel, Anna, Cain, Madelyn G., Placco, Vinicius M., Ji, Alexander P., Abate, Carlo, Ezzeddine, Rana, Karakas, Amanda I., Hansen, Terese T., Sakari, Charli, Holmbeck, Erika M., Santucci, Rafael M., Casey, Andrew R. and Beers, Timothy C., 2018, "The R-Process Alliance: Discovery of the First Metal-poor Star with a Combined r- and s-process Element Signature", *Astrophys. J.*, **862**(2), 174. [DOI], [ADS], [arXiv:1806.00645 [astro-ph.SR]]

Hampel, Melanie, Stancliffe, Richard J., Lugaro, Maria and Meyer, Bradley S., 2016, "The Intermediate Neutron-capture Process and Carbon-enhanced Metal-poor Stars", *Astrophys. J.*, **831**(2), 171. [DOI], [ADS], [arXiv:1608.08634 [astro-ph.SR]]

Hampel, Melanie, Karakas, Amanda I., Stancliffe, Richard J., Meyer, Bradley S. and Lugaro, Maria, 2019, "Learning about the Intermediate Neutron-capture Process from Lead Abundances", *Astrophys. J.*, **887**(1), 11. [DOI], [ADS], [arXiv:1910.11882 [astro-ph.SR]]

Han, Zhanwen, Eggleton, Peter P., Podsiadlowski, Philipp and Tout, Christopher A., 1995, "The formation of barium and CH stars and related objects", *Mon. Not. Roy. Astron. Soc.*, **277**(4), 1443–1462. [DOI], [ADS]

Hansen, C. J., Nordström, B., Hansen, T. T., Kennedy, C. R., Placco, V. M., Beers, T. C., Andersen, J., Cescutti, G. and Chiappini, C., 2016a, "Abundances

of carbon-enhanced metal-poor stars as constraints on their formation", *Astron. Astrophys.*, **588**, A37. [DOI], [ADS], [arXiv:1511.07812 [astro-ph.SR]]

Hansen, C. J., Hansen, T. T., Koch, A., Beers, T. C., Nordström, B., Placco, V. M. and Andersen, J., 2019, "Abundances and kinematics of carbon-enhanced metal-poor stars in the Galactic halo. A new classification scheme based on Sr and Ba", *Astron. Astrophys.*, **623**, A128. [DOI], [ADS], [arXiv:1901.05968 [astro-ph.SR]]

Hansen, T. T., Andersen, J., Nordström, B., Beers, T. C., Placco, V. M., Yoon, J. and Buchhave, L. A., 2016b, "The role of binaries in the enrichment of the early Galactic halo. III. Carbon-enhanced metal-poor stars - CEMP-s stars", *Astron. Astrophys.*, **588**, A3. [DOI], [ADS], [arXiv:1601.03385 [astro-ph.SR]]

Hansen, T. T., Andersen, J., Nordström, B., Beers, T. C., Placco, V. M., Yoon, J. and Buchhave, L. A., 2016c, "The role of binaries in the enrichment of the early Galactic halo. III. Carbon-enhanced metal-poor stars - CEMP-s stars", *Astron. Astrophys.*, **588**, A3. [DOI], [ADS], [arXiv:1601.03385 [astro-ph.SR]]

Hansen, T. T., Simon, J. D., Marshall, J. L., Li, T. S., Carollo, D., DePoy, D. L., Nagasawa, D. Q., Bernstein, R. A., Drlica-Wagner, A., Abdalla, F. B., Allam, S., Annis, J., Bechtol, K., Benoit-Lévy, A., Brooks, D., Buckley-Geer, E., Carnero Rosell, A., Carrasco Kind, M., Carretero, J., Cunha, C. E., da Costa, L. N., Desai, S., Eifler, T. F., Fausti Neto, A., Flaugher, B., Frieman, J., García-Bellido, J., Gaztanaga, E., Gerdes, D. W., Gruen, D., Gruendl, R. A., Gschwend, J., Gutierrez, G., James, D. J., Krause, E., Kuehn, K., Kuropatkin, N., Lahav, O., Miquel, R., Plazas, A. A., Romer, A. K., Sanchez, E., Santiago, B., Scarpine, V., Smith, R. C., Soares-Santos, M., Sobreira, F., Suchyta, E., Swanson, M. E. C., Tarle, G., Walker, A. R. and DES Collaboration, 2017, "An r-process Enhanced Star in the Dwarf Galaxy Tucana III", *Astrophys. J.*, **838**(1), 44. [DOI], [ADS], [arXiv:1702.07430 [astro-ph.SR]]

Heger, Alexander and Woosley, S. E., 2010, "Nucleosynthesis and Evolution of Massive Metal-free Stars", *Astrophys. J.*, **724**(1), 341–373. [DOI], [ADS], [arXiv:0803.3161 [astro-ph]]

Herwig, F., 2000, "The evolution of AGB stars with convective overshoot", *Astron. Astrophys.*, **360**, 952–968. [ADS], [arXiv:astro-ph/0007139 [astro-ph]]

Herwig, Falk, Langer, Norbert and Lugaro, Maria, 2003, "The s-Process in Rotating Asymptotic Giant Branch Stars", *Astrophys. J.*, **593**(2), 1056–1073. [DOI], [ADS], [arXiv:astro-ph/0305491 [astro-ph]]

Herwig, Falk, Pignatari, Marco, Woodward, Paul R., Porter, David H., Rockefeller, Gabriel, Fryer, Chris L., Bennett, Michael and Hirschi, Raphael, 2011, "Convective-reactive Proton-^{12}C Combustion in Sakurai's Object (V4334 Sagittarii) and Implications for the Evolution and Yields from the First Generations of Stars", *Astrophys. J.*, **727**(2), 89. [DOI], [ADS], [arXiv:1002.2241 [astro-ph.SR]]

Hidalgo, Sebastian L., Pietrinferni, Adriano, Cassisi, Santi, Salaris, Maurizio, Mucciarelli, Alessio, Savino, Alessandro, Aparicio, Antonio, Silva Aguirre, Victor and Verma, Kuldeep, 2018, "The Updated BaSTI Stellar Evolution Models and Isochrones. I. Solar-scaled Calculations", *Astrophys. J.*, **856**(2), 125. [DOI], [ADS], [arXiv:1802.07319 [astro-ph.GA]]

Hill, V., Barbuy, B., Spite, M., Spite, F., Cayrel, R., Plez, B., Beers, T. C., Nordström, B. and Nissen, P. E., 2000, "Heavy-element abundances in the CH/CN-strong very metal-poor stars CS 22948-27 and CS 29497-34", *Astron. Astrophys.*, **353**, 557–568. [ADS]

Hill, V., Plez, B., Cayrel, R., Beers, T. C., Nordström, B., Andersen, J., Spite, M., Spite, F., Barbuy, B., Bonifacio, P., Depagne, E., François, P. and Primas, F., 2002, "First stars. I. The extreme r-element rich, iron-poor halo giant CS 31082-001. Implications for the r-process site(s) and radioactive cosmochronology", *Astron. Astrophys.*, **387**, 560–579. [DOI], [ADS], [arXiv:astro-ph/0203462 [astro-ph]]

Hill, V., Christlieb, N., Beers, T. C., Barklem, P. S., Kratz, K. L., Nordström, B., Pfeiffer, B. and Farouqi, K., 2017, "The Hamburg/ESO R-process Enhanced Star survey (HERES). XI. The highly r-process-enhanced star CS 29497-004", *Astron. Astrophys.*, **607**, A91. [DOI], [ADS], [arXiv:1608.07463 [astro-ph.GA]]

Hinkle, Kenneth, Wallace, Lloyd, Valenti, Jeff and Harmer, Dianne, 2000, *Visible and Near Infrared Atlas of the Arcturus Spectrum 3727-9300 A*. [ADS]

Hollowell, David, Iben, Icko, Jr. and Fujimoto, Masayuki Y., 1990, "Hydrogen Burning and Dredge-up during the Major Core Helium Flash in a Z = 0 Model Star", *Astrophys. J.*, **351**, 245. [DOI], [ADS]

Honda, Satoshi, Aoki, Wako, Kajino, Toshitaka, Ando, Hiroyasu, Beers, Timothy C., Izumiura, Hideyuki, Sadakane, Kozo and Takada-Hidai, Masahide, 2004, "Spectroscopic Studies of Extremely Metal-Poor Stars with the Subaru High Dispersion Spectrograph. II. The r-Process Elements, Including Thorium", *Astrophys. J.*, **607**(1), 474–498. [DOI], [ADS], [arXiv:astro-ph/0402298 [astro-ph]]

Husti, Laura, Gallino, Roberto, Bisterzo, Sara, Straniero, Oscar and Cristallo, Sergio, 2009, "Barium Stars: Theoretical Interpretation", *Publications of the Astronomical Society of Australia*, **26**(3), 176–183. [DOI], [ADS], [arXiv:0909.5560 [astro-ph.SR]]

Iben, Jr., I. and Renzini, A., 1983, "Asymptotic giant branch evolution and beyond", *Ann. Rev. Astron. Astrophys.*, **21**, 271–342. [DOI], [ADS]

Ishigaki, M., Chiba, M. and Aoki, W., 2010, "Chemical Abundances of Outer Halo Stars in the Milky Way", *Pub. Astron. Soc. Japan*, **62**, 143–178. [DOI], [ADS], [arXiv:0912.0329]

Ivans, I. I., Sneden, C., Gallino, R., Cowan, J. J. and Preston, G. W., 2005, "Near-Ultraviolet Observations of CS 29497-030: New Constraints on Neutron-Capture Nucleosynthesis Processes", *Astrophys. J. Lett.*, **627**, L145–L148. [DOI], [ADS], [astro-ph/0505002]

Ivans, Inese I., Kraft, Robert P., Sneden, Christopher, Smith, Graeme H., Rich, R. Michael and Shetrone, Matthew, 2001, "New Analyses of Star-to-Star Abundance Variations among Bright Giants in the Mildly Metal-poor Globular Cluster M5", *Astron. J.*, **122**(3), 1438–1463. [DOI], [ADS], [arXiv:astro-ph/0106249 [astro-ph]]

Iwamoto, Nobuyuki, Kajino, Toshitaka, Mathews, Grant J., Fujimoto, Masayuki Y. and Aoki, Wako, 2004, "Flash-Driven Convective Mixing in Low-Mass, Metal-deficient Asymptotic Giant Branch Stars: A New Paradigm for Lithium Enrichment and a Possible s-Process", *Astrophys. J.*, **602**(1), 377–388. [DOI], [ADS]

Jacobson, Heather R. and Frebel, Anna, 2014, "Observational nuclear astrophysics: neutron-capture element abundances in old, metal-poor stars", *Journal of Physics G Nuclear Physics*, **41**(4), 044001. [DOI], [ADS], [arXiv:1309.0037 [astro-ph.GA]]

Ji, Alexander P. and Frebel, Anna, 2018, "From Actinides to Zinc: Using the Full Abundance Pattern of the Brightest Star in Reticulum II to Distinguish between Different r-process Sites", *Astrophys. J.*, **856**(2), 138. [DOI], [ADS], [arXiv:1802.07272 [astro-ph.SR]]

Ji, Alexander P., Frebel, Anna, Chiti, Anirudh and Simon, Joshua D., 2016a, "R-process enrichment from a single event in an ancient dwarf galaxy", *Nature*, **531**(7596), 610–613. [DOI], [ADS], [arXiv:1512.01558 [astro-ph.GA]]

Ji, Wei, Cui, Wenyuan, Liu, Chao, Luo, Ali, Zhao, Gang and Zhang, Bo, 2016b, "Carbon Stars from LAMOST DR2 Data", *Astrophys. J. Suppl.*, **226**(1), 1. [DOI], [ADS], [arXiv:1606.08932 [astro-ph.SR]]

Johnson, Dean R. H. and Soderblom, David R., 1987, "Calculating Galactic Space Velocities and Their Uncertainties, with an Application to the Ursa Major Group", *Astron. J.*, **93**, 864. [DOI], [ADS]

Johnson, J. A., 2002, "Abundances of 30 Elements in 23 Metal-Poor Stars", *Astrophys. J. Suppl.*, **139**, 219–247. [DOI], [ADS], [astro-ph/0111181]

Johnson, J. A. and Bolte, M., 2002, "Abundances in the Very Metal Poor s-Process-rich Star CS 22183-015", *Astrophys. J. Lett.*, **579**, L87–L90. [DOI], [ADS]

Johnson, J. A. and Bolte, M., 2004, "The s-Process in Metal-Poor Stars: Abundances for 22 Neutron-Capture Elements in CS 31062-050", *Astrophys. J.*, **605**, 462–471. [DOI], [ADS], [astro-ph/0402003]

Jones, S., Ritter, C., Herwig, F., Fryer, C., Pignatari, M., Bertolli, M. G. and Paxton, B., 2016, "H ingestion into He-burning convection zones in super-AGB stellar models as a potential site for intermediate neutron-density nucleosynthesis", *Mon. Not. Roy. Astron. Soc.*, **455**(4), 3848–3863. [DOI], [ADS], [arXiv:1510.07417 [astro-ph.SR]]

Jonsell, K., Edvardsson, B., Gustafsson, B., Magain, P., Nissen, P. E. and Asplund, M., 2005, "Chemical abundances in 43 metal-poor stars", *Astron. Astrophys.*, **440**, 321–343. [DOI], [ADS], [astro-ph/0505118]

Jonsell, K., Barklem, P. S., Gustafsson, B., Christlieb, N., Hill, V., Beers, T. C. and Holmberg, J., 2006, "The Hamburg/ESO R-process enhanced star survey (HERES). III. HE 0338-3945 and the formation of the r + s stars", *Astron. Astrophys.*, **451**, 651–670. [DOI], [ADS], [astro-ph/0601476]

Jorissen, A., Van Eck, S., Mayor, M. and Udry, S., 1998, "Insights into the formation of barium and Tc-poor S stars from an extended sample of orbital elements", *Astron. Astrophys.*, **332**, 877–903. [ADS], [arXiv:astro-ph/9801272 [astro-ph]]

Jorissen, A., Hansen, T., Van Eck, S., Andersen, J., Nordström, B., Siess, L., Torres, G., Masseron, T. and Van Winckel, H., 2016a, "HE 0017+0055: A probable pulsating CEMP-rs star and long-period binary", *Astron. Astrophys.*, **586**, A159. [DOI], [ADS], [arXiv:1510.06045 [astro-ph.SR]]

Jorissen, A., Van Eck, S., Van Winckel, H., Merle, T., Boffin, H. M. J., Andersen, J., Nordström, B., Udry, S., Masseron, T., Lenaerts, L. and Waelkens, C., 2016b, "Binary properties of CH and carbon-enhanced metal-poor stars", *Astron. Astrophys.*, **586**, A158. [DOI], [ADS], [arXiv:1510.05840 [astro-ph.SR]]

Jorissen, A., Boffin, H. M. J., Karinkuzhi, D., Van Eck, S., Escorza, A., Shetye, S. and Van Winckel, H., 2019, "Barium and related stars, and their white-dwarf companions. I. Giant stars", *Astron. Astrophys.*, **626**, A127. [DOI], [ADS], [arXiv:1904.03975 [astro-ph.SR]]

Kang, Wonseok and Lee, Sang-Gak, 2012, "Tool for Automatic Measurement of Equivalent width (TAME)", *Mon. Not. Roy. Astron. Soc.*, **425**(4), 3162–3171. [DOI], [ADS], [arXiv:1207.2845 [astro-ph.SR]]

Karakas, Amanda I. and Lattanzio, John C., 2014, "The Dawes Review 2: Nucleosynthesis and Stellar Yields of Low- and Intermediate-Mass Single Stars", *Publications of the Astronomical Society of Australia*, **31**, e030. [DOI], [ADS], [arXiv:1405.0062 [astro-ph.SR]]

Karinkuzhi, D. and Goswami, A., 2014, "Chemical analysis of CH stars - I. Atmospheric parameters and elemental abundances", *Mon. Not. Roy. Astron. Soc.*, **440**, 1095–1113. [DOI], [ADS], [arXiv:1410.0111 [astro-ph.SR]]

Karinkuzhi, D., Van Eck, S., Jorissen, A., Goriely, S., Siess, L., Merle, T., Escorza, A., Van der Swaelmen, M., Boffin, H. M. J., Masseron, T., Shetye, S. and Plez, B., 2018, "When binaries keep track of recent nucleosynthesis. The Zr-Nb pair in extrinsic stars as an s-process diagnostic", *Astron. Astrophys.*, **618**, A32. [DOI], [ADS], [arXiv:1807.06332 [astro-ph.SR]]

Karinkuzhi, D., Van Eck, S., Goriely, S., Siess, L., Jorissen, A., Merle, T., Escorza, A. and Masseron, T., 2021, "Low-mass low-metallicity AGB stars as an efficient i-process site explaining CEMP-rs stars", *Astron. Astrophys.*, **645**, A61. [DOI], [ADS], [arXiv:2010.13620 [astro-ph.SR]]

Karinkuzhi, Drisya, Goswami, Aruna and Masseron, Thomas, 2017, "Chemical Analysis of a Carbon-enhanced Very Metal-poor Star: CD-27 14351", *Astrophys. J.*, **834**(1), 61. [DOI], [ADS], [arXiv:1611.01637 [astro-ph.SR]]

Kaufer, Andreas and Pasquini, Luca, 1998, "FEROS: the new fiber-linked echelle spectrograph for the ESO 1.52-m telescope", in *Optical Astronomical Instrumentation*, (Ed.) D'Odorico, Sandro, Society of Photo-Optical Instrumentation Engineers (SPIE) Conference Series, 3355, [DOI], [ADS]

Keenan, Philip C., 1942, "The Spectra of CH Stars", *Astrophys. J.*, **96**, 101. [DOI], [ADS]

Keller, S., Bessell, M., Schmidt, B. and Francis, P., 2007a, "The SkyMapper Southern Sky Survey", in *The Future of Photometric, Spectrophotometric and Polarimetric Standardization*, (Ed.) Sterken, C., Astronomical Society of the Pacific Conference Series, 364, [ADS]

Keller, S. C., Schmidt, B. P., Bessell, M. S., Conroy, P. G., Francis, P., Granlund, A., Kowald, E., Oates, A. P., Martin-Jones, T., Preston, T., Tisserand, P., Vaccarella, A. and Waterson, M. F., 2007b, "The SkyMapper Telescope and The Southern Sky Survey", *Publications of the Astronomical Society of Australia*, **24**(1), 1–12. [DOI], [ADS], [arXiv:astro-ph/0702511 [astro-ph]]

Keller, S. C., Bessell, M. S., Frebel, A., Casey, A. R., Asplund, M., Jacobson, H. R., Lind, K., Norris, J. E., Yong, D., Heger, A., Magic, Z., da Costa, G. S., Schmidt, B. P. and Tisserand, P., 2014, "A single low-energy, iron-poor supernova as the source of metals in the star SMSS J031300.36-670839.3", *Nature*, **506**(7489), 463–466. [DOI], [ADS], [arXiv:1402.1517 [astro-ph.SR]]

Kennedy, C. R., Sivarani, T., Beers, T. C., Lee, Y. S., Placco, V. M., Rossi, S., Christlieb, N., Herwig, F. and Plez, B., 2011, "[O/Fe] Estimates for Carbon-enhanced Metal-poor Stars from Near-infrared Spectroscopy", *Astron. J.*, **141**, 102. [DOI], [ADS], [arXiv:1101.2260 [astro-ph.SR]]

Kraft, Robert P., Sneden, Christopher, Smith, Graeme H., Shetrone, Matthew D., Langer, G. E. and Pilachowski, Catherine A., 1997, "Proton Capture Chains in Globular Cluster Stars.II.Oxygen, Sodium, Magnesium, and Aluminum Abundances in M13 Giants Brighter Than the Horizontal Branch", *Astron. J.*, **113**, 279. [DOI], [ADS]

Larson, Richard B., 1998, "Early star formation and the evolution of the stellar initial mass function in galaxies", *Mon. Not. Roy. Astron. Soc.*, **301**(2), 569–581. [DOI], [ADS], [arXiv:astro-ph/9808145 [astro-ph]]

Lattimer, J. M. and Schramm, D. N., 1974, "Black-Hole-Neutron-Star Collisions", *Astrophys. J. Lett.*, **192**, L145. [DOI], [ADS]

Lau, Herbert H. B., Stancliffe, Richard J. and Tout, Christopher A., 2008, "An explosive end to intermediate-mass zero-metallicity stars and early Universe nucleosynthesis", *Mon. Not. Roy. Astron. Soc.*, **385**(1), 301–309. [DOI], [ADS], [arXiv:0712.1160 [astro-ph]]

Lau, Herbert H. B., Stancliffe, Richard J. and Tout, Christopher A., 2009, "The evolution of low-metallicity asymptotic giant branch stars and the formation of carbon-enhanced metal-poor stars", *Mon. Not. Roy. Astron. Soc.*, **396**(2), 1046–1057. [DOI], [ADS], [arXiv:0903.2324 [astro-ph.SR]]

Liu, Nan, Gallino, Roberto, Bisterzo, Sara, Davis, Andrew M., Savina, Michael R. and Pellin, Michael J., 2014, "The ^{13}C-Pocket Structure in AGB Models: Constraints from Zirconium Isotope Abundances in Single Mainstream SiC Grains", *Astrophys. J.*, **788**(2), 163. [DOI], [ADS], [arXiv:1405.1441 [astro-ph.SR]]

Liu, S., Nissen, P. E., Schuster, W. J., Zhao, G., Chen, Y. Q. and Liang, Y. C., 2012, "Abundances of neutron-capture elements in ¡ASTROBJ¿G 24-25¡/ASTROBJ¿. A halo-population CH subgiant", *Astron. Astrophys.*, **541**, A48. [DOI], [ADS], [arXiv:1203.5682 [astro-ph.SR]]

Lu, Phillip K., 1991, "Taxonomy of Barium Stars", *Astron. J.*, **101**, 2229. [DOI], [ADS]

Lucatello, S., Gratton, R., Cohen, J. G., Beers, T. C., Christlieb, N., Carretta, E. and Ramírez, S., 2003, "Stellar Archaeology: A Keck Pilot Program on Extremely Metal-Poor Stars From the Hamburg/ESO Survey. III. The Lead (Pb) Star HE 0024-2523", *Astron. J.*, **125**, 875–893. [DOI], [ADS], [astro-ph/0211050]

Lucatello, Sara, Gratton, Raffaele G., Beers, Timothy C. and Carretta, Eugenio, 2005, "Observational Evidence for a Different Initial Mass Function in the Early Galaxy", *Astrophys. J.*, **625**(2), 833–837. [DOI], [ADS], [arXiv:astro-ph/0412423 [astro-ph]]

Lugaro, M., Campbell, S. W. and de Mink, S. E., 2009, "The Mystery of CEMPs+r Stars and the Dual Core-Flash Neutron Superburst", *Publications of the Astronomical Society of Australia*, **26**, 322–326. [DOI], [ADS]

Lugaro, M., Campbell, S. W., Van Winckel, H., De Smedt, K., Karakas, A. I. and Käppeler, F., 2015, "Post-AGB stars in the Magellanic Clouds and neutron-capture processes in AGB stars", *Astron. Astrophys.*, **583**, A77. [DOI], [ADS], [arXiv:1509.03518 [astro-ph.SR]]

Lugaro, Maria, Karakas, Amanda I., Stancliffe, Richard J. and Rijs, Carlos, 2012, "The s-process in Asymptotic Giant Branch Stars of Low Metallicity and the Composition of Carbon-enhanced Metal-poor Stars", *Astrophys. J.*, **747**(1), 2. [DOI], [ADS], [arXiv:1112.2757 [astro-ph.SR]]

Maeder, André and Meynet, Georges, 2015, "The first stars: a classification of CEMP-no stars", *Astron. Astrophys.*, **580**, A32. [DOI], [ADS], [arXiv:1506.04508 [astro-ph.SR]]

Marigo, P., 2002, "Asymptotic Giant Branch evolution at varying surface C/O ratio: effects of changes in molecular opacities", *Astron. Astrophys.*, **387**, 507–519. [DOI], [ADS], [arXiv:astro-ph/0203036 [astro-ph]]

Marshall, J. L., Hansen, T., Simon, J. D., Li, T. S., Bernstein, R. A., Kuehn, K., Pace, A. B., DePoy, D. L., Palmese, A., Pieres, A., Strigari, L., Drlica-Wagner, A., Bechtol, K., Lidman, C., Nagasawa, D. Q., Bertin, E., Brooks,

D., Buckley-Geer, E., Burke, D. L., Carnero Rosell, A., Carrasco Kind, M., Carretero, J., Cunha, C. E., D'Andrea, C. B., da Costa, L. N., De Vicente, J., Desai, S., Doel, P., Eifler, T. F., Flaugher, B., Fosalba, P., Frieman, J., García-Bellido, J., Gaztanaga, E., Gerdes, D. W., Gruendl, R. A., Gschwend, J., Gutierrez, G., Hartley, W. G., Hollowood, D. L., Honscheid, K., Hoyle, B., James, D. J., Kuropatkin, N., Maia, M. A. G., Menanteau, F., Miller, C. J., Miquel, R., Plazas, A. A., Sanchez, E., Santiago, B., Scarpine, V., Schubnell, M., Serrano, S., Sevilla-Noarbe, I., Smith, M., Soares-Santos, M., Suchyta, E., Swanson, M. E. C., Tarle, G., Wester, W. and DES Collaboration, 2019, "Chemical Abundance Analysis of Tucana III, the Second r-process Enhanced Ultra-faint Dwarf Galaxy", *Astrophys. J.*, **882**(2), 177. [DOI], [ADS], [arXiv:1812.01022 [astro-ph.GA]]

Masseron, T., Johnson, J. A., Plez, B., van Eck, S., Primas, F., Goriely, S. and Jorissen, A., 2010, "A holistic approach to carbon-enhanced metal-poor stars", *Astron. Astrophys.*, **509**, A93. [DOI], [ADS], [arXiv:0901.4737 [astro-ph.SR]]

Matrozis, E. and Stancliffe, R. J., 2016, "Radiative levitation in carbon-enhanced metal-poor stars with s-process enrichment", *Astron. Astrophys.*, **592**, A29. [DOI], [ADS], [arXiv:1605.02791 [astro-ph.SR]]

Mayall, M. W. and Cannon, A. J., 1940, "New Peculiar Spectra", *Harvard College Observatory Bulletin*, **913**, 7–7. [ADS]

McClure, R. D., 1983, "The binary nature of the barium stars. II. Velocities, binary frequency, and preliminary orbits.", *Astrophys. J.*, **268**, 264–273. [DOI], [ADS]

McClure, R. D., 1984, "The binary nature of the CH stars.", *Astrophys. J. Lett.*, **280**, L31–L34. [DOI], [ADS]

McClure, Robert D. and Woodsworth, A. W., 1990, "The Binary Nature of the Barium and CH Stars. III. Orbital Parameters", *Astrophys. J.*, **352**, 709. [DOI], [ADS]

McDonald, I., Zijlstra, A. A. and Boyer, M. L., 2012, "Fundamental parameters and infrared excesses of Hipparcos stars", *Mon. Not. Roy. Astron. Soc.*, **427**(1), 343–357. [DOI], [ADS], [arXiv:1208.2037 [astro-ph.SR]]

McWilliam, A., 1998, "Barium Abundances in Extremely Metal-poor Stars", *Astron. J.*, **115**, 1640–1647. [DOI], [ADS]

Mennessier, M. O., Luri, X., Figueras, F., Gomez, A. E., Grenier, S., Torra, J. and North, P., 1997, "Barium stars, galactic populations and evolution.", *Astron. Astrophys.*, **326**, 722–730. [ADS]

Meynet, G., Hirschi, R., Ekstrom, S., Maeder, A., Georgy, C., Eggenberger, P. and Chiappini, C., 2010, "Are C-rich ultra iron-poor stars also He-rich?", *Astron. Astrophys.*, **521**, A30. [DOI], [ADS], [arXiv:1004.5024 [astro-ph.SR]]

Mirizzi, Alessandro, 2015, "Breaking the symmetries in self-induced flavor conversions of neutrino beams from a ring", , **92**(10), 105020. [DOI], [ADS], [arXiv:1506.06805 [hep-ph]]

Mishenina, T. V., Soubiran, C., Kovtyukh, V. V. and Korotin, S. A., 2004, "On the correlation of elemental abundances with kinematics among galactic disk stars", *Astron. Astrophys.*, **418**, 551–562. [DOI], [ADS], [astro-ph/0401234]

Noguchi, Kunio, Aoki, Wako, Kawanomoto, Satoshi, Ando, Hiroyasu, Honda, Satoshi, Izumiura, Hideyuki, Kambe, Eiji, Okita, Kiichi, Sadakane, Kozo, Sato, Bun'ei, Tajitsu, Akito, Takada-Hidai, Tasahide, Tanaka, Wataru, Watanabe, Etsuji and Yoshida, Michitoshi, 2002, "High Dispersion Spectrograph (HDS) for the Subaru Telescope", *Pub. Astron. Soc. Japan*, **54**, 855–864. [DOI], [ADS]

Nomoto, K., Sugimoto, D. and Neo, S., 1976, "Carbon deflagration supernova, an alternative to carbon detonation", *Astrophys. Space Sci.*, **39**, L37–L42. [DOI], [ADS]

Nomoto, Ken'ichi, Kobayashi, Chiaki and Tominaga, Nozomu, 2013, "Nucleosynthesis in Stars and the Chemical Enrichment of Galaxies", *Ann. Rev. Astron. Astrophys.*, **51**(1), 457–509. [DOI], [ADS]

Norris, John E., Gilmore, Gerard, Wyse, Rosemary F. G., Yong, David and Frebel, Anna, 2010, "An Extremely Carbon-rich, Extremely Metal-poor Star in the Segue 1 System", *Astrophys. J. Lett.*, **722**(1), L104–L109. [DOI], [ADS], [arXiv:1008.0450 [astro-ph.GA]]

Norris, John E., Yong, David, Bessell, M. S., Christlieb, N., Asplund, M., Gilmore, Gerard, Wyse, Rosemary F. G., Beers, Timothy C., Barklem, P. S., Frebel, Anna and Ryan, S. G., 2013, "The Most Metal-poor Stars. IV. The Two Populations with [Fe/H] ¡~-3.0", *Astrophys. J.*, **762**(1), 28. [DOI], [ADS], [arXiv:1211.3157 [astro-ph.GA]]

North, P., Berthet, S. and Lanz, T., 1994, "The nature of the F STR λ4077 stars. V. Spectroscopic data", *Astron. Astrophys. Suppl.*, **103**, 321–347. [ADS]

Obergaulinger, M., Just, O. and Aloy, M. A., 2018, "Core collapse with magnetic fields and rotation", *Journal of Physics G Nuclear Physics*, **45**(8), 084 001. [DOI], [ADS], [arXiv:1806.00393 [astro-ph.HE]]

Ono, M., Hashimoto, M., Fujimoto, S., Kotake, K. and Yamada, S., 2012, "Explosive Nucleosynthesis in Magnetohydrodynamical Jets from Collapsars. II — Heavy-Element Nucleosynthesis of s, p, r-Processes", *Progress of Theoretical Physics*, **128**(4), 741–765. [DOI], [ADS], [arXiv:1203.6488 [astro-ph.SR]]

Pereira, C. B. and Drake, N. A., 2009, "High-resolution spectroscopic observations of two chemically peculiar metal-poor stars: HD 10613 and BD+04deg2466", *Astron. Astrophys.*, **496**, 791–804. [DOI], [ADS]

Piersanti, L., Cristallo, S. and Straniero, O., 2013, "The Effects of Rotation on s-process Nucleosynthesis in Asymptotic Giant Branch Stars", *Astrophys. J.*, **774**(2), 98. [DOI], [ADS], [arXiv:1307.2017 [astro-ph.SR]]

Pilachowski, C. A., 1977, "The chemical compositions of the mild barium stars.", *Astron. Astrophys.*, **54**, 465–474. [ADS]

Placco, Vinicius M., Frebel, Anna, Beers, Timothy C., Karakas, Amanda I., Kennedy, Catherine R., Rossi, Silvia, Christlieb, Norbert and Stancliffe, Richard J., 2013, "Metal-poor Stars Observed with the Magellan Telescope. I. Constraints on Progenitor Mass and Metallicity of AGB Stars Undergoing s-process Nucleosynthesis", *Astrophys. J.*, **770**(2), 104. [DOI], [ADS], [arXiv:1304.7869 [astro-ph.GA]]

Placco, Vinicius M., Sneden, Christopher, Roederer, Ian U., Lawler, James E., Den Hartog, Elizabeth A., Hejazi, Neda, Maas, Zachary and Bernath, Peter, 2021, "Linemake: An Atomic and Molecular Line List Generator", *Research Notes of the American Astronomical Society*, **5**(4), 92. [DOI], [ADS], [arXiv:2104.08286 [astro-ph.IM]]

Portinari, L., Chiosi, C. and Bressan, A., 1998, "Galactic chemical enrichment with new metallicity dependent stellar yields", *Astron. Astrophys.*, **334**, 505–539. [ADS], [arXiv:astro-ph/9711337 [astro-ph]]

Preston, G. W. and Sneden, C., 2001, "The Incidence of Binaries among Very Metal-poor Carbon Stars", *Astron. J.*, **122**, 1545–1560. [DOI], [ADS]

Prochaska, J. X. and McWilliam, A., 2000, "On the Perils of Hyperfine Splitting: A Reanalysis of MN and SC Abundance Trends", *Astrophys. J. Lett.*, **537**, L57–L60. [DOI], [ADS], [astro-ph/0005471]

Purandardas, Meenakshi, Goswami, Aruna, Goswami, Partha Pratim, Shejeelammal, J. and Masseron, Thomas, 2019, "Chemical analysis of CH stars - III. Atmospheric parameters and elemental abundances", *Mon. Not. Roy. Astron. Soc.*, **486**(3), 3266–3289. [DOI], [ADS], [arXiv:1904.03904 [astro-ph.SR]]

Qian, Y. Z. and Wasserburg, G. J., 2003, "Stellar Sources for Heavy r-Process Nuclei", *Astrophys. J.*, **588**(2), 1099–1109. [DOI], [ADS], [arXiv:astro-ph/0301461 [astro-ph]]

Qian, Y. Z. and Woosley, S. E., 1996, "Nucleosynthesis in Neutrino-driven Winds. I. The Physical Conditions", *Astrophys. J.*, **471**, 331. [DOI], [ADS], [arXiv:astro-ph/9611094 [astro-ph]]

Ram, R. S., Brooke, J. S. A., Bernath, P. F., Sneden, C. and Lucatello, S., 2014, "Improved Line Data for the Swan System $^{12}C^{13}C$ Isotopologue", *Astrophys. J. Suppl.*, **211**, 5. [DOI], [ADS]

Ramírez, I., Allende Prieto, C. and Lambert, D. L., 2013, "Oxygen Abundances in Nearby FGK Stars and the Galactic Chemical Evolution of the Local Disk and Halo", *Astrophys. J.*, **764**(1), 78. [DOI], [ADS], [arXiv:1301.1582 [astro-ph.SR]]

Reddy, B. E., Lambert, D. L. and Allende Prieto, C., 2006, "Elemental abundance survey of the Galactic thick disc", *Mon. Not. Roy. Astron. Soc.*, **367**, 1329–1366. [DOI], [ADS], [astro-ph/0512505]

Ren, J., Christlieb, N. and Zhao, G., 2012, "The Hamburg/ESO R-process Enhanced Star survey (HERES). VII. Thorium abundances in metal-poor stars", *Astron. Astrophys.*, **537**, A118. [DOI], [ADS], [arXiv:1112.4870 [astro-ph.SR]]

Richard, O., Michaud, G., Richer, J., Turcotte, S., Turck-Chièze, S. and VandenBerg, Don A., 2002, "Models of Metal-poor Stars with Gravitational Settling and Radiative Accelerations. I. Evolution and Abundance Anomalies", *Astrophys. J.*, **568**(2), 979–997. [DOI], [ADS]

Roederer, Ian U., Lawler, James E., Cowan, John J., Beers, Timothy C., Frebel, Anna, Ivans, Inese I., Schatz, Hendrik, Sobeck, Jennifer S. and Sneden, Christopher, 2012, "Detection of the Second r-process Peak Element Tellurium in Metal-poor Stars", *Astrophys. J. Lett.*, **747**(1), L8. [DOI], [ADS], [arXiv:1202.2378 [astro-ph.SR]]

Roederer, Ian U., Karakas, Amanda I., Pignatari, Marco and Herwig, Falk, 2016, "The Diverse Origins of Neutron-capture Elements in the Metal-poor Star HD 94028: Possible Detection of Products of I-Process Nucleosynthesis", *Astrophys. J.*, **821**(1), 37. [DOI], [ADS], [arXiv:1603.00036 [astro-ph.SR]]

Roman, Nancy G., 1950, "A Correlation Between the Spectroscopic and Dynamical Characteristics of the Late F - and Early G - Type Stars.", *Astrophys. J.*, **112**, 554. [DOI], [ADS]

Sanford, R. F., 1944, "Radial Velocities of 283 Stars of Spectral Classes R and N.", *Astrophys. J.*, **99**, 145. [DOI], [ADS]

Sbordone, L., Hansen, C. J., Monaco, L., Cristallo, S., Bonifacio, P., Caffau, E., Villanova, S. and Amigo, P., 2020, "A wide angle view of the Sagittarius dwarf spheroidal galaxy. II. A CEMP-r/s star in the Sagittarius dwarf spheroidal galaxy", *Astron. Astrophys.*, **641**, A135. [DOI], [ADS], [arXiv:2005.03027 [astro-ph.SR]]

Scalo, J. M., 1978, "Signatures of the ^{22}Ne neutron source in red giants and planetary nebulae.", *Astrophys. J.*, **221**, 627–634. [DOI], [ADS]

Schönrich, R., Binney, J. and Dehnen, W., 2010, "Local kinematics and the local standard of rest", *Mon. Not. Roy. Astron. Soc.*, **403**, 1829–1833. [DOI], [ADS], [arXiv:0912.3693]

Schramm, David N., 1973, "Explosive r-PROCESS Nucleosynthesis", *Astrophys. J.*, **185**, 293–302. [DOI], [ADS]

Schuler, Simon C., Margheim, Steven J., Sivarani, Thirupathi, Asplund, Martin, Smith, Verne V., Cunha, Katia and Beers, Timothy C., 2008, "Carbon Abundances of Three Carbon-Enhanced Metal-Poor Stars from High-Resolution Gemini-S/bHROS Spectra of the λ8727 [C I] Line", *Astron. J.*, **136**(6), 2244–2258. [DOI], [ADS], [arXiv:0809.1377 [astro-ph]]

Schwarzschild, Martin and Schwarzschild, Barbara, 1950, "A Spectroscopic Comparison Between - and Low-Velocity F Dwarfs.", *Astrophys. J.*, **112**, 248. [DOI], [ADS]

Shejeelammal, J., Goswami, Aruna, Goswami, Partha Pratim, Rathour, Rajeev Singh and Masseron, Thomas, 2020, "Characterizing the companion AGBs

using surface chemical composition of barium stars", *Mon. Not. Roy. Astron. Soc.*, **492**(3), 3708–3727. [DOI], [ADS], [arXiv:2010.06949 [astro-ph.SR]]

Simon, J. D., Drlica-Wagner, A., Li, T. S., Nord, B., Geha, M., Bechtol, K., Balbinot, E., Buckley-Geer, E., Lin, H., Marshall, J., Santiago, B., Strigari, L., Wang, M., Wechsler, R. H., Yanny, B., Abbott, T., Bauer, A. H., Bernstein, G. M., Bertin, E., Brooks, D., Burke, D. L., Capozzi, D., Carnero Rosell, A., Carrasco Kind, M., D'Andrea, C. B., da Costa, L. N., DePoy, D. L., Desai, S., Diehl, H. T., Dodelson, S., Cunha, C. E., Estrada, J., Evrard, A. E., Fausti Neto, A., Fernandez, E., Finley, D. A., Flaugher, B., Frieman, J., Gaztanaga, E., Gerdes, D., Gruen, D., Gruendl, R. A., Honscheid, K., James, D., Kent, S., Kuehn, K., Kuropatkin, N., Lahav, O., Maia, M. A. G., March, M., Martini, P., Miller, C. J., Miquel, R., Ogando, R., Romer, A. K., Roodman, A., Rykoff, E. S., Sako, M., Sanchez, E., Schubnell, M., Sevilla, I., Smith, R. C., Soares-Santos, M., Sobreira, F., Suchyta, E., Swanson, M. E. C., Tarle, G., Thaler, J., Tucker, D., Vikram, V., Walker, A. R., Wester, W. and DES Collaboration, 2015, "Stellar Kinematics and Metallicities in the Ultra-faint Dwarf Galaxy Reticulum II", *Astrophys. J.*, **808**(1), 95. [DOI], [ADS], [arXiv:1504.02889 [astro-ph.GA]]

Sivarani, T., Bonifacio, P., Molaro, P., Cayrel, R., Spite, M., Spite, F., Plez, B., Andersen, J., Barbuy, B., Beers, T. C., Depagne, E., Hill, V., François, P., Nordström, B. and Primas, F., 2004, "First stars IV. CS 29497-030: Evidence for operation of the s-process at very low metallicity", *Astron. Astrophys.*, **413**, 1073–1085. [DOI], [ADS], [astro-ph/0310291]

Skúladóttir, Á., Hansen, C. J., Choplin, A., Salvadori, S., Hampel, M. and Campbell, S. W., 2020, "Neutron-capture elements in dwarf galaxies. II. Challenges for the s- and i-processes at low metallicity", *Astron. Astrophys.*, **634**, A84. [DOI], [ADS], [arXiv:1912.06671 [astro-ph.GA]]

Smith, Verne V., Coleman, Howard and Lambert, David L., 1993, "Abundances in CH Subgiants: Evidence of Mass Transfer onto Main-Sequence Companions", *Astrophys. J.*, **417**, 287. [DOI], [ADS]

Sneden, C., Lambert, D. L. and Pilachowski, C. A., 1981, "A study of CNO elements in barium stars.", *Astrophys. J.*, **247**, 1052–1062. [DOI], [ADS]

Sneden, C., Lucatello, S., Ram, R. S., Brooke, J. S. A. and Bernath, P., 2014, "Line Lists for the A $^2\Pi$-X $^2\Sigma^+$ (Red) and B $^2\Sigma^+$-X $^2\Sigma^+$ (Violet) Systems of CN, $^{13}C^{14}N$, and $^{12}C^{15}N$, and Application to Astronomical Spectra", *Astrophys. J. Suppl.*, **214**, 26. [DOI], [ADS], [arXiv:1408.3828 [astro-ph.SR]]

Sneden, Christopher, Cowan, John J., Ivans, Inese I., Fuller, George M., Burles, Scott, Beers, Timothy C. and Lawler, James E., 2000, "Evidence of Multiple R-Process Sites in the Early Galaxy: New Observations of CS 22892-052", *Astrophys. J. Lett.*, **533**(2), L139–L142. [DOI], [ADS], [arXiv:astro-ph/0003086 [astro-ph]]

Sneden, Christopher Alan, 1973, *Carbon and Nitrogen Abundances in Metal-Poor Stars.*, Ph.D. thesis, The University of Texas at Austin. [ADS]

Spergel, D. N., Bean, R., Doré, O., Nolta, M. R., Bennett, C. L., Dunkley, J., Hinshaw, G., Jarosik, N., Komatsu, E., Page, L., Peiris, H. V., Verde, L., Halpern, M., Hill, R. S., Kogut, A., Limon, M., Meyer, S. S., Odegard, N., Tucker, G. S., Weiland, J. L., Wollack, E. and Wright, E. L., 2007, "Three-Year Wilkinson Microwave Anisotropy Probe (WMAP) Observations: Implications for Cosmology", *Astrophys. J. Suppl.*, **170**(2), 377–408. [DOI], [ADS], [arXiv:astro-ph/0603449 [astro-ph]]

Sriram, S., Kumar, Amit, Surya, Arun, Sivarani, T., Giridhar, Sunetra, Kathiravan, S., Anand, M. N., Jones, Damien, Grobler, Deon, Jakobsson, Robert, Chanumolu, Anantha, Unni, Athira, Dorje, Angchuk, Dorje, Tsewang and Gyalson, Tsewang, 2018, "Hanle echelle spectrograph: design and performance", in *Ground-based and Airborne Instrumentation for Astronomy VII*, (Eds.) Evans,

Christopher J., Simard, Luc, Takami, Hideki, Society of Photo-Optical Instrumentation Engineers (SPIE) Conference Series, 10702, [DOI], [ADS]

Stancliffe, R. J., Glebbeek, E., Izzard, R. G. and Pols, O. R., 2007, "Carbon-enhanced metal-poor stars and thermohaline mixing", *Astron. Astrophys.*, **464**(3), L57–L60. [DOI], [ADS]

Stancliffe, Richard J., Dearborn, David S. P., Lattanzio, John C., Heap, Stuart A. and Campbell, Simon W., 2011, "Three-dimensional Hydrodynamical Simulations of a Proton Ingestion Episode in a Low-metallicity Asymptotic Giant Branch Star", *Astrophys. J.*, **742**(2), 121. [DOI], [ADS], [arXiv:1109.1289 [astro-ph.SR]]

Starkenburg, Else, Shetrone, Matthew D., McConnachie, Alan W. and Venn, Kim A., 2014, "Binarity in carbon-enhanced metal-poor stars", *Mon. Not. Roy. Astron. Soc.*, **441**(2), 1217–1229. [DOI], [ADS], [arXiv:1404.0385 [astro-ph.SR]]

Stephenson, C. B., 1989, "A general catalogue of cool carbon stars", *Observatory*, **3**, 53. [ADS]

Straniero, Oscar, Gallino, Roberto and Cristallo, Sergio, 2006, "s process in low-mass asymptotic giant branch stars", *Nuclear Physics A*, **777**, 311–339. [DOI], [ADS], [arXiv:astro-ph/0501405 [astro-ph]]

Symbalisty, E. M. D., Schramm, D. N. and Wilson, J. R., 1985, "An expanding vortex site for the r-process in rotating stellar collapse", *Astrophys. J. Lett.*, **291**, L11–L14. [DOI], [ADS]

Thévenin, F. and Idiart, T. P., 1999, "Stellar Iron Abundances: Non-LTE Effects", *Astrophys. J.*, **521**(2), 753–763. [DOI], [ADS], [arXiv:astro-ph/9906433 [astro-ph]]

Thielemann, F. K., Eichler, M., Panov, I. V. and Wehmeyer, B., 2017, "Neutron Star Mergers and Nucleosynthesis of Heavy Elements", *Annual Review of Nuclear and Particle Science*, **67**, 253–274. [DOI], [ADS], [arXiv:1710.02142 [astro-ph.HE]]

Tominaga, Nozomu, Iwamoto, Nobuyuki and Nomoto, Ken'ichi, 2014, "Abundance Profiling of Extremely Metal-poor Stars and Supernova Properties in the Early Universe", *Astrophys. J.*, **785**(2), 98. [DOI], [ADS], [arXiv:1309.6734 [astro-ph.SR]]

Travaglio, Claudia, Gallino, Roberto, Arnone, Enrico, Cowan, John, Jordan, Faith and Sneden, Christopher, 2004, "Galactic Evolution of Sr, Y, And Zr: A Multiplicity of Nucleosynthetic Processes", *Astrophys. J.*, **601**(2), 864–884. [DOI], [ADS], [arXiv:astro-ph/0310189 [astro-ph]]

Tsuji, T., Lye, M., Tomoika, K., Okada, T. and Sato, H., 1991, "A very high 12C/13C ratio in some CH stars : implications for dredge-up in AGB evolution during the metal-poor era.", *Astron. Astrophys.*, **252**, L1. [ADS]

Umeda, Hideyuki and Nomoto, Ken'ichi, 2005, "Variations in the Abundance Pattern of Extremely Metal-Poor Stars and Nucleosynthesis in Population III Supernovae", *Astrophys. J.*, **619**(1), 427–445. [DOI], [ADS], [arXiv:astro-ph/0308029 [astro-ph]]

Valenti, J. A. and Piskunov, N., 1996, "Spectroscopy made easy: A new tool for fitting observations with synthetic spectra.", *Astron. Astrophys. Suppl.*, **118**, 595–603. [ADS]

Van Eck, S., Goriely, S., Jorissen, A. and Plez, B., 2003, "More lead stars", *Astron. Astrophys.*, **404**, 291–299. [DOI], [ADS], [astro-ph/0302075]

van Winckel, Hans, 2003, "Post-AGB Stars", *Ann. Rev. Astron. Astrophys.*, **41**, 391–427. [DOI], [ADS]

Vanture, A. D., 1992, "The CH Stars. III. Heavy Element Abundances", *Astron. J.*, **104**, 1997–2004. [DOI], [ADS]

Vernet, J., Dekker, H., D'Odorico, S., Kaper, L., Kjaergaard, P., Hammer, F., Randich, S., Zerbi, F., Groot, P. J., Hjorth, J., Guinouard, I., Navarro, R., Adolfse, T., Albers, P. W., Amans, J. P., Andersen, J. J., Andersen, M. I.,

Binetruy, P., Bristow, P., Castillo, R., Chemla, F., Christensen, L., Conconi, P., Conzelmann, R., Dam, J., de Caprio, V., de Ugarte Postigo, A., Delabre, B., di Marcantonio, P., Downing, M., Elswijk, E., Finger, G., Fischer, G., Flores, H., François, P., Goldoni, P., Guglielmi, L., Haigron, R., Hanenburg, H., Hendriks, I., Horrobin, M., Horville, D., Jessen, N. C., Kerber, F., Kern, L., Kiekebusch, M., Kleszcz, P., Klougart, J., Kragt, J., Larsen, H. H., Lizon, J. L., Lucuix, C., Mainieri, V., Manuputy, R., Martayan, C., Mason, E., Mazzoleni, R., Michaelsen, N., Modigliani, A., Moehler, S., Møller, P., Norup Sørensen, A., Nørregaard, P., Péroux, C., Patat, F., Pena, E., Pragt, J., Reinero, C., Rigal, F., Riva, M., Roelfsema, R., Royer, F., Sacco, G., Santin, P., Schoenmaker, T., Spano, P., Sweers, E., Ter Horst, R., Tintori, M., Tromp, N., van Dael, P., van der Vliet, H., Venema, L., Vidali, M., Vinther, J., Vola, P., Winters, R., Wistisen, D., Wulterkens, G. and Zacchei, A., 2011, "X-shooter, the new wide band intermediate resolution spectrograph at the ESO Very Large Telescope", *Astron. Astrophys.*, **536**, A105. [DOI], [ADS], [arXiv:1110.1944 [astro-ph.IM]]

Villar, V. A., Guillochon, J., Berger, E., Metzger, B. D., Cowperthwaite, P. S., Nicholl, M., Alexander, K. D., Blanchard, P. K., Chornock, R., Eftekhari, T., Fong, W., Margutti, R. and Williams, P. K. G., 2017, "The Combined Ultraviolet, Optical, and Near-infrared Light Curves of the Kilonova Associated with the Binary Neutron Star Merger GW170817: Unified Data Set, Analytic Models, and Physical Implications", *Astrophys. J. Lett.*, **851**(1), L21. [DOI], [ADS], [arXiv:1710.11576 [astro-ph.HE]]

Wanajo, Shinya, Kajino, Toshitaka, Mathews, Grant J. and Otsuki, Kaori, 2001, "The r-Process in Neutrino-driven Winds from Nascent, "Compact" Neutron Stars of Core-Collapse Supernovae", *Astrophys. J.*, **554**(1), 578–586. [DOI], [ADS], [arXiv:astro-ph/0102261 [astro-ph]]

Wanajo, Shinya, Nomoto, Ken'ichi, Iwamoto, Nobuyuki, Ishimaru, Yuhri and Beers, Timothy C, 2006, "Enrichment of Very Metal Poor Stars with Both

r-Process and s-Process Elements from 8-10 M⊙ Stars", *Astrophys. J.*, **636**(2), 842

Warner, B., 1965, "The barium stars", *Mon. Not. Roy. Astron. Soc.*, **129**, 263. [DOI], [ADS]

Wisotzki, L., Koehler, T., Groote, D. and Reimers, D., 1996, "The Hamburg/ESO survey for bright QSOs. I. Survey design and candidate selection procedure.", *Astron. Astrophys. Suppl.*, **115**, 227. [ADS]

Worley, C. C., Hill, V., Sobeck, J. and Carretta, E., 2013, "Ba and Eu abundances in M 15 giant stars", *Astron. Astrophys.*, **553**, A47. [DOI], [ADS], [arXiv:1302.6122 [astro-ph.SR]]

Wu, Meng-Ru, Fernández, Rodrigo, Martínez-Pinedo, Gabriel and Metzger, Brian D., 2016, "Production of the entire range of r-process nuclides by black hole accretion disc outflows from neutron star mergers", *Mon. Not. Roy. Astron. Soc.*, **463**(3), 2323–2334. [DOI], [ADS], [arXiv:1607.05290 [astro-ph.HE]]

Yang, Guo-Chao, Liang, Yan-Chun, Spite, Monique, Chen, Yu-Qin, Zhao, Gang, Zhang, Bo, Liu, Guo-Qing, Liu, Yu-Juan, Liu, Nian, Deng, Li-Cai, Spite, Francois, Hill, Vanessa and Zhang, Cai-Xia, 2016, "Chemical abundance analysis of 19 barium stars", *Research in Astronomy and Astrophysics*, **16**(1), 19. [DOI], [ADS], [arXiv:1602.08704 [astro-ph.SR]]

Yong, David, Norris, John E., Bessell, M. S., Christlieb, N., Asplund, M., Beers, Timothy C., Barklem, P. S., Frebel, Anna and Ryan, S. G., 2013, "The Most Metal-poor Stars. II. Chemical Abundances of 190 Metal-poor Stars Including 10 New Stars with [Fe/H] ¡= -3.5", *Astrophys. J.*, **762**(1), 26. [DOI], [ADS], [arXiv:1208.3003 [astro-ph.GA]]

Yoon, Jinmi, Beers, Timothy C., Placco, Vinicius M., Rasmussen, Kaitlin C., Carollo, Daniela, He, Siyu, Hansen, Terese T., Roederer, Ian U. and Zeanah, Jeff, 2016, "Observational Constraints on First-star Nucleosynthesis. I. Evidence

for Multiple Progenitors of CEMP-No Stars", *Astrophys. J.*, **833**(1), 20. [DOI], [ADS], [arXiv:1607.06336 [astro-ph.SR]]

Yoon, Jinmi, Whitten, Devin D., Beers, Timothy C., Lee, Young Sun, Masseron, Thomas and Placco, Vinicius M., 2020, "Identification of a Group III CEMP-no Star in the Dwarf Spheroidal Galaxy Canes Venatici I", *Astrophys. J.*, **894**(1), 7. [DOI], [ADS], [arXiv:1910.10038 [astro-ph.SR]]

Zacs, L., Nissen, P. E. and Schuster, W. J., 1998, "The chemical composition of HD 196944: a carbon and s-process rich, very metal-poor star", *Astron. Astrophys.*, **337**, 216–222. [ADS]

Zamora, O., Abia, C., de Laverny, P. and Domínguez, I., 2004, "An attempt to derive Mg isotopic ratios in carbon stars", *Memorie della Societa Astronomica Italiana*, **75**, 596. [ADS]

Začs, L., Schmidt, M. R. and Schuster, W. J., 2000, "A carbon rich star BD $+75^{deg}$ 348: a binary?", *Astron. Astrophys.*, **358**, 1022–1026. [ADS]

Zhang, L., Ishigaki, M., Aoki, W., Zhao, G. and Chiba, M., 2009, "Chemical Compositions of Kinematically Selected Outer Halo Stars", *Astrophys. J.*, **706**, 1095–1113. [DOI], [ADS], [arXiv:0907.0076 [astro-ph.GA]]

Zhang, L., Karlsson, T., Christlieb, N., Korn, A. J., Barklem, P. S. and Zhao, G., 2011, "The Hamburg/ESO R-process Enhanced Star survey (HERES). VI. The Galactic chemical evolution of silicon", *Astron. Astrophys.*, **528**, A92. [DOI], [ADS], [arXiv:1006.3594 [astro-ph.SR]]

Zijlstra, A. A., 2004, "Low-mass supernovae in the early Galactic halo: source of the double r/s-process enriched halo stars?", *Mon. Not. Roy. Astron. Soc.*, **348**, L23–L27. [DOI], [ADS], [astro-ph/0312481]